

# **Parallel and Miniaturized Combinatorial Synthesis and Analysis of Small Molecules on Droplet Microarray**

Zur Erlangung des akademischen Grades eines

DOKTORS DER NATURWISSENSCHAFTEN

(Dr. rer. nat.)

von der KIT-Fakultät für Chemie und Biowissenschaften

des Karlsruher Instituts für Technologie (KIT)

genehmigte

DISSERTATION

von

**M. Sc. Julius Höpfner**

aus Landau i. d. Pfalz

Dekan: Prof. Dr. Martin Bastmeyer

Referent: Prof. Dr. Pavel Levkin

Korreferent: Prof. Dr. Michael Meier

Tag der mündlichen Prüfung: 06.02.2024



---

“Dreams without goals are just dreams, and ultimately, they fuel disappointment. On the road to achieving your dreams, you must apply discipline, but more importantly, consistency. Without commitment, you'll never start, but without consistency, you'll never finish.”

Denzel Washington

---

**Parallele und Miniaturisierte Kombinatorische  
Synthese und Analyse kleiner Moleküle auf dem  
Droplet Microarray**

---





## Kurzfassung

Die immer größer werdenden Kosten der pharmazeutischen Forschung stellen derzeit Herausforderungen für die Produktivität der Arzneimittelforschung und -entwicklung dar, wobei die Kosten 2,5 Milliarden US-Dollar übersteigen und die Zeitspannen von der Identifizierung des Zielmoleküls bis zur potenziellen FDA-Zulassung bis zu 20 Jahre betragen. Die Miniaturisierung der Synthese und Screenings neuer Verbindungen stellt eine potenzielle Lösung dar, um dieser Herausforderung zu begegnen. Der Droplet Microarray, eine vielseitige Plattform, die die Bildung von Nanoliter-großen Tröpfchen ermöglicht, die durch superhydrophobe Grenzen getrennt sind und als unabhängige Reaktionsgefäße dienen, hat sich für miniaturisierte biologische Screenings als wirksam erwiesen. Allerdings ist sein Potenzial als integrierte Plattform für Synthese, Analyse und biologische Screenings noch nicht ausgeschöpft. Die Reduzierung der erforderlichen Reaktionsvolumina auf Nanoliter und anschließende Analyse der Synthesergebnisse und biologischen Aktivität auf dem Chip könnte Zeit und Ressourcen sparen.

Diese Dissertation ist in drei Hauptabschnitte unterteilt, wobei der Schwerpunkt des ersten Teils auf der Integration von Mehrkomponentenreaktionen durch einen Festphasenansatz liegt, um eine vielfältige Palette von lipidähnlichen Verbindungen zu synthetisieren. Dies umfasste die Kombination der Vierkomponenten Ugi Reaktion mit der Dreikomponenten Thiolacton-Aminolyse-Disulfid-Austauschreaktion, was zu einem synthetischen Setup führte, das in der Lage ist, über 10.000 neuartige lipidähnliche Verbindungen zu generieren. Um die Machbarkeit der Methode zu veranschaulichen, wurden 128 lipidähnliche Verbindungen im Nanoliter-Maßstab synthetisiert, wobei lediglich 94  $\mu\text{L}$  Reaktionslösungen und 54 nmol Reagenzien für die gesamte synthetische Kaskade benötigt wurden. Die Effizienz der Synthese wurde durch die on-chip MALDI-TOF-MS Analyse weiter demonstriert, wodurch die erfolgreiche Synthese von 91% der gewünschten Produkte bestätigt wurde. Um das Potenzial der Plattform zu verdeutlichen, wurden die 128 synthetisierten Verbindungen direkt on-chip auf ihre antibakteriellen Eigenschaften in einem kolorimetrischen Assay gescreent. Darüber hinaus wurde ein alternativer synthetischer Pfad für die Produktion von lipidähnlichen Verbindungen erforscht.

In der zweiten Phase der Dissertation wurde eine Bibliothek von 325 neuartigen MEK-Inhibitoren mithilfe der palladiumkatalysierten SUZUKI-MIYAUURA Reaktion konstruiert, wobei nur bemerkenswerte 300 nL Reaktionslösungen pro Verbindung verbraucht wurden. Die on-chip-Synthese wurde sowohl durch on-chip MALDI-TOF-MS als auch durch Messungen von einer herkömmlichen MALDI-TOF-MS steel plate validiert, wobei Identifikationsraten von bis zu 93% erreicht wurden. Zur weiteren Charakterisierung der synthetisierten Verbindungen wurden die Kinetik der UV-induzierten Freisetzung von der Oberfläche durch LC-MS untersucht, was zu einer Endkonzentration von 10  $\mu$ L für jede Verbindung führte, die als ausreichend für anschließende zellbasierte Screenings gegen HT-29-Zellen betrachtet wurde. Das on-chip-Screening zeigte 49 Verbindungen mit verbesserten antikanzerogenen Eigenschaften, was die Wirksamkeit der synthetisierten MEK-Inhibitoren zeigte. Unter diesen wurden zwei wirksame Moleküle in größerem Maßstab synthetisiert und durch NMR- und ESI-MS-Analysen charakterisiert. Anschließend wurden diese beiden Verbindungen einem konventionellen zellbasierten Assay unterzogen, die in 384-Well-Platten durchgeführt wurden.

Im letzten Teil der Thesis fungierte das Droplet Microarray als miniaturisierte und parallelisierte Plattform zur Optimierung der Reaktionsbedingungen der on-chip HECK Reaktion. Unter Verwendung eines Festphasenansatzes wurden verschiedene Reaktionsbedingungen systematisch auf ihre Wirksamkeit bei der Synthese einer repräsentativen Verbindung untersucht. Dies führte zur Synthese der Verbindung mit einer maximalen Reinheit von 82%. Allerdings zeigte eine Untersuchung der Auswirkungen anderer Substrate bestehende Einschränkungen der Plattform auf.



## Abstract

The escalating costs of pharmaceutical research are currently posing challenges to the productivity of drug discovery and development, with costs exceeding 2.5 billion dollars and timelines extending up to 20 years from target identification to potential FDA approval. Miniaturization of the synthesis and screening of new compounds presents a potential solution to address this challenge. The Droplet Microarray, a versatile platform that allows the formation of nanoliter sized droplets that are separated by superhydrophobic borders and serve as independent reaction vessels, has proven effective for miniaturized biological screenings. However, its potential as an integrated platform for synthesis, analysis, and biological screening is not yet fully realized. Scaling down the required reaction volumes to nanoliters and subsequently analyzing synthesis outcomes and biological activity on-chip could save time and resources.

This thesis is divided into three key sections, the primary focus centered on integrating multi-component reactions through a solid-phase approach to synthesize a diverse array of lipid-like compounds. This involved combining the four-component Ugi reaction with the three-component thiolactone-aminolysis disulfide-exchange reaction, resulting in a synthetic setup capable of generating over 10,000 novel lipid-like compounds. To illustrate the method's feasibility, 128 lipid-like compounds were synthesized at the nanoliter scale, utilizing a mere 94  $\mu\text{L}$  of reaction solutions and a minimal 54 nmol of reagents for the entire synthetic cascade. The efficiency of the synthesis was further demonstrated by on-chip MALDI-TOF-MS analysis, confirming the successful formation of 91% of the desired products within the compound library. To showcase the potential of the platform, the 128 synthesized compounds underwent direct on-chip screening for antibacterial properties in a colorimetric assay. Furthermore, an alternative synthetic pathway for the production of lipid-like compounds was explored. The process involved immobilizing the reactive 2-pyridyl disulfide group onto the surface, followed by a thiolactone-aminolysis exchange reaction. This approach reduced the required number of reaction steps to two and decreased the overall reaction time by 33% compared to the alternative synthetic cascade.

In the second phase of the thesis, a library of 325 novel MEK inhibitors was constructed using the palladium-catalyzed SUZUKI-MIYAURO reaction, with a remarkably economical consumption of only 300 nL of reaction solutions per compound. The on-chip synthesis was validated using both on-chip MALDI-TOF-MS and measurements from a ground steel plate, achieving identification rates of up to 93%. To further characterize the synthesized compounds,

the kinetics of UV-induced release from the surface were investigated through LC-MS, leading to a final concentration of 10  $\mu$ L for each compound, which was considered sufficient for subsequent cell-based screening against HT-29 cells. The on-chip screening revealed 49 compounds with enhanced anti-cancer activity, showcasing the effectiveness of the synthesized MEK inhibitors. Among these, two potent molecules were synthesized in larger scale and analyzed through NMR and ESI-MS analyses. Subsequently, these two compounds underwent more conventional cell-based assays, conducted in 384-well plates.

In the final part of the thesis, the Droplet Microarray functioned as a miniaturized and parallelized platform for optimizing the reaction conditions of the on-chip HECK reaction. Employing a solid-phase approach, various reaction conditions were systematically explored for their efficacy in synthesizing a representative compound. This effort resulted in the attainment of the compound with a maximum purity of 82%. However, an investigation into the impact of other substrates revealed existing limitations of the platform.



## Preface

This thesis is based on results of my research in the group of Prof. Dr. Pavel Levkin between April 2021 and January 2024 at the INSTITUTE OF BIOLOGICAL AND CHEMICAL SYSTEMS – FUNCTIONAL MATERIAL SYSTEMS (IBCS-FMS) at KARLSRUHE INSTITUTE OF TECHNOLOGY (KIT).

All LC-MS measurements throughout the thesis took place at the INSTITUTE OF TECHNOLOGY (INT) in the laboratory of DR. FLORIAN FEIST. All bacterial work was performed in PROF. DR. THOMAS SCHWARTZ'S laboratory at the Institute of Functional Interfaces (IFG). Initial cultivation of HT-29 cells was executed by CHARLOTTE LUCHENA (KIT). All MALDI-TOF-MS measurements were carried out by DR. STEFAN SCHMIDT (CeMOS, Mannheim).

The optimization and the purity analysis of the Ugi products, as well as the optimization of the thermically induced thiol-ene reactions in Chapter 3.1 was conducted by MARIUS BREHM. His PhD thesis is cited at the corresponding passages in the text.

In order to expand the toolbox of reliable reactions on DMA the SUZUKI-MIYAURA reaction (SMR) was introduced. The workflow and purity analysis was initially developed in previous works by MARIUS BREHM, which resulted in joint publication.<sup>[1]</sup> The work of BREHM will be summarized as a short introduction to the method.

The results shown in chapters 3.2.2 - 3.2.5 were obtained in close collaboration with MAXIMILIAN SEIFERMANN (KIT). The preparation of the substrates as well as the amidation steps were performed by MAXIMILIAN SEIFERMANN (KIT). All SUZUKI-MIYAURA reactions on-chip and in flask were performed by JULIUS HÖPFNER (KIT), the experimental planning was performed together. Sample preparation for the MALDI-TOF-MS measurements was performed by JULIUS HÖPFNER. The performance of the anti-cancer screening on-chip was performed by MAXIMILIAN SEIFERMANN (KIT). The screening in 384-well plates and the preparation of the LC-MS samples was performed together. The analysis of the entire raw data was done independently.

Parts of the results were presented at the following conferences as poster:

ELRIG DRUG DISCOVERY 2022 (4<sup>th</sup>-5<sup>th</sup> October 2022, London, UK)  
EFMC-ASMC International Symposium on Advances in Synthetic and Medicinal Chemistry (3<sup>rd</sup>-7<sup>th</sup> September 2023, Zagreb, Croatia)







Hiermit versichere ich, diese Arbeit selbstständig verfasst zu haben, dass ich keine anderen als die angegebenen Quellen und Hilfsmittel benutzt habe, dass ich die wörtlich oder inhaltlich übernommenen Stellen als solche kenntlich gemacht habe und die Satzung des KIT zur Sicherung guter wissenschaftlicher Praxis in der jeweils gültigen Fassung beachtet habe.

Karlsruhe, den 08.01.2024

X

# Table of Contents

Kurzfassung.....	I
Abstract .....	IV
Preface .....	VII
Table of Contents .....	XI
1 General Introduction .....	1
1.1 Miniaturized Synthesis and Analytics.....	1
1.1.1 Small Scale Synthesis – Theory and Application .....	1
1.1.2 High-Throughput Analytics .....	3
1.2 The Droplet Microarray .....	5
1.2.1 Wetting of Solid Surfaces – Theoretical Background and Application .....	5
1.2.2 Manufacturing and Surface Functionalization .....	7
1.2.3 Application in Biology and Chemistry.....	10
2 Motivation .....	17
3 Results and Discussion.....	19
3.1 Combining Multi-Component Reactions on Droplet Microarrays for Parallel and Miniaturized Synthesis and Analysis of Antibacterial Small Molecules .....	19
3.1.1 Introduction .....	19
3.1.2 Optimization of the Reaction Conditions and Purity Analysis using Liquid Chromatography – Mass Spectrometry .....	22
3.1.3 High-Throughput Analysis using Matrix-assisted Laser Desorption/Ionization Mass Spectrometry .....	34
3.1.4 Antibacterial Activity of the Lipid-Like Compounds .....	44
3.1.5 Alternative Route for the Synthesis of Lipid-Like Compounds .....	52
3.2 Miniaturization of the Palladium-Catalyzed Suzuki-Miyaura Reaction .....	56
3.2.1 Synthesis of Biphenyls on Droplet Microarrays at Nanoliter Scale.....	56

3.2.2	Combinatorial Synthesis of Potential MEK-Inhibitors in Nanoliter Scale .....	62
3.2.3	Purity Analysis and Photorelease from the Surface of the Droplet Microarray...	68
3.2.4	Downscaling and Conformation of Synthetic Success in High-Throughput .....	76
3.2.5	Miniaturized cell-based assay for MEK Inhibitors .....	80
3.3	Miniaturization of the Heck Reaction .....	88
3.3.1	Introduction .....	88
3.3.2	Nanomolar Synthesis of Stilbenes and Cinnamates on Droplet Microarrays .....	90
3.3.3	Defining the optimal reaction conditions via LC-MS .....	91
4	Conclusion and Outlook.....	97
5	Experimental Part.....	104
5.1	Methods.....	104
5.1.1	Fabrication of the Droplet Microarray .....	104
5.1.2	Dispensing on Droplet Microarray.....	105
5.1.3	Preparation of the Droplet Microarray for Synthesis .....	105
5.1.4	Solid-phase UGI Reaction.....	105
5.1.5	Solid-phase UV-induced Thiol-Ene Reaction.....	106
5.1.6	Solid-phase Thiolactone-Aminolysis Disulfide-Exchange Reaction.....	106
5.1.7	Synthesis of the 2-Pyridyl Disulfide Derivatives .....	106
5.1.8	Synthesis of the Homocysteine Thiolactone Derivatives.....	110
5.1.9	Bacterial assay on Droplet Microarray.....	113
5.1.10	Immobilization of Amino Acids .....	114
5.1.11	Attachment of the Structural Motif OTV .....	114
5.1.12	Solid-phase SUZUKI-MIYAUURA Reaction.....	114
5.1.13	Synthesis of SMR1.....	115
5.1.14	Synthesis of MEK Inhibitors.....	116
5.1.15	Cell Based Assay on Droplet Microarray .....	119

5.1.16	Cell Based Assay in 384-Well Plate .....	120
5.1.17	Solid-phase Heck Reaction .....	120
5.1.18	Cleavage from the Surface .....	120
5.1.19	Analytical Methods .....	121
6	List of Abbreviations.....	124
7	List of Figures .....	127
8	List of Tables.....	135
9	Literature .....	137
10	Appendix .....	145
10.1	LC-MS Spectra.....	145
10.2	NMR spectra .....	159
10.3	Tables .....	179
10.4	CellTiter Glo .....	180



# 1 General Introduction

## 1.1 Miniaturized Synthesis and Analytics

The increasing costs associated with pharmaceutical research are presently impeding the effectiveness of drug discovery and development. The development of new drugs typically requires an extensive timeframe of over 20 years, accompanied by costs surpassing 2 billion dollars per drug.<sup>[2]</sup> Furthermore, the success rate in discovering and obtaining approval for new antimicrobial substances suitable for clinical use remains notably low.<sup>[3]</sup> It's crucial to note that these costs do not encompass the expenses related to the synthesis of compound libraries, a pivotal element in the drug discovery process. To confront these challenges, the field of pharmaceutical and medicinal research has embraced miniaturization approaches in the early stages of drug discovery. While current platforms often lack seamless integration of synthesis, analysis, and biological activity screening, there is a recognized need for an integrated system. Additionally, the trend of miniaturization is frequently coupled with parallelization. This integration aims not only to achieve cost- and emission-efficient processes but also to foster heightened scientific progress that may be unattainable through individual experiments. As scientist seek more streamlined and cost-effective methods, the drive towards integrated, miniaturized, and parallelized systems becomes increasingly evident in the quest for advancements in drug discovery.

### 1.1.1 Small Scale Synthesis – Theory and Application

The synthesis of novel, extensive compound libraries poses a significant challenge in early drug discovery. Conventional solution-based organic synthesis is typically conducted in relatively large flasks, requiring chemicals at least in the milligram and solvents in the milliliter scale to manage the subsequent isolation and characterization steps of the generated products. Combinatorial chemistry emerges as an approach to streamline the synthesis of such libraries. It involves systematically and repetitively linking various 'building blocks' to create a large array of structurally diverse compounds, forming what is known as a chemical library. Once synthesized, these compounds in the chemical library can be simultaneously screened for individual interactions with biological targets of interest.<sup>[4]</sup> Solid-phase synthesis (SPS) stands out as one of the most common strategies for constructing combinatorial libraries.<sup>[5, 6]</sup> Developed initially by MERRIFIELD in 1963 for peptide preparation,<sup>[7]</sup> SPS provides an elegant solution to challenges posed by solution-based synthesis, such as intricate work-ups of crude

reaction mixtures and compound loss during transfer steps. While these issues may be negligible at larger scales, they become crucial considerations when miniaturizing chemical reactions.

The synthesis of the target compounds involves using a linker attached to a solid anchor. The linker contains a reactive site that can be employed to construct the molecules either in a single reaction or through a reaction cascade. Excess reagents are typically used to compensate for the sluggish kinetics of reactions on interfaces. Once the reaction is complete, the remaining starting materials, reagents, and side products, along with the solvent, can be easily removed. Subsequently, the linker is cleaved, releasing the target compound. This approach achieves comparatively high purities without the need for additional purification steps. However, it requires careful planning to prevent side reactions involving the linker unit. The solid support commonly consists of beads made of porous polymer or crystalline porous glass.<sup>[8, 9]</sup>

A widely employed method for generating compound libraries through SPS is the "split and pool" approach. In this technique, a set of beads is divided into groups, and each group is modified with a distinct building block. Subsequently, the groups are combined and separated once more, with each subgroup now carrying different beads modified with various building blocks from the initial step. These subgroups then undergo a second reaction step, where each group is once again modified with a distinct building block. This process exponentially increases the number of compounds. Essentially, if the same reaction with the same building blocks is iterated, the achievable number of compounds grows exponentially with the number of reaction cycles, while the number of steps grows linearly. Ideally, the beads modified through this method each contain only one compound, leading to the designation of these libraries as one bead one compound (OBOC) libraries.<sup>[10]</sup>

In addition to the conventional SPS method, various alternative platforms have emerged for miniaturized HT synthesis. The group led by FRANK pioneered the SPOT technique, employing a cellulose membrane as the solid support for stepwise, combinatorial, and parallel peptide synthesis.<sup>[11]</sup> Over time, this approach has been expanded to encompass other chemical processes, including small molecules.<sup>[12]</sup> The cost-effectiveness of cellulose and its user-friendly handling constitute significant advantages of this platform. However, the size of the spots is influenced by the volume of the reaction solution pipetted, introducing the risk of cross-contamination or incomplete reactions if the applied solution is too much or too little.



In addition to miniaturized approaches employing SPS, there is extensive research focused on downscaling reactions in the solution phase. Many studies are directed towards optimizing experimental conditions on a smaller scale. Key considerations include parameters like the choice of solvent, potential evaporation issues, and compatibility of reagents with automated systems, such as non-contact liquid dispensers or liquid-handling robots. SANTANILLA *et al.* demonstrated the optimization of Pd-catalyzed cross-couplings in a 1536-well plate.<sup>[13]</sup> In this study, the primary focus was on optimizing the reaction, with the synthesized product utilized solely for determining the reaction yield. The entire process was facilitated by an automated pipetting robot capable of aspirating and mixing within the needle before dispensing the well-mixed reaction solution in a single droplet. The reactions were conducted in high-boiling and plastic-compatible solvents such as dimethyl sulfoxide (DMSO) and N-methyl-2-pyrrolidone (NMP). The readout involved a multiplexed approach using LC-MS after quenching the reaction mixture. Confirmatory analysis of hits was performed using ultra-performance liquid chromatography (UPLC)- mass spectrometry (MS).

Another example comes from the work of GAO *et al.*, where 384-well plates were used for various multicomponent reactions on a 10  $\mu$ L scale with 300-500 nmol of starting material. Stock solutions were prepared in the high-boiling solvent dispensed in low volumes. The main reaction solvent was added using multichannel pipettes. Solvents with lower boiling points, like dichloromethane (DCM) and methanol (MeOH), were used, and the well plates were sealed for incubation at room temperature without significant loss. The resulting libraries were not further utilized for biological screening. The primary focus was on comparing different multicomponent reactions and their yields. The synthesized products were analyzed through a chemoinformatic approach to evaluate and compare their biophysical properties with FDA-approved drugs.<sup>[14]</sup>

### **1.1.2 High-Throughput Analytics**

To validate the outcomes of small-scale reactions, it is crucial to utilize suitable analytical methods. These methods must be capable of extracting valuable information about the results of observed reactions in a HT manner. This ability is essential to monitor synthetic success efficiently during the synthesis of extensive compound libraries. The most commonly used analytical methods used in HT screenings will be shortly discussed.

Although spectrophotometric techniques, such as UV-VIS spectroscopy, have been integrated into both plate-based and flow-based reactors for monitoring reactions<sup>[15, 16]</sup> their role is confined due to the necessity of employing additional methods for precise product identification. Furthermore, the application of UV-VIS spectroscopy is constrained by the optical characteristics of the platform used. While spectroscopic methods offer significant advantages, particularly in terms of parallelization, as demonstrated in plate-reader setups, the major drawback is need inherent need for additional analytical methods.

The most notable alternative to spectroscopic analytics are MS-based systems. These systems are inherently label-free and offer significantly higher molecular specificity compared to optical methodologies. As a result, mass spectrometry has gained increasing popularity as the analytical platform of choice for HT screening.<sup>[17, 18]</sup>

Various MS-based platforms have been developed for high-throughput screenings, starting with established liquid chromatography (LC)–MS systems. However, these platforms come with an inherent trade-off in terms of speed. LC-MS is notably slower compared to optical detection techniques, mainly due to the time-consuming chromatographic separation, with a single run lasting up to 10 – 20 minutes.<sup>[19]</sup> This extended analysis time poses a significant drawback, especially when dealing with large libraries. To address this limitation, novel LC sampling approaches have been introduced to HT systems. Techniques such as multiple injections in a single experiment run (MISER) and mixed-MISER<sup>[20]</sup> allow for the mixing and monitoring of a target species, reducing the analysis time to approximately seven seconds per sample when analyzing 1536-density arrays.<sup>[21]</sup> Despite these improvements, there still exists a substantial gap in both the timescale and cost when compared to optically based techniques. Additionally, the multidimensional data obtained from each single run require high capacities for evaluation.

LC-free MS-based platforms, particularly laser-based techniques like matrix-assisted laser desorption ionization (MALDI), offer higher throughputs, exceeding one sample per second. However, these well-established methods come with the drawback of requiring time-consuming multistep plate preparation and the necessity for ionization to be performed under vacuum conditions.<sup>[22, 23, 24]</sup> A modified form of MALDI, known as self-assembled monolayers for MALDI (SAMDI), employs monolayers to provide precise control over surface chemistry, enhancing MALDI sensitivity to specific analytes of interest.<sup>[25]</sup> MALDI-MS has been successfully employed in an ultra HT screening utilizing 1536-well plates, with an analysis speed of 1.2 s/sample, showcasing the possibilities of the method.<sup>[26]</sup> Another LC-free MS-based

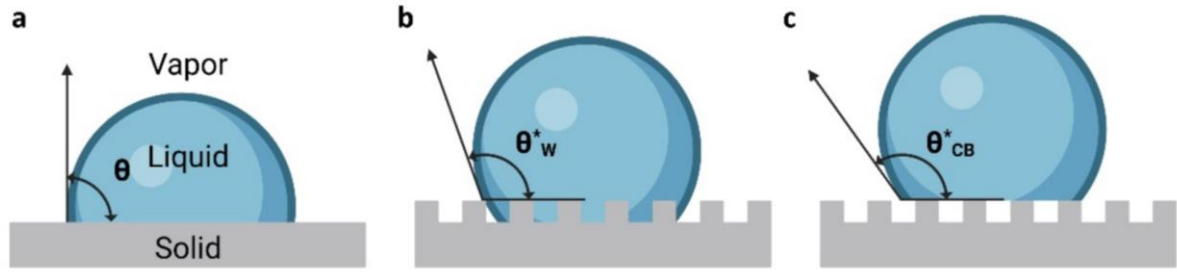
method, the droplet-based systems, commonly rely on acoustic or microfluidic methods for droplet generation and manipulation. The most recent version of acoustic-based systems employs acoustic desorption ejection coupled to an open port interface (ADE-OPI). This configuration enables analysis times faster than 0.3 seconds per sample, though specific considerations regarding solvent selection are necessary.<sup>[27, 28]</sup> Desorption-based methods, exemplified by desorption electrospray ionization (DESI), offer contactless, ambient, rapid analysis (>1 sample per second), and direct sample analysis. DESI demonstrates excellent matrix tolerance and eliminates the need for sample preparation.<sup>[29, 30]</sup> It has proven successful in studying various organic reactions in high-throughput screenings, including the SONOGASHIRA coupling<sup>[31]</sup> and the SUZUKI-MIYAUURA reaction.<sup>[32]</sup>

A frequently employed technique for assessing both the purity and structural information of new compounds is Nuclear Magnetic Resonance (NMR). However, this method has its limitations, including relatively long measurement times and the necessity for a high quantity of highly concentrated samples in the milligram range. Additionally, the solvent must be exchanged to deuterated solvents, requiring extra handling steps. The measurement itself needs to be conducted in a specific glass tube, adding another transferring step to the process. As a result, NMR is typically reserved for analyzing hit candidates that are resynthesized in larger quantities.

## **1.2 The Droplet Microarray**

### **1.2.1 Wetting of Solid Surfaces – Theoretical Background and Application**

The investigation of solid surface wettability is an enduring topic that has spanned various scientific and technological fields over the years. From ancient cave paintings to modern microfluidic devices, this subject has consistently attracted research interest due to its impact on practical applications such as oil–water separation, self-cleaning surfaces, and anti-fogging solutions.<sup>[33, 34, 35]</sup> Wettability, measured through the contact angle of a liquid droplet on a solid surface, serves as a direct indicator of wetting behavior. The contact angle's magnitude is directly linked to interfacial tensions at the solid-liquid-gas interface, shaping the overall wettability.<sup>[36]</sup> To exemplify this concept, Figure 1a shows schematic droplet exhibiting an acute contact angle on an ideal solid surface. This surface is characterized by its smoothness, homogeneity, and resistance to deformation.



**Figure 1:** Schematic depiction of different contact angle scenarios. (a) Contact angle of a liquid on an ideal surface. (b) Contact angle described by WENZEL, including the surface roughness increasing the overall wetted area. (c) Contact angle described by CASSIE and BAXTER. Surface cavities are partially occupied by trapped air.

If the liquid is water, we talk about hydrophilicity ( $\theta < 65^\circ$ ), hydrophobicity ( $\theta > 65^\circ$ ), superhydrophilicity ( $\theta < 10^\circ$ ) and superhydrophobicity ( $\theta > 150^\circ$ ). Historically, THOMAS YOUNG, often regarded as the pioneer of contact angle ( $\theta$ ) and wettability studies, provided the first description of the contact angle in 1805 (Equation ( I )) based on the energies of the three different interfaces liquid-vapor ( $\gamma_{lv}$ ), liquid-solid- ( $\gamma_{ls}$ ) and solid-vapor ( $\gamma_{sv}$ ).<sup>[37]</sup>

$$\cos(\theta) = \frac{\gamma_{sv} - \gamma_{ls}}{\gamma_{lv}} \quad (I)$$

Given that real surfaces rarely exhibit the ideal attributes described by *Young*, it becomes essential to consider additional factors, particularly surface roughness. The prediction of contact angles on diverse surfaces is addressed by theories proposed by CASSIE–BAXTER<sup>[38]</sup> and WENZEL.<sup>[39]</sup> These theories take into account the surface roughness, offering a more realistic framework for understanding and predicting wetting behavior on non-ideal surfaces. In the Wenzel state, the droplet fully wets the surface asperities, effectively increasing the overall wetted area (Figure 1b). The apparent contact angle ( $\theta_w^*$ ) in the Wenzel state is influenced by both the intrinsic contact angle on a flat, smooth surface ( $\theta$ ) and the ratio ( $r$ ) of the actual surface area to the projected surface area (Equation( II )).

$$\cos(\theta_w^*) = \cos(\theta) * r \quad (II)$$

In the Cassie-Baxter state, when a liquid droplet encounters a rough surface, it partially occupies the spaces between surface asperities, creating air pockets underneath (Figure 1c). This arrangement reduces the actual contact area between the liquid and the solid surface, resulting in a higher apparent contact angle compared to the Wenzel state on the same textured surface. The mathematical description is given in Equation ( III ). Here,  $\theta_{CB}^*$  is the apparent contact angle in the Cassie-Baxter state and  $\phi_s$  represents the fractional area of the solid surface in direct contact with the liquid.

$$\cos(\theta_{CB}^*) = \phi_s * [\cos(\theta) + 1] - 1 \quad (\text{III})$$

The mathematical explanations provided above underscore that the wettability of surfaces is fundamentally shaped by two critical factors: the surface structure and interface energies, directly linked to the surface chemistry. A famous example illustrating this synergy is observed in lotus leaves, where the combination of a microstructured surface and a hydrophobic wax coating results in the development of a superhydrophobic surface.<sup>[40]</sup>

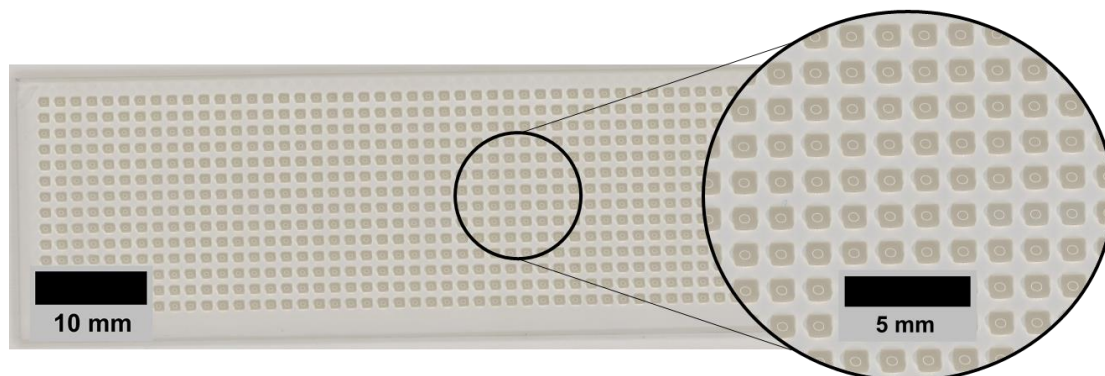
Although this discovery has inspired the creation of numerous bioinspired materials, the focus in this section of the introduction will be on the primary material extensively utilized throughout the thesis: a nanoporous copolymer composed of 2-hydroxyethyl methacrylate (HEMA) and ethylene dimethacrylate (EDMA). LEVKIN *et al.* showcased, that the copolymerization of HEMA and EDMA in a free radical polymerization forms a smooth polymer surface, while addition of porogens like cyclohexanol and 1-decanol introduce roughness in micro- and nanoscale to the surface.<sup>[41]</sup> This increase in surface roughness not only drastically changes the observed water contact angles after chemical modification of the polymer, it also alters the scattering of light.

Utilizing these early findings, GEYER *et al.* developed a microarray that eventually evolved into the precursor of the droplet microarray (DMA). They modified a glass substrate by applying thin layer of nanoporous HEMAcoEDMA polymer, transforming it into a superhydrophilic surface. The use of photolithography allowed for accurate adjustments to this surface, introducing superhydrophobic barriers composed of 2,2,3,3,3-pentafluoropropyl methacrylate. This technique facilitated the creation of highly accurate patterns at the micrometer scale.<sup>[42]</sup>

### 1.2.2 Manufacturing and Surface Functionalization

Expanding on this initial concept, the development of the DMA involved creating an array of hydrophilic spots on a superhydrophobic background. Figure 2 shows a photograph of a HEMAcoEDMA based DMA with 14 x 48 hydrophilic square spots. Although various DMAs exhibit different surface properties and undergo diverse manufacturing procedures, they share common attributes. Typically, they are crafted from microscope glass slides measuring 76 x 25 mm. These glass slides undergo modification to create a reactive layer that showcase either a high density of surface functional groups, heightened roughness, or a combination of both. The creation of hydrophilic and superhydrophobic areas occurs in the final step of the preparation process through UV-induced radical addition of hydrophilic thiols like 2-mercaptoethanol and cysteamine, or hydrophobic thiols such as 1*H*,1*H*,2*H*,2*H*-perfluorodecanthiol (PFDT) to alkene or alkyne moieties present on the surface. Utilizing photolithography ensures high resolution

and precision, enabling the creation of an extensive array of experimental vessels in an easy two-step process, reaching up to 2187 per DMA.<sup>[43]</sup>



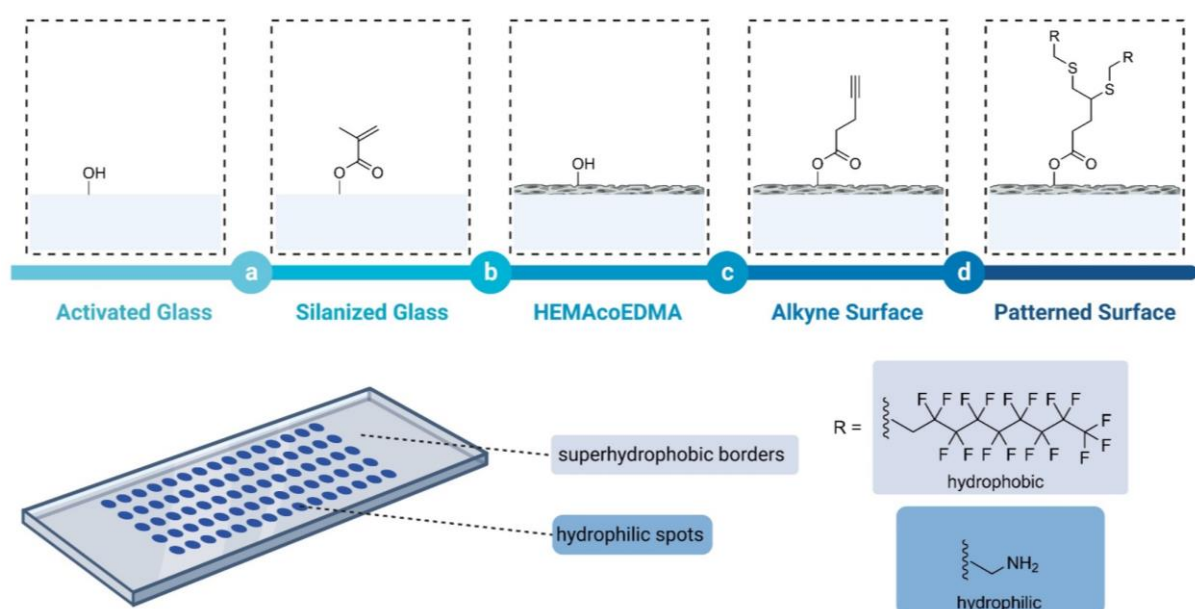
**Figure 2:** Image of a Droplet Microarray containing 672 square spots containing water. The spots have an edge length of 1 mm.

There exist three distinct versions of the DMA, each employing different principles for constructing the reactive layer on the glass substrate. These methods involve the utilization of a porous layer of HEMAcOEDMA polymer, directly extending the earlier work by GEYER *et al.*, nanoparticle coating, or the construction of dendritic structures attached to the glass substrate. This thesis exclusively utilizes the HEMAcOEDMA based DMA, and as such, will be described in detail. Additionally, brief introductions to the other two DMA versions will be provided, implementing a concise comparison between them.

The manufacturing process for the polymer-based DMA, as introduced by FENG *et al.* in 2014, is schematically illustrated in Figure 3.<sup>[44]</sup> Initially, the activated surface of a standard microscope glass slides (25 mm x 75 mm) is treated with a solution of 3-(trimethoxysilyl)propyl methacrylate in ethanol. In this step, silane crosslinks covalently to the surface's hydroxyl groups, forming silyl ethers (Figure 3a). Following the silanization step, a polymerization mixture containing HEMA, EDMA, porogens, and a photoinitiator is applied. UV light at 254 nm is used to initiate polymerization. The methacrylate groups on the surface act as anchor points for the polymer coating, ensuring robust attachment to the glass slide (Figure 3b). The polymer layer, post-polymerization, has a thickness of between 5 - 15  $\mu\text{m}$  and is hydrophilic due to HEMA-derived hydroxyl groups. To introduce alkyne-groups to the surface, these hydroxyl groups are modified via STEGLICH esterification with 4-pentynoic acid (Figure 3c).<sup>[45]</sup> The final step involves a UV-induced thiol-yne click reaction with PFDT and cysteamine chloride (Figure 3d). PFDT is applied to the entire surface, with areas to be hydrophilic covered by a photomask. UV irradiation at 254 nm covalently binds PFDT to 4-pentynoic acid. After washing, a solution of hydrophilic thiol is applied, and the slide is covered with non-patterned

quartz glass before UV irradiation. This photolithographic process precisely controls the spatial attachment of different thiols, creating distinct wettability areas: PFDT-modified regions are non-wettable (static WCA of  $170^\circ$ ), while areas with cysteamine chloride are wettable (static WCA of  $4^\circ$ ).

The DMA's mechanical and chemical stability arises from inherent material properties and covalent attachment of each layer and modification. It withstands common solvents, tolerates mild acidic or basic conditions, and can be dried with an air gun without losing coating or pattern components. Droplet formation is possible with various polar solvents. The polymer surface offers a high density of functional groups for further modification or solid-phase synthesis approaches. Significant limitations of this DMA variant included the unevenness of the polymer surface and the pronounced adsorption of molecules to the highly polar polymer surface in the hydrophilic spots.

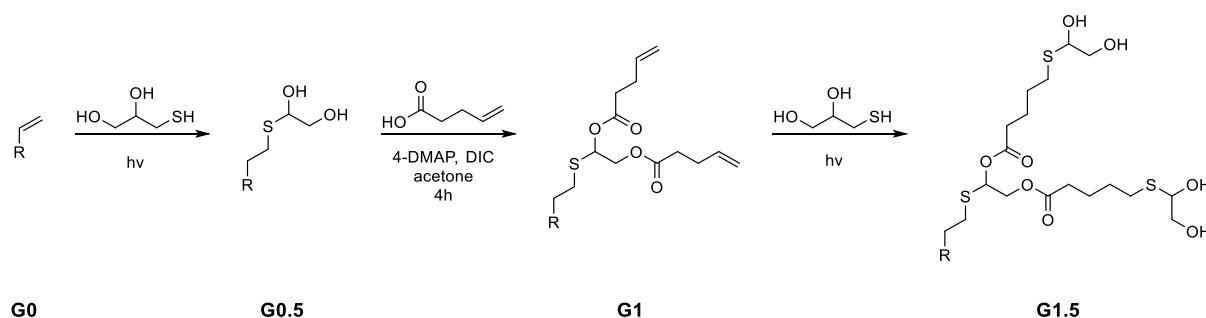


**Figure 3:** Schematic representation of the surface modifications involved in the manufacturing of the HEMAcOEDMA DMA. (a) Covalent attachment of 3-(trimethoxysilyl)propyl methacrylate which serves as an anchor point for the subsequent steps. (b) Photoinduced radical polymerization of nanoporous HEMAcOEDMA polymer. (c) Introduction of alkyne groups to the surface via STEGLICH esterification using 4-pentynoic acid. (d) Surface patterning through UV induced thiol-yne click chemistry using PFDT and cysteamine.

To overcome certain limitations of the polymer-based DMA, the Z-Slide was developed. Unlike its predecessor, the Z-Slide no longer features a covalently attached polymer layer to the glass substrate. Instead, it employs a coating of nanoparticles that are modified with trimethoxyvinylsilane before being spin-coated onto the glass surface. The vinyl groups on the nanoparticles can be modified using UV-induced thiol-ene reactions to attach various thiols, thereby creating superhydrophobic and hydrophilic areas. This design results in a surface that

effectively stabilizes aqueous droplets with reduced adsorption compared to the polymer. However, the stabilization of organic liquids is notably diminished.<sup>[45]</sup> Additionally, due to the limited degree of covalent attachment of the modified nanoparticles to the glass surface, the coating layer exhibits poor mechanical stability and a lower density of functional groups compared to the polymer-based DMA.

The latest iteration of the DMA incorporates a direct covalent modification of the glass substrate through dendritic growth. Initially, the glass substrate is modified with triethoxyvinylsilane, introducing vinyl groups to serve as anchor points for surface-dendron formation (Figure 4, G0). Using the thiol-ene reaction with thioglycerol doubles the number of reactive hydroxyl groups on the surface (Figure 4, G0.5). Subsequent modification with 4-pentenoic acid regenerates the vinyl groups for the next cycle (Figure 4, G1). This reaction sequence repeats until generation 3. The final layer of vinyl groups is employed for thiol-ene-based photopatterning using PFDT and thioglycerol.<sup>[46]</sup>



**Figure 4:** Schematic representation of the creation of the dendritic structure on DMA. *R* represents the immobilized silane on the glass substrate. The dendrons are synthesized by alternating the UV induced thiol-ene reaction using thioglycerol with Steglich esterification using 4-pentenoic acid.

A notable drawback of this DMA version, in comparison to other iterations, is the absence of increased surface roughness. The low roughness results in lower hydrophobicity ( $\theta_{St} = 104.3^\circ$ ) and hydrophilicity ( $\theta_{St} = 55.9^\circ$ ) of the patterned areas, leading to an overall lower confinement. Despite the general decrease in confinement, this version compensates by partially confining organic liquids with low surface tension, such as acetonitrile, which are not suitable for other types of DMA. Additionally, the complete covalent attachment contributes to a high binding energy, enhancing the stability of the Dendrimer DMA compared to its predecessors.

### 1.2.3 Application in Biology and Chemistry

Since its initial release, the DMA has found application in a diverse range of projects. Initially designed as a platform for high-throughput cell screenings with the aim of reducing material



consumption and generating large datasets in cell-based screenings, the earliest approach involved immersing the entire patterned surface in a cell suspension.<sup>[42]</sup> This resulted in cell attachment to the hydrophilic regions while being retained by the superhydrophobic borders, producing a high number of single spots but with a considerable risk of cross-contamination.

To address this issue, a more sophisticated approach was developed.<sup>[47]</sup> By pulling a larger droplet containing reagents or cell suspension across the patterned surface of the DMA, a small portion would be retained, forming an individual droplet due to discontinuous dewetting. This method created an array of single droplets containing cells, minimizing the risk of cross-contamination. To further enhance precision and reduce the risk of contamination, commercially available low-volume non-contact liquid dispensers were employed.<sup>[48, 49, 50]</sup>

The DMA has been widely applied in various biological contexts, including adherent and suspension cells<sup>[51]</sup>, spheroids<sup>[52]</sup>, embryoid bodies<sup>[53]</sup>, bacteria<sup>[50, 54]</sup> and even zebrafish embryos.<sup>[55]</sup> In a study by POPOVA *et al.*, the DMA was used for a drug sensitivity test of patient-derived chronic lymphocytic leukemia cells, demonstrating successful cell culture with only 100 cells, 0.03 nmol of the tested drug, and 50 nL of medium—reducing raw material usage by a factor of 200 compared to experimentation in 384 well plates.<sup>[56]</sup>

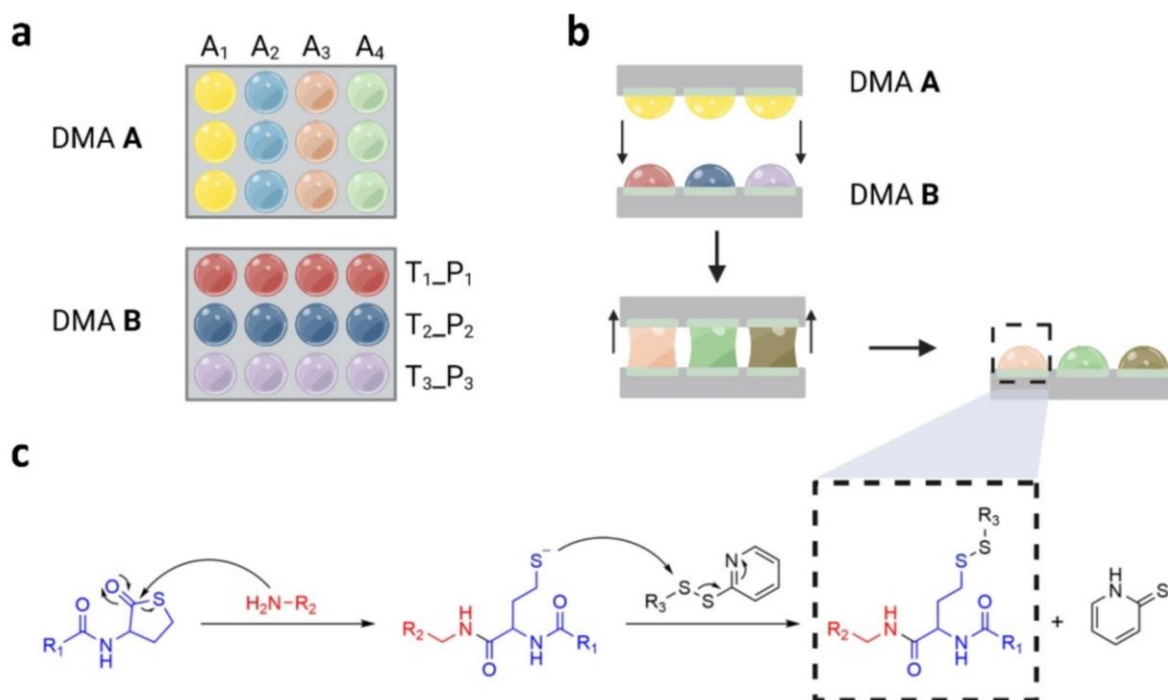
Another study by CUI *et al.* focused on 3D cell culturing on the DMA, creating spherical cell structures (spheroids) by seeding cell suspension onto the hydrophilic spots and inverting the DMA. Gravity led to sedimentation, forming spheroids.<sup>[57]</sup> The lack of walls in the DMA allowed the suspension to adhere to the surface without additional measures, facilitating the inversion process. Controlled merging of different liquid-containing spots enabled the creation of multi-spheroidal architectures, enhancing the model's resemblance to actual tissue.<sup>[58]</sup>

In addition to cell-related applications, the DMA has proven versatile for microbiological experiments. LEI *et al.* showcased a workflow for culturing diverse bacteria on the hydrophilic spots of the DMA. In two recent studies, they explored the bacterial response to treatment with different drugs.<sup>[50, 59]</sup> For instance, they treated carbapenem-resistant *Klebsiella pneumoniae*, methicillin-resistant *Staphylococcus aureus*, and *Pseudomonas aeruginosa* with a library of over 2000 compounds, aiming to identify new antibiotics for treating infections caused by resistant pathogens. The integration of this approach with a colorimetric assay based on the metabolization of the tetrazolium dye provided a straightforward and adaptable analysis pipeline applicable to various bacterial types.

Expanding beyond biological applications, SEIFERMANN *et al.* applied the DMA to material development.<sup>[60]</sup> They generated an array of hydrogels with varied compositions, subsequently screening them for photodegradability. In a highly parallelized and miniaturized approach, they screened 918 different polymeric compositions for photodegradation, utilizing only 551  $\mu\text{L}$  of reaction solution.

The previously highlighted research primarily involved adding compounds prepared in entirely different setups to discover new drugs or materials. However, to harness the full advantages of miniaturization, a crucial focus lies in the evolution of an integrated platform that seamlessly combines both chemistry and biology. It is imperative to optimize the chemistry to be not only compatible with the miniaturized format but also with biological assays.

To progress towards the ultimate objective of an integrated platform for chemical synthesis and biological screening, BENZ *et al.* introduced CHEMBIOS, utilizing the dendrimer version of the DMA.<sup>[61]</sup> This platform was designed as an optimized solution-phase synthesis platform. To demonstrate the compatibility of the chip with chemical reactions, they conducted the synthesis of lipid-like structures on round spots with a diameter of 3 mm using the three-component thiolactone-aminolysis disulfide-exchange (TADE) reaction (Figure 5c). In this approach, solutions of various amines were sequentially applied in columns on DMA slide A, forming an array of different amines in each row. On DMA slide B, solutions of thiolactone and 2-pyridyl disulfide derivatives were premixed in various combinations and applied in rows (Figure 5a). Merging both slides initiated the chemical reaction simultaneously in each droplet of the array, forming the lipid-like compounds (Figure 5b).

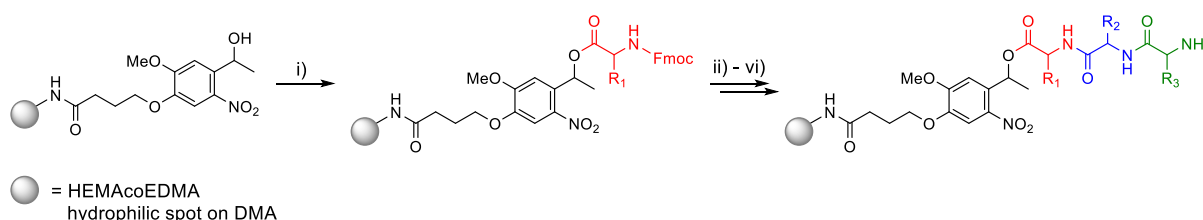


**Figure 5:** Application of the Dendrimer DMA for the solid-phase synthesis of lipid-like compounds. (a) Schematic representation of the experimental setup. Amine solutions are applied on DMA A in a column-wise manner, while thiolactone/2-pyridyl disulfide mixtures are applied in row-wise manner on DMA B. (b) Sandwiching of the slides leads to merging of the droplets, thus the start of the reaction. After 2 h of reaction time, the slides were detached from another, yielding the synthesized library of lipid-like compounds. (c) Schematic depiction of the mechanism of the used TADE reaction. The driving force of the reaction is the pyridine-2(1H)thione that prevents the reverse reaction.

The reaction occurred at room temperature and was characterized on the same platform using UV/Vis, IR-Spectroscopy, and MALDI-MS. The MALDI-MS measurements demonstrated high sensitivity, detecting as low as 0.1 femtomoles on a 500  $\mu\text{m}$  square spot. To underscore the platform's general biocompatibility, it was shown that the dendritic surface allows for the culture of both adherent and suspension cell lines, with viabilities exceeding 97% for three different cell lines. In a separate study, the same platform and reaction scheme were employed to prepare a library of lipidoids, which was subsequently screened on-chip for their transfection efficiency.<sup>[46]</sup>

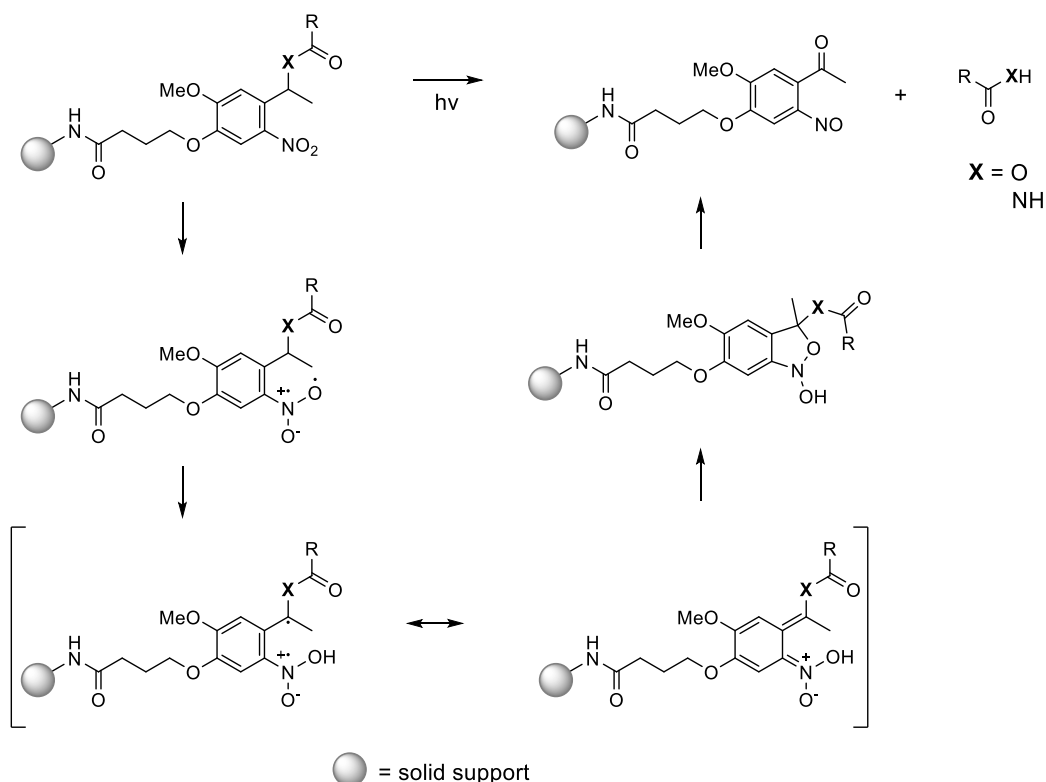
Despite the biocompatible surface, miniaturized solution chemistry faces challenges in purification. Addressing this, WIEDMANN *et al.* adapted liquid-liquid extraction (LLE) for the microarray format. They placed the extractant droplet at the hydrophobic border between the sample and an adjacent empty spot. Using 1-octanol with lower vapor pressure than water, they achieved faster extraction through aqueous droplet evaporation, efficiently transferring the extracted compounds to the empty spot.<sup>[49]</sup>

While LLE is potent for purifying chemical compounds, complex separation techniques like chromatography are often required for chemical reactions, ensuring sufficient purity for reliable screening. In a bid to simplify purification processes, ROSENFELD *et al.* adapted a solid-phase synthesis approach to the DMA, utilizing the high density of surface functionalities in the HEMAcOEDMA DMA. They modified the surface amines of the hydrophilic spots with a photolabile linker as a starting point for solid-phase synthesis, embarking on a synthetic route to a combinatorial library of tripeptides in the array format.<sup>[62]</sup> The process involved immobilizing initial Fmoc-protected amino acids to the photolinker through STEGLICH esterification (Figure 6i). The classical solid-phase peptide synthesis sequence of Fmoc-deprotection and carbodiimide-mediated, 1-hydroxybenzotriazole (HOBt)-catalyzed amide coupling then facilitated the formation of a small library of tripeptides (Figure 6ii-vi).



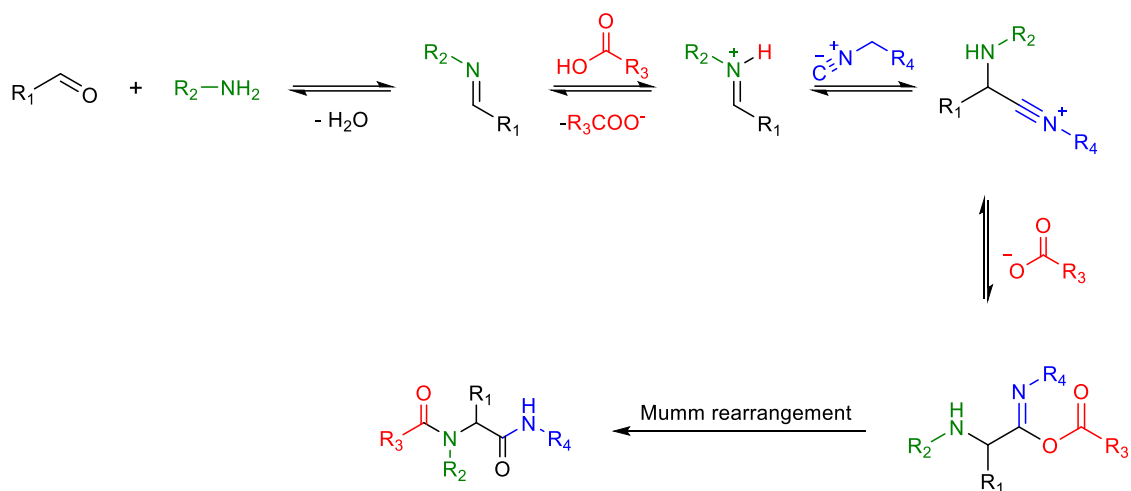
**Figure 6:** Overview reaction of the solid-phase synthesis of tripeptides on HEMAcOEDMA DMA. Starting with the immobilization of amino acids to the surface bound photolinker via Steglich esterification (i), followed by the standard solid-phase peptide synthesis containing deprotection of the immobilized amino acid (ii), coupling of the next amino acid (iii). These steps will be repeated (iv-vi) until the respective tripeptide is formed.

The selected photocleavable linker, 4-[4-(1-hydroxyethyl)-2-methoxy-5-nitrophenoxy] butanoic acid (hydroxyethyl photolinker, HEPL), features a *o*-nitrobenzylalcohol core motif. The hydroxy group serves for the reversible attachment of starting materials to the solid phase. Upon completion of the synthesis, irradiating the linker with UV light ( $\lambda = 365 \text{ nm}$ ) initiates a Norrish type 2 reaction, leading to product release through cleavage of the C-O bond in the benzylic position (Figure 7).<sup>[63]</sup>



**Figure 7:** Generalized mechanism of the UV induced cleavage of the photolinker utilized for solid-phase synthesis on DMA.<sup>[63]</sup> Hydrophilic spots on the HEMAcoEDMA DMA serve as solid-support.

Employing a similar solid-phase strategy, BREHM *et al.* extended the concept to adapt a multi-component reaction protocol for the one-step preparation of combinatorial libraries. They utilized immobilized amino acids on the surface, employing the surface amines for the Ugi four-component reaction.<sup>[64]</sup> This reaction begins with the condensation of an amine with an aldehyde, forming an iminium ion intermediate. This intermediate reacts with a carboxylic acid and an isocyanide to produce bisamides, although the mechanism is not conclusively clarified (Figure 8).<sup>[65]</sup> The most noteworthy side reaction to the Ugi reaction is the PASSERINI reaction, which involves only three components: an acid, an aldehyde, and an isocyanide. By choosing to attach the product through surface amines, contamination of the target compound with the Passerini side product could be avoided.<sup>[66]</sup>



**Figure 8:** Generalized mechanism of the Ugi four-component reaction. The reaction is initiated with the formation of an imine, which is subsequently protonated by a carboxylic acid. Following this, the isocyanide is added to the protonated imine. Further addition of the carboxylic acid results in the formation of an imide. It's important to note that all reaction steps in this sequence are reversible up to the point of the Mumm rearrangement. The Mumm rearrangement then occurs, yielding the bisamide product.<sup>[65]</sup>

Multi-component reactions, such as the UGI reaction, significantly increase the number of product molecules from a given set of starting materials compared to reactions with only two partners, making it an excellent choice for library construction. To demonstrate its potential in combinatorial drug synthesis, the UGI reaction was employed to synthesize a library of 588 products on a single DMA. For product analysis, larger droplets were combined for LC-MS analysis, and the entire library was detected with MALDI-MS after transferring the samples from the HEMA-EDMA slide to a non-patterned indium tin oxide (ITO) glass slide. To exemplify the release mechanism, doxorubicin was bound, and its time-dependent release upon irradiation with 365 nm UV light was demonstrated. Additionally, cells cultured on the DMA containing the bound model drug exhibited a significant decrease in viability when the drug was released.<sup>[64]</sup>

## 2 Motivation

The increasing demand for innovative pharmaceutical compounds, driven by the continuous emergence of complex diseases and the need for more effective treatments, underscores the urgency for innovation in drug discovery. Conventional approaches to drug synthesis encounter significant challenges, including time-consuming processes, high costs, and environmental concerns associated with large-scale reagent consumption. Accelerating hit identification in early drug discovery can be effectively achieved through the promising strategy of miniaturization, parallelization, and integration of all essential steps. This innovative approach not only speeds up the process but also diminishes the amount of material needed.

The primary aim of this work was to optimize the utilization of the Droplet Microarray, transforming it into a miniaturized and highly parallelized integrated platform. This platform was designed to incorporate on-chip synthesis, on-chip analysis, and subsequent on-chip biological screenings. This approach has the potential to address the challenges in traditional drug discovery, accelerating drug discovery in combination with highly reduced amount of needed reagents.

Divided into three key sections, the initial focus of the thesis involved the integration of multi-component reactions through a solid-phase approach to synthesize a diverse range of novel lipid-like compounds. These compounds underwent subsequent screening for antibacterial activity on-chip. In the second part of the work, the palladium-catalyzed SUZUKI-MIYAURO reaction was employed to construct a library of novel MEK inhibitors on a nanoliter scale, followed by on-chip cell screening to assess their potential anti-cancer properties.

The first part of the thesis aimed to showcase the capability of generating a diverse range of novel compounds through highly miniaturized and parallelized methods using DMA. By combining the four-component UGI reaction with the three-component thiolactone-aminolysis disulfide-exchange reaction, a significant quantity of unique compounds could be produced with minimal starting materials. The next steps involve optimizing reaction conditions on a larger scale, followed by the downsizing of the synthetic cascade to the nanoliter scale. For effective analysis of the extensive compound library, MALDI-TOF-MS is recommended to confirm the successful formation of desired products. To highlight the full potential of the platform, the synthesized compounds should undergo direct screening for their antibacterial properties. To streamline the synthetic process, it is advisable to explore an alternative route that involves fewer steps, thereby reducing the number of reactions needed. This approach not

only simplifies the synthetic pathway but also increases the potential variety of the produced compounds.

The first part of the study highlighted the remarkable throughput achieved with the DMA. The subsequent section focuses on incorporating the palladium-catalyzed SUZUKI-MIYAUURA reaction for the synthesis of novel MEK inhibitors. The construction of the compound library involves employing the well-established solid-phase synthesis approach. While this approach has been used in a previous study to synthesize biphenyls on a nanoliter scale, it was not yet possible to analyze the obtained small molecules in a high-throughput fashion. The implementation of MALDI-TOF-MS to validate the success of on-chip synthesis is essential, reducing the needed volumes and amounts of the product in comparison to established methods. To compare the novel on-chip MALDI-TOF-MS measurement to measurements conducted on traditional platforms like the ground steel plate, a droplet transfer of the synthesized library should be conducted. Additional fragment spectra could further demonstrate the successful synthesis of novel MEK inhibitors on DMA. For the subsequent on-chip cell-based screening of anti-cancer activity using the synthesized compounds, it is crucial to investigate the kinetics of UV-induced release from the surface. This investigation aims to ensure a rational final concentration of compounds for the screening process. To achieve this, the conversion of the intermediates should be investigated as well, providing insights into the conversion to the final compounds. The ultimate goal is to demonstrate the potential anti-cancer activity of the novel compounds through cell-based screening. A robust assay needs to be conducted to obtain valuable information about the potential biological activity of the compounds. Any potentially active compounds should be synthesized in larger quantities and tested in a more traditional fashion using 384-well plates.

Certainly, as an integrated platform for synthesis, analysis, and biological screening, expanding the DMA's toolbox is crucial. Implementing the HECK reaction could diversify the range of accessible compounds through solid-phase synthesis on-chip and make stilbenes and cinnamates a viable group of compounds to be synthesized on DMA. The DMA itself could serve as the ideal platform to screen various experimental setups and reaction conditions in a miniaturized and parallelized way. Assessing the purities of obtained products using different variations of catalytic species, bases, and solvents should lead to the optimization of the on-chip HECK reaction. Further investigation of possible UV-induced isomerizations could lead to the development of novel linker systems that have not yet been applied on DMA.



## 3 Results and Discussion

### 3.1 Combining Multi-Component Reactions on Droplet Microarrays for Parallel and Miniaturized Synthesis and Analysis of Antibacterial Small Molecules

The optimization and the purity analysis of the Ugi products, as well as the optimization of the thermally induced thiol-ene reactions in Chapter 3.1 was conducted by MARIUS BREHM. His PhD thesis is cited at the corresponding passages in the text. MALDI-TOF-MS measurements were carried out by DR. STEFAN SCHMIDT (CeMOS, Mannheim). LC-MS measurements took place at the INSTITUTE OF TECHNOLOGY (INT) in the laboratory of DR. FLORIAN FEIST. All bacterial work was performed in PROF. DR. THOMAS SCHWARTZ'S laboratory at the Institute of Functional Interfaces (IFG).

#### 3.1.1 Introduction

##### 3.1.1.1 Antimicrobial Resistance and Innovative Solutions

The discovery of penicillin by ALEXANDER FLEMING marked a turning point in modern medicine, revolutionizing the treatment of bacterial infections and laying the foundation for essential medical practices, including chemotherapy, immunosuppression, and complex surgeries.<sup>[67]</sup> However, the triumph of antibiotics was short-lived, as the emergence of penicillin-resistant strains of pathogens such as *Staphylococcus aureus*, *Streptococcus pneumoniae*, *Pseudomonas aeruginosa*, and *Mycobacterium tuberculosis* diminished the effectiveness of this groundbreaking therapeutic tool.<sup>[68]</sup> Despite numerous subsequent antibiotic discoveries, the persistent evolution of antibiotic resistance has turned antibiotic development into an ongoing race against bacterial adaptation.<sup>[69]</sup>

In recent decades, bacterial infections have emerged as a critical health concern due to the relentless development of resistance to existing antibiotics in combination with a lack of new antibacterial agents.<sup>[70, 71]</sup> Globally, reports of antibiotic resistance have become alarmingly common in bacteria causing prevalent infections like urinary tract infections, pneumonia, bloodstream infections, and skin infections.<sup>[72]</sup> Particularly worrisome is the rise of resistance among human facultative pathogenic bacteria from the ESKAPE group (*Enterococcus faecium*, *Staphylococcus aureus*, *Klebsiella pneumoniae*, *Acinetobacter baumannii*, and *Pseudomonas aeruginosa*, and *Enterobacter species*), responsible for serious hospital-acquired infections.<sup>[73]</sup> Multi-resistant strains of *Staphylococcus aureus* (MRSA), already affect around 20% of the population, posing severe challenges in treatment.<sup>[74]</sup> Even the last line of defense, vancomycin, faces threats from vancomycin-resistant strains of *Staphylococcus aureus* (VRSA)<sup>[75]</sup> and

Enterococcus (VRE)<sup>[76]</sup>. The projected cost of continued antibiotic resistance, coupled with a shortage of new antibiotics, is estimated to claim 30 million lives globally by 2050.<sup>[77]</sup>

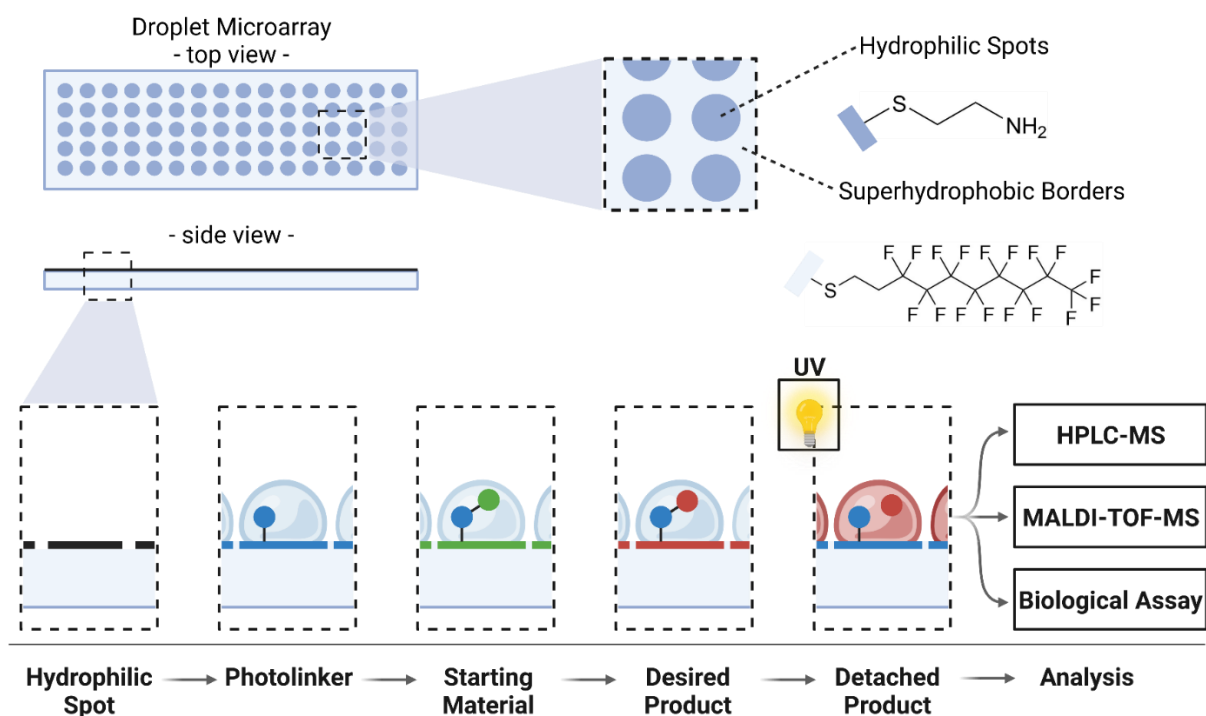
Despite the pressing need for solutions, efforts by major pharmaceutical companies to address this crisis have been slowed down by challenges such as the difficulty of discovering new antibiotics, low returns on investment due to short drug regimens, and limited treatment opportunities restricted to specific bacterial infections. Urgent and novel approaches are required to discover antibacterial agents capable of combating infections caused by pathogenic and multidrug-resistant bacteria.<sup>[72]</sup>

Historically, natural products have been a valuable source for bioactivity screening, including antimicrobial activity.<sup>[78]</sup> Extracts from plants<sup>[79]</sup>, fungi<sup>[80]</sup>, and bacteria<sup>[81]</sup> have been explored for potential antibacterial compounds, drawing inspiration from nature's own arsenal. Examples like free fatty acids<sup>[82]</sup>, host defense peptides<sup>[83]</sup> and some small molecules showed activity against bacterial membranes.<sup>[84]</sup> Additionally, synthetic molecule libraries (SML) have gained attention for their capacity to rapidly screen thousands of compounds against microorganisms or proteins.<sup>[85, 86]</sup> However, despite these efforts, the lack of diversity in SML often hinders the identification of new bioactive compounds, leading to a stagnation in antibacterial drug discovery. Combinatorial chemistry-based high-throughput screening (HTS) has also fallen short in identifying novel antibacterial agents, contributing to the stagnation observed in antibacterial drug discovery research over the last 30 years.<sup>[87]</sup>

The critical need for new antibiotics, coupled with the demand for a faster pace of discovery, underscores the importance of exploring new natural sources and adopting creative screening strategies in contemporary antibacterial drug discovery efforts. As we navigate this stagnant stage in antibacterial drug discovery, the imperative is not only to discover new antibiotics but to do so with unprecedented speed and innovation.

### **3.1.1.2 Motivation and Aim**

The main goal of the project was to establish an integrated workflow for on-chip high-throughput nanoliter-scale synthesis, analysis and screening of potentially antibacterial compounds. Combinatorial solid-phase synthesis on DMA utilizing the UGI reaction has been reported by BREHM *et al.*<sup>[64, 88]</sup> They immobilized a photocleavable linker to the hydrophilic spots of the DMA, which acted as an anchor for the combinatorial synthesis of 840 unique compounds utilizing only 23 starting materials. Irradiation with UV light detaches the desired product into distinct droplets, allowing for on-chip analysis (e. g. MALDI-TOF-MS) and screening for biological activity (Figure 9).

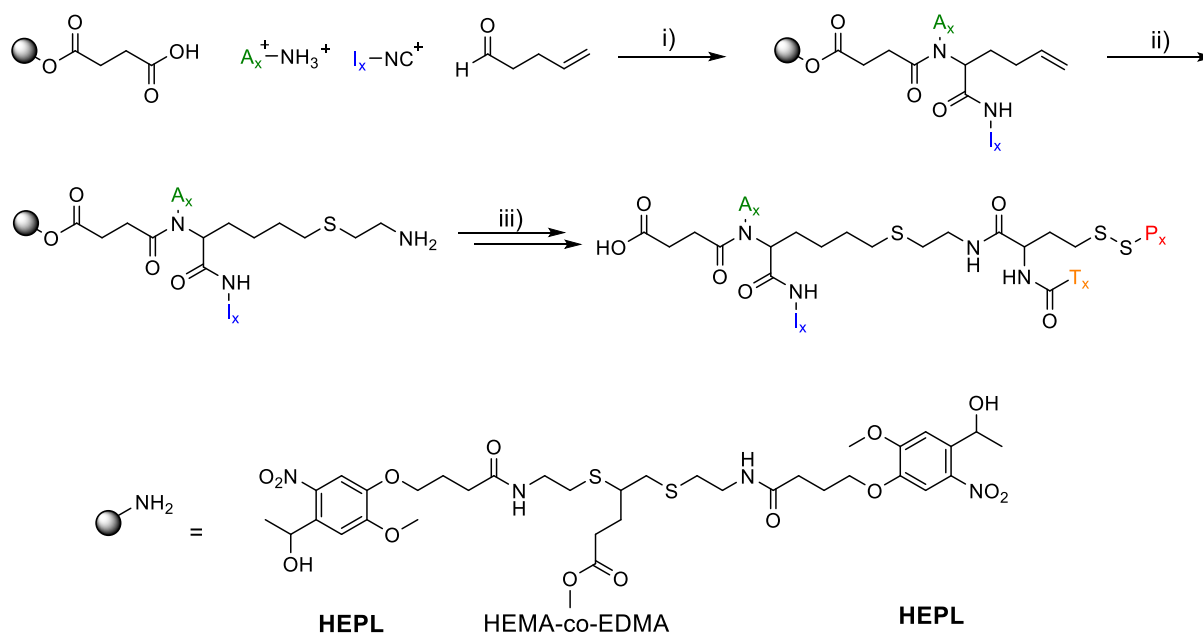


**Figure 9:** Scheme showing a generalized workflow using the DMA platform. Covalent immobilization of a photolabile linker in the hydrophilic (HL) spots forms the anchor for the solid phase combinatorial synthesis. Synthesized compounds can be released by UV irradiation at 365 nm into distinct nanodroplets formed in the hydrophilic spots to be either screened in biological assays or analyzed, e.g., via MALDI-TOF mass spectrometry.

It was decided to further expand the scope of combinatorial synthesis on DMA based on the initial results from BREHM *et al.* Therefore, a synthetic combinatorial strategy was designed based on the combination of the four component UGI reaction and the three component thiolactone aminolysis-disulfide exchange (TADE) reaction<sup>[89]</sup>, aiming to generate a library of novel lipid-like compounds (Figure 10). Using only 47 different building blocks allows for the synthesis of over 10.000 different compounds. By incorporating a diverse array of functional moieties in the chosen building blocks, we can achieve significant structural diversity in the generated libraries. The produced lipid-like molecules exhibit variations in positive or negative charges, hydrophilic or hydrophobic regions as well as fluorinated, aromatic or alkylated moieties.

The combination of on-chip UGI reaction with the TADE reaction facilitates high throughput with a minimal number of building blocks. To put this into perspective, synthesizing the same number of compounds through a one-by-one approach would take a chemist approximately 43 years, even if producing just one compound per day. Additionally, the miniaturization of reactions in 200 nL droplets results in substantial savings in terms of reagents and solvents. Previous reports<sup>[84, 90]</sup> indicate that amphiphilic compounds such as lipids or peptides possess

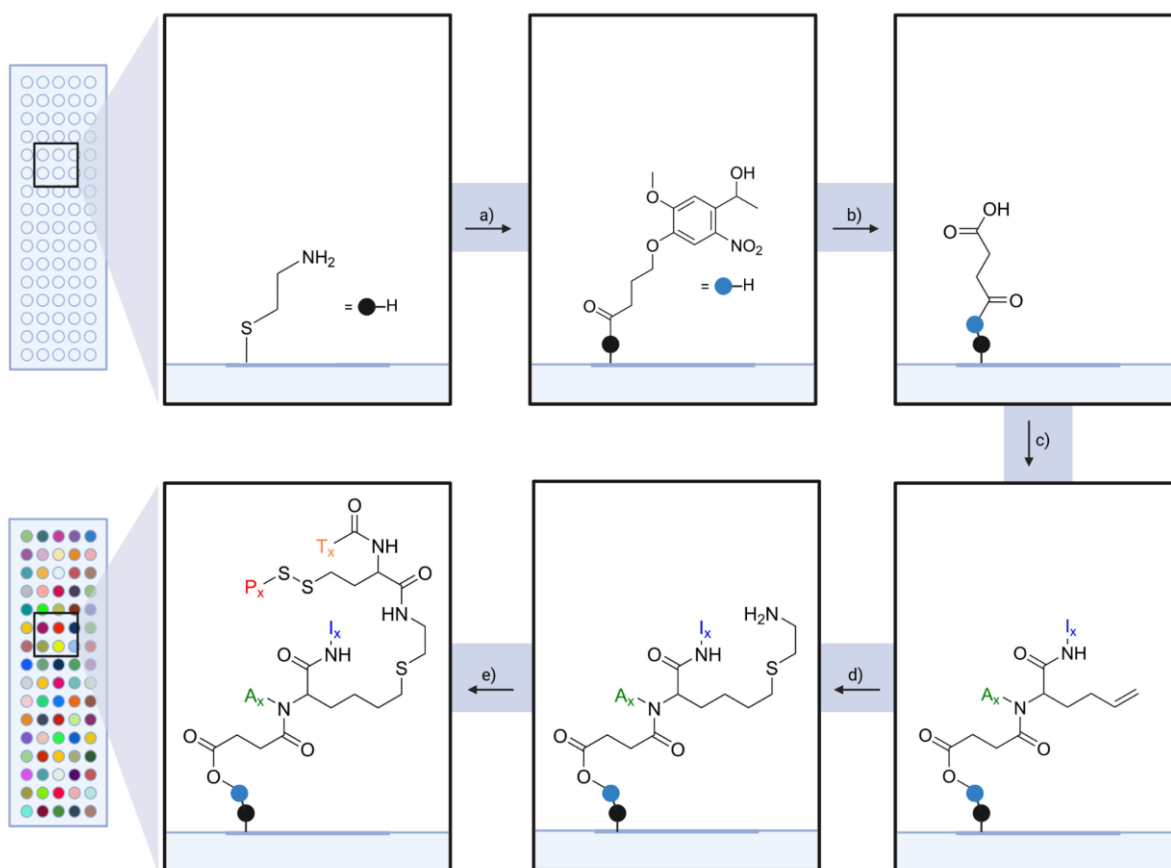
antibacterial properties through cell wall disruption, the hypothesis of this project centers on the potential of lipid-like molecules as promising candidates for identifying novel antibacterial compounds.



**Figure 10:** Scheme of the synthetic sequence for the on-chip high-throughput synthesis of a chemical library of antimicrobial compounds: i) Ugi four-component reaction with surface anchored succinic acid, 4-pentenal, variable entries for surface-anchored amines  $A_x$  and isocyanides  $I_x$ . ii) Thiol-ene reaction to introduce an amine functionality. iii) Three component thiolactone-disulfide reaction, followed by UV induced cleavage from the surface to yield the desired lipid-like product, variable entries for 2-pyridyl disulfide derivatives  $P_x$  and thiolactone derivatives  $T_x$ . Representation of the solid-phase chemistry: UV-cleavable linker (hydroxyethyl photolinker, HEPL) is covalently immobilized in the hydrophilic spots of the DMA, forming the anchor of the solid-phase combinatorial synthesis.

### 3.1.2 Optimization of the Reaction Conditions and Purity Analysis using Liquid Chromatography – Mass Spectrometry

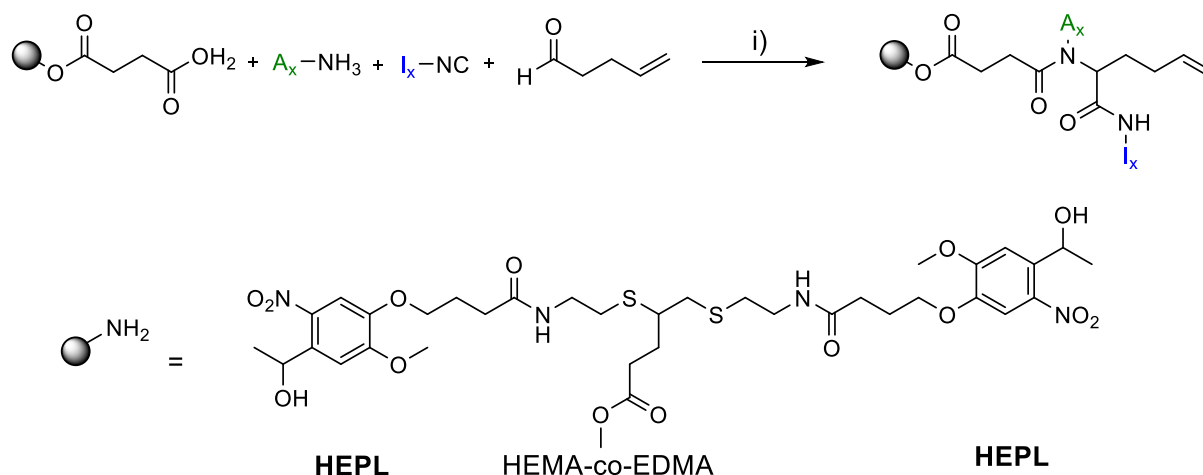
The synthetic cascade employed for the generation of the beforementioned library of lipid-like molecules consists of three major reaction steps: the four component Ugi reaction (Figure 11c), the UV-induced thiol-ene reaction (Figure 11d) and the TADE reaction (Figure 11e). Prior to these reactions the photocleavable linker HEPL is immobilized to the hydrophilic (HL) spots of the DMA (Figure 11a). Subsequent modification with succinic acid (Figure 11b) creates the anchor point for the synthetic cascade. The forthcoming discussion will delve into the specifics of each major reaction step.



**Figure 11:** Workflow for the synthesis of library of lipid-like molecules on DMA via a sequence of **a)** covalent attachment of the hydroxyethyl photolinker (HEPL) to the HL spots as an anchor for the solid phase synthesis, **b)** immobilization of succinic acid to introduce a surface bound carboxylic acid, **c)** four component Ugi reaction with variable entries for amines A<sub>x</sub> and isocyanides I<sub>x</sub>, **d)** Thiol-ene click reaction to convert the vinyl moiety into an amine functionality, **e)** three component TADE reaction with variable entries for homocysteine thiolactone derivatives T<sub>x</sub> and 2,2'-pyridyl disulfide derivatives P<sub>x</sub>.

### Performance of the Ugi reaction

The optimization of the reaction conditions, as well as the synthetic procedure and outcome of the Ugi reaction was investigated by BREHM *et al.*<sup>[64, 88]</sup> Given that the subsequent reaction steps in the formation of the lipid-like library build upon the findings of these optimizations, a brief discussion of these results is warranted.



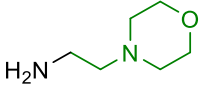
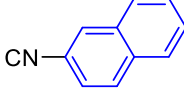
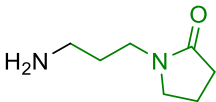
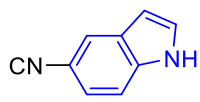
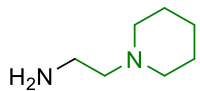
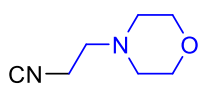
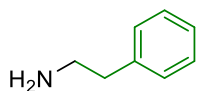
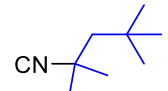

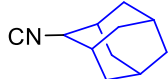
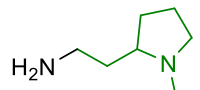
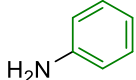
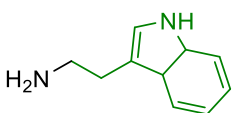
**Figure 12:** Scheme of the four component Ugi reaction between the surface bound succinic acid, amine **A<sub>x</sub>**, isocyanide **I<sub>x</sub>** and 4-pentenal.

The implementation of the four-component Ugi reaction (Figure 12) enabled the formation of the first part of the target compound with two variable entries (amine **A<sub>x</sub>**, isocyanide **I<sub>x</sub>**), while simultaneously attaching to the photolinker. To immobilize the photolinker to the HL spots (1 mm<sup>2</sup>, square), a 150 nL of a solution of 0.1 M HEPL and 0.1 M HOBt in NMP was freshly mixed with 5% (v/v) diisopropylcarbodiimide (DIC) was dispensed in every spot. Subsequently, the succinic acid was coupled to the photolinker by adding in each spot a solution containing 0.1 M succinic anhydride and 0.01 M 4-(dimethylamino)pyridine (4-DMAP) in NMP and letting it react for 18 h.

The attached succinic acid served as the solid bound anchor for the Ugi reaction. 60 nL of each 0.5 M solution of the amine **A<sub>x</sub>**, the isocyanide **I<sub>x</sub>** and 4-pentenal in  $\gamma$ -butyrolactone (GBL) were added to each HL spot and the DMA was incubated in the dark for 72 h.

For a better overview of the possible products, they were named as combinations of the respective amine (**A<sub>x</sub>**) and isocyanide (**I<sub>x</sub>**) which are presented in Table 1.

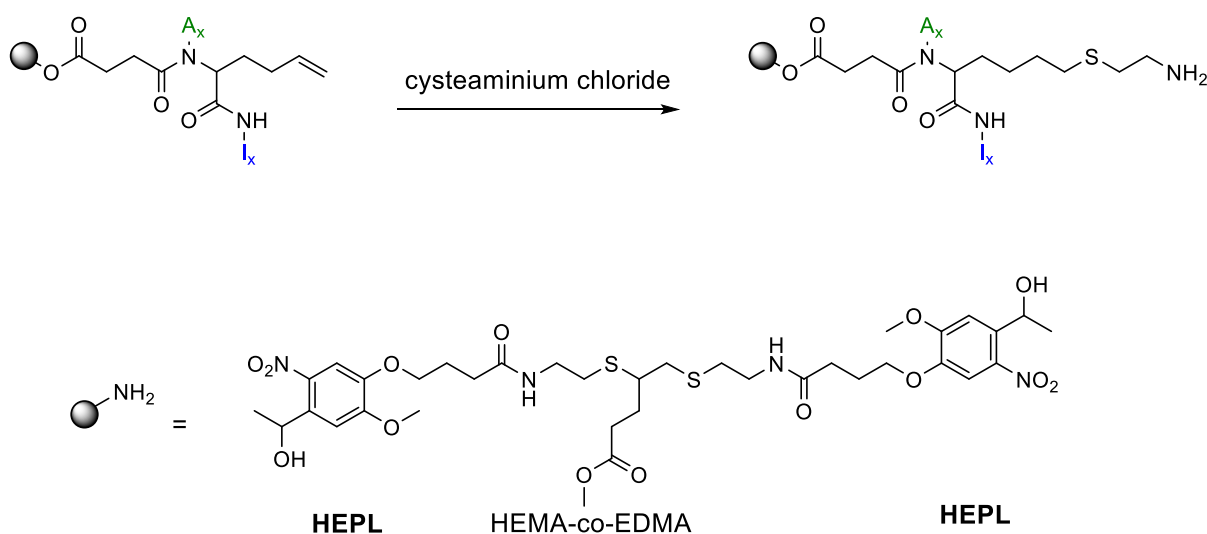
**Table 1:** Structures of tested amines  $A_x$  and isocyanides  $I_y$  for the UGI reaction which formed the headgroups of the products. This set of starting materials was selected based on the structures reported by Brehm et al.<sup>[88]</sup>

#	Amine $A_x$	#	Isocyanide $I_x$
$A_1$		$I_1$	
$A_2$		$I_2$	
$A_3$		$I_3$	
$A_4$		$I_4$	
$A_5$		$I_5$	
$A_6$			
$A_7$			
$A_8$			

The success of these reactions on the DMA was investigated by LC-MS analysis of the formed products after UV triggered release from the surface into the distinct volume of the spot. All 40 reactions were performed in larger scale using round spots with a diameter of 2.8 mm. Collecting the solution of five spots with the same target compound after cleavage was enough for automated injection into the LC-MS system. All combinations led to formation of the desired compound with an average purity of 70% for compounds synthesized from  $I_1$ ,  $I_2$ ,  $I_4$  and  $I_5$ . The ionic and non-aromatic character of  $I_3$  led to inhomogeneous ionization of the products and UV absorbance, which made a parallel purity analysis via UV or MS signal integration infeasible. However, all masses of the respective products were clearly present and indicating a successful reaction.

### Thiol-Ene reaction

In the context of aminolysis during the TADE reaction, the vinyl group introduced into the molecule through the 4-pentenal during the UGI reaction must be converted to an amino functionality. The thiol-ene reaction (Figure 13) is chosen for this purpose, given its orthogonality to the UGI reaction. Importantly, this step can be performed directly after the UGI reaction without the need for deprotection or activation steps. Cysteaminium hydrochloride was selected as the reactant due to its simplicity as a combination of a thiol and an amine.



**Figure 13:** Conversion of the vinyl group of the Ugi headgroup to a primary amine using the thiol-ene reaction. Cysteamine is employed as a simple combination of thiol and amine.

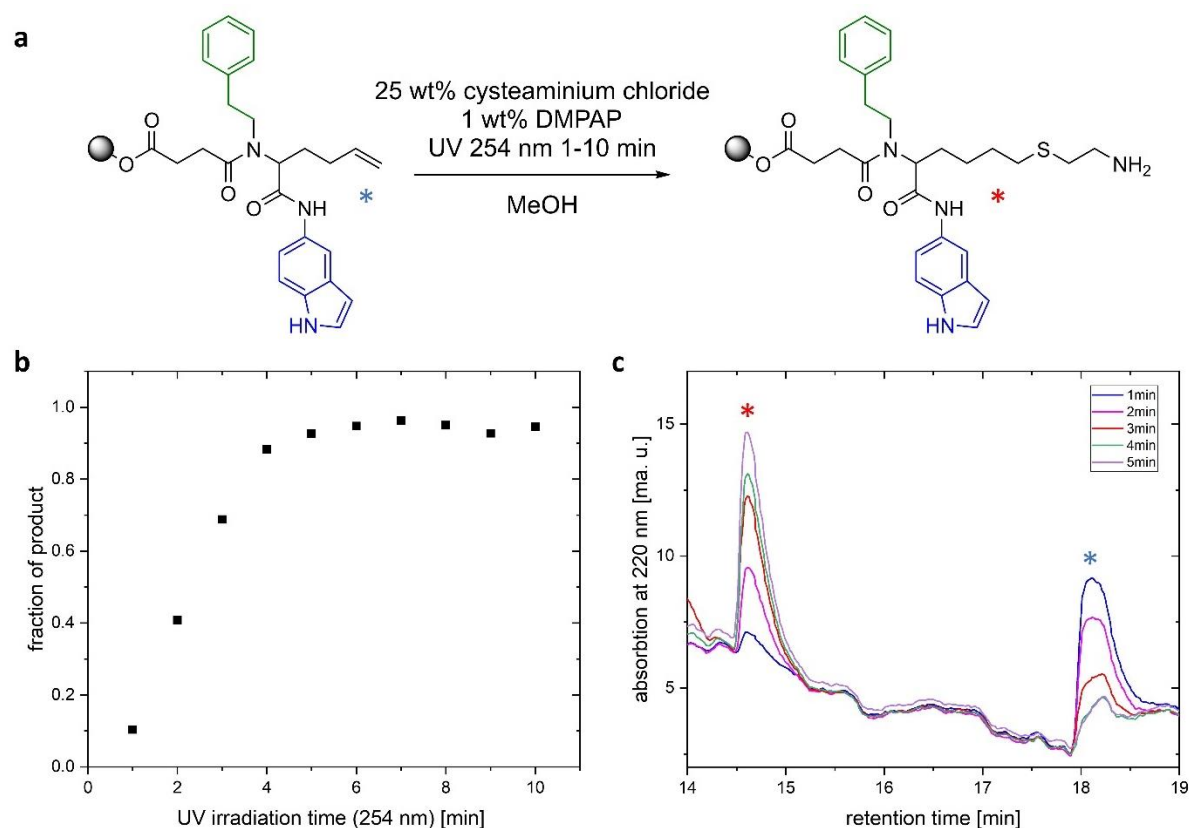
There are two main conditions to convert the vinyl group to the amino functionality, while utilizing radical-based thiol-ene chemistry: thermal or UV induced generation of the radical. BREHM *et al.*<sup>[88]</sup> employed the thermal initiated thiol-ene coupling using water soluble 4,4'-Azobis(4-cyanovaleric acid) as initiator. Despite providing good conversion of the vinyl after incubation of the slide for 18 h at 65°C in a solution consisting of 25 w% cysteaminium chloride in water/ethanol (1:1, v/v) with 1 w% of the thermal radical initiator the amount of used starting material was excessive in respect to the small area of reactive sites on DMA. Additionally, thermal generation of radicals was not suitable for the reaction on ITO-DMA (see chapter 3.1.3). In short, the ITO-DMA has an additional layer of indium tin oxide between the glass substrate and the polymer layer of the DMA, which makes the chip conductive. High temperature in combination with free radicals lead to chemical etching of the ITO layer, resulting in detachment of the ITO and polymer layer from the surface.



To address the detachment of the ITO layer and minimize resource requirements, the UV-induced thiol-ene reaction was employed. It was first investigated how the linker – which is usually treated with UV light at 365 nm for the cleavage – reacts to UV-induced thiol-ene click reaction conditions at 254 nm.

To monitor the conversion from the vinyl moiety to the amino group an exemplary Ugi product (**A4I2**) was employed in the UV induced thiol-ene reaction (Figure 14a) on larger scale using round spots with a diameter of 2.8 mm. These spots have a capacity of up to 10  $\mu$ L of solvent and are sufficiently large to be filled and emptied manually using pipetting. By collecting the cleavage solution from 5 spots per product, a total of 50  $\mu$ L of sample was obtained after cleavage. This volume proved suitable for handling with our LC-MS autosampler.

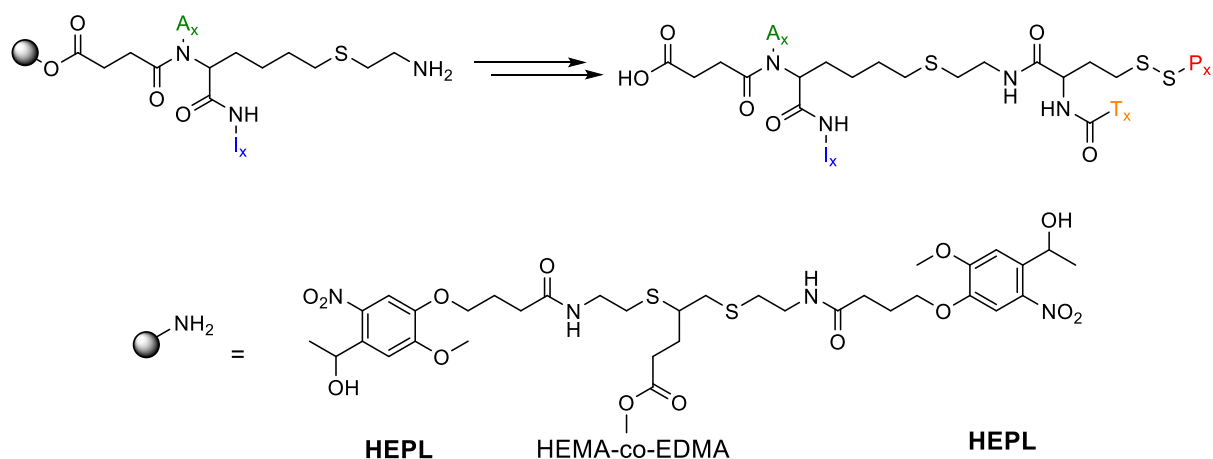
For the reaction, 5  $\mu$ L of a solution comprising 25 w% cysteaminium chloride and 1 w% 2,2-dimethoxy-2-phenylacetophenone (DMPAP) in methanol were manually dispensed in 5 spots containing the same UGI product **A4I2**. These spots were then irradiated with UV light at 254 nm for varying durations (1-10 min). To assess the fraction of the thioether product relative to the Ugi headgroup, each set of five spots containing the same thioether product underwent cleavage from the surface according to the procedure described in the experimental part and analyzed via LC-MS. Figure 14b illustrates the fraction of the product in relation to the UV irradiation time at 254 nm, showing a linear increase between 1-5 min of UV exposure, after which it reaches a plateau. An overlay of the chromatograms of the product solutions between 1-5 min UV exposure at 254 nm is shown in Figure 14c. For subsequent experimentation an irradiation time of 5 min at 254 nm with the given experimental conditions will be applied to convert the vinyl group to the amino moiety.



**Figure 14:** (a) Ugi product **A4I<sub>2</sub>** (blue asterisk) was synthesized on the photolinker and the UV induced thiol-ene reaction was carried out by applying a solution of 25 wt% cysteaminium chloride and 1 wt% DMPAP in MeOH to each HL spot to form the thioether (red asterisk). Irradiation wavelength was 254 nm with varied irradiation time. (b) Fraction of the product peak from the summarized peak areas of the starting material (blue asterisk) and product (red asterisk) plotted against the irradiation time. Longer irradiation times increased the conversion of the Ugi product to the thioether. Peak areas were determined by spectroscopic analysis of the solutions at 220 nm using a LC/MS system. (c) Overlay of LC/MS chromatograms at 220 nm after different irradiation times during the thiol-ene reaction of compound **A4I<sub>2</sub>**. Asterisks indicate corresponding structures.

### Aminolysis of the thiolactone and subsequent disulfide exchange

The last step of the synthetic cascade to yield the lipid-like compounds is the TADE reaction. The TADE reaction was first introduced by Molla *et al.* in a one-pot synthesis of lipids for gene delivery<sup>[89]</sup>. It was also employed by Benz *et al.* for the synthesis of a lipidoid library on DMA using a sandwiching approach.<sup>[61]</sup> In this work, the TADE reaction will be employed in a solid-phase synthesis approach for the first time (Figure 15).



**Figure 15:** TADE reaction and subsequent UV induced cleavage from the surface to yield the desired lipid-like compound with four tunable moieties  $A_x$ ,  $I_x$ ,  $T_x$  and  $P_x$ .

Although the TADE reaction usually has high yields with little side product formation the tested set of starting materials was limited to 2-pyridyl disulfide (PDS) and thiolactone derivatives having residues consisting of alkyl chains with different lengths. To increase the variety of the starting materials a set of 16 PDS derivatives and 16 thiolactone derivatives was synthesized according to the described procedure in the experimental part. These derivatives include a variety of functional groups, like fluorinated chains, bulky alkyl molecules, carboxylic acids, different charged molecules and aromatic moieties. Exemplary structures are shown in Table 2.

**Table 2:** Exemplary structures of used 2-pyridyl disulfide derivatives  $P_x$  and thiolactone derivatives  $T_y$  for the solid-phase aminolysis and subsequent disulfide exchange reaction.

#	2-Pyridyl disulfide $P_x$	#	Thiolactone $T_x$
$P_5$		$T_4$	
$P_6$		$T_8$	
$P_7$		$T_{10}$	
$P_{15}$		$T_{14}$	
$P_{16}$		$T_{16}$	
	$R_S = $		$R_T = $

In contrast to the previously published reaction conditions - equimolar amounts of PDS and thiolactone derivative, 0.5 eq. amine in DCM – the solvent was changed to DMSO. DMSO forms stable droplets in the HL spots of the DMA. To ensure the reactivity of the starting materials in DMSO a selection of 20 random combinations was chosen to perform the reactions on a more conventional, larger scale. Hexylamine was used as sterically non-hindered nucleophile to ensure fast reaction times.

To carry out the reactions, 0.5 M solutions of all individual components in DMSO were prepared. Subsequently, 50  $\mu$ L of a thiolactone derivative solution was mixed with 50  $\mu$ L of the corresponding PDS derivative solution and 50  $\mu$ L of the hexylamine solution in an Eppendorf tube. The reaction mixture was placed on a shaker for 20 min to allow the reaction to proceed. Following this incubation period, 50  $\mu$ L from each sample were extracted and diluted with 950  $\mu$ L of acetonitrile (MeCN). The combined solution was then subjected to analysis using LC-MS. 95% of the tested combinations showed the formation of the desired product (see appendix). This leads to the conclusion, that the chosen solvent is suitable for the TADE

reaction. Obtained conversion from starting materials to product was not quantified, the reactions only served the purpose of a qualitative statement.

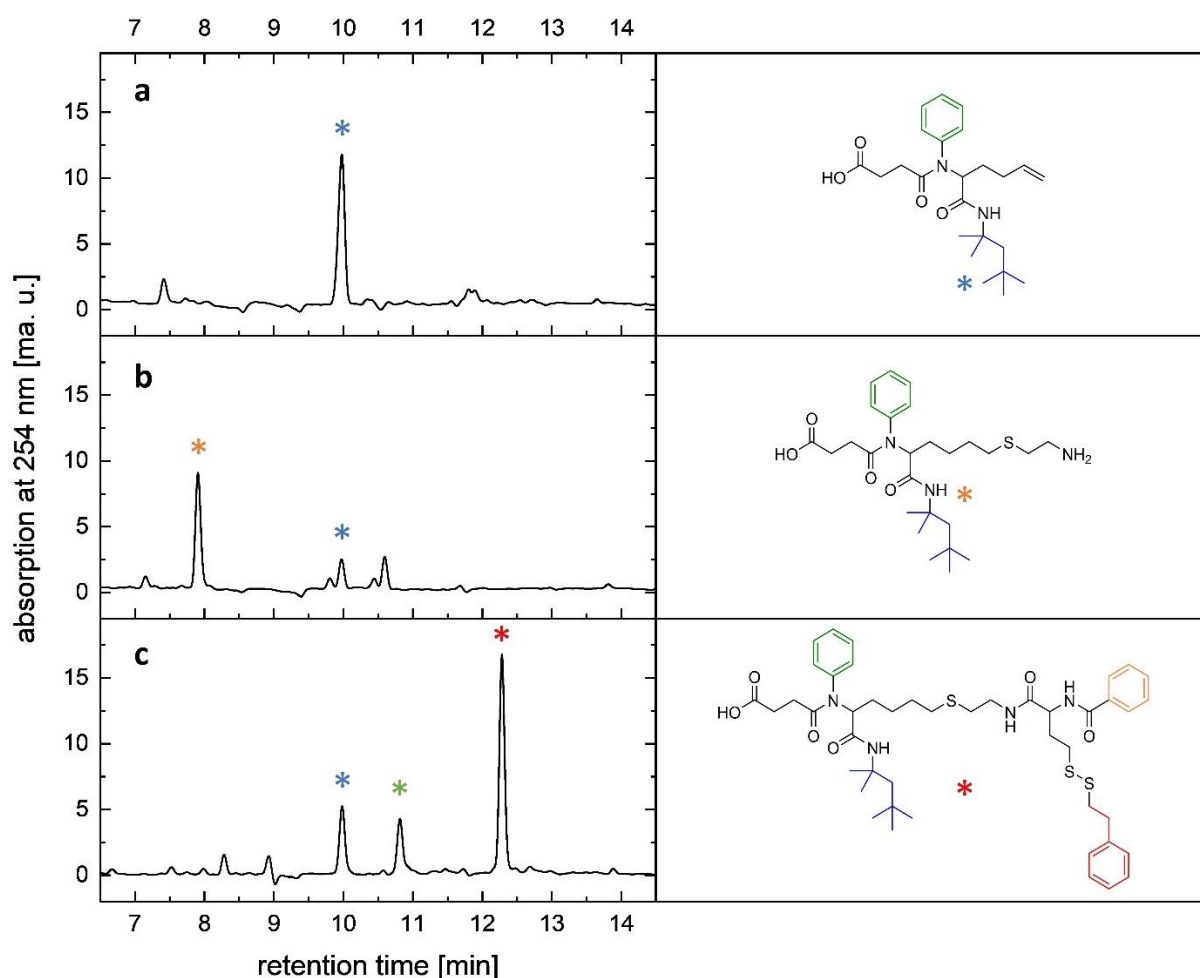
The adjusted reaction conditions were transferred to the on-chip TADE reaction. Each 75 nL of a 0.5 M thiolactone derivative solution in DMSO and 0.5M PDS derivative solution in DMSO were dispensed onto each HL spot (1 mm<sup>2</sup>, square). The slide was incubated for 18 h in the dark. To monitor the conversion and the purity of the desired products, 11 exemplary lipid-like compounds were synthesized on a larger scale using round spots with diameter of 2.8 mm. This spot size enables manual pipetting of the reaction solutions. The combined cleavage solutions of five spots per product yielded 50 µL of sample, which is enough to be handled by our LC-MS autosampler. The results of the different products are presented in Table 3. Purities range between 25% and 72%, while conversion is generally higher (49% - 99%).

**Table 3:** Purity of exemplary compounds synthesized in 2.8 mm spots to monitor synthetic success via LC-MS analysis. Product was identified by MS, while purity was calculated as the fraction of the product's peak integral (product peak and oxidized product peak) with respect to the sum of integrals of all peaks at 254 nm absorbance. Conversion was calculated as the ratio between the absorbance of the thioether-amino intermediate and the product at 254 nm. <sup>[a]</sup>purity and conversion was calculated using the total ion chromatogram (TIC).

Compound	Purity [%]	Conversion [%]
<b>A<sub>4</sub>I<sub>5</sub>T<sub>4</sub>P<sub>4</sub></b>	42	70
<b>A<sub>4</sub>I<sub>5</sub>T<sub>4</sub>P<sub>1</sub></b>	54	75
<b>A<sub>7</sub>I<sub>5</sub>T<sub>4</sub>P<sub>4</sub></b>	32	49
<b>A<sub>7</sub>I<sub>5</sub>T<sub>4</sub>P<sub>1</sub></b>	72	79
<b>A<sub>1</sub>I<sub>1</sub>T<sub>1</sub>P<sub>1</sub></b>	25	>99
<b>A<sub>7</sub>I<sub>1</sub>T<sub>2</sub>P<sub>4</sub></b>	40	>99
<b>A<sub>5</sub>I<sub>2</sub>T<sub>4</sub>P<sub>1</sub></b>	59	>99
<b>A<sub>7</sub>I<sub>2</sub>T<sub>4</sub>P<sub>4</sub></b>	25	>99
<b>A<sub>5</sub>I<sub>1</sub>T<sub>2</sub>P<sub>1</sub></b>	34	>99
<b>A<sub>7</sub>I<sub>4</sub>T<sub>3</sub>P<sub>4</sub></b>	48 <sup>[a]</sup>	>99 <sup>[a]</sup>
<b>A<sub>1</sub>I<sub>4</sub>T<sub>2</sub>P<sub>1</sub></b>	38 <sup>[a]</sup>	>99 <sup>[a]</sup>
<b>Total</b>	<b>42 ± 14</b>	<b>88 ± 16</b>

These values fall within an expected range, considering the diverse reaction steps with varying conditions for each stage. Exemplary chromatograms of each of the main intermediates and the

product (**A7I4P1T4**) in the synthetic cascade are shown in Figure 16. Formation of the Ugi product **A7I4** demonstrates high purity (Figure 16a). However, the conversion of the vinyl moiety to the amino group introduces initial impurities and still exhibits some absorption of the Ugi product (indicated by the blue asterisk, Figure 16b). The absorbance of the amino-intermediate becomes undetectable after the TADE reaction (Figure 16c), while the formation of the desired product (red asterisk) occurs. This confirms the generally high conversion of the amino-intermediate into the product. One notable side product arises from the oxidation of the thioether to the sulfoxide (indicated by the green asterisk).

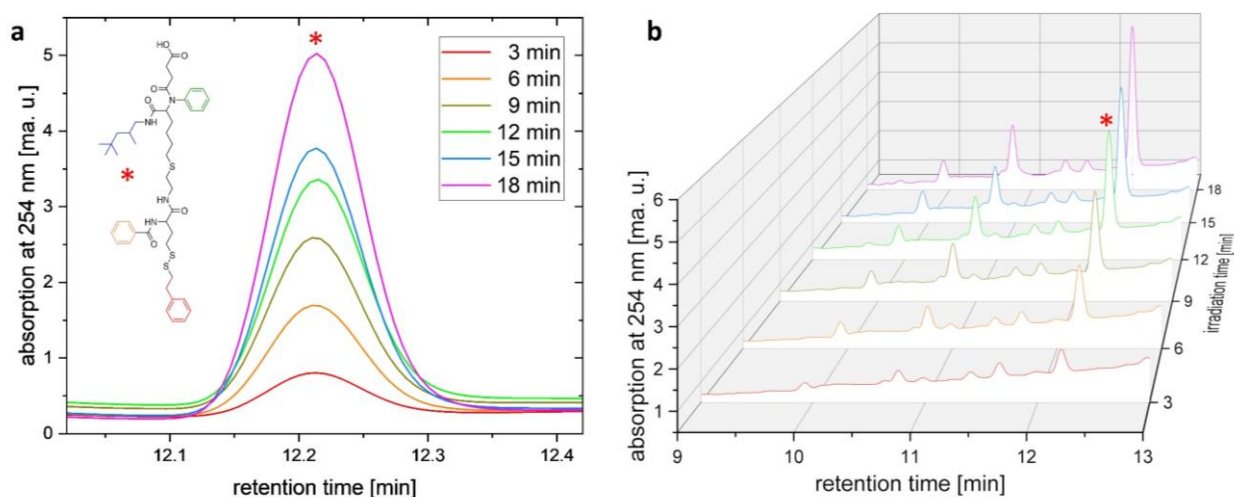


**Figure 16:** Chromatograms at 254 nm of the released compounds after every step of the synthesis (left) and the corresponding structures of the synthesized compounds (right). (a) after Ugi reaction forming Ugi product **A7I4** indicated by the green asterisk, (b) after the formation of the thioether via UV induced thiol-ene reaction denoted by the orange asterisk and (c) after aminolysis of the thiolactone and disulfide exchange yielding compound **A7I4P1T4** highlighted by the red asterisk. The blue asterisk indicates the main side product.

In addition to investigating the purities and conversion of the lipid-like products obtained through the discussed synthesis cascade, it is essential to address cleavage kinetics. Previous studies have investigated the maximum loading per spot. BREHM *et al.* modified the photolinker with chlorambucil and subsequently released the compound, achieving a maximum loading of

4.77 nmol per round spot with a diameter of 2.8 mm.<sup>[64]</sup> In a separate study, HÖPFNER *et al.* achieved a maximum loading after releasing an on-chip synthesized biphenylic compound, with a loading of 0.18 nmol per spot for the same spot size<sup>[1]</sup>. These findings highlight that even a one-step reaction with generally high yields and a more diverse set of starting materials can significantly influence the amount of released compound into the distinct droplet.

Given the complexity of the lipid-like structures it was not possible to synthesize an exemplary compound in higher amounts in this project, which could have been used to determine the exact loading of an exemplary compound to the surface of the DMA. Nevertheless, exemplary compound **A7I4P1T4** was synthesized according to the previously described procedure. The UV induced release from the surface was performed according to the procedure described in the experimental part with irradiation times between 3 and 18 min. Figure 17a illustrates the product peak in the LC-MS chromatogram at 254 nm in relation to the different irradiation times. The chromatogram demonstrates, that the area of the product peak increases with increasing irradiation time. While no quantitative statement about the released compound into distinct droplets is possible, it can be shown, that with increasing irradiation times the amount of released product increases. Unfortunately, as anticipated, the released amounts of impurities also increase with longer irradiation times (Figure 17b).



**Figure 17:** (a) Overlay of LC-MS chromatograms at 254 nm of compound **A7I4P1T4** after different UV irradiation times. Only the respective product peak is shown. (b) 3D waterfall plot of the chromatograms at 254 nm after different irradiation times of compound **A7I4P1T4**.

### **3.1.3 High-Throughput Analysis using Matrix-assisted Laser Desorption/Ionization Mass Spectrometry**

Determination of purities, conversion and cleavage kinetics, as well as optimization of each of the synthetic steps was conducted in relatively large scale. To generate enough sample volume to be analyzed via LC-MS, at least four round spots with a diameter of 2.8 mm need to be cleaved of from the surface. Each measurement using a standard LC-MS system (see experimental part for details) takes at least 10 min to create comprehensive data.

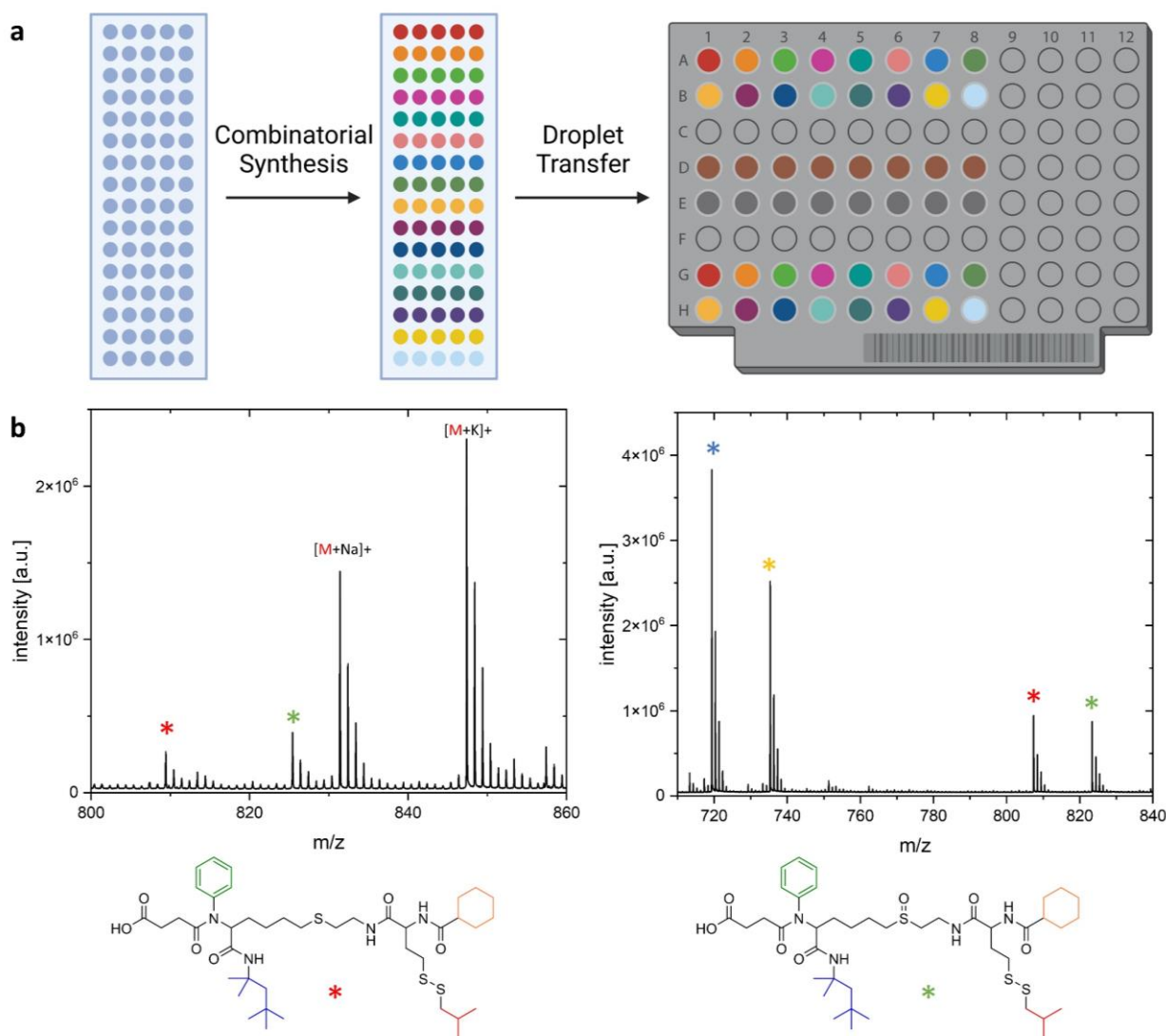
The aim of this project is to generate a vast library of lipid-like compounds. Utilizing eight different amines (**A1-A8**), five different isocyanides (**I1-I5**), 16 PDS derivatives (**P1-P16**) and 16 thiolactone derivatives (**T1-T16**), in addition to 4-pentenal and the surface anchored succinic acid leads to the formation of 10.240 unique compounds (Table 4). Following the analytical procedure using LC-MS would lead to a measuring time of around 71 days. In addition to that, the standard layout for the DMA would have to be  $5 \times 16 = 80$  round spots with a diameter of 2.8 mm. Each four spots need to contain the same compound to be analyzed using LC-MS, leading to a maximum of 20 different compounds per slide. To create data for all 10.240 compounds using LC-MS, at least 512 DMA slides would be needed.



In contrast to LC-MS, matrix-assisted laser desorption/ionization time-of-flight (MALDI-TOF) mass spectrometry (MS) provides a label-free, interference resistant alternative. Its very small sample volume requirements in the nanoliter range, coupled with fast analysis times of around 1 second per sample, highlight suitability of MALDI-TOF-MS for high-throughput applications<sup>[26]</sup>. Previous studies have successfully utilized MALDI-TOF-MS in their high-throughput screenings as well.<sup>[23, 91]</sup>

To verify the feasibility of MALDI-TOF-MS in combination with the lipid-like compounds, preliminary tests were conducted. Nine different lipid-like compounds were synthesized on a larger scale using round spots with a diameter of 2.8 mm, following the described synthetic cascade. After the UV induced cleavage of the compounds, 1  $\mu$ L of each sample solution was transferred in duplicates to a ground steel plate and dried (Figure 18a). For positive mode measurements a solution of 20 mg/mL 2,5-dihydroxybenzoic acid (DHB) in MeCN/water (1:1, v/v) was deposited onto the respective spots on the ground steel plate. For negative polarization measurements, a solution of 7 mg/mL *N*-(1-naphthyl)ethylenediamine hydrochloride (NEDC) in MeCN/water (1:1, v/v) was employed.

Exemplary MALDI-TOF-MS spectra of compound **A7I4P4T1** in positive and negative mode (Figure 17b) confirm the formation of the desired compound. The successful synthesis was confirmed by the appearance of the main product peak (red asterisk), sodium and potassium adducts in positive mode, as well as the appearance of the main side product (green asterisk). Additionally, in negative mode, the appearance of fragment ions (blue and yellow asterisk) validates the formation of the product.

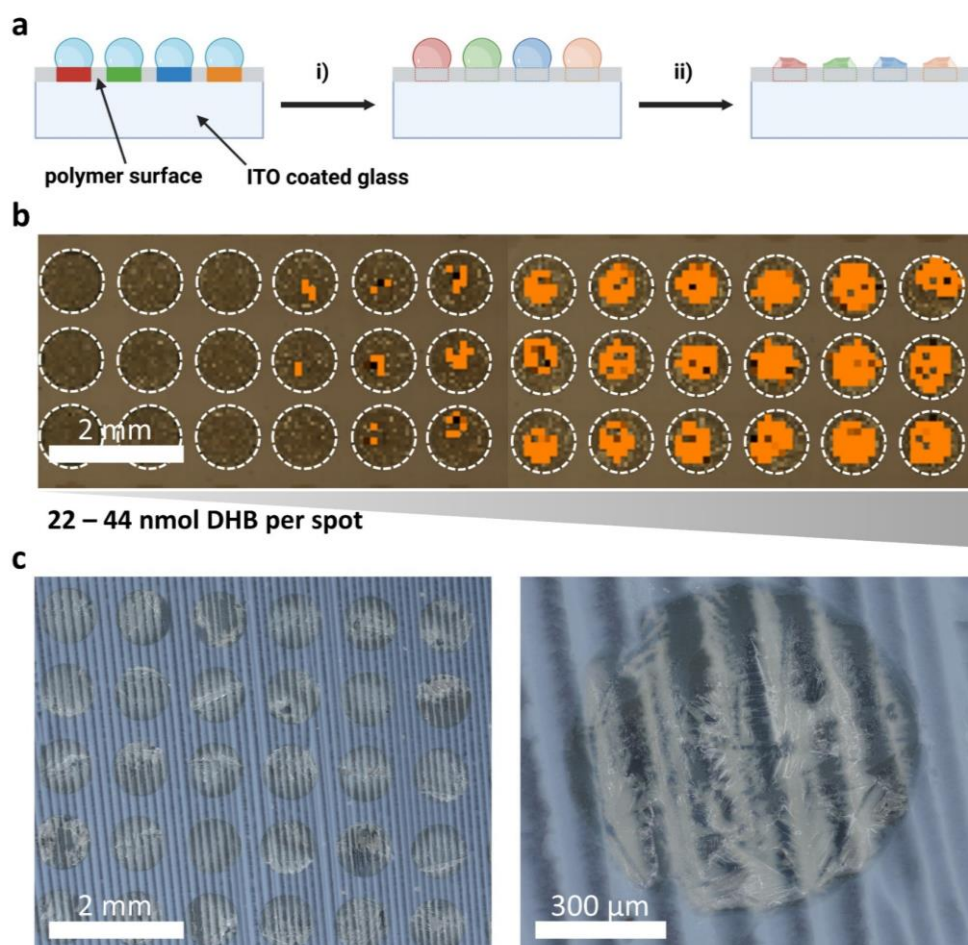


**Figure 18:** (a) Schematic workflow of the combinatorial synthesis followed by the droplet transfer to the ground steel target plate for MALDI-TOF-MS analysis. Each color represents a different compound. Rows D and E on the ground steel plate represent DHB and NEDC to acquire background spectra. (b) Representative MALDI-MS spectra of compound A7LP4T1 acquired in positive mode (left) using DHB as matrix and in negative mode (right) using NEDC as matrix. Asterisks indicate the corresponding structures.

Even though the droplet transfer method demonstrated good results, transferring over 10,000 compounds would be a laborious and time-consuming task. To address this challenge, direct MALDI-TOF-MS measurements from the DMA would be necessary. Preliminary tests by BREHM *et al.* involved the fabrication of the HEMAcOEDMA-DMA on a conductive platform<sup>[88]</sup>. The use of ITO coated glass substrates made the platform conductive and suitable for on-chip MALDI-TOF-MS measurements. Initial measurements, applying doxorubicin, which was dispensed onto the HL spots of the ITO-DMA, was detected as the sodium adduct. In another study, RAMALLOGUEVARA *et al.* utilized a different iteration of ITO-DMA for integrated MALDI-TOF-MS imaging in nanoliter-scale directly from the chip<sup>[92]</sup>.

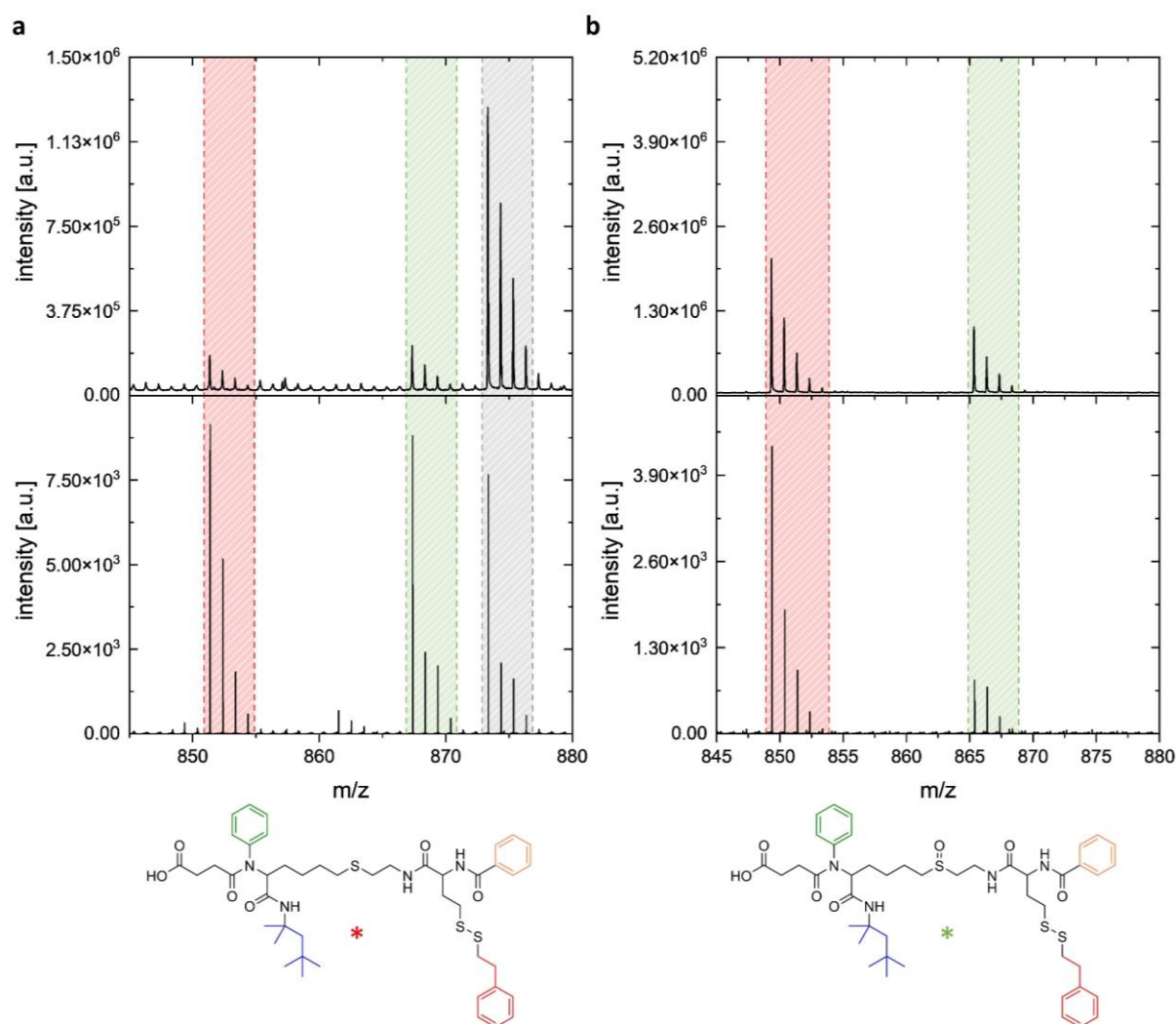
To validate the feasibility of on-chip MALDI-TOF-MS measurements, ITO-DMA was produced using an adapted protocol. To demonstrate the potential of miniaturization on the platform, the pattern was switched from the round hydrophilic spots with a diameter of 2.8 mm, capable of accommodating 10  $\mu$ L, to round spots with a diameter of 900  $\mu$ m and a volume of around 150 nL. This modification increased the potential library on a single DMA glass slide from 80 spots to 1152, and the compound density from 4 spots/cm<sup>2</sup> to 58 spots/cm<sup>2</sup>.

To evaluate the optimal conditions for the on-chip MALDI-TOF-MS measurement, six exemplary compounds were synthesized on ITO-DMA using round spots with a diameter of 900  $\mu$ m. These compounds were already analyzed using the droplet transfer method. After UV induced cleavage of the compounds, different amounts of matrix were deposited on every HL spot (Figure 19a). To ensure a homogenous co-crystallization of the matrix and analyte, dimethylformamide (DMF) was chosen as a solvent, as it offers high solubility for the matrices and the analytes. Figure 19c shows the crystallization of 44 nmol DHB per 900  $\mu$ m spot using DMF as the solvent on ITO-DMA. To determine the optimal amount of needed matrix per spot, different amounts of matrix were deposited in triplicates to each of the compounds. Matrix amounts ranged from 22 nmol to 44 nmol per spot. MALDI-TOF-MS imaging in positive mode using DHB as a matrix for exemplary compound **A7I4P4T1** is shown in Figure 19b. Lower amounts of DHB did not show any detection of the main product adduct  $[M+H]^+$ , while higher amounts (<38 nmol per spot) showed high intensities. For further experimentation, an amount of 44 nmol per spot was chosen.



**Figure 19:** (a) Schematic workflow for the preparation of the ITO-DMA for MALDI-MS measurements: after the synthesis of the lipid-like compounds, water is applied in each hydrophilic spot. i) The DMA is irradiated with UV light at 365 nm for 20 minutes to release the compounds into distinct droplets. ii) Corresponding MALDI-matrix solution is dispensed onto the respective spots and the slide is dried in vacuum before being handed over to MALDI-TOF analysis. (b) MALDI-TOF-MS imaging of an ITO-DMA modified with round 900  $\mu\text{m}$  spots in which the solid-phase synthesis of **A7I4P4T1** was carried out. Measurement was conducted in positive mode. Different amounts of DHB were dispensed in triplicates (top to bottom), ranging from 22 nmol (left) to 44 nmol (right) per spot. Orange color indicates the intensity of the  $[M+H]^+$  ion. (c) Microscopic pictures of dried DHB on a hydrophilic spot (900  $\mu\text{m}$ , round) on ITO-DMA. DMF was used as the solvent.

Comparing the obtained spectra from droplet transfer to ground steel plate with the acquired spectra directly from ITO-DMA using the optimized matrix amounts demonstrates good comparability of the methods. Figure 20 presents a direct comparison between the spectra obtained in positive mode (a) and negative mode (b) from ground steel plate (top) and ITO-DMA (bottom). The obtained spectra of exemplary compound **A7I4P1T4** show the product peak as  $[M+H]^+/[M-H]^-$  (indicated by red band) with the visible isotopic pattern, the main side product (indicated by green band) as well as the sodium adduct (gray band). Although intensities of the measurements on ITO-DMA are significantly lower due to ionization suppression by the polymer backbone of the ITO-DMA, the signal-to-noise ratio is still high enough for data evaluation.



**Figure 20:** Comparison between the MALDI-MS spectra of compound A7I4P1T4 obtained from ground steel target plate after droplet transfer from DMA (top) and directly from ITO-DMA (bottom, average spectrum of the spot) in (a) positive mode using DHB as matrix and (b) negative mode using NEDC as matrix. Colored bands mark the corresponding  $[M+H]^+$  (red, green) and the  $[M+Na]^+$  adduct (grey), as well as the isotopic pattern.

In order to show the possibilities of the on-chip MALDI-TOF-MS measurements in a miniaturized high-throughput screening, a library consisting of 128 lipid-like compounds with four replicates each was synthesized directly on ITO-DMA using round spots with a diameter of 900  $\mu\text{m}$ . The utilized starting materials are listed in Table 5. The subset of starting materials was chosen arbitrarily.

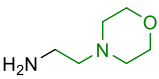
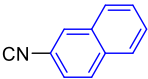
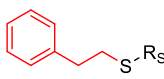
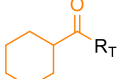
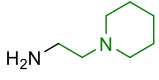
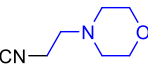
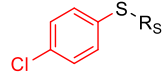
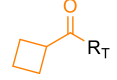
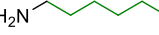
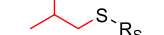

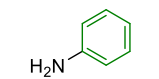

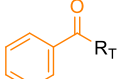
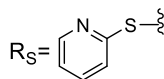
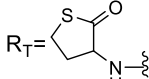
To emphasize the benefits of miniaturization through on-chip measurements, the quantities of starting materials and solvents utilized in the production of this specific set of compounds will be compared to the previously mentioned analysis using LC-MS. In the on-chip synthesis of a single lipid-like compound on a 900  $\mu\text{m}$  spot, the total consumption of reaction solutions was

only 730 nL. This includes the complete synthetic cascade, starting with the immobilization of the photolinker and subsequent modification with succinic acid to the final TADE reaction. In total, only 215 nmol of reagents were used in the synthesis of one lipid-like compound on a 900  $\mu\text{m}$  spot.

Synthesizing four replicates of the 128 compounds in this sub-library required only 375  $\mu\text{L}$  of reaction solutions. Only 110  $\mu\text{mol}$  of reagents were needed for the synthesis of the sub-library. Comparing these numbers with the numbers of the aforementioned synthesis on a larger scale using round spots with a diameter of 2.8 mm showcases the massive reduction in used starting materials and solvents. Synthesis of the same set of compounds in four replicates in 2.8 mm spots would increase the used solvent volumes to almost 13 mL, and the total amount of used reagents to 4 mmol. It needs to be reminded that four spots of the same compound need to be synthesized to analyze the product solution via LC-MS. This leads to a total volume of around 50 mL of solvents and a total of 16 mmol of reagents.

By miniaturizing the synthesis and subsequent analysis via MALDI-TOF-MS, the amount of needed solvents, in comparison to the analysis on a larger scale, was decreased by a factor of 135. The amount of used reagents was reduced by a factor of 145. Additionally, the time needed to measure only one repetition of every compound via LC-MS would take about 22 hours, while measuring the whole library with four repetitions each synthesized in smaller patterns was analyzed within 1 hour.

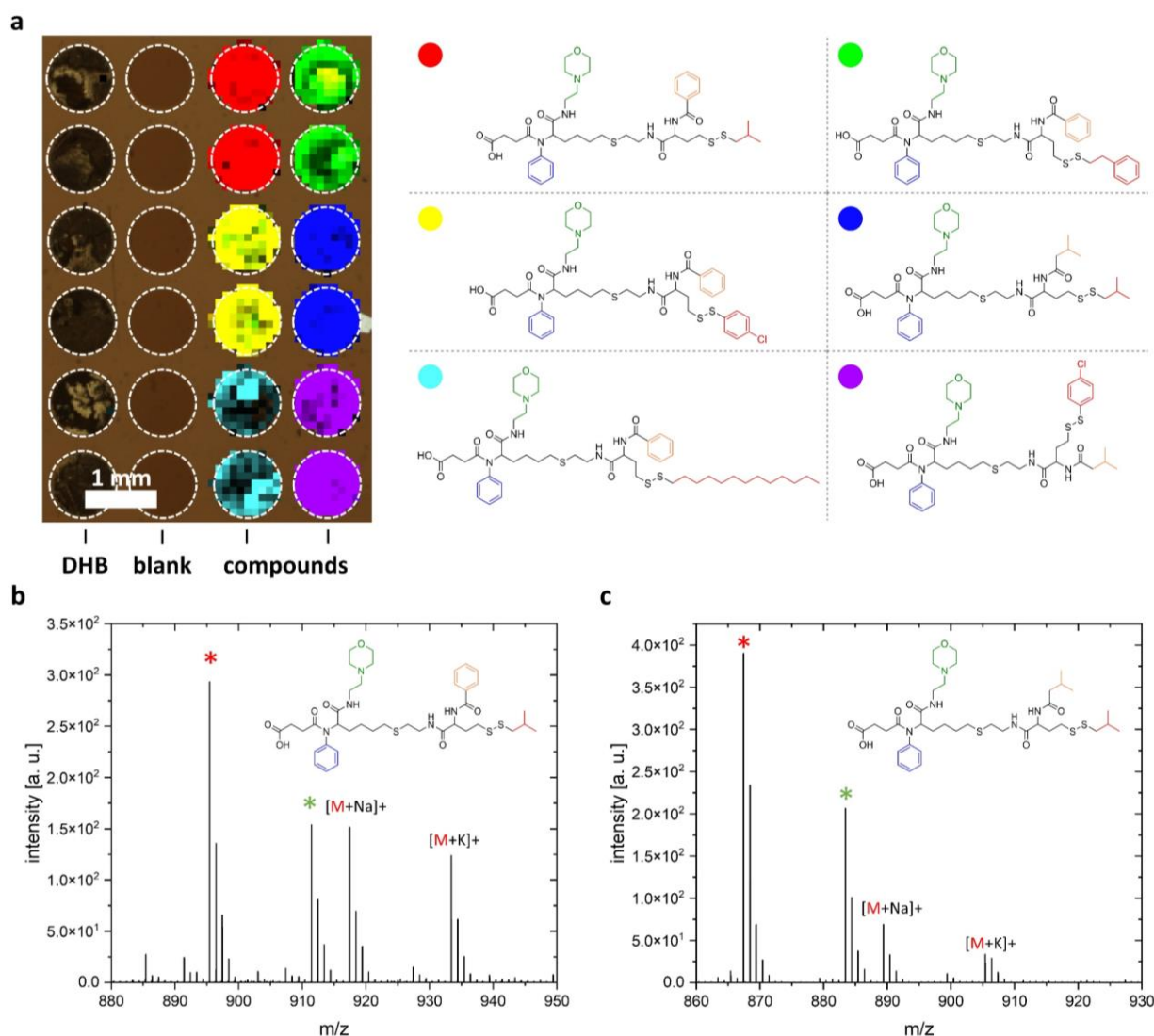
**Table 5:** Overview of the used starting materials for the synthesis of a 128 membered library on ITO-DMA.

#	Structure	#	Structure	#	Structure	#	Structure
A <sub>1</sub>		I <sub>1</sub>		P <sub>1</sub>		T <sub>1</sub>	
A <sub>3</sub>		I <sub>3</sub>		P <sub>3</sub>		T <sub>2</sub>	
A <sub>5</sub>				P <sub>4</sub>		T <sub>3</sub>	
A <sub>7</sub>				P <sub>13</sub>		T <sub>4</sub>	
				$R_S = \text{pyridine-2-ylthio}$ 		$R_T = \text{thioamide}$ 	

MALDI-TOF-MS imaging was employed to evaluate the outcome of the 512 reactions on ITO-DMA. Figure 21a shows the acquired data for 6 exemplary compounds taken from the 128 membered library in duplicates. Color depths represent the intensity of the respective  $[M+H]^+$  adducts. The MALDI-TOF-MS image shows little to no cross contamination between the spots. No product  $[M+H]^+$  was detected in the control regions of the slide (two columns on the left), while only the synthesized compounds could be detected in the corresponding spots on the right. Compounds were identified by their  $[M+H]^+$  (red asterisk),  $[M+Na]^+$  and  $[M+K]^+$  adducts, as



well as the main side products  $[M+H]^+$  (green asterisk) (Figure 21b and c).



**Figure 21:** (a) MALDI-TOF-MS imaging of an ITO-DMA modified with round 900  $\mu\text{m}$  spots. Only DHB was dispensed in the most left column. Second left column was left blank, while the 6 exemplary compounds of the 128 membered library have been synthesized in duplicates in the two columns on the right. Each color represents one compound and the respective structures are shown in the table. Color depth represent the intensity of the  $[M+H]^+$  adduct. (b) and (c) show exemplary mass spectra obtained from on-chip MALDI-TOF-MS. Compounds were identified by their  $[M+H]^+$  (red asterisk),  $[M+Na]^+$  and  $[M+K]^+$  adducts.

The overall screening results of the 128 membered library are summarized in Table 6. Out of 128 synthesized compounds, 114 could be clearly identified by their  $[M+H]^+$  adduct. This translates to a synthetic success rate of 91%. There were no particular trends indicating non-reactivity of specific starting materials, underscoring the versatility of the synthetic approach. Extrapolating this high success rate to the synthesis of the entire library, which comprises 10,240 compounds, suggests the potential identification of approximately 9,300 novel lipid-like compounds. The scalability and efficiency of the method are particularly noteworthy. A single

ITO-DMA has the capacity to host up to 686 spots, each with a diameter of 900  $\mu\text{m}$ , available for synthesis and subsequent analysis using MALDI-TOF-MS.

Remarkably, only 15 ITO-DMAs would be needed to screen the entire library, emphasizing the efficiency of the on-chip approach. In terms of resources, a mere 2.5 mmol of reagents and 7.5 mL of solvents would be required to synthesize the complete library on ITO-DMAs with 900  $\mu\text{m}$  spots, showcasing the substantial reduction in material consumption and high-throughput aspects of this miniaturized synthesis and screening approach.

**Table 6:** Identification rate of each starting material used in the solid-phase synthesis of the 128 membered sub-library of lipid-like compounds.

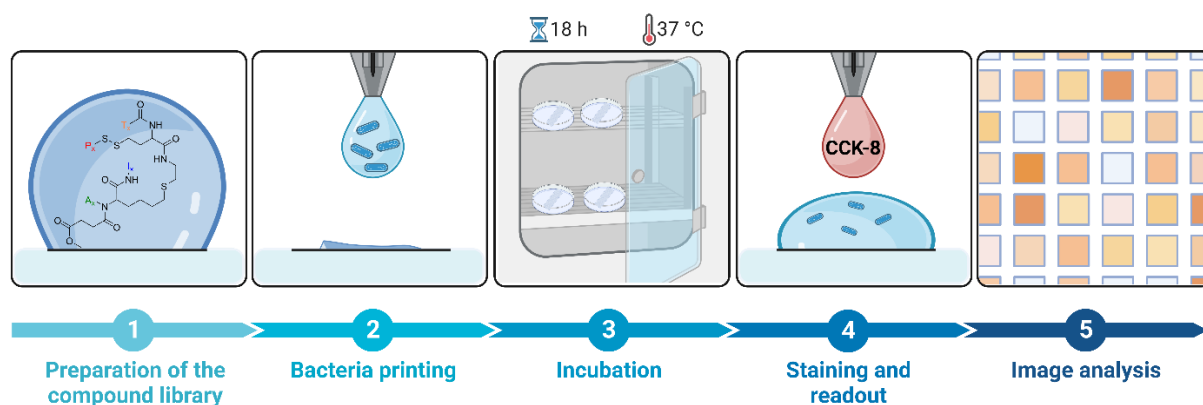
#	Identified [%]	#	Identified [%]	#	Identified [%]	#	Identified [%]
A <sub>1</sub>	94	I <sub>1</sub>	86	P <sub>1</sub>	88	T <sub>1</sub>	100
A <sub>3</sub>	100	I <sub>3</sub>	97	P <sub>3</sub>	91	T <sub>2</sub>	88
A <sub>5</sub>	84			P <sub>4</sub>	97	T <sub>3</sub>	78
A <sub>7</sub>	88			P <sub>13</sub>	91	T <sub>4</sub>	100
<b>Total</b>	91						

### 3.1.4 Antibacterial Activity of the Lipid-Like Compounds

Previous research has highlighted the antibacterial properties found in amphiphilic compounds like antimicrobial lipids (AMP)<sup>[90]</sup> or host defense peptides (HDP)<sup>[93]</sup>. possess antibacterial properties. These compounds are known for their ability to interact with bacterial membranes, demonstrating a membrane-active nature that contributes to their broad range of antimicrobial activity. The strategy of targeting microorganisms' cell membranes proves to be effective and selective, given the subtle differences from mammalian cell membranes<sup>[94]</sup>. Specifically, AMPs interact with the lipid-rich bacterial membrane, leading to its disintegration and subsequent cell death. Building on this understanding, it is hypothesized that lipid-like molecules share similar characteristics, making them promising contenders in the search for new antibacterial compounds.

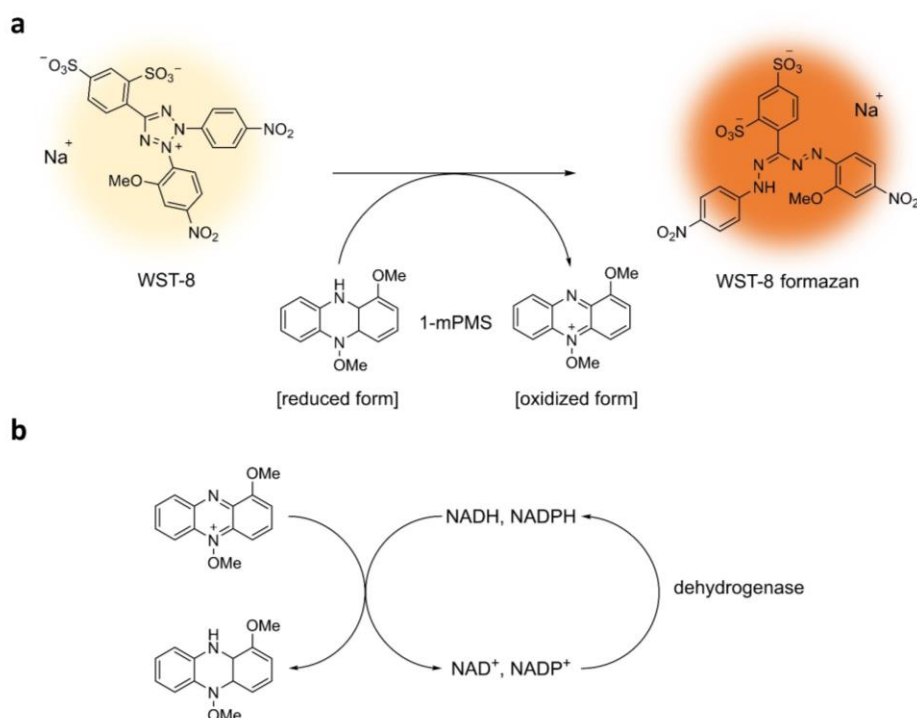
The DMA proved to be a versatile platform for different kinds of biological assays in past studies. LEI *et al.* developed a protocol seed and evaluate the growth of *Pseudomonas aeruginosa* on DMA.<sup>[50]</sup> In later study, they utilized the DMA in a high-throughput screening of over 2000 compounds for their antimicrobial properties against *Klebsiella pneumoniae* (Kp) and methicillin resistant *Staphylococcus aureus* (MRSA).<sup>[95]</sup>

For this project the previously developed screening procedure for DMA was adapted. The workflow, as illustrated in Figure 22, begins with the synthesis of lipid-like compounds on DMA using square spots with an edge length of 1 mm, following the established synthetic pathway. Subsequently, UV induced cleavage releases the synthesized compounds into distinct droplets. After removing any residual solvent under reduced pressure, a suspension of Kp with a predefined optical density in Miller-Hinton medium is precisely dispensed into each HL spot using the non-contact liquid dispenser I.DOT mini. The bacteria and compounds incubate for 18 hours at 37°C. Following the incubation period, droplets are stained with Cell Counting Kit-8 (CCK-8), which turns from transparent to a bright yellow-orange in the presence of living bacteria. The color change is proportionate to the concentration of living bacteria in the droplets, allowing for the visible detection of bacterial growth inhibition. To analyze the color changes in the droplets, a digital image of the entire array is captured using a conventional photo scanner.



**Figure 22:** Schematic representation of the workflow of the biological assay on DMA.

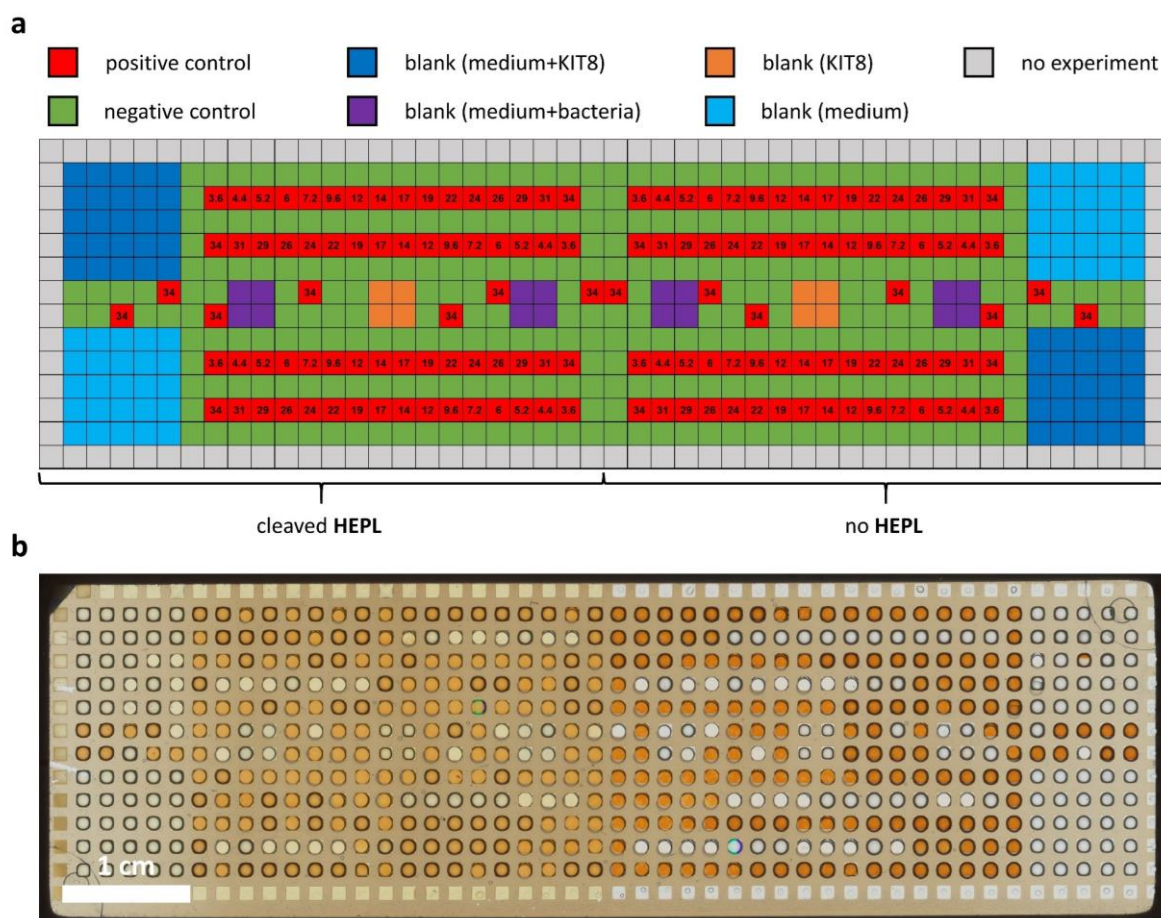
One of the main aspects of the on-chip antibacterial screening is a fast and efficient readout method. Colorimetric readout using CCK-8 was adapted from LEI *et al.*<sup>[95]</sup> While they used it on a nanoparticle-based version of the DMA, CCK-8 was first employed on polymer-based DMA in this project. CCK-8 operates based on the reduction of the highly water-soluble tetrazolium salt WST-8 by dehydrogenase in living bacteria in presence of electron carrier 1-methoxy-5-methylphenazinium methyl sulfate (1-mPMS) to give an orange-color formazan dye (Figure 23a, b). It is commonly employed in proliferation and cytotoxicity assays. In these assays, the proportion of living bacteria is estimated by measuring the optical density of the reduced WST-8.<sup>[96]</sup> Evaluation of the intensity of the color intensity can be achieved by capture and analysis of a digital image of the DMA.



**Figure 23:** Formation of the orange-colored WST-8 formazan. (a) Schematic of the reduction of WST-8 to orange-colored WST-8 formazan in presence of electron carrier 1-mPMS (b) Reduction of the electron carrier by the dehydrogenase in living bacteria.

To validate the screening procedure on polymer-based DMA, preliminary experiments were carried out. These experiments aimed to assess the impact of both the unmodified polymer and the photolinker-modified polymer on bacterial growth, along with the controls. Furthermore, the modified surface, post UV-induced cleavage, develops a yellow color, influencing the background intensity during image analysis. Figure 24a shows the layout of the preliminary experiment on a polymer-based DMA with square spots with an edge length of 1 mm. To assess screening conditions, HL spots on both bare polymer and modified polymer were included on a single chip. For this, only half of the HL spots were modified with a 0.1M solution of the photolinker and subsequently cleaved to replicate the surface conditions post the combinatorial synthesis of lipid-like compounds. Negative and positive controls, as well as blanks were placed on both modified and bare polymer HL spots. The negative control utilized 150 nL of a Kp suspension in Miller-Hinton medium with a predefined optical density of 0.001 at 600 nm per 1 mm spot, while antibiotic *colistin sulfate*<sup>[97]</sup> served as the positive control. To address the minimum inhibitory concentration (MIC) of *colistin sulfate* on polymer-based DMA, different amounts of *colistin sulfate* were deposited. The numbers in the positive controls in Figure 24a represent the final concentration of the antibiotic in the 150 nL droplets. Additionally, several blanks were distributed throughout the chip, all in total volumes of 150 nL per spot. Figure 24b

illustrates the acquired image of the DMA after staining and incubation with CCK-8. There is no cross-contamination detectable.



**Figure 24:** Viability of the assay. (a) Layout of the preliminary experiments to validate the screening conditions on polymer-based DMA. Colors represent negative and positive controls, as well as blanks. Numbers represent the final concentration of colistin sulfate in a 150 nL droplet per spot. (b) Scanned image of stained droplets containing *Kp* incubated overnight on DMA with square spots with an edge length of 1 mm. Previous shown layout was employed.

To determine the MIC of the positive control, *colistin*, on polymer-based DMA – both on photolinker-modified and bare HL spots – against *Kp*, a dilution series was prepared with final *colistin* concentrations ranging from 3.6  $\mu\text{M}$  to 33.6  $\mu\text{M}$ . The scan image obtained was analyzed for the corresponding color depth of the stained droplets, which is indicative of the number of living bacteria. To assess the impact of the photolinker on the MIC of *colistin*, Figure 25a presents the data for photolinker-modified HL spots, while Figure 25b illustrates the data for bare HL spots.

Comparing the data between the two different surfaces it is observable, that the color depths obtained via analysis of the bare HL spots show higher values for the negative controls than the photolinker-modified HL spots, while having lower values for the positive controls. The

comparison of the blanks reveals the previously mentioned higher background for the modified spots due to the color formation of the HL spots after UV-induced cleavage of the photolinker. The differences in the acquired color-depth data can be explained by changes in surface characteristics. Modification with the photolinker, followed by UV irradiation at 365 nm for 15 minutes, induces several alterations in the HL spots. The development of a yellow color influences the color-depth of the background, while residues of the remaining cleaved photolinker in the HL spots also alter the surface wettability, making it more hydrophobic compared to the bare HL spots. This change in wettability affects bacterial growth<sup>[98]</sup>, resulting in lower values of the negative control of the photolinker-modified surface. To assess the performance of an assay, ZHANG *et al.*<sup>[99]</sup> developed the  $Z'$ -factor, which is based on the difference between the means ( $\mu$ ) of the positive (p) and negative (n) controls in relation to the standard deviation ( $\sigma$ ) (Equation ( IV )).

$$Z' = 1 - \frac{3(\sigma_p + \sigma_n)}{|\mu_p - \mu_n|} \quad (IV)$$

In the assay on bare HL spots, the  $Z'$  value is 0.89, and for the results obtained on photolinker-modified HL spots, the value is 0.63. Despite being significantly lower due to the smaller difference between the positive and the negative control for the modified HL spots, both assays on both surfaces are classified as excellent according to Table 7.

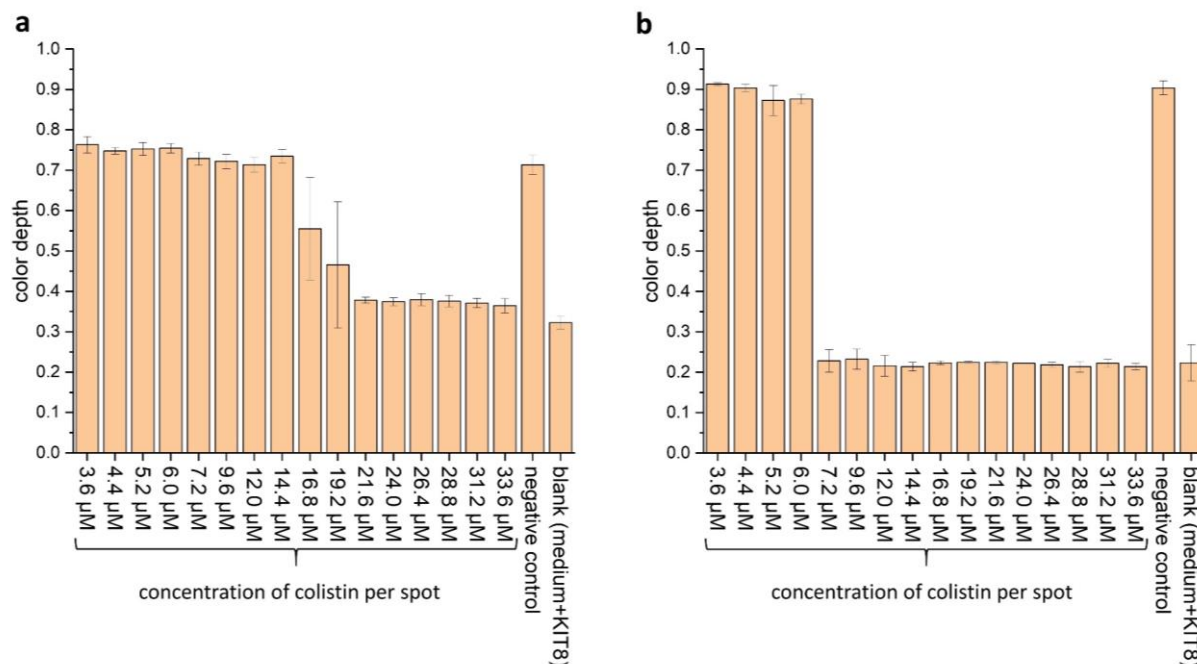
**Table 7:** Classification of  $Z'$  values in assays according to Zhang *et al.*<sup>[99]</sup>

<b><math>Z'</math> value</b>	<b>Classification</b>
1.0	Ideal assay
$1.0 > Z' \geq 0.5$	Excellent assay
$0.5 > Z' > 0$	Acceptable assay
0	Yes/no type assay
$< 0$	Screening impossible

The comparison of the MIC for *colistin* against Kp on both surfaces reveals a notable increase in the assay performed on modified HL spots. In contrast to the bare HL spots where 7.2  $\mu\text{M}$  of *colistin* resulted in 99.9% inhibition, the concentration needed for the same level of inhibition on photolinker-modified spots was three times higher (21.6  $\mu\text{M}$ ). This discrepancy suggests that lower surface wettability might impact the uptake of *colistin* in the droplets on the modified HL spots, leading to a reduction in the actual concentration of colistin in the droplets. Nevertheless,

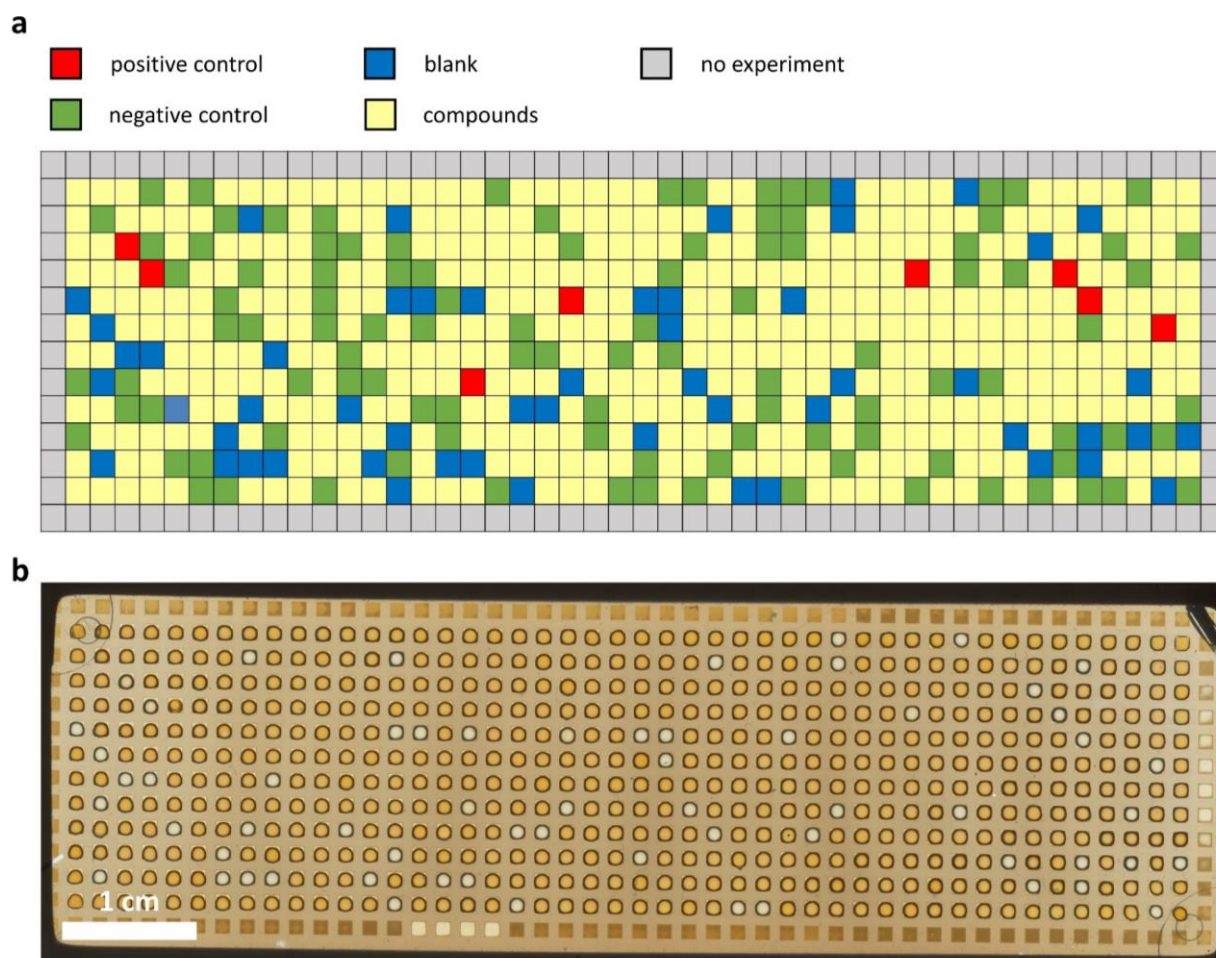


*colistin* at a final concentration exceeding 21.6  $\mu\text{M}$  remains suitable as a positive control when using photolinker-modified HL spots.



**Figure 25:** Evaluation of the viability test. (a) with cleaved HEPL (b) without cleaved HEPL

Having demonstrated the viability of using photolinker-modified HL spots in an antibacterial assay, the 128-membered library previously analyzed via MALDI-TOF-MS was synthesized on square spots with an edge length of 1 mm. Following the UV-induced release of the compounds into distinct droplets, the described workflow for the antibacterial screening was executed. The 128 compounds were synthesized in triplicates and randomly distributed across the DMA. *Colistin*, at a final concentration of 33  $\mu\text{M}$ , was employed as a positive control and placed randomly in eight repetitions. The remaining spots were filled with blanks and negative controls (Figure 26a). The corresponding scan image after CCK-8 staining is shown in Figure 26b.



**Figure 26:** Screening for antibacterial activity of 128 lipid-like compounds. **(a)** Layout of the slide. Compounds have been randomly distributed across the DMA. Colistin served as positive control in eight randomly placed repetitions. Leftover spots were filled up negative controls and blanks. **(b)** Scanned image of stained droplets containing *Kp* incubated overnight on DMA with square spots with an edge length of 1 mm. Previous shown layout was employed.

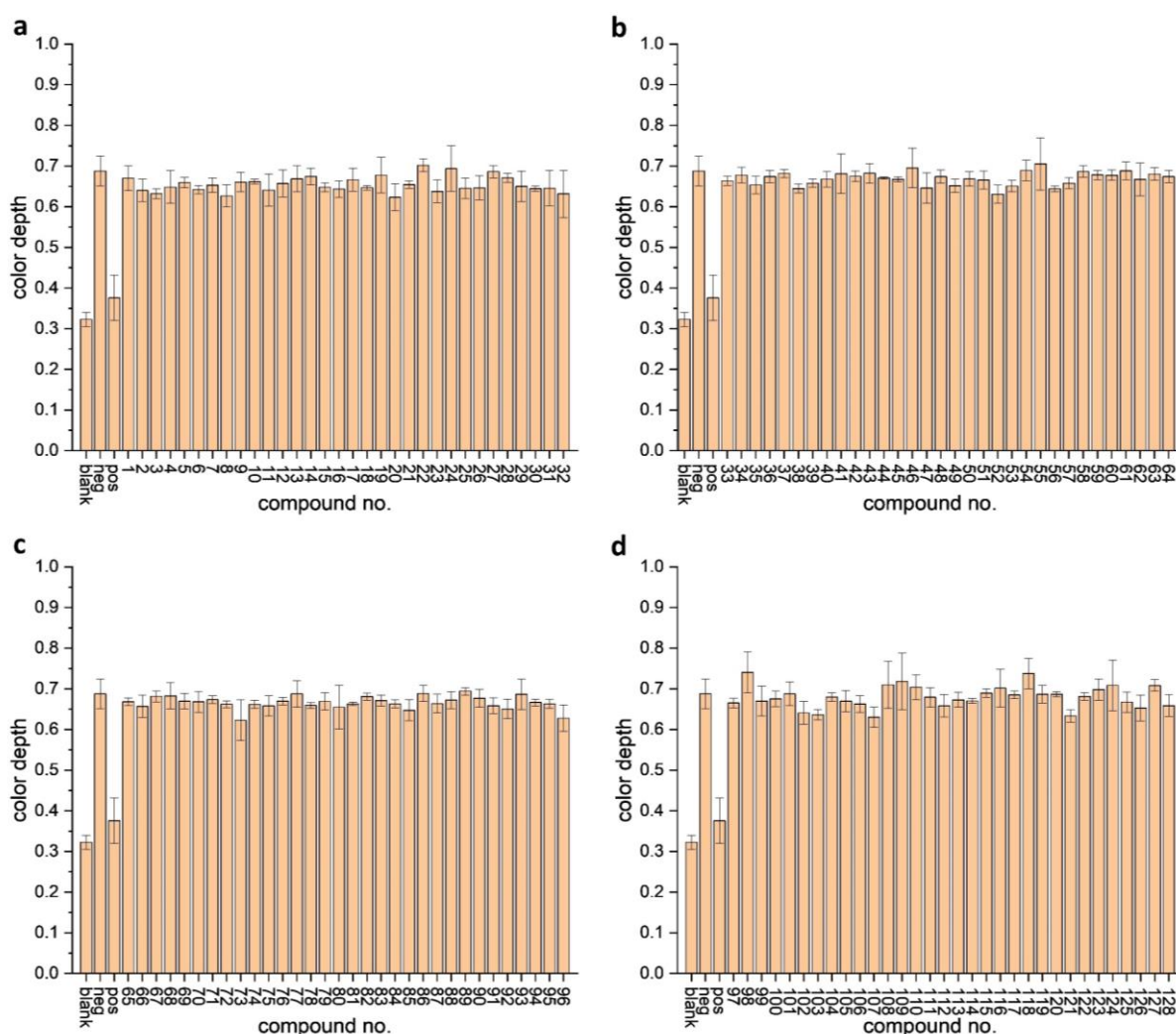
The antibacterial screening of the 128-membered library of solid-phase synthesized lipid-like compounds, using a DMA with square spots of 1 mm edge length, did not show any antibacterial activity of these compounds against *Kp* (Figure 27). The controls and blanks exhibited the expected responses, confirming the reliability of the assay. Despite the lack of antibacterial activity in the compounds, the outcomes fell within anticipated ranges given the small subset.

The efficiency of solvents and reagents in minimal quantities demonstrated the advantages of miniaturization. The synthesis utilized only 280  $\mu\text{L}$  of solvents and 82  $\mu\text{mol}$  of reagents. The subsequent antibacterial assay consumed a total volume of 75  $\mu\text{L}$  of bacterial suspension and 55  $\mu\text{L}$  of CCK-8. Timewise, the triplicate synthesis of 128 compounds spanned one week, while the subsequent on-chip antibacterial assay was completed in just two days. The optimized



workflow, encompassing on-chip solid-phase synthesis, UV-induced compound release, and antibacterial screening, consumed only 410  $\mu\text{L}$  of solvents and completed within 9 days.

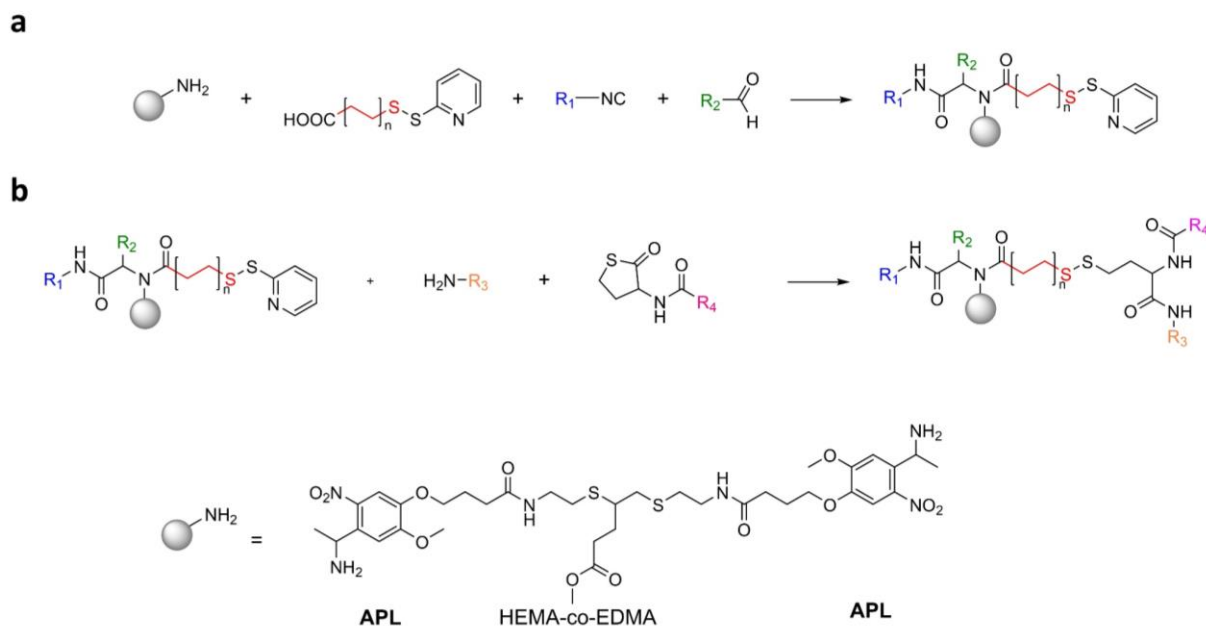
This novel approach, utilizing DMA and miniaturization, demonstrated significant advantages over traditional well plates. The reduction in solvent and reagent volumes contributes to cost-effectiveness, while the integration of the synthesis saves time. The speed of the on-chip assay, accomplished within a fraction of the time required for traditional methods, offers rapid screening capabilities, enabling efficient high-throughput experimentation. Despite the compounds showing no antibacterial activity, this study highlights the efficiency, economy, and speed facilitated by the DMA platform. The integration of synthesis and antibacterial screening on a chip opens new possibilities for drug discovery and optimization processes. The ability to swiftly assess a large compound library in a compact and resource-efficient manner provides a promising strategy for future advancements in pharmaceutical research.



**Figure 27:** Results of the screening for antibacterial activity of 128 compounds against *Kp*. The first three entries in each plot correspond to blank, negative control (neg), and positive control (pos). Each data point is the average of three measurements. Error bars represent standard deviations.

### 3.1.5 Alternative Route for the Synthesis of Lipid-Like Compounds

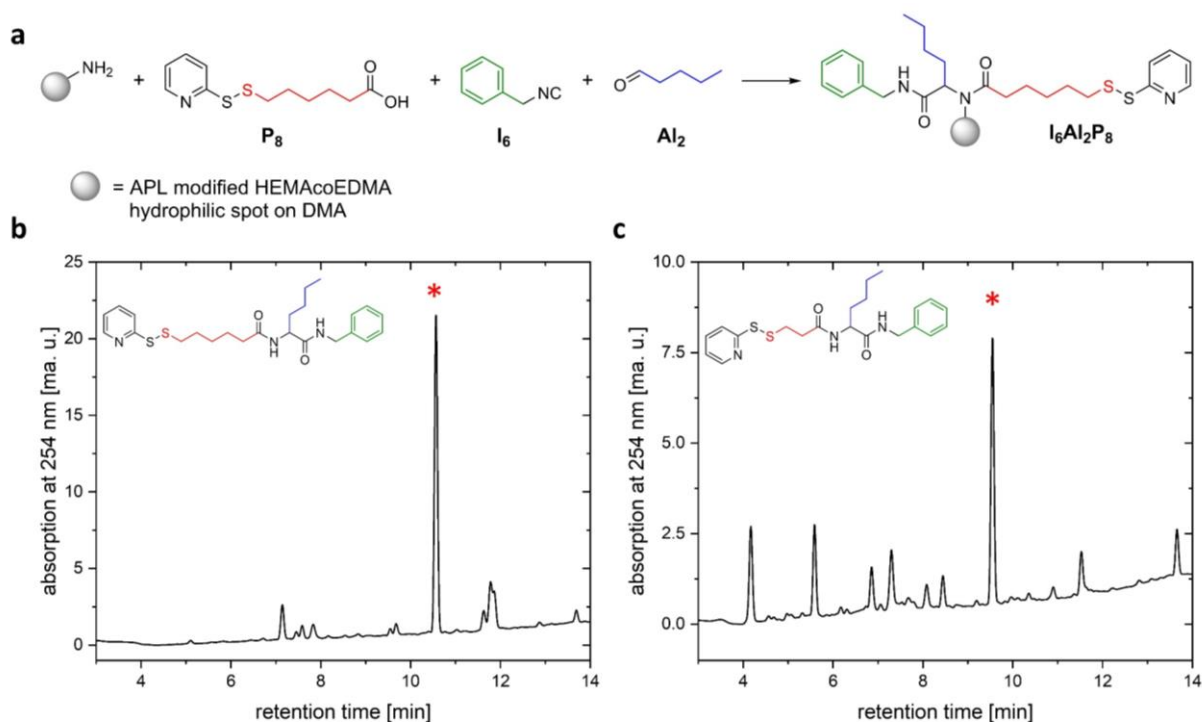
The previously described synthetic pathway for lipid-like compound synthesis demonstrated promising results; however, the incorporation of anchor points for subsequent synthesis steps – immobilization of succinic acid to the photolinker and introduction of a primary amine through thiol-ene click chemistry - proved to be a laborious process. To streamline the procedure and minimize the number of reaction steps, a modified approach was adopted. In this revised method, the HL spots of the DMA were altered by introducing an amino photolinker, creating a surface that is directly reactive towards the four component UGI reaction. A carboxylic acid, previously modified as a PDS derivative, was employed to provide the necessary reactive groups for disulfide exchange in the initial synthesis step (Figure 28a). Subsequent TADE reaction with the immobilized PDS derivative and a primary amine yields the lipid-like compound ((Figure 28b), eliminating the need for additional intermediary steps. Despite the reduction in the number of synthesis steps to just two reactions, it's noteworthy that the quantity of changeable residues remains unchanged. The novel approach not only reduces the overall number of synthesis steps but also introduces a new variable—specifically, the length of the alkyl chain between the disulfide and the carboxylic acid moiety—adding an additional dimension to the customization of the synthesized compounds.



**Figure 28:** Synthetic route to decrease the steps in the synthesis of lipid-like compounds on DMA. (a) Four component UGI reaction to introduce the reactive 2-pyridyl disulfide moiety to the surface. (b) TADE reaction including a primary amine, a thiolactone derivative and the immobilized PDS derivative to form the lipid-like compounds. Utilizing this approach only needs two steps to synthesize the final compound, while still having four different moieties for diversification.

To investigate this hypothesis, the compound **I<sub>6</sub>Al<sub>2</sub>P<sub>8</sub>** was synthesized on a larger scale using round spots with a diameter of 2.8 mm. To create the reactive surface, the HL spots were initially modified with the amino photolinker by manually adding 5  $\mu$ L of the linker coupling solution, which included 0.1 M Fmoc-amino photolinker (FAPL) and 0.1 M HOBt in NMP/DIC (9:1, v/v). This modification reaction proceeded for 18 hours. After washing the slide with acetone and ethanol, the subsequent deprotection of the Fmoc-protecting group was achieved by immersing the entire slide in piperidine/water (4:1, v/v) for 1 hour, resulting in the formation of the amine surface. The Ugi reaction was initiated by adding 2.5  $\mu$ L of each 0.5 M solution of the PDS derivative **P<sub>8</sub>**, benzyl isocyanide **I<sub>6</sub>**, and n-pentanal **Al<sub>2</sub>** (Figure 29a). The reaction proceeded for 72 hours, and the product **I<sub>6</sub>Al<sub>2</sub>P<sub>8</sub>** was released from the surface through UV irradiation at 365 nm.

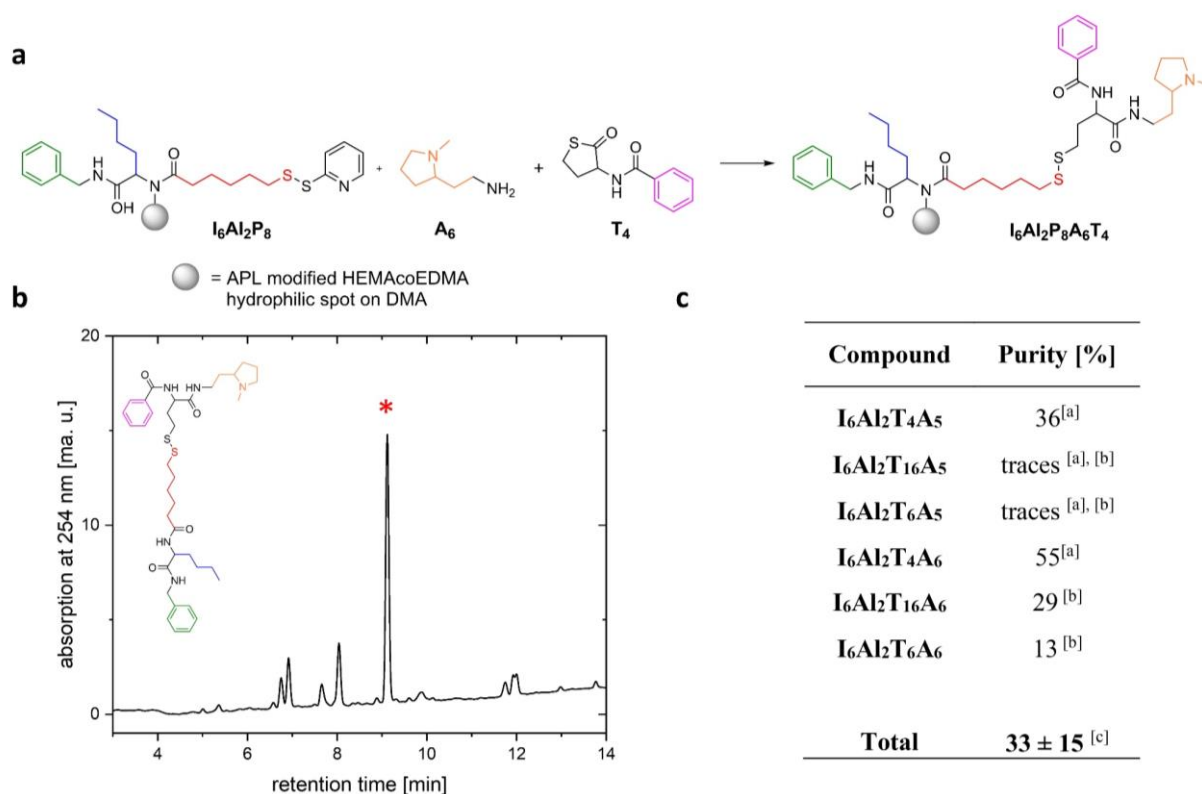
To assess the purities of the reactive intermediates, two exemplary reactions were conducted, each involving PDS derivatives with varying lengths of the alkyl chains (**P<sub>8</sub>** and **P<sub>7</sub>**). The corresponding chromatograms are presented in Figure 29 a und b. Both compounds exhibit satisfactory purities, with the longer alkyl chain-bearing PDS derivative (**P<sub>8</sub>**) achieving an 80% purity and the shorter alkyl chain-bearing PDS derivative (**P<sub>7</sub>**) attaining a 44% purity. It's noteworthy that aldehyde **Al<sub>2</sub>** and isocyanide **I<sub>6</sub>** were utilized in both exemplary reactions.



**Figure 29:** (a) Exemplary reaction to form the reactive intermediate **I<sub>6</sub>Al<sub>2</sub>P<sub>8</sub>** utilizing a solid-phase approach. Exemplary chromatograms of synthesized reactive intermediates (b) **I<sub>6</sub>Al<sub>2</sub>P<sub>8</sub>** and (c) **I<sub>6</sub>Al<sub>2</sub>P<sub>7</sub>** at 254 nm. Asterisk indicate the product peak.

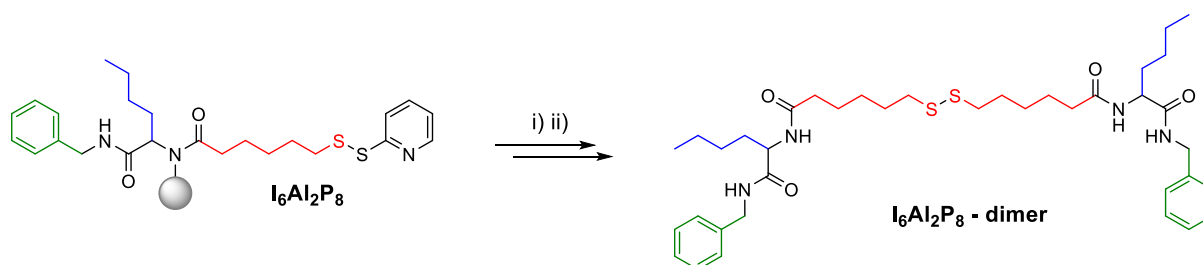
To further assess the efficiency of the shortcut approach in lipid-like compound synthesis, the reactive intermediate **I<sub>6</sub>Al<sub>2</sub>P<sub>8</sub>** was employed in six different on-chip Target-Assisted Disulfide Exchange (TADE) reactions, utilizing 2.8 mm spots. The reactions were initiated by applying 3.5  $\mu$ L of a 0.5 M solution of the thiolactone derivative and the amine in DMSO to each spot. After 18 hours, the reaction was completed, and subsequent UV-induced release resulted in the formation of the desired lipid-like compound. The solid-phase synthesis of compound **I<sub>6</sub>Al<sub>2</sub>P<sub>8</sub>A<sub>6</sub>T<sub>4</sub>** is illustrated in Figure 30a, and the corresponding chromatogram at 254 nm is shown in Figure 30b.

In testing the purities of six exemplary compounds using previously synthesized building blocks (chapter 3.1.2 – 3.1.4), the results revealed a mixed outcome (Figure 30c). Unfortunately, the overall success rate of the TADE reactions was not high, as only four out of six compounds were successfully synthesized. The average purity of the successfully synthesized compounds ranged between 13% and 55%. Attempts to improve the yield and purities by employing GBL and NMP as solvents for TADE did not yield different outcomes. Interestingly, an increase in reaction temperature to 50 °C even resulted in a decreased success rate of the reactions.



**Figure 30:** (a) Exemplary TADE reaction to form the lipid like compound **I<sub>6</sub>Al<sub>2</sub>P<sub>8</sub>A<sub>6</sub>T<sub>4</sub>**. (b) Representative chromatogram at 254 nm of the synthesized lipid like compound. (c) Overview of the purities of exemplary lipid like compounds synthesized via two-step approach. <sup>[a]</sup>Purity was calculated as the fraction of the product's peak integral with respect to the sum of integrals of all peaks at 254 nm absorbance. <sup>[b]</sup>Purity was calculated using the total ion chromatogram (TIC). <sup>[c]</sup>unsuccessful synthesized compounds were excluded.

The decline in purities, possibly accompanied by increased consumption of the reactive intermediate, can be attributed to the formation of the disulfide dimer of the intermediate. Although no visible formation was observed during the synthesis and UV release of the intermediates (Figure 29a), it is likely that the in-situ generated thiol is triggering the dimerization of the intermediate. Suppressing this undesired reaction could potentially enhance purities and overall success rates of the reaction. It's important to note that while only a limited set of reactions was initially tested, addressing this issue could have broader implications for the efficiency of the synthesis.



**Figure 31:** Formation of the dimer of the reactive intermediate during the TADE reaction as the major side-product of the synthetic cascade. i) TADE reaction ii) UV induced release from the surface.

### 3.2 Miniaturization of the Palladium-Catalyzed Suzuki-Miyaura Reaction

In order to expand the toolbox of reliable reactions on DMA the SUZUKI-MIYAUURA reaction (SMR) was introduced. The workflow and purity analysis was initially developed in previous works by MARIUS BREHM, which resulted in joint publication.<sup>[1]</sup> The work of BREHM will be summarized as a short introduction to the method.

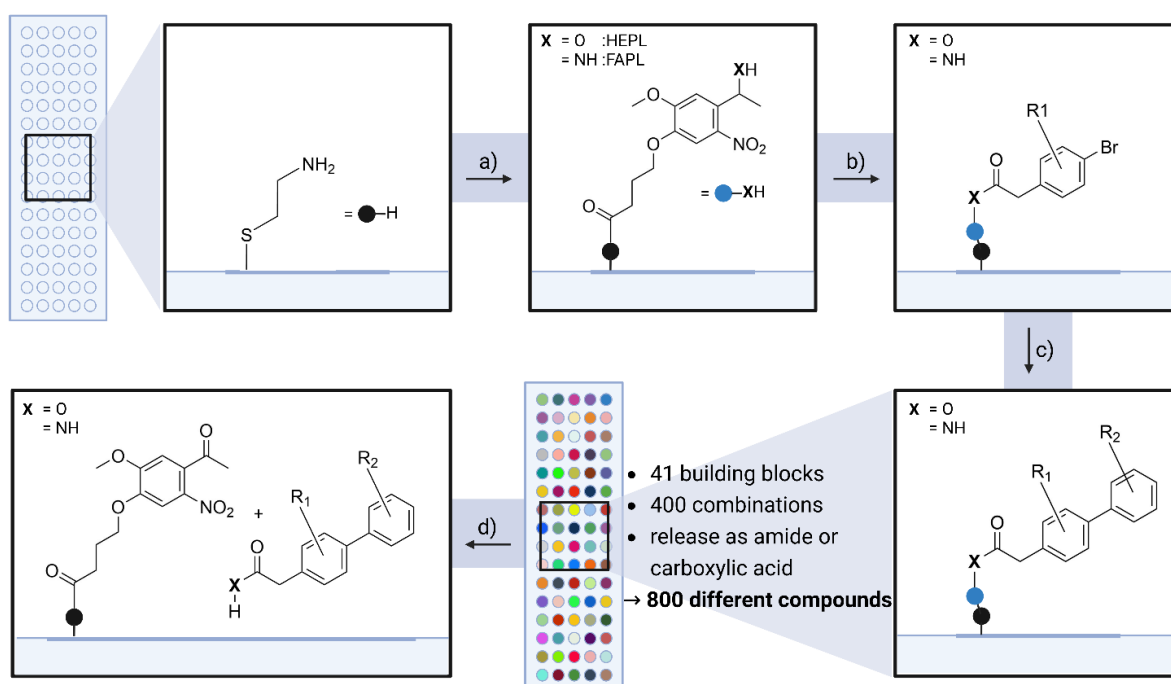
#### 3.2.1 Synthesis of Biphenyls on Droplet Microarrays at Nanoliter Scale

To implement the SMR on DMA, the adapted generalized solid-phase synthesis approach illustrated in Figure 1 was employed. The SMR was conducted in larger scale, using HL spots with a diameter of 2.8 mm, which allowed the manual collection of 5 spots per compound after UV induced cleavage. This resulted in a total of 50  $\mu\text{L}$ , which was enough to be analyzed using LC-MS.

A detailed workflow for the synthesis of biphenylic compounds on DMA is illustrated in Figure 32. Initially, HL spots were treated with 5  $\mu\text{L}$  of linker coupling solution each for 18 h (Figure 32a). The linker coupling solution, consisting of 0.1 M photolinker (HEPL or Fmoc amino photolinker (FAPL)) and 0.1 M HOBt in NMP, was freshly mixed with 5% (v/v) DIC before dispensing. After coupling, the DMA underwent rinsing with ethanol and acetone, followed by drying in an airflow. For FAPL, deprotection was performed using a solution of 20% (v/v) piperidine in NMP. Subsequently, aromatic halides (containing a carboxylic acid) were coupled to the linker by dispensing 5  $\mu\text{L}$  of a solution in each spot containing 0.1 M of the carboxylic acid, 0.01 M 4-DMAP, and 5% (v/v) DIC in NMP, allowing it to react for 18 h (Figure 32b). The attached aryl halides were utilized in the SMR, where 1.5  $\mu\text{L}$  of each 0.5 M dibenzyl diisopropylphosphoramidite and 0.2 M solution of disodium tetrachloropalladate in water were dispensed into every spot. Incubation for 15 min at room temperature facilitated the on-chip synthesis of the catalyst. Subsequently, 3  $\mu\text{L}$  nL of a solution containing 0.5 M boronic acid derivative in NMP and 2  $\mu\text{L}$  of a saturated sodium carbonate solution were added, and the DMA was incubated in the dark at room temperature for 18 h (Figure 32c). The reactions were concluded by washing off the mixtures, followed by immersion of the entire slide in a 0.1 M solution of potassium cyanide (KCN) in DMSO/water (1:1) for 3 h to eliminate precipitated palladium. The photoinduced cleavage from the surface using UV light at 365 nm released the biphenylic compounds of interest into distinct droplets, with the cleaved linker remaining on the surface of the HL spots (Figure 32d).

To monitor the synthetic success of the employed SMR on DMA, 25 exemplary reactions were conducted. The cleaved biphenylic compounds were analyzed via LC-MS for their purity. The resulting purities of the products were in the range between 55% and 95% with an average of  $84\% \pm 10\%$ . Precipitated palladium during the SMR was removed from the DMA in a efficient way, leaving only traces ( $35 \pm 4$  ppm) of palladium in the cleaved samples.

All results presented in the following of Chapter 3.2 are obtained in this PhD work. Contributions by other people are clearly indicated.



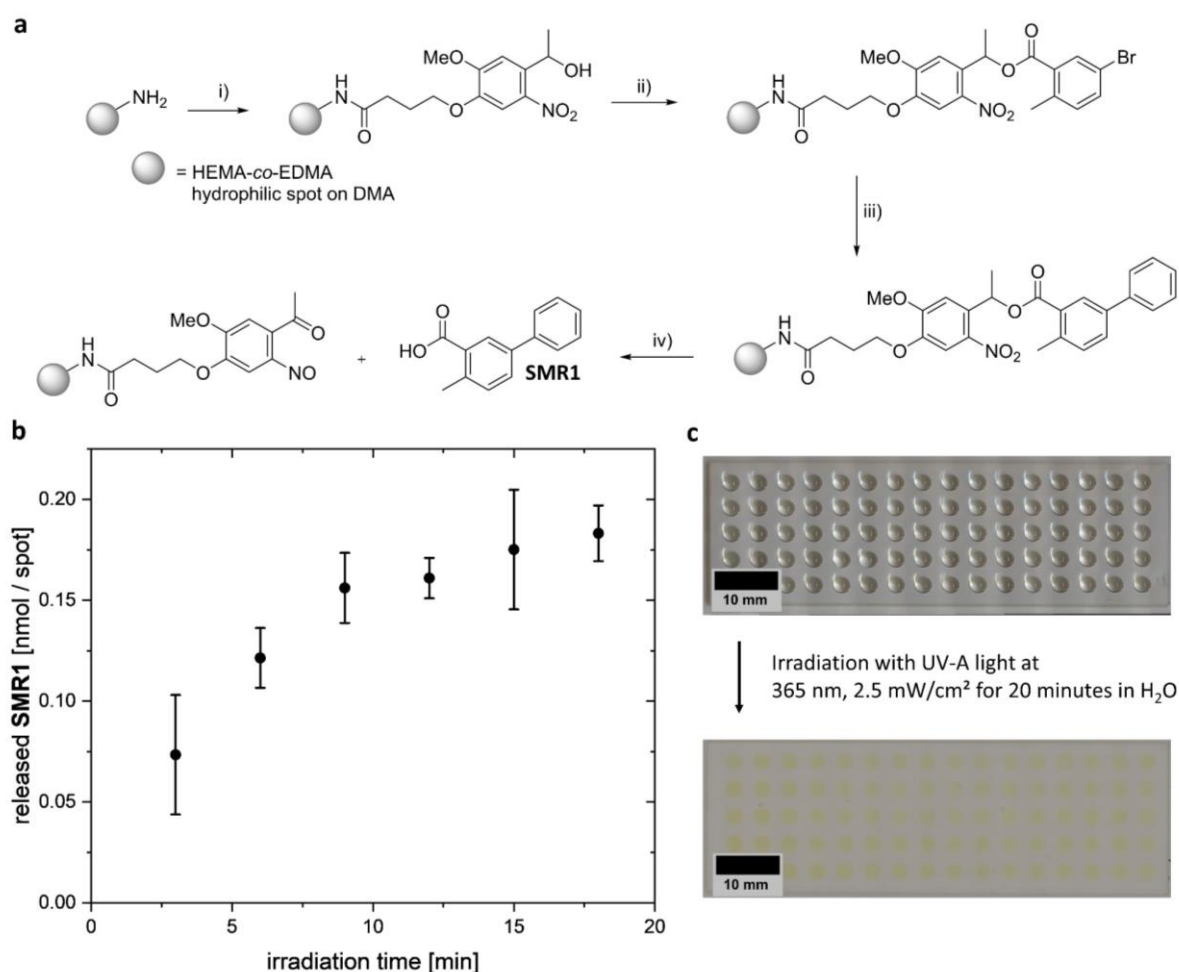
**Figure 32:** General workflow to obtain a 800 membered library of biphenyls in nanoliter scale using the Suzuki-Miyaura reaction. (a) Immobilization of the photolinker to the hydrophilic spots. HEPL or FAPL, HOBt, DIC in NMP. (b) Binding of different aryl halides to the surface anchored photolinker: carboxylic acid, DIC, 4-DMAP in NMP. (c) SMR with variable boronic acids: aryl boronic acid,  $\text{Na}_2\text{CO}_3$ ,  $\text{Na}_2\text{PdCl}_4$ , dibenzyl diisopropylphosphoramidite in NMP/ $\text{H}_2\text{O}$  (9:1). (d) UV induced cleavage of the desired biphenylic compound into distinct droplets: 365 nm, 2.5 mW/cm<sup>2</sup> for 20 minutes in  $\text{H}_2\text{O}$ . The image is used from the joint publication<sup>[1]</sup>.

In order to evaluate the efficiency of the downscaled on-chip palladium-catalyzed SMR the kinetics of the photocleavable linker cleavage process were examined. Specifically, the release of the exemplary compound **SMR1** (Figure 33a) into the droplets was analyzed after varying UV irradiation durations. To gather these data, four round spots with a diameter of 2.8 mm, each containing 5  $\mu\text{L}$  of water, were subjected to different UV light exposure times at 365 nm.

Subsequent to UV exposure, the combined cleavage solution from the four spots, totaling 40  $\mu\text{L}$  of cleavage solution, underwent analysis using LC-MS, with absorbance at 280 nm measured. This wavelength corresponds to the previously determined modified extinction coefficient

( $\epsilon = 70,000 \text{ L } \mu\text{mol}^{-1}$ , see appendix). The modified extinction coefficient was established by synthesizing compound **SMR1** on a milligram scale in a flask, purifying it, and utilizing it as a standard for quantitative analysis of photoinduced cleavage (experimental part). Applying the Beer–Lambert law, the loading was determined as 0.18 nmol per round 2.8 mm spot (with an area of  $7.01 \text{ mm}^2$ ) and was plotted against the varying irradiation time (Figure 33b). The outcomes indicated that the photolinker's half-life under UV exposure at 365 nm with  $2.5 \text{ mW cm}^{-2}$  was 5 minutes. Achieving a maximum loading of 0.18 nmol per spot of compound **SMR1**, this amount was released into the droplets after 15 minutes of UV irradiation time (365 nm,  $2.5 \text{ mW cm}^{-2}$ ). When filling a 2.8 mm round spot with  $5 \text{ } \mu\text{L}$  of solvent, a maximum concentration of  $36 \times 10^{-6} \text{ M}$  was attained. These findings underscore the efficiency and reliability of the photocleavable linker for releasing the synthesized compounds into the droplets.





**Figure 33:** (a) Schematic representation of the synthetic pathway for the production of biphenyl XX on DMA for the evaluation of UV-induced photorelease kinetics: i) Immobilization of HEPL onto hydrophilic spots on DMA. ii) covalent attachment of 5-bromo-2-methyl benzoic acid to the immobilized photolinker. iii) Solid-phase SMR employing phenylboronic acid. iv) UV induced cleavage from the surface leading to the formation of the target biphenylic compound SMR1. (b) Analysis of UV-triggered release kinetics of XX into 5  $\mu$ L droplets following various irradiation durations. Determination carried out through spectroscopic examination of solutions at 280 nm using an LC/MS system. Each data point is an average derived from three measurements, and error bars denote standard deviation. (c) Depiction of HEMA-co-EDMA DMA with 2.8 mm round spots before (top, filled with 5  $\mu$ L H<sub>2</sub>O) and after (bottom) UV-induced cleavage. The emergence of a yellow color signifies the occurrence of cleavage. The figure has been adapted from Höpfner et al.<sup>[1]</sup>

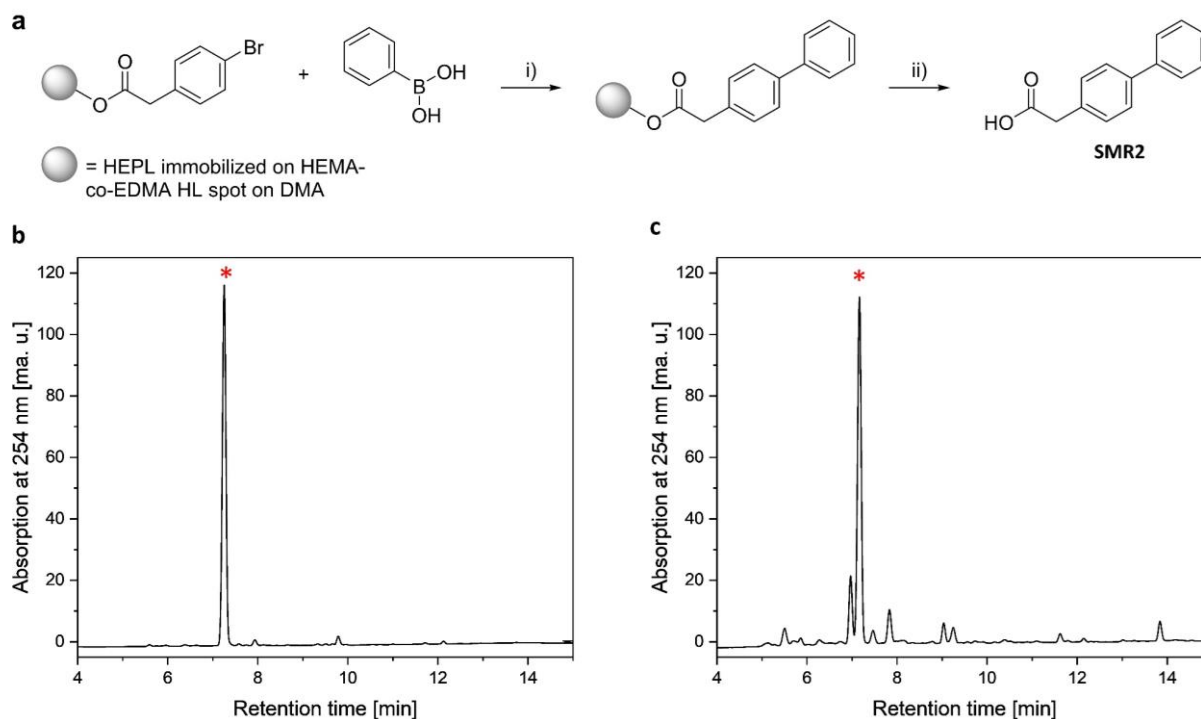
To showcase the viability of miniaturization on the platform, a switch was made from utilizing round HL spots with a 2.8 mm diameter to employing square spots with a 1 mm edge length. This shift, facilitated by a high-precision liquid dispenser, led to a significant reduction in reaction volume to approximately 100 nL. The adoption of square spots resulted in a higher density of reaction vessels, minimizing the consumption of starting materials and generated waste. Specifically, 20–40 nmol of starting materials and a mere 8 nmol of precious palladium precatalyst were used per spot. This modification allowed for a substantial increase in the number of individual reactions on a single DMA slide. The number of spots increased from 80

to 672, and spot density rose from 4 to 34 spots  $\text{cm}^{-2}$ . This enhanced spot density enabled the execution of more reactions in parallel, thereby boosting the throughput of the platform.

Initial tests with 2.8 mm round spots revealed product purities of ~90% for most compounds, a standard that was aimed to be maintained during further downsizing of the reaction volume. To assess the benefits of miniaturization, an exemplary reaction (Figure 34a) was conducted using both 2.8 mm round spots and 1 mm square spots, comparing the purities of the obtained biphenylic compound **SMR2**. A non-contact liquid dispenser was utilized to print 40 nL of sodium tetrachloropalladate solution (0.2 M in H<sub>2</sub>O) and 40 nL of dibenzyl diisopropylphosphoramidite solution (0.5 M in NMP) into each spot on the DMA. The entire slide was incubated in a closed Petri dish for 15 minutes to form the precatalyst. Subsequently, 80 nL of phenylboronic acid solution (0.5 M in NMP) and 40 nL of saturated sodium carbonate solution (in H<sub>2</sub>O) were printed into each spot to initiate the reaction. The DMA was incubated for 18 hours in the dark at room temperature in a closed Petri dish, containing an NMP-soaked paper tissue to prevent evaporation. After 18 hours, the reaction mixtures were washed off with acetone and ethanol before immersing the entire slide in a 0.1 M solution of KCN in DMSO/water (1:1) for 3 hours to remove the precipitated palladium. For the final washing step, only water and ethanol were used, and 100 nL of deionized water were printed into each spot. To release the product, the whole DMA was irradiated with UV light of 365 nm (2.5 mW  $\text{cm}^{-2}$ ) for 20 minutes, causing the products to be released into individual separate droplets. To prepare the slide for sample collection, the water was evaporated using reduced pressure. Once the slide was completely dry, 250  $\mu\text{L}$  of water and 250  $\mu\text{L}$  of DMF were spread evenly across the entire slide. Afterward, each 25  $\mu\text{L}$  of the water and DMF mixture was carefully pipetted off into an LC-MS vial, leading to a total volume of 50  $\mu\text{L}$ , mimicking the procedure used for larger spot sizes. The results of this comprehensive procedure demonstrated that the purities using the 1 mm square spots (Figure 34c) were comparable to those obtained using the larger 2.8 mm round spots (Figure 34b). This suggests that miniaturization on the platform does not compromise the quality of the reaction products.

To examine a potential library of biphenylic compounds, MALDI-TOF-MS was applied for the analysis of representative biphenylic samples. Despite the successful synthesis of biphenylic compounds on conductive ITO-DMA, the detection of any products using MALDI-TOF-MS was not possible. The primary hindrance was the interference of matrix-related peaks in the low  $m/z$  region. To address this issue, various alternative matrices have been reported, including metal-phthalocyanines<sup>[100]</sup>, graphene<sup>[101]</sup> and modified silica<sup>[102]</sup>. The compatibility of these

unconventional matrices on ITO-DMA requires comprehensive testing, particularly with regard to their potential suppression effects on the ionization of the polymer backbone of the ITO-DMA.



**Figure 34:** (a) Schematic illustration of the synthetic route employed for the formation of biphenylic compound XX: i) Solid-phase SMR utilizing immobilized 4-bromophenylacetic acid and phenylboronic acid. ii) UV induced cleavage from the surface, resulting in the production of the desired biphenylic compound **SMR2**. (b) UV chromatogram recorded at 254 nm. Post-irradiation, the volume of five spots with a diameter of 2.8 mm (50  $\mu$ L in total) was extracted from the surface and analyzed via LC-MS. The red asterisk denotes the corresponding peak. (c) UV chromatogram at 254 nm. Following irradiation, a cumulative volume of 50  $\mu$ L was collected from all HL spots and subsequently analyzed using LC-MS. The red asterisk highlights the associated peak. This figure has been adapted from<sup>[1]</sup>.

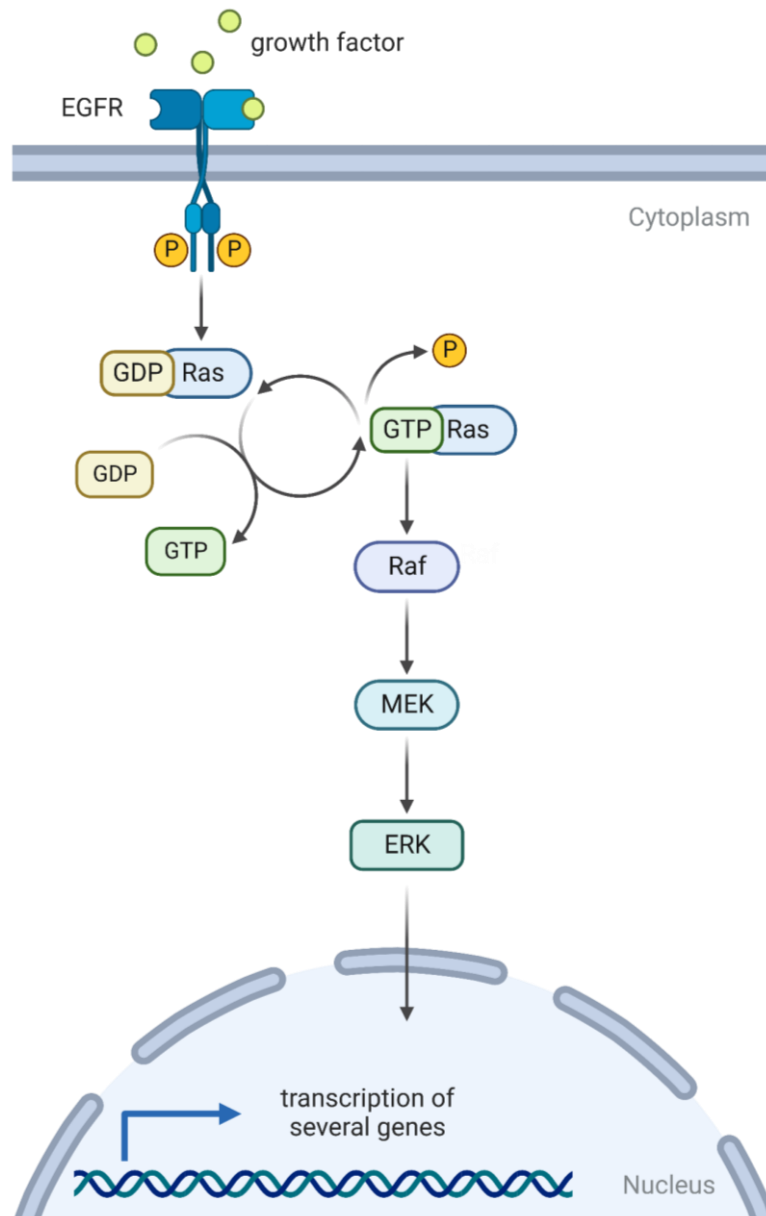
### **3.2.2 Combinatorial Synthesis of Potential MEK-Inhibitors in Nanoliter Scale**

The results shown in chapters 3.2.2 - 3.2.5 were obtained in close collaboration with MAXIMILIAN SEIFERMANN (KIT). The preparation of the substrates as well as the amidation steps were performed by MAXIMILIAN SEIFERMANN (KIT). All SUZUKI-MIYaura reactions on-chip and in flask were performed by JULIUS HÖPFNER (KIT), the experimental planning was performed together. Sample preparation for the MALDI-TOF-MS measurements was performed by JULIUS HÖPFNER. The performance of the anti-cancer screening on-chip was performed by MAXIMILIAN SEIFERMANN (KIT). The screening in 384-well plates and the preparation of the LC-MS samples was performed together. The analysis of the entire raw data was done independently. MALDI-TOF-MS measurements were carried out by DR. STEFAN SCHMIDT (CeMOS, Mannheim). LC-MS measurements took place at the Institute of Technology (INT) in the laboratory of DR. FLORIAN FEIST. HT-29 cells were initially cultured by CHARLOTTE LUCHENA (KIT).

#### **3.2.2.1 The ERK pathway and its importance in Targeted Therapy**

The escalating global incidence and mortality rates of cancer present an alarming challenge to improving life expectancy on a worldwide scale. In 2022 alone, a total of 9.96 million people died from cancer, emerging as the second leading cause of death, surpassed only by cardiovascular diseases.<sup>[103]</sup> Mitogen-activated protein kinases (MAPKs) play a pivotal role in the development of diverse cancer types. As a family of conservative protein serine/threonine kinases, MAPKs respond to various extracellular stimuli and participate in crucial cellular processes, including gene expression, cell metabolism, proliferation, differentiation, and apoptosis. Among the MAPK pathways, the RAS–Raf–MEK–ERK cascade, commonly known as the ERK-pathway, takes center stage, exhibiting aberrant activation in more than one-third of all human cancers and a staggering 90% of cutaneous melanomas..<sup>[104, 105]</sup>

The initiation of the ERK pathway involves the binding of extracellular mitogens to cell surface receptors, such as the epidermal growth factor receptor (EGFR). This triggers a cascade of molecular events, with RAS proteins (KRAS, NRAS, HRAS) exchanging a GDP molecule for a GTP molecule, thereby turning the signaling pathway on and off, subsequently activating Raf kinases (BRAF, CRAF, ARAF). This activation sequence culminates in the phosphorylation of MEK1/2 and the subsequent activation of ERK1/2. The orchestrated actions of ERK1/2 extend to the regulation of gene expression, influencing vital cellular processes such as cell cycle progression, differentiation, survival, apoptosis, migration and invasion (Figure 35).<sup>[106, 107]</sup> Moreover, when ERK is activated, it triggers an increase in the expression of EGFR ligands, establishing an autocrine loop that fuels tumor growth.<sup>[108]</sup>

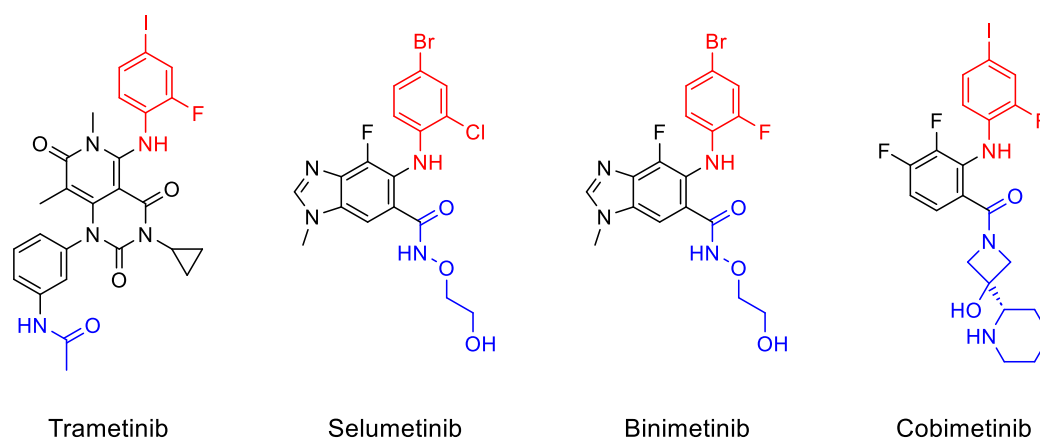


**Figure 35:** Schematic representation of the ERK-signaling cascade, starting with the activation of RAS through EGFR. This activation triggers a sequence of events, including the phosphorylation of RAF, MEK, and ERK, ultimately influencing transcription processes.

The primary strategy to suppress the ERK pathway functionality involves the use of small-molecule inhibitors, offering several promising therapeutic approaches. Notably, the RAF inhibitor *Vemurafenib* demonstrated significant efficacy in inducing partial or total regression in the majority of BRAF-mutant melanoma cases.<sup>[109, 110]</sup> However, targeting upstream regulators like RAF introduces the risk of negative feedback loops, as observed in BRAF-mutant colorectal cancer. The inhibition of BRAF can lead to excessive activation of CRAF and RAS due to increased phosphor-EGFR levels, hindering the reduction in phosphorylated ERK.<sup>[111]</sup> Combining BRAF and EGFR inhibitors has shown promise in suppressing these feedback loops, resulting in a positive response to non-small cell lung cancer treatment.<sup>[112]</sup>

MEK1/2 stands out as the most prominent candidate in the RAS-Raf-MEK-ERK pathway, holding a unique position as the exclusive activators of ERK1/2. Referred to as the "ERK1/2 gatekeeper" kinases, MEK1/2 play a critical role in processing inputs from multiple upstream kinases, making them pivotal in orchestrating the signaling cascade.<sup>[113]</sup> Contrary to a solely RAS- or Raf-centered perspective, it is essential to recognize that Raf proteins constitute only a subset of the MEK1/2 activators in cells. Beyond Raf, multiple MAP kinase kinases have the capacity to activate MEK1/2, and noteworthy among these is the fact that some are found to be mutated in cancer.<sup>[114]</sup> Inhibiting MEK1/2 with allosteric inhibitors not only targets their pivotal role but also has the potential to induce significant changes in signaling networks, offering a nuanced approach to therapeutic interventions in the ERK pathway.

To date, Four MEK inhibitors - *trametinib*, *cobimetinib*, *selumetinib*, and *binimetinib* - have received FDA approval (Figure 36). *Trametinib*, the first to gain approval in May 2013, effectively targets metastatic or terminal BRAF V600E/K-mutated melanoma. It operates as an allosteric, non-competitive, and ATP-accessible inhibitor of the protein kinases MEK1 and MEK2.<sup>[115]</sup> The second MEK1/2 inhibitor to receive approval was *cobimetinib*, also being an allosteric, non-ATP-competitive MEK inhibitor.<sup>[116]</sup> Demonstrating high selectivity and efficacy, *cobimetinib* acts as a reversible inhibitor, effectively preventing the phosphorylation of ERK1/2.<sup>[117]</sup> *Selumetinib*, an oral second-generation kinase inhibitor, received FDA approval in May 2016.<sup>[118]</sup> Renowned for its strong and selective non-ATP-competitive inhibition of MEK1/2, it earned orphan drug designation for treating stage III or IV differentiated thyroid cancer and neurofibromatosis type 1 (NF1) in the US and EU.<sup>[119]</sup> *Binimetinib*, an anticancer small molecule with the potential to treat various tumors, is an orally available, highly selective, non-ATP-competitive MEK inhibitor. This compound received FDA approval in June 2018 for its application in treating patients with metastatic or incurable BRAF<sup>V600E/V600K</sup>-positive melanoma when combined with *encorafenib*.<sup>[120]</sup>



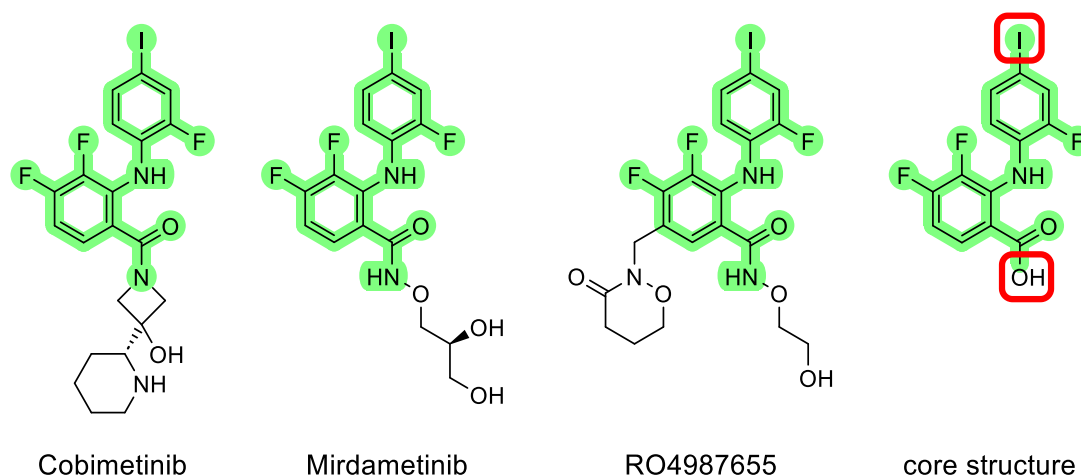
**Figure 36:** Structures of FDA approved MEK inhibitors trametinib, selumetinib, binimetinib and cobimetinib.

### 3.2.2.2 Motivation and Aim

The aim of this work was to establish a streamlined process for efficiently synthesizing, analyzing and screening a library of potential MEK inhibitors using the DMA. Reducing the scale to sub-microliter dimensions minimizes the amount of used reagents, while amplifying the number of parallel reactions and screenings.

For the identification of a lead compound, an examination of the structural similarities among FDA-approved MEK inhibitor *cobimetinib*<sup>[117]</sup>, along with clinical trial MEK inhibitors *mirdametinib*<sup>[121]</sup> and *RO4987655*<sup>[122]</sup>, was conducted (Figure 37). Notably, two key similarities were observed: a halogenated aniline fragment and a substituted carbonyl. The carbonyl primarily interacts with the K97 residue of MEK, while the aromatic fragment binds to the hydrophobic pocket containing L115, L118, V127, and M143.<sup>[123]</sup> It was hypothesized that modification of these two fragments significantly impact the binding affinity. Consequently, 3,4-difluoro-2-(2-fluoro-4-iodophenylamino)benzoic acid (Figure 37) was

selected as the initial point for further derivatization, providing the core structure found in the aforementioned lead compounds.

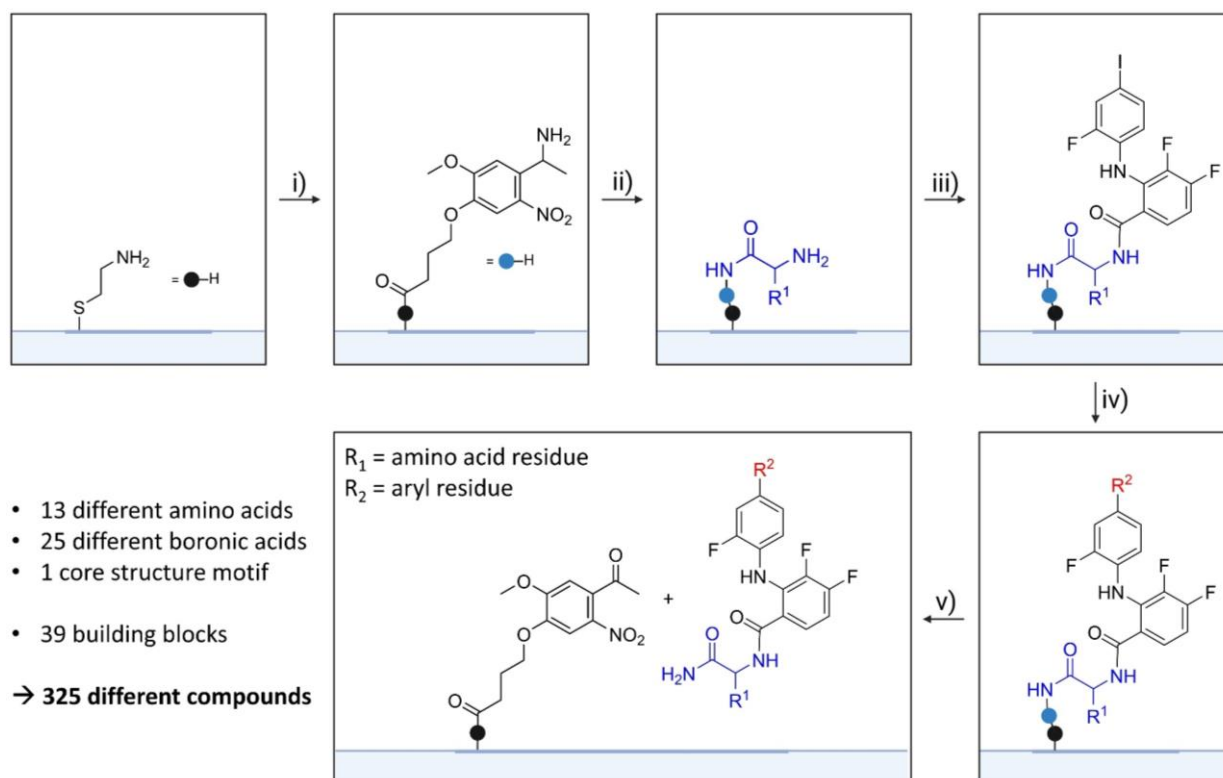


**Figure 37:** Structures of FDA approved MEK inhibitor cobimetinib, along with clinical trial MEK inhibitors mirdametinib and RO4987655. Core structure 3,4-Difluoro-2-(2-fluoro-4-iodophenylamino)benzoic acid is presented on the right, with red rectangles indicating potential moieties for diversification.

The core structure's derivatization was facilitated by employing two established reaction types on the DMA. The carboxylic acid moiety of the core structure underwent modification through amidation with naturally occurring amino acids. Subsequently, the substitution of iodine with more hydrophobic groups was carried out using the SMR. The integration of these two modifications was anticipated to enhance the affinity of the novel compounds for the hydrophobic pocket and increase their binding to the K97 residue.

The developed synthetic cascade was adapted from the generalized workflow for solid-phase synthesis on DMA (Figure 9). The initiation of the reaction cascade involves immobilization of the photolinker to the HL spots of the DMA (Figure 38i). The photocleavable linker was used as an anchor point on the surface, while also enabling the controlled release of the product using only UV irradiation. Subsequent modification with natural occurring amino acids **A1-A13** introduces the first part of the lead compound's derivatization (Figure 38ii). The coupling of 3,4-difluoro-2-(2-fluoro-4-iodophenylamino)benzoic acid (OTV) to the immobilized amino acids establishes the core structural motif (Figure 38iii). The second derivatization of the lead compound is achieved by displacing the iodine using a boronic acid **B1-B25** (Figure 38iv). UV induced cleavage from the surface releases the novel MEK inhibitors into distinct droplets (Figure 38v).





**Figure 38:** Scheme of the synthetic cascade for the on-chip solid-phase high-throughput synthesis of potential MEK inhibitors using the HL spots of the DMA. The usage of 13 amino acids (**A1-A13**) and 25 boronic acid derivatives (**B1-B25**) leads to the formation of a 325 membered library of novel compounds. i) Immobilization of the photocleavable linker to the HL spots. ii) Attachment of Fmoc-protected amino acids through amide coupling follows by Fmoc deprotection. iii) Coupling of the core structure motif (3,4-difluoro-2-((2-fluoro-4-iodophenyl)amino)benzoic acid) to the free amines of the surface bound amino acids. iv) Solid-phase SMR to modify the iodo-aniline fragment. v) UV induced cleavage of the target compounds.

In order to achieve a comprehensive diversity in both identified modification fragments, a broad variety of building blocks was chosen. In total, 13 different natural occurring amino acids (**A1-A13**) and 25 structural diverse boronic acids (**B1-B25**) were employed in the described synthetic cascade (Table 8). Combining these 38 building blocks with the core structural motif leads to the synthesis of 325 novel compounds.

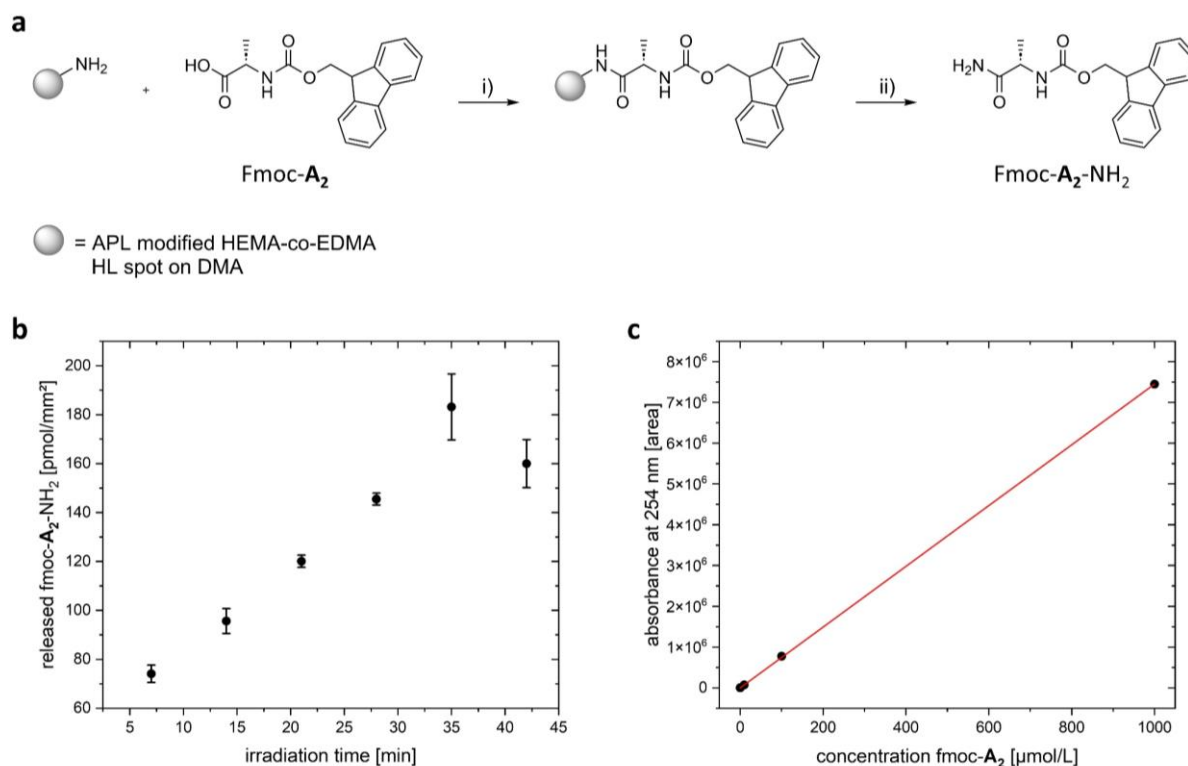
The application of this high-throughput approach utilizing the ITO-DMA extends to on-chip analysis of the compounds through MALDI-TOF-MS. Additionally, it facilitates cell screening for MEK inhibition of the novel compounds using HT-29 as a model cell line known for its sensitivity to MEK inhibition. Through the integration of these analytical components, an all-in-one platform has been successfully established, seamlessly combining high-throughput synthesis, analysis, and cell screening, all conducted on a sub-microliter scale using DMA.

### 3.2.3 Purity Analysis and Photorelease from the Surface of the Droplet Microarray

68

protecting group was carried out by immersing the entire slide in a solution of dimethylformamide (DMF) and piperidine (4:1, v/v) for 1 h. This process generated the reactive amino photolinker (APL) on the surface of the HL spots. Following this, 5  $\mu$ L of a solution containing 1 M Fmoc-alanine (Fmoc-A<sub>2</sub>) and 1 M HOBt in a mixture of NMP and DIC (9:1, v/v) was applied, leading to the formation of **Fmoc-A<sub>2</sub>** modified HL spots (Figure 39a, i). The excess reagents were then removed from the solid-phase using acetone and ethanol, after which the samples were exposed to UV light at 365 nm for varying durations to release the corresponding Fmoc-A<sub>2</sub> amide from the surface (Figure 39a, ii).

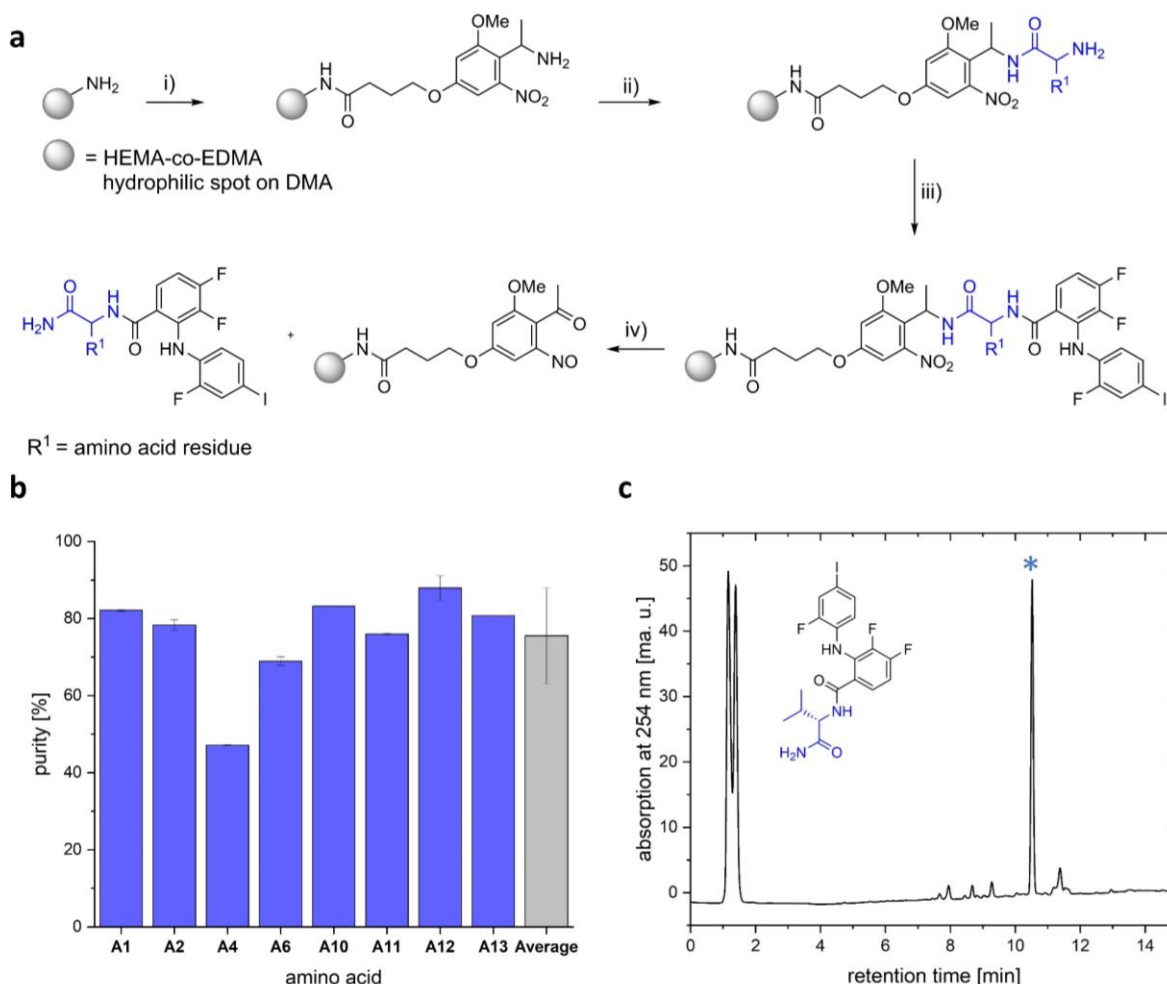
For each set of four spots, each containing 5  $\mu$ L of water, varying UV irradiation times were applied. The combined solutions of the released exemplary compound Fmoc-A<sub>2</sub>-NH<sub>2</sub> were collected in a mixture of DMF and water (1:1, v/v) and subjected to analysis using LC-MS, with absorbance measurements at 254 nm recorded (Figure 39b). The absorbance values were determined based on the previously established modified extinction coefficient of **Fmoc-A<sub>2</sub>** ( $\epsilon = 7450 \text{ L } \mu\text{mol}^{-1}$ , Figure 39c). To determine the modified extinction coefficient, **Fmoc-A<sub>2</sub>** was employed as a standard for the quantitative analysis of photoinduced cleavage. Applying the Lambert-Beer law enabled the determination of the accessible loading, expressed as pmol per mm<sup>2</sup>. The maximum loading of 160 pmol/mm<sup>2</sup> of **Fmoc-A<sub>2</sub>-NH<sub>2</sub>** was attained after UV light irradiation in the range between 30 minutes and 35 minutes at 365 nm. Filling a 2.8 mm round spot (with an area of 7.01 mm<sup>2</sup>) with 5  $\mu$ L of solvents resulted in a maximum concentration of 32  $\mu$ M.



**Figure 39:** (a) Schematic depiction of the synthetic steps involved in the (i) immobilization of **Fmoc-A<sub>2</sub>** to the photolinker modified surface and (ii) subsequent UV induced release as **Fmoc-A<sub>2</sub>-NH<sub>2</sub>** from the surface. (b) Amount of released **Fmoc-A<sub>2</sub>-NH<sub>2</sub>** in relation to the irradiation time with UV light at 365 nm, determined via LC-MS. The release reaches a plateau after more than 30 min of UV irradiation. (c) Calibration curve of **Fmoc-alanine** at 254 nm with linear fit (red). A dilution series of Fmoc-alanine was prepared and absorbance of every was measured for its absorbance at 254 nm.

Following these initial findings, an assessment of overall purities and conversions was conducted after the subsequent step in the synthetic cascade: the immobilization of the core structural motif OTV. To quantify the overall purity of the amino acid-coupled intermediates, a selection of eight different amino acids was chosen, and the sample preparation started with modification of the HL spots using FAPL coupling solution, followed by deprotection following the aforementioned procedure (Figure 40a, i). The subsequent step involved coupling the Fmoc-protected amino acids, followed by Fmoc deprotection (Figure 40a, ii), resulting in the formation of reactive amino acid modified HL spots. The immobilization of the core structural motif OTV was carried out by applying 5 μL of a solution containing 0.1 M OTV and 0.1 M HOBt in a solution of NMP/DIC (9;1, v/v) (Figure 40a, iii). Subsequent irradiation at 365 nm of five HL spots containing the same compound for 40 min released the corresponding compounds from the surface (Figure 40a, iv). The combined product solutions were then analyzed for their absorption at 254 nm using LC-MS.

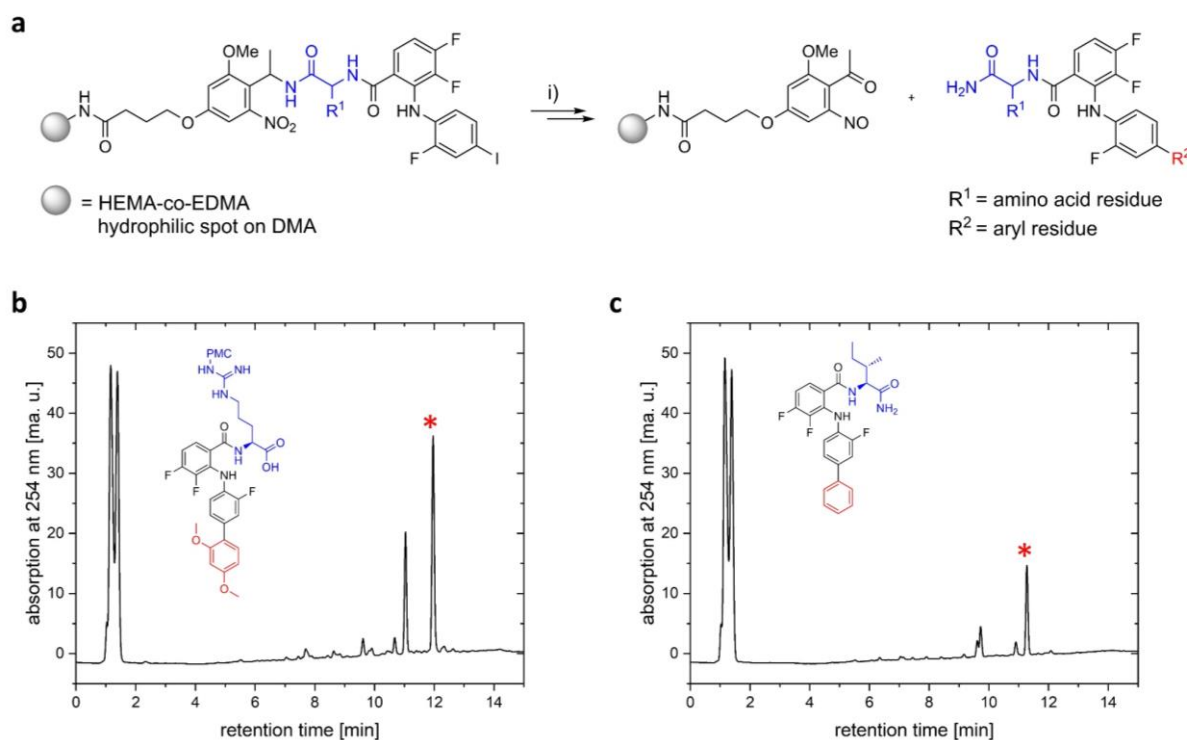
The overall purity of each product was assessed by calculating the ratio of the integral of the product signal in the HPLC chromatogram at 254 nm to the sum of all integral values. Purity values for the eight exemplary intermediates varied between 47% and 88% (Figure 40b), with an average of  $76 \pm 12\%$ . An exemplary chromatogram at 254 nm for intermediate **A1-OTV** is presented in Figure 40c.



**Figure 40:** (a) Schematic representation of the synthesis of the amino-acid intermediate. Immobilization and subsequent deprotection of FAPL to the surface (i) is followed by modification of the linker with an Fmoc protected amino acid. Subsequent deprotection yields the reactive amino acid modified surface (ii). Application of the coupling solution containing the core structural motif OTV leads to the formation of the amino acid intermediate (iii). UV induced cleavage from the surface releases the amino acid-intermediate into distinct droplets (iv). (b) Purity of eight exemplary amino-acid intermediates after UV induced release from the surface. Purity was measured as percentage of the product's integral divided by the total integration value of the HPLC chromatogram at 254 nm. Error bars represent standard deviation between two independent repetitions. (c) Representative chromatogram of amino acid intermediate **A1-OTV**. The corresponding product peak is highlighted with the blue asterisk.

The next step was to evaluate the conversion of the amino acid-intermediates to the final product, as well as quantifying the purities of the products after the last synthetic step. We conducted 16 exemplary reactions on-chip, combining the eight previously examined amino-

acid intermediate with two boronic acids. On-chip synthesis of the amino acid-intermediates was conducted as previously described. Replacement of the iodine with the corresponding boronic acid was conducted using the established SMR approach on DMA.<sup>[1]</sup> In short, the formation of the catalyst on-chip involved dispensing 1.5  $\mu\text{L}$  each of 0.5 M dibenzyl diisopropylphosphoramidite and a 0.2 M solution of disodium tetrachloropalladate in water. The mixture was incubated for 15 minutes at room temperature. Subsequently, 3  $\mu\text{L}$  of a solution containing a 0.5 M boronic acid derivative in NMP and 2  $\mu\text{L}$  of a saturated sodium carbonate solution were added. The reaction mixture was incubated in the dark at room temperature for 18 hours. To conclude the reactions, the mixtures were washed off with acetone and ethanol, followed by immersing the entire slide in a 0.1 M solution of KCN in DMSO/water (1:1, v/v) for 3 h to remove the precipitated palladium. Subsequent UV induced release from the surface yielded the corresponding product (Figure 41a).



**Figure 41:** (a) Schematic representation of the conversion of the amino-acid intermediate's iodine utilizing the SMR, with subsequent UV induced cleavage from the surface. Representative chromatograms at 254 nm for final compound (b) A<sub>4</sub>B<sub>5</sub> and (c) A<sub>12</sub>B<sub>18</sub>. Red asterisk highlights the corresponding product peak in the chromatogram.

Analysis of the cleaved product solutions via LC-MS showed an overall purity of  $54 \pm 11\%$ , with a range spanning between 35% and 68% (Table 9), demonstrating the suitability for primary screening purposes. In the chromatograms at 254 nm, the primary peak for all samples corresponded to the desired product. Representative chromatograms are illustrated in Figure 41 (b and c). The determination of the conversion from amino acid-intermediate to the product was

calculated as ratio of the product's peak integral at 254 nm to the sum of the integrals for both the products and the amino acid-intermediates. A notably high coupling efficiency of  $86 \pm 10\%$  was observed for this step (Table 9).

**Table 9:** Purity of the final product and conversion of the amino acid-intermediate to the product for reaction paths involving various amino acids and different boronic acids. Purity was determined as a percentage, calculated by dividing the product integral by the total integration value of the HPLC chromatogram. The conversion rate was calculated as the ratio of the product's integral divided by the sum of the product and the amino acid-intermediate integrals.

Amino acid $A_x$	Boronic acid $B_y$	Purity [%]	Conversion [%]
<b>A<sub>1</sub></b>	<b>B<sub>5</sub></b>	49	79
	<b>B<sub>18</sub></b>	62	86
<b>A<sub>2</sub></b>	<b>B<sub>5</sub></b>	58	83
	<b>B<sub>18</sub></b>	58	83
<b>A<sub>4</sub></b>	<b>B<sub>5</sub></b>	37	>99
	<b>B<sub>18</sub></b>	35	>99
<b>A<sub>6</sub></b>	<b>B<sub>5</sub></b>	60	>99
	<b>B<sub>18</sub></b>	66	92
<b>A<sub>10</sub></b>	<b>B<sub>5</sub></b>	39	79
	<b>B<sub>18</sub></b>	64	90
<b>A<sub>11</sub></b>	<b>B<sub>5</sub></b>	54	>99
	<b>B<sub>18</sub></b>	48	72
<b>A<sub>12</sub></b>	<b>B<sub>5</sub></b>	52	83
	<b>B<sub>18</sub></b>	68	87
<b>A<sub>13</sub></b>	<b>B<sub>5</sub></b>	45	65
	<b>B<sub>18</sub></b>	65	86
<b>Total</b>		<b><math>54 \pm 10</math></b>	<b><math>86 \pm 10</math></b>

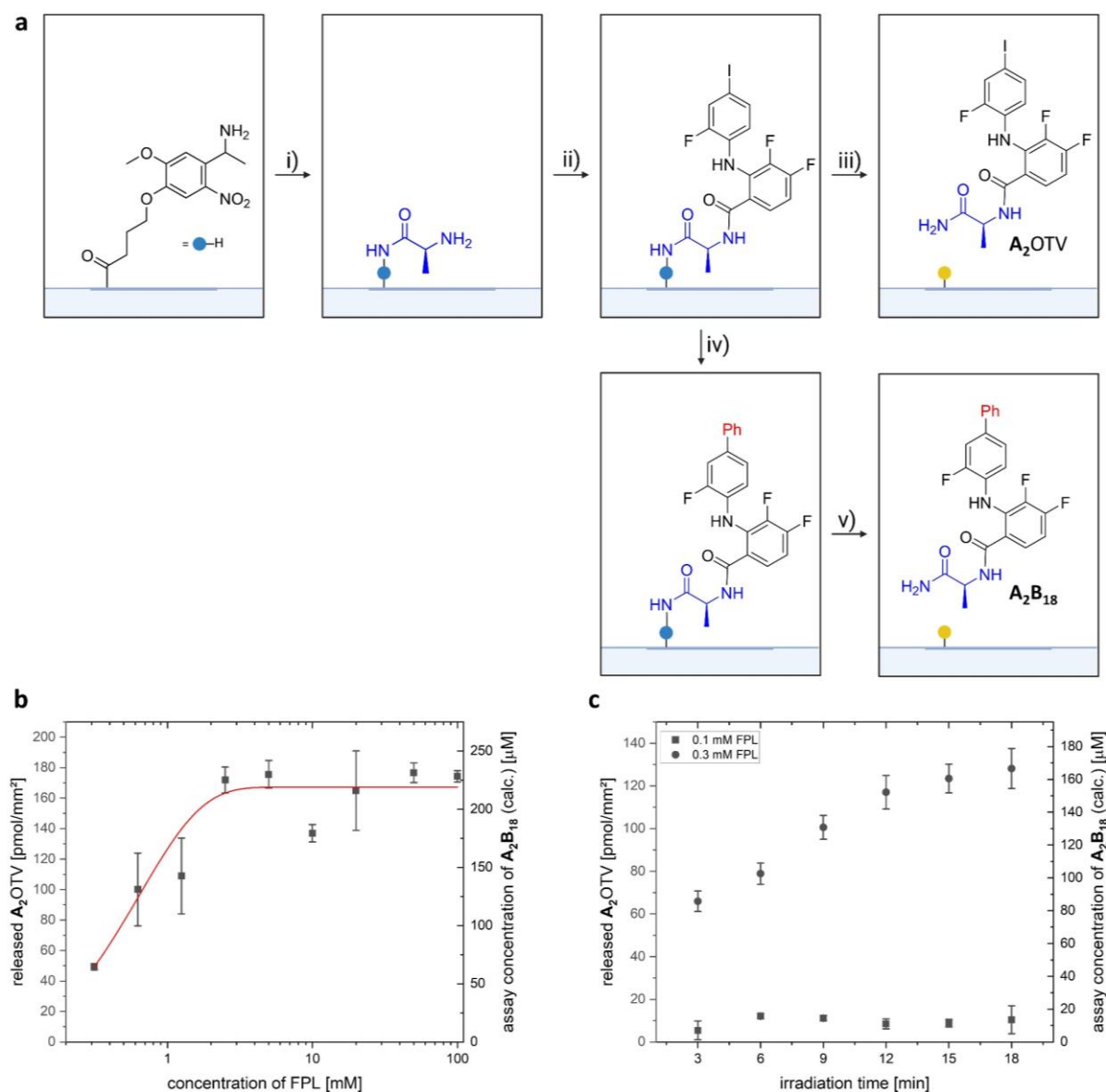
Apart from evaluating purities and conversions between synthetic steps, it is crucial to investigate the overall quantity of cleaved product. This assessment is essential for calculating the final concentration of compounds in cell screening. Considering the synthetic steps needed for the synthesis of the final product, a deeper investigation of the UV induced release in relation to UV irradiation time and initially used photolinker concentration was conducted.

To assess the cleavage kinetics of the amino acid-intermediate, the exemplary compound **A<sub>2</sub>OTV** was synthesized on-chip following the previously described procedure (Figure 42a, i-iii), with variations in the starting concentration of the photolinker ranging between 0.3 mM to 100 mM. The UV irradiation time was kept constant at 40 min. LC-MS analysis was performed on the cleaved product solutions. Additionally, compound **A<sub>2</sub>OTV** was synthesized on a milligram scale in flask to serve as a standard (see appendix). The quantity of the formed amino acid-intermediate was measured to calculate a final product loading, based on the previously determined 85% conversion in the SMR step. The experimental data (Figure 42b) indicated saturation in the amount of released product above 2.5 mM of the photolinker solution, with a rapid decrease below this concentration. With a photolinker concentration of 0.3 mM and 40 min of irradiation time for the photorelease of the product, a final loading of  $35.1 \pm 1.4$  pmol/mm<sup>2</sup> was observed. This corresponds to a final assay concentration of approximately 55 μM, taking into account the switch to square HL spots with an edge length of 1.4 mm and a final volume of 1 μL for the cell screening.

To achieve a more precise measurement of product formation at low photolinker concentrations below 2.5 μM, two independently prepared solutions with concentrations of 0.3 mM and 0.1 mM were selected. Different UV irradiation times between 3 min and 18 min were investigated. The surface was modified following the previously described procedure, and the model reaction was conducted to produce compound **A<sub>2</sub>OTV**. Subsequently, the compound was cleaved off the surface, and both the surface loading of **A<sub>2</sub>OTV** and the final assay concentration of **A<sub>2</sub>B<sub>18</sub>** were calculated based on the overall SMR conversion (Figure 42a, v). The results indicated a reduced time for full cleavage at low concentrations, with product release completed after 18 min at 0.3 mM and below 6 min at 0.1 mM photolinker solution (Figure 42c). The overall product loading of **A<sub>2</sub>OTV** with a 0.1 mM photolinker solution was approximately 12 pmol/mm<sup>2</sup>, resulting in a final assay concentration of compound **A<sub>2</sub>B<sub>18</sub>** at around 10 μM, which was regarded suitable for a primary screening of inhibitors.

Validation of these results involved the synthesis of **A<sub>2</sub>B<sub>18</sub>** in triplicates on a surface modified with a 0.1 mM photolinker solution. The compound was then released from the solid phase and analyzed via LC-MS. The absolute amount of compound **A<sub>2</sub>B<sub>18</sub>** was determined by comparing it with a serial dilution of pure compound **A<sub>2</sub>B<sub>18</sub>** prepared in flask (see appendix), resulting in a loading of  $6.31 \pm 0.14$  pmol/mm<sup>2</sup>. This corresponded to an assay concentration of  $9.71 \pm 0.22$  μM, confirming that the synthetic parameters would indeed yield the desired concentration.





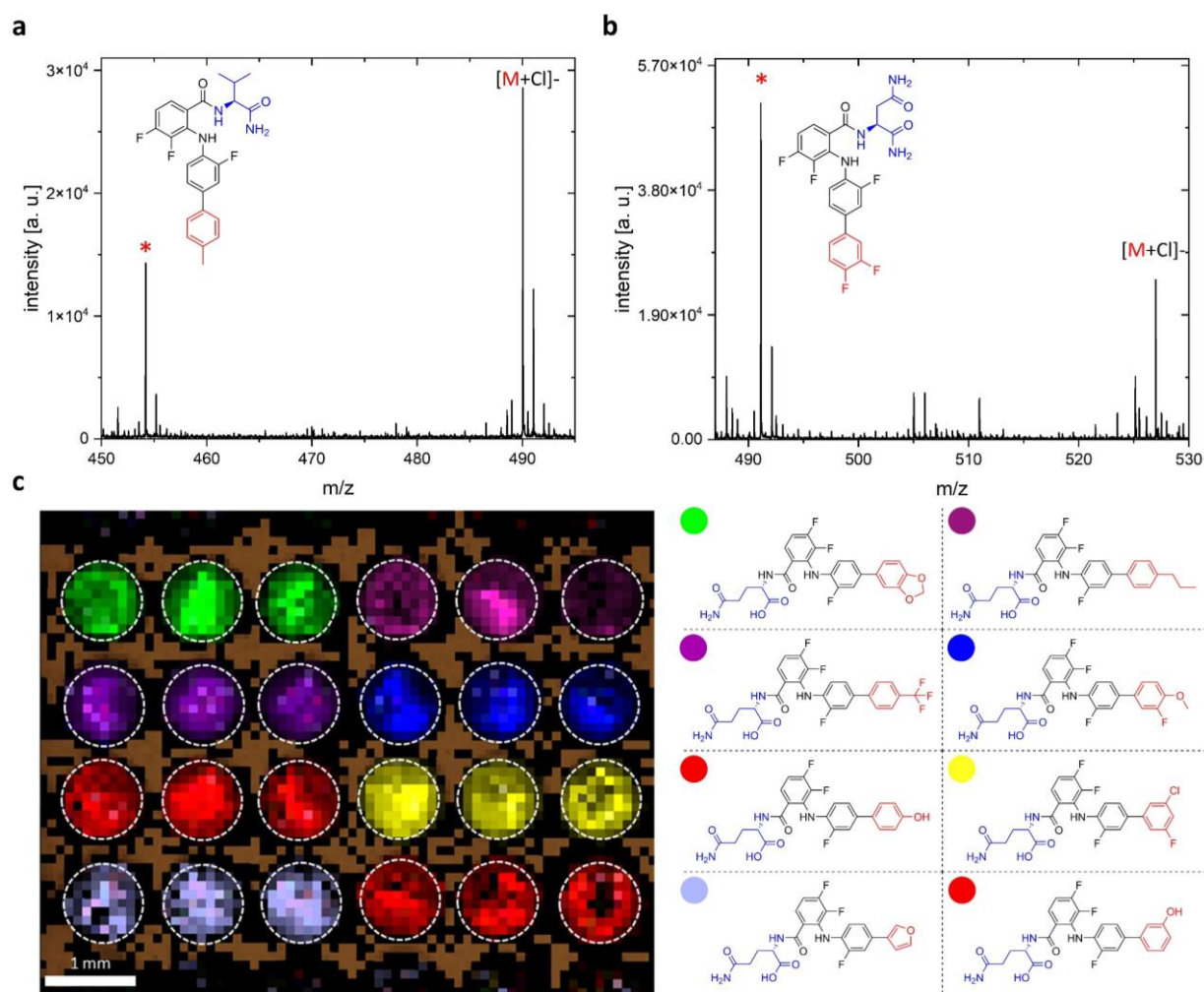
**Figure 42:** (a) Reaction Scheme for the preparation of compounds A<sub>2</sub>OTV and A<sub>2</sub>B<sub>18</sub> through solid-phase cascade synthesis. (i) Modification of the linker with Fmoc-A<sub>2</sub> and subsequent deprotection. (ii) Immobilization of OTV to the reactive amino acid. (iii) UV induced release of amino acid intermediate A<sub>2</sub>OTV. (iv) Solid-phase SMR with boronic acid B<sub>18</sub> and (v) subsequent cleavage from the surface to yield A<sub>2</sub>B<sub>18</sub>. (b) Released amount of A<sub>2</sub>OTV after 40 min of UV treatment for different concentrations of photolinker-modification solutions. The corresponding assay concentration of A<sub>2</sub>B<sub>18</sub> was calculated for a 1 µL solution, with an 85% yield in the Suzuki-Coupling step. Each value represents the average of three repetitions, and error bars indicate the standard deviation. (c) Released amount of A<sub>2</sub>OTV after different irradiation times for two concentrations of photolinker-modification solutions and the respective assay concentration of A<sub>2</sub>B<sub>18</sub> calculated for 1 µL solution and a yield in the Suzuki-Coupling step of 86 %. Each value represents the average of three repetitions, and error bars indicate the standard deviation.

### 3.2.4 Downscaling and Conformation of Synthetic Success in High-Throughput

The final goal of this project is to conduct on-chip cell screening of the synthesized compounds for MEK inhibition using the DMA. Previous project phases concentrated on assessing purities, conversions and cleavage kinetics of each step in the synthetic cascade on a relatively large scale using round spots with a diameter of 2.8 mm.

To reduce reagent usage in the synthesis, consequently, minimize the amount of cell suspension needed, a transition to round spots with a diameter of 1.4 mm was implemented. This spot size will be used in the cell screening. It offers an increase in spot density from 4 to 16 spots per mm<sup>2</sup> and in absolute values from 80 to 320 spots. This spot size will be utilized in the cell screening, offering an increase in spot density from 4 to 16 spots per mm<sup>2</sup>, and an increase in absolute values from 80 to 320 spots. To assess the feasibility of the applied synthetic procedure on smaller spots, a library of 320 compounds was prepared according to the described process in two independent repetitions on DMA. The miniaturization to 1.4 mm spots reduced the required volume of reaction solutions to 700 nL per compound, resulting in only 224 µL needed for the synthesis of the entire library.

Evaluation of the reactions conducted on these smaller spots was challenging using the established LC-MS approach due to the small volume of the cleaved compound solutions (only 1 µL per compound). To analyze these small volumes, droplet transfer (see Chapter 3.1.3) from the round 1.4 mm spots after UV-induced cleavage of the compounds to a ground steel target plate was performed. After solvent evaporation, the plate was spray-coated with NEDC as the matrix. The samples were then analyzed via MALDI-TOF-MS to detect the presence of the respective target compound. In total, 297 out of 320 compounds were identified, yielding a success rate of 93% (Table 10). Figure 43 (a) and (b) illustrate representative mass spectra obtained from ground steel target plate after droplet transfer. Compounds have been identified by their [M-H]<sup>-</sup> adduct (red asterisk) and their chloro adduct.



**Figure 43:** Representative MALDI-MS spectra of compound (a) A1B14 and (b) A5B6 acquired on a ground steel target plate in negative mode using NEDC as matrix. Compounds were synthesized on 1.4 mm spots and the cleavage solution was transferred to the plate. Asterisks indicate the corresponding structures. (c) MALDI-TOF-MS imaging of an ITO-DMA modified with 900 μm spots in which the synthetic cascade was carried out. Colors indicate the intensity of the [M-H]<sup>-</sup> ion for seven different chemical formulas. Target structures with the corresponding color of their [M-H]<sup>-</sup> peak are given on the right.

To enhance high-throughput analysis, MALDI-TOF-MS was performed without manual transfer by synthesizing a library of 320 compounds in triplicates on ITO-DMA (further information in Chapter 3.1.3) using round spots with a diameter of 900 μm. Transitioning from 1.4 mm round spots to 900 μm round spots further reduced the required volume of reaction solutions per compound. A mere 300 nL reaction volume per spot was utilized, resulting in a total consumption of only 288 μL for the synthesis of the whole library in triplicates. Compared to the 1.4 mm spots, the use of solvents was reduced by 43%. After the reaction, the compounds were released from the surface of the ITO-DMA into distinct HL spots through UV irradiation, and 44 nmol of NEDC in DMF was dispensed to every spot containing a sample. After drying, the slide was used for on-chip MALDI-TOF-MS imaging. In this analysis, 261 of 325 compounds (82%, Table 10) were clearly identified by their [M-H]<sup>-</sup> and chloro adducts.

Additionally, the confinement of the compounds to their respective spots could be visualized (Figure 9c).

The results indicate a reduction in sensitivity compared to the ground steel plate, particularly for compounds that are challenging to ionize, such as those synthesized from amino acid A4. However, the increased throughput and qualitative measurement for the majority of compounds showcase the platform's potential. This finalizes the chemical characterization of the platform, allowing for the progression to the biological screening of the compound library.

**Table 10:** Identification rates of final products in MALDI-TOF-MS were determined for each tested building block in measurements on the ground steel target plate (MTP) and ITO-DMA, respectively.

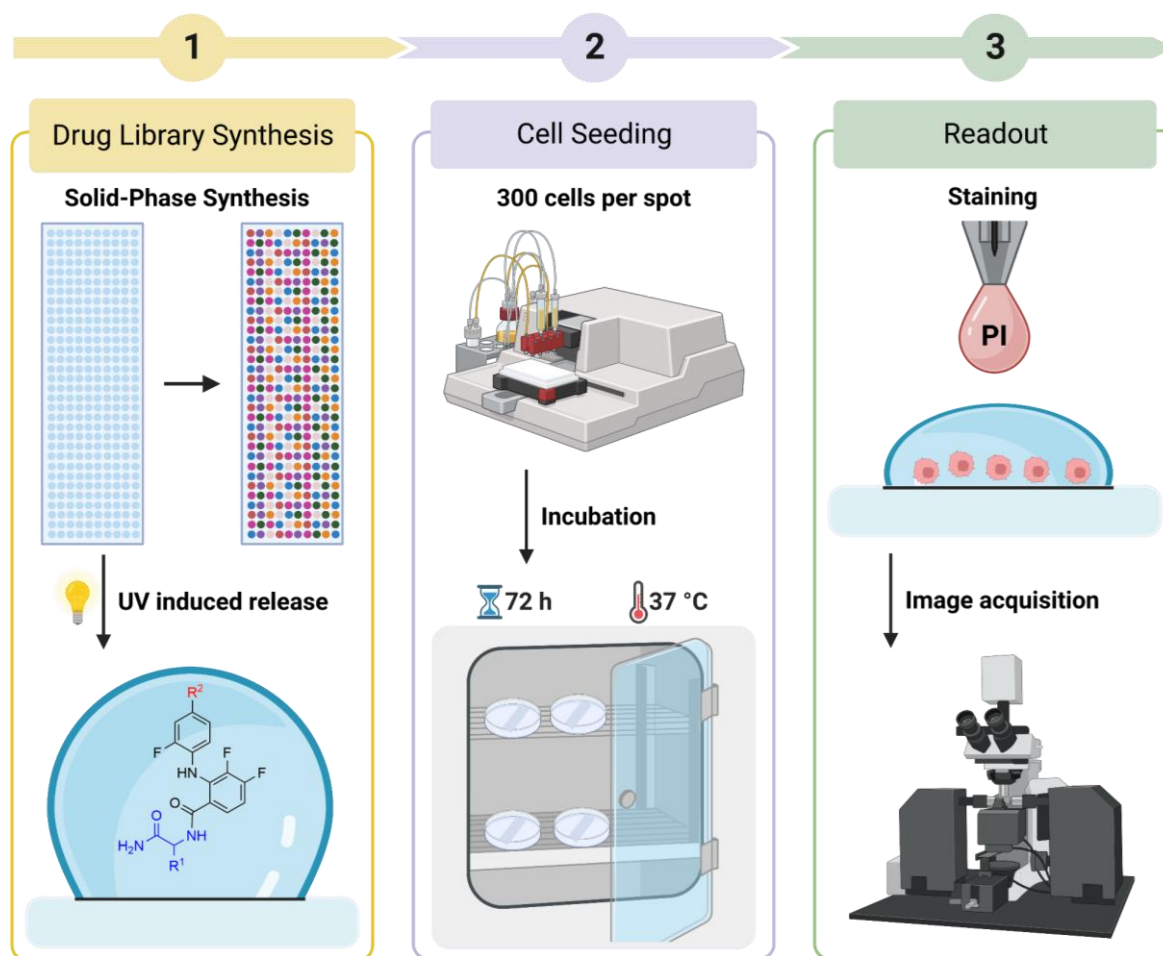
Amino acid $A_x$	Identified on MTP [%]	Identified on chip [%]	Boronic acid $B_y$	Identified on MTP [%]	Identified on chip [%]
<b>A1</b>	84	88	<b>B1</b>	100	92
<b>A2</b>	88	92	<b>B2</b>	92	85
<b>A3</b>	96	84	<b>B3</b>	85	92
<b>A4</b>	56	4	<b>B4</b>	100	77
<b>A5</b>	92	96	<b>B5</b>	92	77
<b>A6</b>	100	96	<b>B6</b>	92	92
<b>A7</b>	100	64	<b>B7</b>	100	77
<b>A8</b>	100	64	<b>B8</b>	100	92
<b>A9</b>	100	80	<b>B9</b>	100	92
<b>A10</b>	100	80	<b>B10</b>	92	92
<b>A11</b>	100	84	<b>B11</b>	100	85
<b>A12</b>	96	88	<b>B12</b>	100	85
<b>A13</b>	96	92	<b>B13</b>	92	92
			<b>B14</b>	100	92
			<b>B15</b>	100	85
			<b>B16</b>	100	92
			<b>B17</b>	77	54
			<b>B18</b>	54	54
			<b>B19</b>	100	77
			<b>B20</b>	100	85
			<b>B21</b>	100	92
			<b>B22</b>	100	92
			<b>B23</b>	85	62
			<b>B24</b>	62	77
			<b>B25</b>	77	15
<b>Total</b>				<b>93</b>	<b>81</b>

### 3.2.5 Miniaturized cell-based assay for MEK Inhibitors

The DMA has found application in a diverse array of cell-based experiments in recent years, including the screening of suspension cells<sup>[51]</sup>, the formation of tumor spheroids<sup>[124]</sup>, and the high-throughput screening of embryoid bodies<sup>[53]</sup>, among others. A recent study by CUI *et al.* employed the DMA in a highly miniaturized high-throughput screening of 2208 FDA approved drugs for temozolomide-resistant IDH1 glioma.<sup>[125]</sup> This study featured a straight forward workflow, where drugs were dispensed on each spot of the DMA, followed by cell seeding, on-chip incubation and subsequent assessment of cell viability. While CUI *et al.* utilized an iteration of the DMA that was not polymer based, BREHM *et al.* demonstrated that the photolinker modified surface of the polymer-based DMA was suitable for cell viability experiments. They modified the linker with chlorambucil and released it into droplets containing CHO-K1 cells, resulting in a significant drop in viability. This outcome suggested the possibility of “storing” a drug using the photolabile linker until it is released by UV induced cleavage.<sup>[64]</sup>

In the most recent yet-to-be-published work by TIAN *et al.*, the polymer-based DMA was employed for the synthesis of a library of proteolysis targeting chimeras (PROTACs) through a solid-phase synthesis approach. To assess the anti-cancer activity of the synthesized PROTACs, they cultured the colorectal adenocarcinoma HT-29 cell line on the modified DMA. On-chip, they optimized seeding conditions, selected the clinical trial MEK inhibitor *mirdametinib* as positive controls, and established two distinct on-chip readout methods: colorimetric readout using CCK-8 for viability studies and propidium iodide (PI) staining for counting dead cells.<sup>[126]</sup>

The HT-29 cell line, previously employed successfully in the study of FDA approved MEK inhibitors *selumetinib*<sup>[127]</sup>, *trametinib*<sup>[128]</sup>, and *cobimetinib*<sup>[129]</sup>, was chosen as the model cell line for the cell screening in this project. The workflow for the cell-based screening is illustrated in Figure 44. Following the initial solid-phase synthesis and subsequent release of the compounds from the surface (Figure 44, 1), the DMA was incubated over night to ensure the uptake of the compounds into solution. Subsequently, 300 cells per spots were seeded using the liquid-dispenser Certus Flex by GYGER, and the DMA was incubated for 72h at 37°C (Figure 44, 2). Optimized seeding conditions were adapted from TIAN *et al.*<sup>[126]</sup> Finally, PI staining solution was added to each spot, and the slide was incubated for 15 min at 37°C. The slide was then imaged through fluorescence microscopy to count PI-positive cells (Figure 44, 3).



**Figure 44:** Workflow of the on-chip screening of MEK inhibitors for anti-cancer activity. (1) Solid-phase synthesis of MEK inhibitors on DMA, followed by UV release of the compounds into distinct droplets. (2) Addition of 300 cells per spot using Certus Flex by Gyger and subsequent incubation of the DMA for 72 h at 37 °C. (3) Addition of PI staining solution to each droplet. After 15 min of incubation the DMA was imaged through fluorescence microscopy.

To achieve a sufficient number of replications for each compound and controls per slide, the synthesis of the 325 compounds was divided among five DMA slides, featuring round spots with a 1.4 mm diameter. To prevent evaporation, a one-column and one-row border were left on each side of the slide. Each slide accommodated 240 spots available for experimentation. A random distribution of compounds and controls was selected, with each compound synthesized in three repetitions and controls in five repetitions. Non-contact liquid dispenser Certus Flex by GYGER was employed in all dispensing steps throughout the process, including the printing the cell suspension.

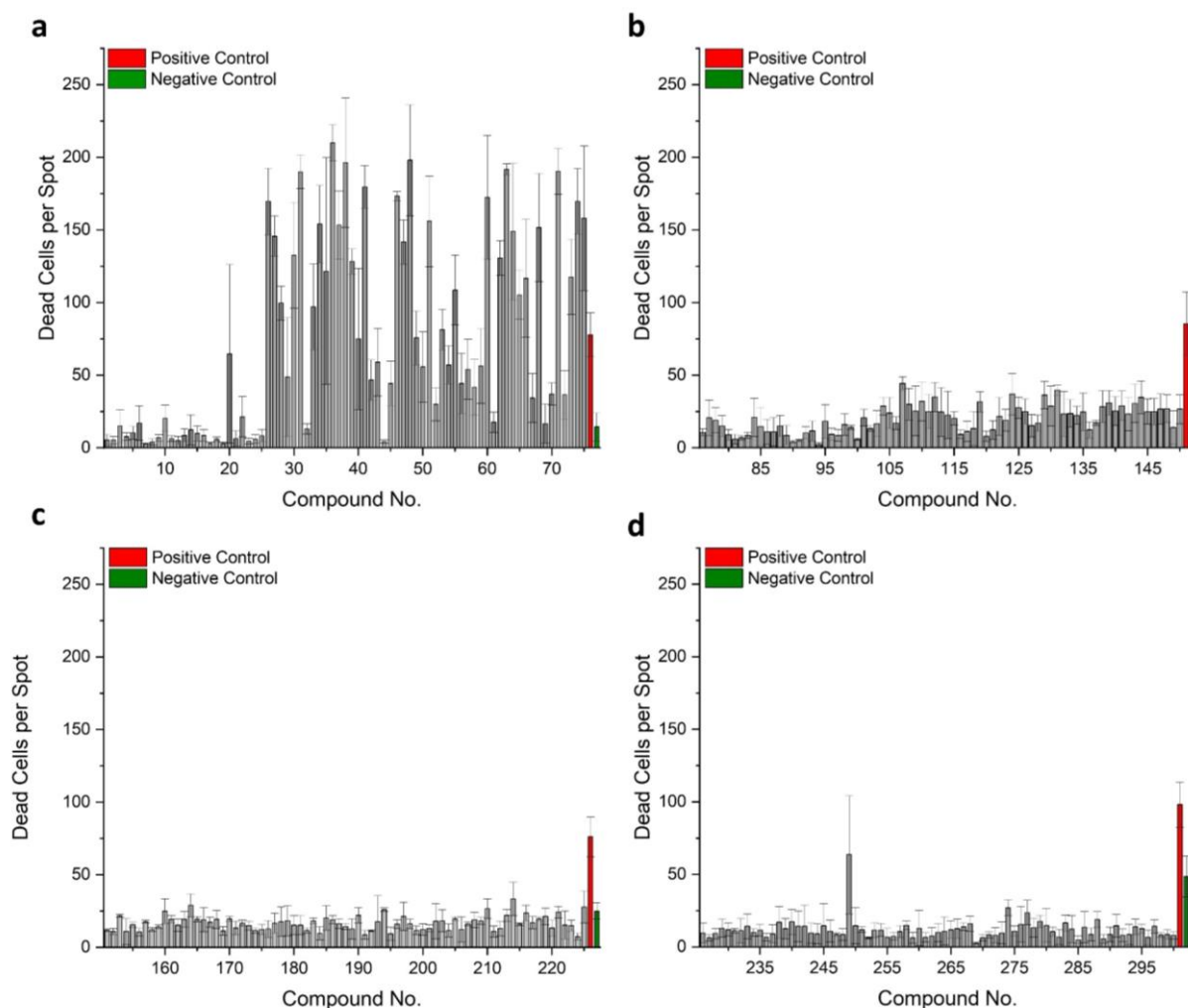
The synthesis was conducted as previously described. Briefly, all HL spot were modified with 0.1 M FAPL, ensuring a final concentration of ~10  $\mu\text{M}$  for each compound. Amino acids were immobilized, and further modification with the core structural motif OTV led to the formation of the amino acid-intermediate. The desired product was obtained through the conversion of

the iodine fragment using the SMR. Precipitated palladium was dissolved by immersing the entire slide in a 0.1M KCN solution in water/DMSO (1:1, v/v).

To prepare the slides for cell screening, a thorough cleaning process was initiated. The slides underwent a sequential wash with acetone and ethanol. To ensure sterility, each slide was immersed in a 70% ethanol solution in water (v/v) for 15 minutes. Following this sterilization step, the slides were carefully dried under sterile conditions for 10 minutes. Subsequently, 700 nL of cell medium, supplemented with 0.17% DMSO, was added to all reaction spots and negative controls. Positive controls received a specific volume of 350 nL. To minimize solvent evaporation, the slides were sealed within a petri dish containing 2 mL of phosphate-buffered saline (PBS) at the bottom. The entire setup was irradiated for 20 minutes at 365 nm, facilitating the release of compounds into the droplets. Further, 350 nL of the positive control (*mirdametinib*, 28.6 $\mu$ M) was introduced to the designated positive control spots. The slides were incubated overnight to ensure complete dissolution of the compounds in the droplets. Following this incubation period, 300 nL of a cell suspension ( $1.0 \times 10^6$  cells/mL, HT-29) in medium was carefully printed onto each spot. The slides were resealed and then incubated for 72 hours at 37 °C. Finally, 100 nL of a solution of propidium iodide (PI) in PBS (10  $\mu$ g/mL) was added to each spot, and the slides were incubated for 15 minutes at 37 °C. Subsequent to this incubation, the slides were subjected to fluorescence microscopy for imaging, and the captured images were subjected to analysis to count the number of PI-positive cells.

The results of the analysis for PI-positive cells of the initial 300 compounds are depicted in Figure 45. The graphs present the count of dead cells per spot for each synthesized compound, along with the corresponding data for the positive control spots (indicated by red bars) and the negative control spots (indicated by green bars). Encouragingly, compounds 26 – 75 demonstrated a notable increase in cell death, as measured by PI staining against HT-29 cells (Figure 45a). In contrast, the remaining compounds exhibited relatively low anti-cancer activity (Figure 45a, b, c).

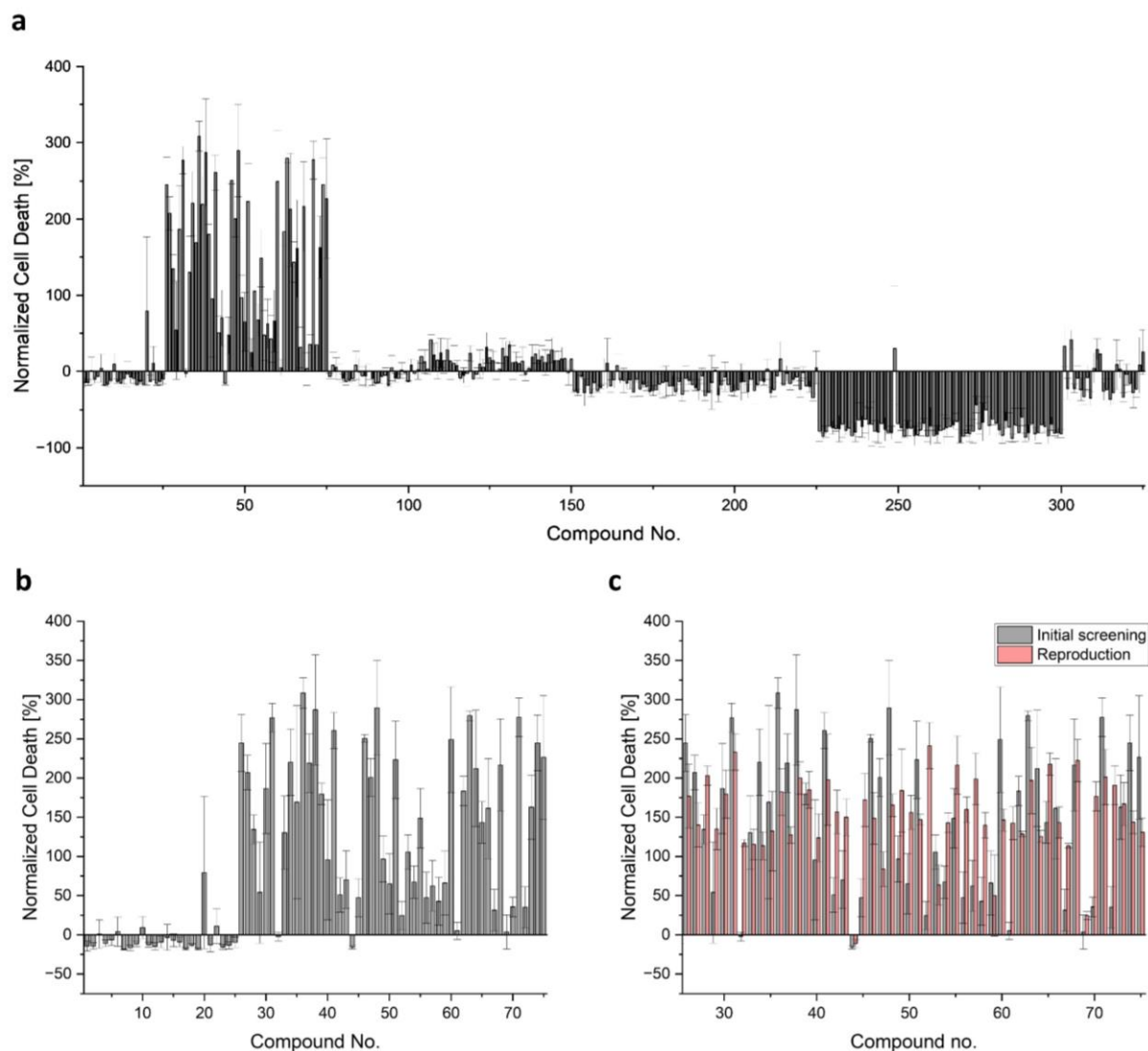




**Figure 45:** Results of the on-chip screening for anti-cancer activity of 300 novel compounds. Graphs present the number of dead cells per spot for each compound. Each bar represents the average of three repetitions. Error bars indicate the standard deviation. Red bars indicate the number of dead cells in the positive control spots, green bars the number of dead cells in negative control spots. **(a)** Increase of dead cells per spot in respect to the positive control for compounds 26 – 75. **(b – d)** Relatively low anti-cancer activity for compounds 76-300.

In order to visualize the anti-cancer activity of all compounds, the data was normalized to the difference between positive and negative control. Additionally, the number of dead cells measured in the negative controls was subtracted from all compounds. Figure 46a presents the normalized data of all 325 compounds. Compounds 26 – 75 exhibited a substantial increase in the induction of cell death when compared to the positive control *mirdametinib* (Figure 46b). The building blocks employed for these compounds included alanine (**A**<sub>2</sub>, compounds 26 -50) and  $\beta$ -alanine (**A**<sub>3</sub>, compounds 51 - 75), each in combination with one of the boronic acids (**B**<sub>1</sub>-**B**<sub>25</sub>). To validate the consistency of the acquired data, the anti-cancer screening for compounds 26-75 was conducted once again, following the previously outlined procedure. The general patterns in activity were confirmed, as all compounds (except for compound 44) demonstrated a substantial increase in induced cell death compared to the positive control (Figure 46c).

Unfortunately, the data obtained also shows, that the impact of the boronic acid derivative could not be completely reproduced.

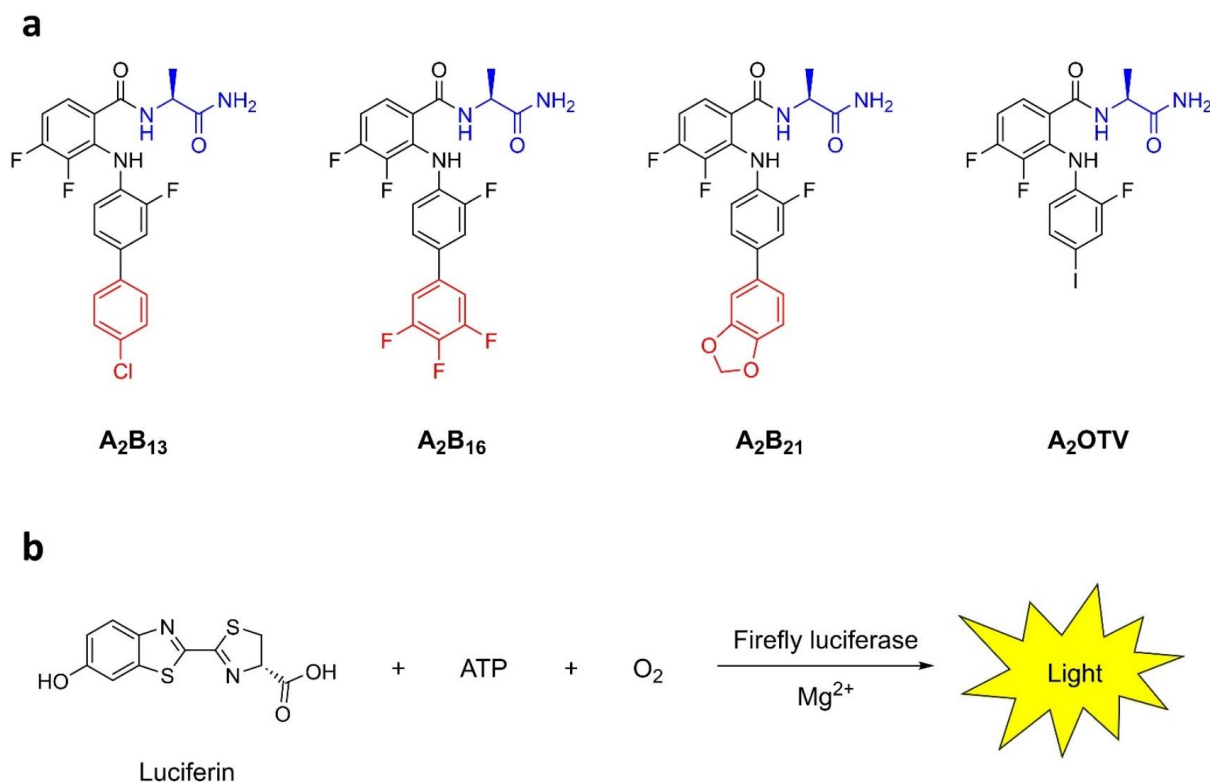


**Figure 46:** (a) Overview of the normalized cell death for all 325 compounds. Compounds 26 – 75 show substantial increase in anti-cancer activity, reaching a maximum of over three-fold activity compared to the positive control. (b) Magnification of the most active compounds. (c) Comparison of the initial on-chip screening data of compounds 26 – 75 with a reproduction of the screening. General increase of anti-cancer activity of amino acids  $A_2$  and  $A_3$  could be reproduced, while the effects of the boronic acid derivatives  $B_1$ - $B_{25}$  differed from the initial screening. Each bar represents the average of three repetitions. Values were normalized to the difference of positive and negative control. Error bars indicate the standard deviation.

To further investigate the anti-cancer activity of the compounds that showed an increased activity on-chip, three compounds showing explicitly high numbers of dead cells per spot on DMA were synthesized in milligram scale in flask according to the procedure described in the Experimental Part. Additionally, the amino-acid intermediate was synthesized in flask to evaluate its anti-cancer activity. The structures of these compounds, as well as the structure of the intermediate are shown in Figure 47a. In order to investigate dose-response relationship of

these compounds against HT-29 cells, the setup was changed to a more conventional 384 well plate.

To measure viability of the cells CELLTITER-GLO assay was employed.<sup>[130]</sup> It is a luminescent assay to determine the number of viable cells in culture based on quantification of the adenosine triphosphate (ATP) present, an indicator of metabolically active cells. ATP is consumed by the reaction of the firefly luciferase in the presence of oxygen and magnesium ions (Figure 47b). To validate the linearity of the luminescence in relation to the number of viable HT-29 cells, a series of different HT-29 cell numbers were seeded in triplicates in a 384 well plate and measured for its luminescence. The data showed good linearity in the range between 1000 – 10.000 cells per well (see appendix).



**Figure 47:** (a) Structures of the synthesized compounds that showed high anti-cancer activity in the on-chip screening (A<sub>2</sub>B<sub>13</sub>, A<sub>2</sub>B<sub>16</sub>, A<sub>2</sub>B<sub>21</sub>) and the amino acid-intermediate A<sub>2</sub>OTV. (b) Schematic representation of the CELLTITER-GLO assay. Firefly luciferase consumes ATP in the presence of luciferin, oxygen and magnesium (II) to emit light. ATP is an indicator of metabolically active cells.

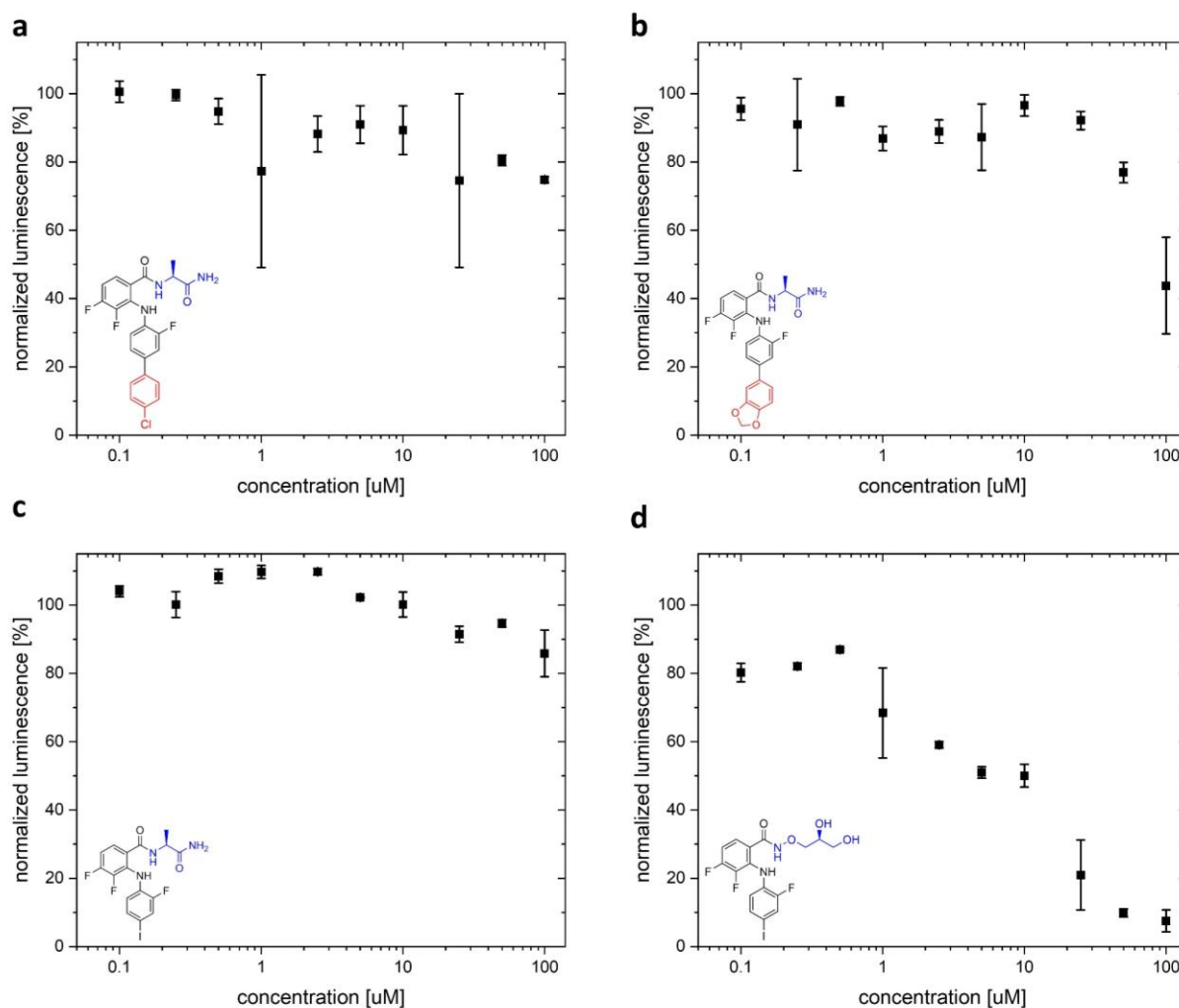
To assess the anti-cancer activity in a 384-well plate, a dilution series of exemplary compounds A<sub>2</sub>B<sub>13</sub>, A<sub>2</sub>B<sub>16</sub>, A<sub>2</sub>B<sub>21</sub>, amino acid-intermediate A<sub>2</sub>OTV, and positive control *mirdametinib* in DMSO supplemented medium was prepared, with concentrations ranging from 0.1 to 100  $\mu$ M. Unfortunately, due to poor solubility in the used solvents, compound A<sub>2</sub>B<sub>16</sub> was excluded from the assay. To replicate the on-chip assay, compound solutions and positive controls were

incubated in triplicates in each respective well for 1 hour at 37 °C. Subsequently, 8000 cells in medium were added to each well containing compounds, yielding a total volume of 25  $\mu$ L per well. The plate was then sealed and incubated for 72 hours at 37 °C. Finally, 25  $\mu$ L of CellTiter-Glo was added to each well (excluding blanks) and incubated for another 10 minutes at room temperature. Luminescence was measured using a CLARIOstar Plus plate reader.

The normalized luminescence for each tested compound in dependence on the compounds concentration is depicted in Figure 48. Unfortunately, tested compound **A<sub>2</sub>B<sub>13</sub>** did not exhibit substantial anti-cancer activity in the tested concentration range (Figure 48a), and amino-acid intermediate **A<sub>2</sub>OTV** (Figure 48c) also showed limited impact. In contrast, compound **A<sub>2</sub>B<sub>16</sub>** (Figure 48b) demonstrated a significant reduction of luminescence, indicating a reduction in living cells at a concentration of 100  $\mu$ M. The calculated half-maximal inhibitory concentration (IC<sub>50</sub>) was 72  $\mu$ M, which is notably higher than expected based on the initial on-chip screening results. The positive control *mirdametinib* exhibited high suppression of luminescence emission at low concentrations with an IC<sub>50</sub> value of 4.8  $\mu$ M.

Despite not aligning with the initial on-chip screening results, the assay evaluation provided valuable insights into the novel MEK inhibitors. Although both tested compounds did not yield anticipated low IC<sub>50</sub> values, the impact of further derivatization of the amino-acid intermediate **A<sub>2</sub>OTV** was evident. Compared to the intermediate, compound **A<sub>2</sub>B<sub>16</sub>** showed a significant increase in anti-cancer activity in the tested concentration range against HT-29, highlighting the impact of the conversion of the iodine fragment.

The discrepancies between the outcomes of the on-chip screening and the CellTiter-Glo assay could be attributed to various reasons. While TIAN *et al.* demonstrated the viability of HT-29 cell culturing on the DMA, the modified polymer surface's impact on cell vitality might have led to an overall decrease compared to the well-established 384-well plates. Another potential factor for the reduced activity could be the racemization of the amino acid residue in the tested compounds. Although not subjected to heating during solid-phase synthesis using the DMA, upscaling the synthesis in a flask required heating the compounds in basic conditions, known to induce amino acid racemization.<sup>[131]</sup> This racemization might affect the interaction with the allosteric pocket of MEK1/2. To further evaluate these findings, the compound scope needs expansion, and the use of other cell lines and assays is warranted.



**Figure 48:** Normalized luminescence of the CellTiter-Glo assay of compound (a)  $A_2B_{13}$ , (b)  $A_2B_{21}$  (c) amino acid-intermediate  $A_2OTV$  and (d) the positive control mirdametininb. All compounds were measured in a concentration range between 0.1 and 100  $\mu\text{M}$ . Each data point is the average of three repetitions, error bars indicate standard deviations. Values were normalized to the negative control.

### 3.3 Miniaturization of the Heck Reaction

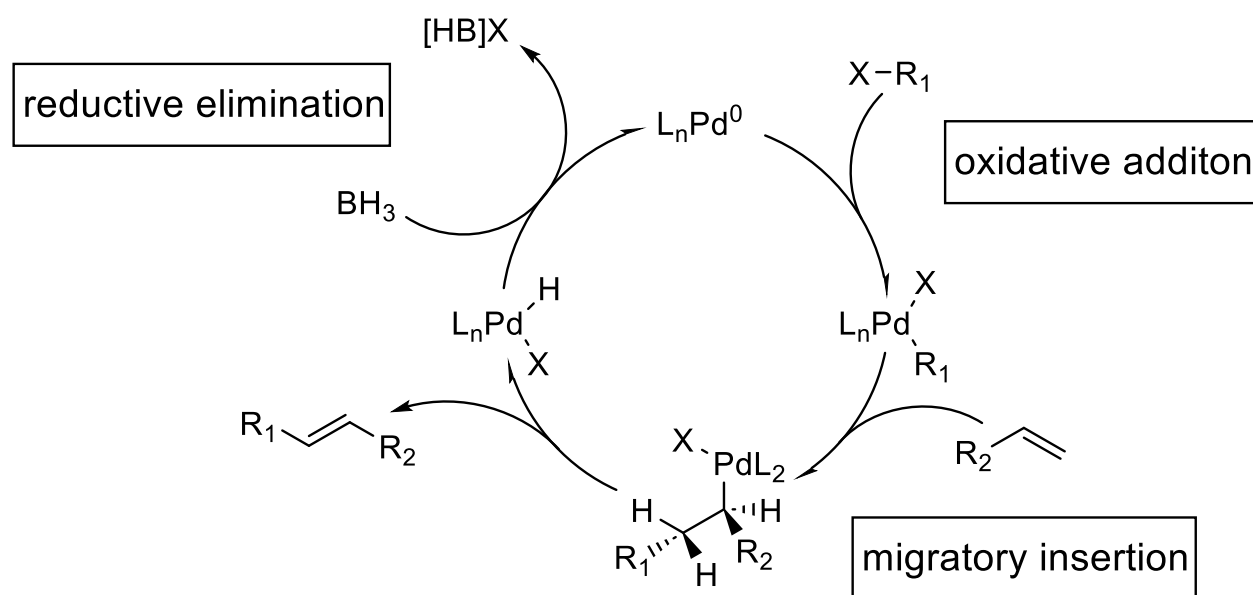
Initial investigation of iodine substrates was conducted by MORITZ ENGHOFFER as a part of a bachelor's thesis and is not included in this chapter. LC-MS measurements took place at the Institute of Technology (INT) in the laboratory of DR. FLORIAN FEIST.

#### 3.3.1 Introduction

##### 3.3.1.1 The Heck Reaction

The palladium-catalyzed vinylation of aryl halides, introduced independently by MIZOROKI<sup>[132]</sup> and HECK<sup>[133]</sup> more than four decades ago, is a cornerstone in organic synthesis. The HECK reaction, often referred to as the vinylation of olefins, encompasses a broad range of substrates, including derivatives of acrylates, styrenes, and intramolecular double bonds. A simplified depiction of the catalytic cycle is illustrated in Figure 49.

The catalytic cycle initiates with the oxidative addition of the aryl or vinyl halide ( $R_1-X$ ) to the  $Pd(0)$  catalyst. During this step, the  $Pd(0)$  catalyst inserts into the carbon-halogen bond of the aryl or vinyl halide, yielding a  $Pd(II)$  complex. Subsequently, the olefin ( $R_2-H$ ) coordinates to the  $Pd(II)$  center, forming a complex with the palladium catalyst. The following step involves the insertion of the olefin into the  $Pd(II)-Ar-X-R_2$  complex, leading to the formation of a  $Pd(II)$  alkyl complex. The final stage includes the elimination of a proton from the beta position of the alkyl group, resulting in the formation of the desired product and regeneration of the  $Pd(0)$  catalyst.



**Figure 49:** Simplified catalytic cycle of the palladium-catalyzed HECK reaction.

The HECK reaction exhibits remarkable versatility, accommodating a diverse range of alkenes and organic halides. It proves effective with functional groups such as esters, ethers, and carboxylic acids. Despite its broad applicability, certain limitations must be considered. An essential requirement is the absence of a  $\beta$ -hydrogen in the organic halide. Therefore, aryl, benzyl, or vinyl groups are preferable choices. The reaction rate is significantly influenced by the strength of the carbon-halogen (C-X) and palladium-halogen (Pd-X) bonds, as well as the nature of the leaving group (nucleofuge). In terms of reactivity, the order can be summarized as follows:  $I \gg OTf > Br \gg Cl$ .<sup>[134]</sup>

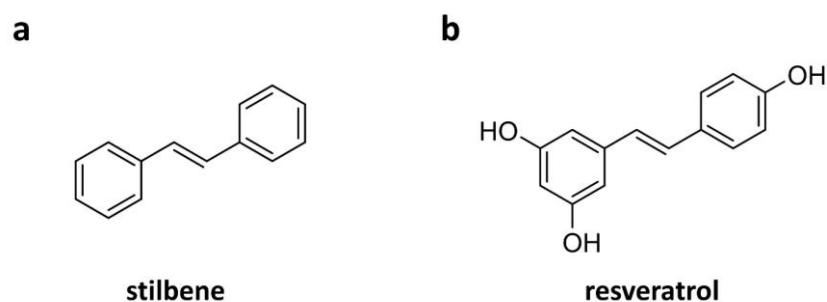
The choice of catalyst is pivotal in determining the success of the reaction. Palladium is the metal of choice due to its ability to tolerate a diverse array of functional groups and its remarkable capacity to forge C-C bonds between suitably functionalized substrates. Palladium-based methodologies generally exhibit excellent stereo- and regioselectivity, yielding high reaction yields.<sup>[135]</sup> Typically, the less sterically hindered structure is favored in Heck reactions, often leading to the formation of trans products. Quaternary ammonium salts, as demonstrated by Jeffrey<sup>[136]</sup>, play a crucial role in optimizing reaction conditions. They serve as effective phase-transfer agents, facilitating reactant transfer in solid-liquid and liquid-liquid systems. Additionally, these salts form anionic complexes, accelerating reaction rates. They support the active Pd(0) catalyst by preventing the growth of large clusters and participate in ion exchange processes, contributing to faster reactions. Common solvents for the HECK reaction include dipolar aprotic solvents like DMF and NMP, although the reaction is adaptable to various other solvents, offering flexibility in experimental setups. The Heck reaction stands as a versatile and powerful tool in modern organic synthesis, facilitating the construction of complex molecular structures with high efficiency and selectivity.

### 3.3.1.2 Motivation and Aim

This section of the thesis aims to enhance the capabilities of DMA by integrating the palladium-catalyzed HECK reaction. DMA has proven to be an integrated platform for synthesis, analysis, and screening. In this phase of the research, DMA will serve as a HT experimentation platform to screen suitable experimental conditions for solid-phase HECK reactions. Employing the established solid-phase approach from previous chapters, the DMA will be utilized for parallelized and miniaturized screening of various catalytic systems, bases, and solvents. This approach is expected to save time, costs, and resources, particularly precious palladium, in the exploration of optimal reaction conditions. Successful implementation would open avenues for

synthesizing stilbenes and cinnamates on DMA, expanding possibilities for subsequent screening of their biological activities.

Stilbenes, in particular, represent an intriguing class of naturally derived compounds, characterized by a versatile scaffold consisting of two aromatic rings linked by an ethylene bridge (Figure 50a). These compounds serve as defense mechanisms in plants, produced in response to pathogen attacks and environmental stressors. Stilbenes are prevalent in natural products,<sup>[137]</sup> exhibiting diverse biological activities.<sup>[138]</sup> Structurally categorized into Z-type and E-type based on their central double bond configuration, stilbenes can undergo Z/E isomerization, influencing their overall configuration and biological activity. Compounds containing stilbenes have garnered attention from chemists and pharmacologists due to their significant biological properties, including antioxidant, anti-inflammatory, and anticancer activities.<sup>[139, 140, 141]</sup> Notably, the stilbene derivative resveratrol (Figure 50b) has been particularly studied for its potential in treating various types of cancer.<sup>[142, 143]</sup>



**Figure 50:** (a) Structure of *E*-stilbene. (b) Structure of stilbene derivative resveratrol.

### 3.3.2 Nanomolar Synthesis of Stilbenes and Cinnamates on Droplet Microarrays

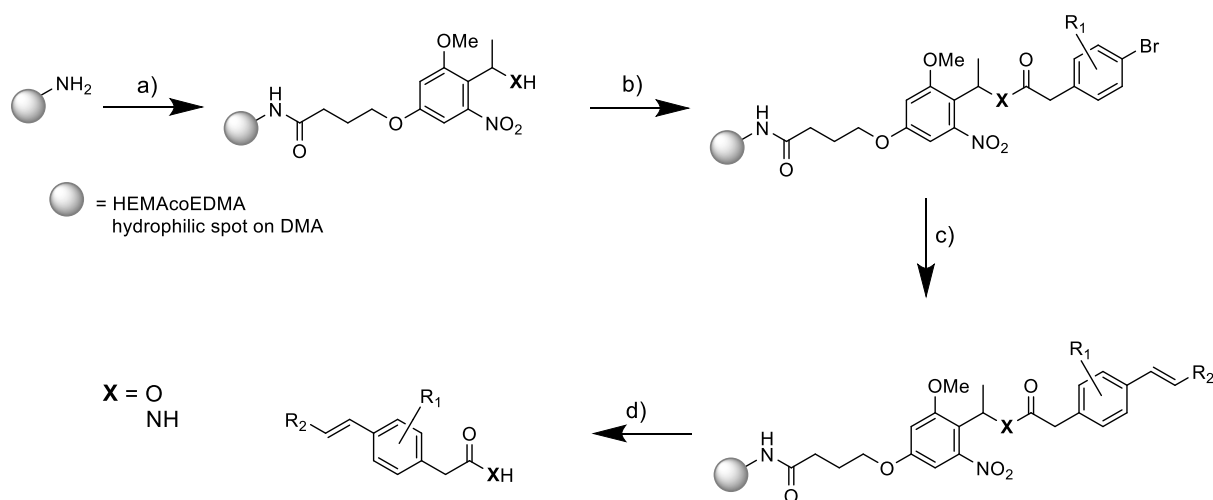
Although the on-chip SMR was extensively explored and detailed in chapter 3.2, the application of the HECK reaction in conjunction with the DMA remains unexplored. To demonstrate the feasibility of the Heck reaction in a solid-phase approach on DMA, a qualitative screening for suitable reaction conditions was conducted on a larger scale using round spots with a diameter of 2.8 mm. This approach underscores the versatility of DMA as a platform, showcasing its capability not only for screening compounds produced by established reactions but also for evaluating suitable reaction conditions in a miniaturized open platform.

To establish a starting point, the well-established synthetic pathway was chosen, given its robustness in the context of the palladium-catalyzed SMR. The synthetic cascade is depicted in Figure 51. The initial steps of the synthesis include the already detailed described modification



of the HL spots with either HEPL or APL in order to create the anchor point for the synthesis (a). Subsequent immobilization of different aryl bromides lead to the formation of the starting point for the Heck reaction (b). The focus in this part of the thesis lies on the following step: The on-chip Heck reaction (c). Subsequent UV induced release cleaves the desired product from the surface, either as carboxylic acid or amide derivative (d).

The primary objective of this project was to identify suitable reaction conditions for the efficient execution of the HECK reaction on DMA. Although the initial steps had been previously established, the primary emphasis was on screening various catalytic systems, starting materials, and experimental conditions.



**Figure 51:** Schematic depiction of the synthetic pathway to synthesize stilbenes and cinnamates on DMA. a) Immobilization of the photolinker. b) Modification of the linker with different aryl bromides. c) HECK reaction with variable alkenes. d) UV induced cleavage of the desired compound from the surface.

### 3.3.3 Defining the optimal reaction conditions via LC-MS

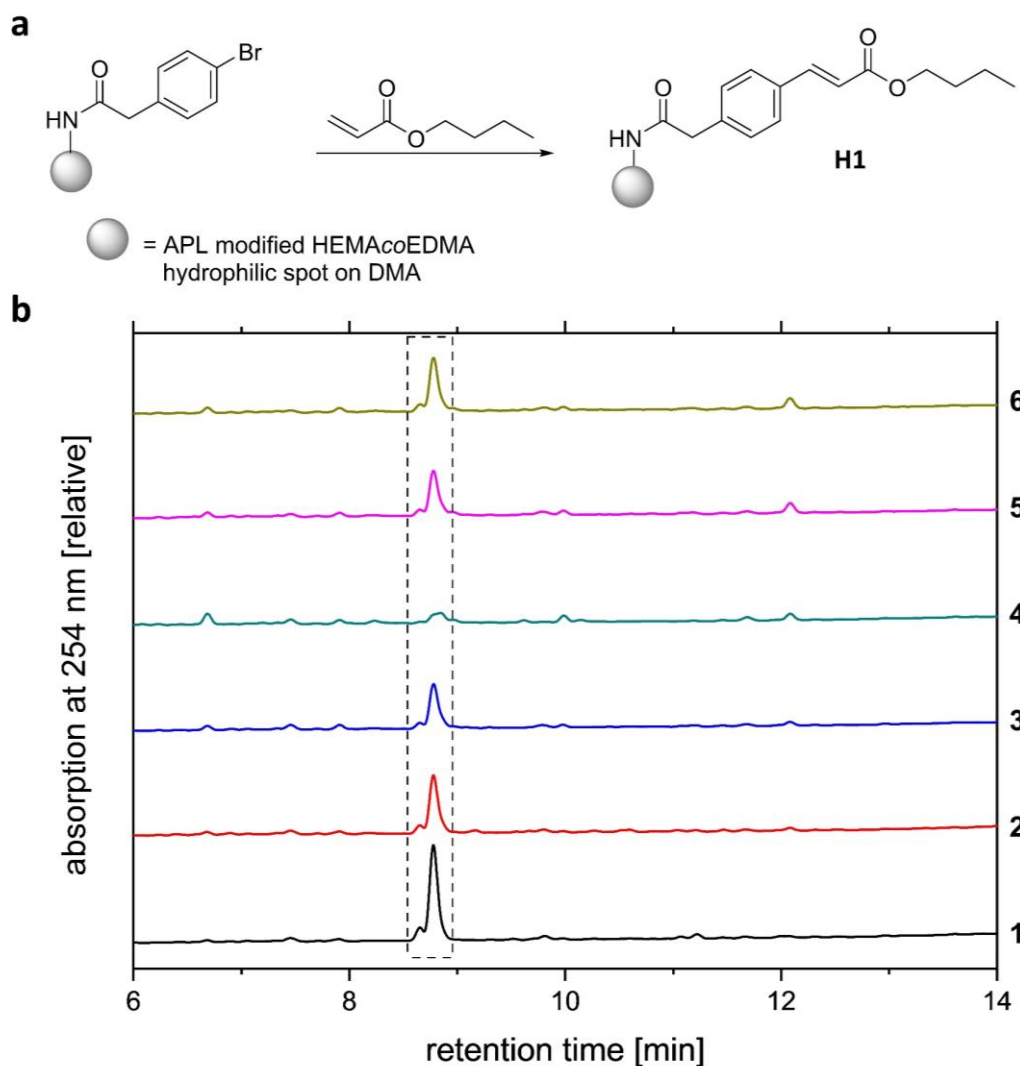
To assess a suitable experimental setup for the successful synthesis of desired compounds on DMA, a screening of various catalytic systems from the literature was conducted to evaluate their catalytic activity on DMA. Despite numerous options, certain limiting factors must be considered in advance. DMA is an open platform, and while manual pipetting on larger spot sizes in an inert atmosphere is feasible, using a non-contact liquid dispenser in such an environment poses challenges. Additionally, the range of usable solvents is constrained. Although commonly employed setups for the HECK reaction use solvents compatible with DMA, such as DMF, NMP, and dimethylacetamide (DMAc), there are other challenges to address.

One notable challenge is the requirement for elevated temperatures for the successful execution of the HECK reaction, typically in the range of 80–120 °C. While heating DMA is possible with

the right setup, employing nanoliter-sized droplets becomes challenging due to the rapid evaporation of solvents. Another consideration is the need for the application of a base in the Heck reaction. Low pH, especially in combination with high temperatures, can lead to hydrolysis, potentially releasing the immobilized starting materials or compromising the polymer backbone of the surface. These factors contribute to the complexity of designing a suitable and effective experimental setup for the Heck reaction on DMA.

To initiate the screening of possible experimental conditions, a test reaction was designed involving the reaction between immobilized 4-bromophenylacetic acid and butyl acrylate, resulting in the formation of cinnamate derivative **H1** (Figure 52a). For the preliminary screening, a set of basic catalytic systems was chosen, including palladium (II) acetate with inorganic bases such as potassium carbonate and sodium acetate in a binary solvent system of NMP/water (4:1, v/v), as well as in combination with the organic base triethylamine in DMF. The catalytic system previously described, which proved to be efficient in the SMR, was also adapted. Sodium tetrachloropalladate (II) was used as the palladium source, and dibenzyl-*N,N*-diisopropyl-phosphoramidite (DDP) served as the ligand. The same solvent systems as those for palladium (II) acetate were employed (Table 11).

In specific detail, 3  $\mu$ L of the 0.2 M palladium catalyst in a solution of either DMF or NMP was applied to each spot. Subsequently, 3  $\mu$ L of butyl acrylate (0.5 M) in either of the organic solvents was added. To initiate the reaction, a 0.3 M solution of the base, either in the organic solvents or water, was added to each spot. The slide was sealed in a Petri dish, which contained a humidifying pad wetted with the corresponding solvent used in the respective reaction to prevent evaporation of the droplets. To facilitate the reaction, the slide was heated to 80 °C on a sand bath for 3 h in this initial setup. Subsequent immersion of the slide in 0.1 M KCN solution in DMSO/water (1;1, v/v) resulted in the removal of the precipitated palladium. UV irradiation for 15 min at 365 nm released the desired compounds from the surface.



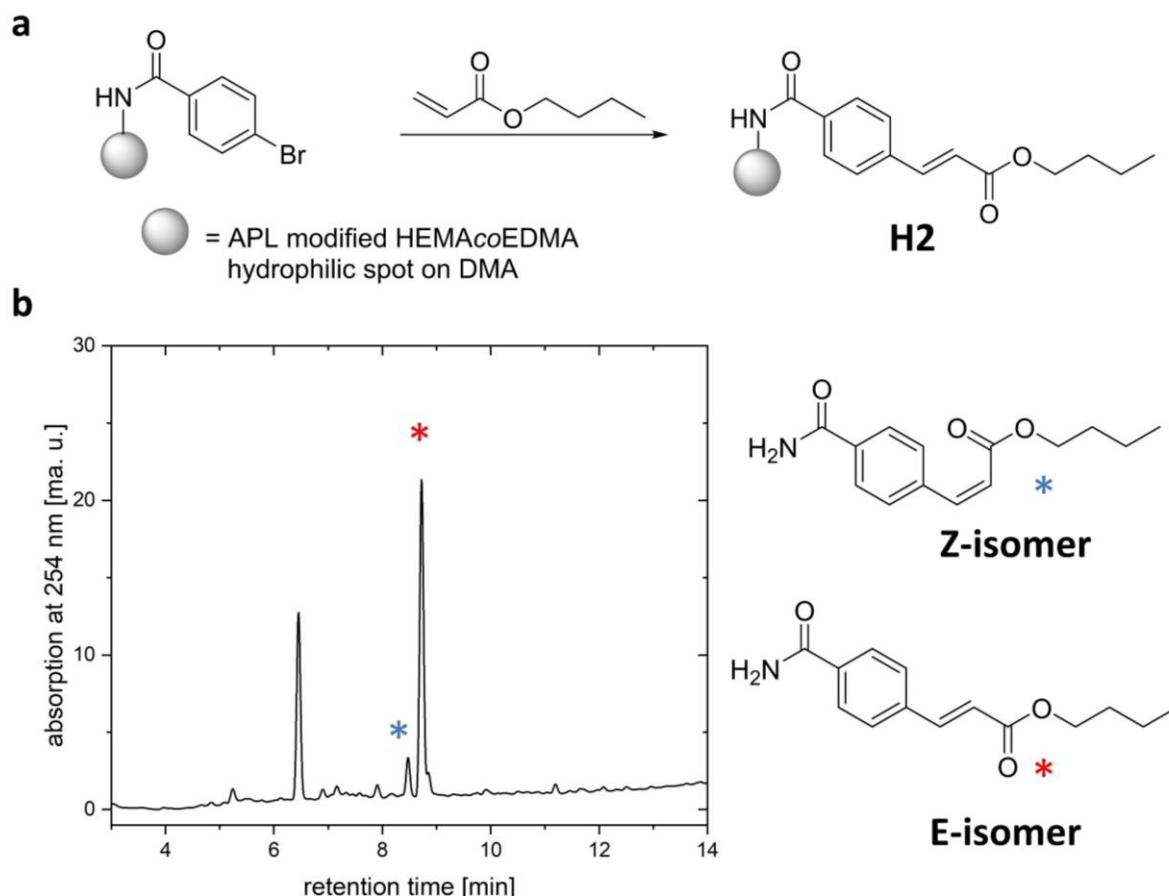
**Figure 52:** (a) Exemplary reaction utilizing immobilized 4-bromophenylacetic acid and butyl acrylate, yielding product **H1**. (b) Overview of the chromatograms of cleaved product **H1**. The highlighted area contains the product peak. Indicated numbers on the right (1 – 6) refer to Table 11.

The formation of the **H1** was examined using LC-MS. Surprisingly, five out of the six initially tested experimental setups resulted in the production of the desired product. The stacked chromatograms of the different setups are depicted in Figure 52b, with the highlighted area indicating the peak of the desired compound **H2**. Excluding the unsuccessful setup **4**, the average purity of the tested setups averaged at 66%. Surprisingly, setup **1**, despite being the most rudimentary among those tested, resulted in the formation of **H1** with the highest purity, reaching 82% (Table 11). Furthermore, all catalytic systems were tested without heating the DMA. None of the tested systems resulted in the formation of the desired compound **H1** without heating. Additionally, the entire screening process was repeated using HEPL as the anchor point on the solid substrate, but it yielded no results due to the premature cleavage of the starting material caused by hydrolysis.

**Table 11:** Overview of a subset of the utilized catalytic systems to investigate the on-chip HECK reaction on DMA. Purity was calculated as the fraction of the product's peak integral with respect to the sum of integrals of all peaks at 254 nm absorbance. <sup>[a]</sup> Unsuccessful setup **4** was excluded in the calculation.

#	Pd Source	Ligand	Base	Solvent	Purity [%]
<b>1</b>	Pd(OAc) <sub>2</sub>	-	NEt <sub>3</sub>	DMF	82
<b>2</b>	Pd(OAc) <sub>2</sub>	-	K <sub>2</sub> CO <sub>3</sub>	NMP/H <sub>2</sub> O	66
<b>3</b>	Pd(OAc) <sub>2</sub>	-	NaOAc	NMP/H <sub>2</sub> O	60
<b>4</b>	Na <sub>2</sub> PdCl <sub>4</sub>	DDP	NEt <sub>3</sub>	DMF	0
<b>5</b>	Na <sub>2</sub> PdCl <sub>4</sub>	DDP	K <sub>2</sub> CO <sub>3</sub>	NMP/H <sub>2</sub> O	60
<b>6</b>	Na <sub>2</sub> PdCl <sub>4</sub>	DDP	NaOAc	NMP/H <sub>2</sub> O	62
<b>Total</b>					<b>66±8<sup>[a]</sup></b>

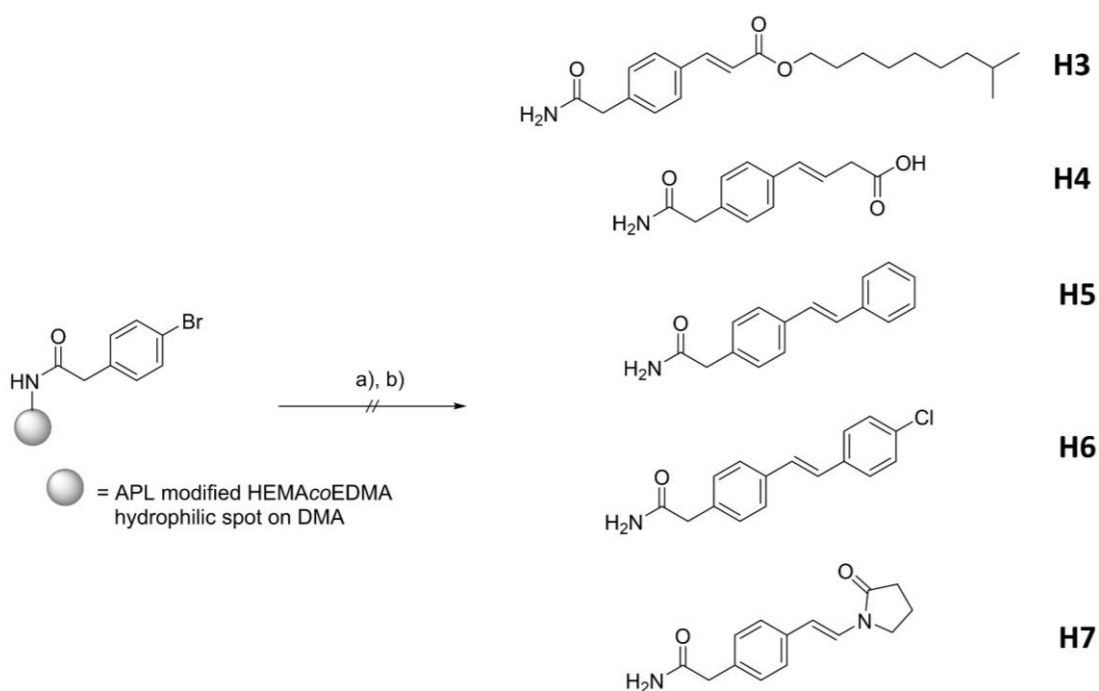
Building upon this promising start, a slight modification was made to the substrate to investigate the impact of the aryl halide on the reaction outcome. 4-Bromophenylbenzoic acid was selected, combined with butyl acrylate to yield product **H2**. To replicate the previously obtained data, the four best-performing tested experimental conditions were applied to this reaction. The formation of compound **H2** was observed for all tested conditions, with condition **1** again achieving the highest product purity at 61%. The chromatogram at 254 nm using condition **1** to yield compound **H2** is depicted in Figure 51b. Conversely, the other tested experimental conditions (**2**, **5**, and **6**) showed much lower purities between 4% and 37%. Notably, the formation of the Z-isomer of **H2** was observed for all tested conditions, with 13% of the formed product isomerizing from E- to Z-alkene. While it is documented in the literature that UV irradiation can lead to the isomerization of Z-alkenes to E-alkenes<sup>[144]</sup>, the prevalence of the Z-isomer after the UV release of **H1** highlights the influence of the substrate's structure. Nevertheless, the outcome of this second round of screening reaffirmed the initial findings that only Pd(OAc)<sub>2</sub> in combination with triethylamine led to the formation of the desired products with the highest purity.



**Figure 53:** (a) Exemplary solid-phase HECK reaction between 4-bromobenzoic acid and butyl acrylate to form compound **H2** utilizing the  $\text{Pd}(\text{OAc})_2$  and  $\text{NEt}_3$  in DMF.. (b) Chromatogram of cleaved compound **H2** at 254 nm. The chromatogram shows the formation of two isomers of the desired product indicated by the blue (Z-isomer) and red (E-isomer) asterisk.

To broaden the range of starting materials, a more diverse set of alkenes was chosen to synthesize compounds **H3** – **H8** (Figure 54). Unfortunately, the application of the previously well-performing catalytic system 1 did not yield any product. To overcome this problem, another round of screening for suitable catalytic systems was conducted. This time, more sophisticated systems were chosen, such as the Herrmann's catalyst<sup>[145]</sup>, routinely used triphenylphosphine ligand-based systems<sup>[146]</sup>, and the addition of phase transfer catalysts was employed.<sup>[2]</sup> Unfortunately, none of the tested systems demonstrated an enhanced conversion of the aryl bromide to the desired product compared to the previously tested system consisting of  $\text{Pd}(\text{OAc})_2$  and  $\text{NEt}_3$ .

While the initial results demonstrated the feasibility of the Heck reaction on DMA, the outcomes of the latter experiments led to the conclusion that more complex starting materials do not tolerate the harsh reaction conditions and the absence of an inert atmosphere. To overcome this problem, a thorough investigation under a completely inert atmosphere needs to be conducted. Another approach could involve exchanging the initially immobilized aryl bromide with a surface-immobilized alkene. To completely suppress the isomerization of the formed product, different linker systems should be investigated. The cleavage process needs to be realizable without destroying the surface of the DMA or influencing the confinement of the spots.



**Figure 54:** On-chip Heck reaction with various starting materials to yield compounds H3 – H8. a) Heck reaction employing  $\text{Pd}(\text{OAc})_2$  and  $\text{NEt}_3$  in DMF. b) UV induced release from the surface. None of the reactions led to the synthesis of the desired compound.

## 4 Conclusion and Outlook

This work explores miniaturization and parallelization within high-throughput drug development, covering synthesis, characterization, and screening. In an environment where costs are substantial, the central challenge is conserving valuable resources such as compounds, materials, solvents, and time. The goal is to integrate all critical stages of early-stage drug discovery onto a compact yet versatile platform. The Droplet Microarray is the chosen platform, having proven its effectiveness in high-throughput biological screenings involving eukaryotic and prokaryotic cells, various bacteria, and initial compound library synthesis through solid-phase chemistry. However, prevailing approach involves utilizing an array of  $5 \times 16$  droplets, each with a 2.8 mm diameter - similar to a 384-well microtiter plate still employing microliters of reagents for a single experiment. To fully exploit the advantages of an open platform with dimensions limited solely by photomasks, the objective of this work is to further shrink to a scale and throughput surpassing that of microtiter plates. Achieving this involves using smaller spots to showcase the platform's capabilities, thereby increasing the number of spots to 1152 per slide and reducing the required experiment volume to the nanoliter range.

The initial section of the thesis involved synthesizing a library of new lipid-like compounds and subsequently analyzing and screening them for antibacterial activity on DMA. The synthetic approach employed a solid-phase method, combining two multi-component reactions: the four-component Ugi reaction and the three-component thiolactone-aminolysis disulfide-exchange reaction. The optimization of reaction conditions for the Ugi reaction was previously carried out by MARIUS BREHM. However, this work focuses on the subsequent development of the synthetic cascade.

The multi-step synthesis of the lipid-like compounds involved converting the solid-bound Ugi products into primary amines for further modification. The traditional thermally initiated hydrothiolation approach, targeting the alkene moiety of the Ugi product, was not feasible due to the construction of the library on a conductive ITO-DMA, which was utilized for MALDI-TOF-MS analysis. As an alternative, the method was altered to a UV-initiated thiol-ene reaction at 254 nm, employing 2,2-dimethoxy-2-phenylacetophenone as a photoinitiator. This modification not only reduced the amount of reagent solution used from milliliters to microliters compared to the thermally initiated approach but also shortened the required reaction time from 18 hours to just 5 minutes. The following three-component reaction resulted in the production of the lipid-like products. Diversifying the array of initial materials for this reaction facilitated the straightforward incorporation of diverse functional groups, such as fluorinated compounds,

positive and negative charges, and alkylated moieties. The uncomplicated synthesis of these building blocks allowed for the broadening of potential products, with a total of 32 novel starting materials being synthesized in a flask and subsequently analyzed. The purities of the lipid-like compounds averaged approximately 44%, which is sufficient for a primary screening. Qualitative investigations into the kinetics of UV-induced release were conducted, confirming that variations in the duration time had an impact on the quantity of released compounds. All the aforementioned reactions were executed on a relatively large scale, employing round spots with a diameter of 2.8 mm to facilitate the utilization of the established analytical method LC-MS.

The ultimate goal of this project was to employ a combination of all 47 starting materials for the synthesis of over 10,000 novel lipid-like compounds. Analyzing such a large number of compounds using LC-MS, if synthesized on a large scale using 512 DMAs with a measuring time of at least 71 days and utilizing liters of solvent, would be impractical. To address this challenge, the size of the used spots was reduced to round spots with a diameter of 900  $\mu\text{m}$ . By employing these smaller spots, the total consumption of reaction solutions per compound was reduced to only 730 nL, representing a decrease by a factor of 135 compared to the larger 2.8 mm spots. Notably, only 15 DMAs would be needed to synthesize the entire library, highlighting the efficiency of the on-chip approach. In terms of resources, a mere 2.5 mmol of reagents and 7.5 mL of solvents would be required to synthesize the complete library on DMAs with 900  $\mu\text{m}$  spots.

To analyze these small reaction volumes, on-chip MALDI-TOF-MS analysis was employed. The synthesis of compounds on a conductive DMA, based on ITO-coated glass, enabled direct measurements from the chip. Comparing the results obtained from this approach to data obtained from conventional ground steel plates revealed good comparability of the methods. However, measurements on ITO-DMA showed lower intensity due to ionization suppression caused by the polymer substrate. To demonstrate the viability of this approach, a library comprising 128 compounds was synthesized in four replicates on ITO-DMA and subsequently analyzed using MALDI-TOF-MS. Remarkably, 91% of the synthesized compounds were successfully identified, underscoring the effectiveness and feasibility of the method.

To validate the versatility of the DMA, a screening for antibacterial activity of the lipid-like compounds against *Klebsiella pneumoniae* was carried out, utilizing a fast and efficient colorimetric assay. Already being employed on nanoparticle-based DMA, preliminary tests had to be conducted to confirm the viability of the assay on modified polymer-based DMA. The



results indicated an impact of the modified polymer substrate compared to the nonmodified polymer, although the assay was still classified as an "excellent assay" based on the  $Z'$ -factor. To further demonstrate the viability of the antibacterial assay on DMA, the library of 128 compounds, already analyzed by MALDI-TOF-MS, was synthesized in a randomized layout in triplicates on DMA and screened for antibacterial activity. Unfortunately, none of the screened compounds exhibited antibacterial activity.

In summary, the results of this project highlight the potential use of the DMA as an integrated platform for high-throughput miniaturized synthesis, analysis, and screening. The expansion of existing chemical reactions on DMA lead to the development of a synthetic sequence involving five steps, transforming unmodified hydrophilic spots into spots containing immobilized lipid-like compounds on the surface. The use of MALDI-TOF-MS as a high-throughput method allowed for the direct identification of synthesized compounds from the chip, significantly reducing the required measurement time in relation to LC-MS from days to hours. Furthermore, the antibacterial activity assay was successfully adapted to be viable on modified polymer-based DMA. A subset of the library was screened for antibacterial activity, although, unfortunately, none of the compounds exhibited such activity. Despite this specific outcome, the project demonstrates the DMA's potential as an efficient and versatile platform for streamlined high-throughput processes in synthesis, analysis, and screening. The comprehensive synthesis and screening of all 10,240 compounds will ultimately reveal the true potential of the platform. While the miniaturization of the synthesis has significantly reduced the time, reagents, and solvents required for each individual reaction, there is still plenty of room for improvement. Automation of the construction of layouts for non-contact dispensers, as well as the evaluation of data obtained from MALDI-TOF-MS measurements, is crucial to efficiently manage such extensive datasets. This step towards automation will enhance the overall efficiency and scalability of the platform for large-scale applications in high-throughput drug discovery.

To streamline the synthesis of lipid-like compounds on DMA, a simplified two-step approach was investigated. This shortcut route involved the well-established UGI reaction followed by the TADE reaction. In this case, the reactive surfaces were created by applying the amino photolinker to serve as an anchor point for the UGI reaction. Subsequently, a 2-pyridyl disulfide derivative was introduced into the intermediate generated by the UGI reaction. This maintained the same number of possible derivatizations of the intermediate as compared to the previous approach, while allowing for variation in the alkyl chain length of the PDS derivative. Examination of two exemplary intermediates revealed high purities of up to 80%. The

subsequent TADE reaction formed the desired lipid-like compounds with modest purities of 33%. A major side product resulted from the dimerization of the intermediate during the TADE reaction. Suppressing this side reaction could potentially lead to optimized yields, reducing the total number of reactions from five to only two, and consequently decreasing the total reaction time by 33%. This easily applicable approach could find use in the synthesis of antibacterial compounds or potential transfection reagents in the future.

The second part of the thesis centered on the utilization of the palladium-catalyzed SUZUKI-MIYaura reaction. MARIUS BREHM had previously optimized the reaction on DMA at a larger scale during the synthesis of basic biphenyls. To highlight the capabilities of the DMA, the reaction scale was downsized by employing smaller square spot sizes with an edge length of 1 mm. Although not detectable by MALDI-TOF-MS, a rudimentary approach was chosen to analyze the combined cleavage solutions of all spots on the 1 mm DMA. The results demonstrated comparable outcomes to the larger scale synthesis, indicating that the miniaturization did not compromise the purity of the product. Additionally, the cleavage kinetics of an exemplary biphenyl were investigated, revealing that the total release of the compound was achieved after 18 minutes of UV irradiation at 365 nm, resulting in a maximum loading of 0.18 nmol per 2.8 mm spot.

The earlier examination of the SUZUKI-MIYaura reaction primarily served a qualitative purpose, confirming the compatibility of the DMA with the reaction. This project put the focus towards integrating the reaction into a synthetic cascade for novel MEK inhibitors. This holds significant research interest, especially considering that only four MEK inhibiting compounds have been approved by the FDA for use in anti-cancer treatment. Employing the established solid-phase approach, a library of 325 novel MEK inhibitors was synthesized on DMA. These compounds were subsequently analyzed by MALDI-TOF-MS using a droplet transfer method, along with the established on-chip measurements. Following this, on-chip screening for anti-cancer activity against HT-29 cells demonstrated the DMA as an integrated platform for synthesis, analysis, and screening of potential MEK inhibitors with anti-cancer properties.

A core structural motif was selected, drawing inspiration from existing MEK inhibitors, to serve as the foundation for this study. Two fragments of this lead compound were then modified to explore the impact of these alterations on anti-cancer activity. This approach facilitated a streamlined synthetic cascade, involving the immobilization of an amino acid to the photolinker-modified spots. The subsequent immobilization of the lead compound to the amino acid produced the intermediate product, which was further transformed into the final product

through the Suzuki-Miyaura reaction. This approach integrated existing synthetic procedures on the DMA to potentially create novel MEK inhibitors.

To synthesize the 325 compounds, a total of 13 amino acids and 25 boronic acid derivatives were combined with the lead compound in the described synthetic cascade. The overall purities of these compounds were assessed by synthesizing 16 exemplary compounds, with an average purity of 56% and good conversion rates reaching around 86%. To gain a better understanding of the reaction kinetics, the purities of the intermediates were also analyzed. A crucial aspect of the solid-phase approach employing a photocleavable linker is the accessible amount of the final product. An in-depth analysis of the UV-induced release kinetics was conducted to determine the precise concentration of the employed photolinker solution to be 0.1M and the required irradiation time to be 40 min to release the wanted amount of the final product into the distinct droplets for the desired final concentration of 10  $\mu$ M.

To assess the synthetic outcome of the 320 compounds, the library was analyzed using MALDI-TOF-MS through two different approaches. The first involved the previously established on-chip measurement using ITO-DMA, and the second utilized a droplet transfer method. In the second approach, the synthesis was carried out on 1.4 mm spots on a regular DMA, subsequently released from the surface. The droplets containing the product were then transferred to a ground steel target plate, sprayed with matrix, and measured using MALDI-TOF-MS. Comparing these two approaches revealed a slight decrease in the number of identified compounds between the target plate and ITO-DMA. Compounds that were challenging to ionize showed limited to no identification directly from the chip due to additional suppression of ionization caused by the polymer substrate. In total, both approaches provided satisfactory results. Measurements on the target plate resulted in a total identification rate of 93%, while on-chip measurements still achieved an 82% identification rate. The total consumption of reaction solution volumes was only 288  $\mu$ L for the synthesis of the entire library in triplicates using 900  $\mu$ m round spots. Even when compared to slightly larger 1.4 mm spots, the usage of reaction solutions was reduced by 43%.

The characterization of the synthetic process was completed by evaluating purities, conversions, release kinetics, and identification rates. To screen the synthesized compounds for their anti-cancer activity against HT-29 cells, the screening procedure previously developed by MAXIMILIAN SEIFERMANN was employed. The synthesis of the 325 compounds was divided onto five independent DMAs to ensure an adequate number of replicates. The clinical trial MEK inhibitor, *mirdametinib*, served as the positive control. The screening of the library revealed a

significantly increased anti-cancer activity on-chip for compounds bearing alanine and beta-alanine modifications. The subset of active compounds was repeatedly synthesized and screened on-chip, confirming the same trends. However, the impact of the boronic acid derivative was not entirely reproducible. To further investigate the identified hit structures, three exemplary compounds that showed high activity on-chip were synthesized in a flask. A more traditional assay in 384-well plates was conducted to determine  $IC_{50}$  values for these compounds. Contrary to the predicted activity, the compounds exhibited an overall lower activity than the positive control.

This project once again highlighted the DMA as a potent tool for integrated drug discovery. The combination of well-established chemical reactions on DMA with the newly developed on-chip MALDI-TOF-MS measurement from polymer-based ITO-DMA enabled the synthesis of a library of MEK inhibitors. In-depth analysis of the release kinetics facilitated the precise release of compounds into the droplets. The usage of the DMA as a screening platform in an anti-cancer activity assay showcased the versatility of the platform. Considering the relatively small number of tested compounds, the number of compounds demonstrating increased anti-cancer activity compared to the positive control is substantial. To evaluate the outcomes of the on-chip screening, the synthesis of the hit compounds on a larger scale needs to be conducted. Subsequent screening in a more traditional manner using 384-well plates will help understand the activity of these compounds on a larger scale. Expanding the set of starting materials will contribute to a more comprehensive understanding of the structure-activity relationship. While a relatively small subset allowed for manual fabrication of layouts and data evaluation, increasing the number of compounds will necessitate the implementation of automation throughout the synthetic and analytical pathway.

The final section of the thesis introduced the DMA as a versatile platform for screening reaction conditions. The successful implementation of the SMR paved the way for exploring palladium-catalyzed reactions on the DMA. To expand the repertoire of reactions compatible with the DMA, the HECK reaction was chosen. Unlike the previously described reactions, the reaction conditions had to be investigated from the ground up. To establish a starting point, the synthetic approach utilized for the SMR was adapted. A simple test reaction enabled the parallel screening of various catalytic systems and experimental conditions on the DMA. The initial findings suggest the feasibility of synthesizing cinnamate derivatives using a solid-phase approach on DMA with good purities of up to 82%, employing a straightforward catalytic system.

Exploration of other surface-immobilized starting materials revealed the unwanted UV-induced isomerization of the desired product. While the E-isomer of many naturally derived stilbenes and cinnamates exhibits biological activity, the Z-isomers do not. To progress towards synthesizing and subsequently screening synthetic stilbene and cinnamate derivatives for biological activity on DMA, the isomerization must be suppressed. Different linker strategies need to be employed to circumvent the UV-induced release from the surface. Unfortunately, the use of more complex starting materials did not yield any desired product. Investigation of more sophisticated catalytic systems did not enhance purities or success rates. Novel catalytic systems that are more stable under oxygen atmosphere and do not require excessive heating for catalytic activity need to be explored. Until now, only commercially available and well-known catalytic systems have been utilized.

This thesis underscores the effectiveness of the DMA as a versatile tool for integrated synthesis, analytics, and biological assays. It not only expands the repertoire of possible reactions and their combinations but also demonstrates the potential for generating novel antibiotics and anti-cancer drugs. While the exemplary HECK reaction illustrates the capabilities of DMA as a screening platform for reaction conditions, there is a need to broaden the scope of usable reactions in general to maximize the established routines for synthesis and analytics. Incorporating asymmetric reactions and other multi-component reactions, as well as enhancing the range of cross-coupling reactions, is crucial for further advancement. However, challenges encountered in working with DMA include issues arising from the polymer substrate itself. The substrate's susceptibility to damage under harsh conditions and its limited compatibility with certain solvents constrain the overall synthetic possibilities. Additionally, the evaporation of nanoliter-sized droplets proved to be a challenge in all projects, necessitating attention to optimized experimental setups, particularly in the design of a humidifying chamber and exploration of heating possibilities. Addressing these challenges is essential to unlock the full potential of DMA in facilitating advanced synthesis and analytics.

## 5 Experimental Part

### 5.1 Methods

#### 5.1.1 Fabrication of the Droplet Microarray

A microscopic glass slide (75 x 26 x 1 mm) was activated by immersing in 1 M sodium hydroxide (NaOH) solution for 1 h, followed by immersing in 1 M hydrochloric acid (HCl), followed by washing with water.

To modify the activated glass slide, a method involving the application of a 20% v/v ethanol solution of 3-(trimethoxysilyl)propyl methacrylate was employed. The solution was spread over the activated glass slides and allowed to incubate for a duration of 30 minutes. Subsequently, the slides were washed with ethanol and dried under a stream of nitrogen.

In order to create a porous polymer layer the following polymerization mixture was utilized: 24 wt% 2-hydroxyethyl methacrylate (HEMA), 16 wt% ethylene dimethacrylate (EDMA), 12 wt% 1-decanol, 48 wt% cyclohexanol, and 0.4 wt% 2,2-dimethoxy-2-phenylacetophenone. Subsequently, 30  $\mu$ L of the polymerization mixture was applied to a fluorinated glass slide and covered with a modified slide. Polymerization took place by exposing the glass mold to UV irradiation at a wavelength of 254 nm for 15 minutes using a Biolink BLX UV chamber (Witec AG, Sursee, Switzerland) with 2.5 mW/cm<sup>2</sup>. The fluorinated glass slide was then removed, and the polymer surface was cleansed with ethanol and dried using an air gun. To enhance the roughness of the polymer surface, thereby increasing its hydrophobicity and hydrophilicity, the smooth top layer of the polymer was eliminated by applying adhesive tape (EAN 4042448036223, Tesa, Offenburg, Germany) to the surface and swiftly removing it.

Prior to the patterning step, the surface underwent modification by immersing the slides in a solution composed of 50 mL of acetone, 56 mg of 4-(dimethylamino)pyridine, 111.6 mg of 4-pentynoic acid, and 180  $\mu$ L of *N,N'*-diisopropylcarbodiimide. The incubation took place for 4 h at room temperature with stirring.

To create a superhydrophobic (SH) pattern, a 10% v/v solution of 1*H*,1*H*,2*H*,2*H*-perfluorodecanethiol in isopropanol was applied onto the polymer surface. The slide was then exposed to 254 nm UV light using a Biolink BLX UV chamber (Witec AG, Sursee, Switzerland) with 2.5 mW/cm<sup>2</sup> through a quartz photomask. Subsequently, the porous polymer surface was thoroughly rinsed with acetone and dried using an air gun.

Superhydrophilic (SL) spots were created by applying a 15% wt solution of cysteaminium chloride in a 1:1 v/v mixture of water and ethanol onto the patterned surface. The slide was

irradiated with 254 nm UV light using a Biolink BLX UV chamber (Witec AG, Sursee, Switzerland) with 2.5 mW/cm<sup>2</sup>) through a quartz slide.

### **ITO-DMA**

ITO coated glass slides underwent activation through immersion in a 30% H<sub>2</sub>O<sub>2</sub> solution for 45 minutes, followed by thorough washing with water and acetone. Subsequently, the activated slides were dried using a flow of nitrogen. The slides were submerged in a 3% solution of silane in toluene and heated to 80°C for 18 h. The slides were washed with acetone and placed in an open petri dish. They were then subjected to further heating at 80°C for 2 h. Afterwards the slides were used like silanized slides (see above)

#### **5.1.2 Dispensing on Droplet Microarray**

Automated liquid dispensing in all miniaturized synthesis steps, as well as cell dispensing onto the DMA, was performed by Certus Flex by Fritz Gyger AG (Gwatt, Switzerland). The precision and the CV of the dispensed volumes in the range between 50 – 500 nL is < ±3.0 %, that is ± 6 nL for 200 nL droplets according to the manufacturer.

Automated liquid dispensing of prepared bacteria suspension, MH medium and KIT-8 solution was performed using I.DOT mini by Dispendix (Stuttgart, Germany).

#### **5.1.3 Preparation of the Droplet Microarray for Synthesis**

The hydrophilic spots underwent treatment with 5 µL (150 nL for 900 µm pattern) of linker coupling solution per spot for 18 hours. The linker coupling solution was composed of 0.1 M photolinker (HEPL or FAPL) and 0.1 M HOBt in NMP, freshly mixed with 5 v% DIC before dispensing. At the end of the coupling process, the modified glass slide was rinsed with ethanol and acetone and then dried with a flow of air. The FAPL was subsequently deprotected with 5 µL of 20 v% piperidine in NMP for 4 h, followed by another round of washing.

#### **5.1.4 Solid-phase UGI Reaction**

##### **Modification of the HEPL:**

Succinic acid was coupled to the linker by adding 5 µL of solution containing 0.1 M succinic anhydride and 0.1 M 4-DMAP in NMP to each spot (2.8 mm diameter, round). The DMA was incubated for 18h in the dark at room temperature. Corresponding volumes for the smaller pattern (1 mm<sup>2</sup>, square; 900 µm diameter, round) were 100 nL. By the end of the coupling the DMA was rinsed with acetone and ethanol and dries in air flow.

**Solid-phase Ugi Reaction:**

The starting materials (amines **A1-A8**, isocyanides **I1-I5** and 4-pentenal) were used as stock solutions with concentrations of 0.5 M in GBL. For a round spot with a diameter of 2.8 mm, 2  $\mu$ L of 4-pentenal solution and 2  $\mu$ L of the corresponding amine solution were mixed on the spot and incubated for 15 minutes in the dark at room temperature. The reaction was started by adding 3  $\mu$ L of the isocyanide solution to each spot and the slide was incubated for 48 h in the dark at room temperature. Corresponding volumes for the smaller pattern (1 mm<sup>2</sup>, square; 900  $\mu$ m diameter, round) were 40 nL for the amine and aldehyde and 60 nL for the isocyanide. Subsequently, the DMA was rinsed with acetone and ethanol to remove excess reactants.

**5.1.5 Solid-phase UV-induced Thiol-Ene Reaction**

5  $\mu$ L (2.8 mm diameter, round) or 150 nL (1 mm<sup>2</sup>, square; 900  $\mu$ m diameter, round) of a solution containing 25 w% of cysteamine hydrochloride and 1 w% 2,2-dimethoxy-2-phenylacetophenone (DMPAP) in water/EtOH (3:1, v/v) were added to each spot. The slide was irradiated with UV light at 254 nm in a Biolink BLX UV chamber (Witec AG, Sursee, Switzerland) with 4.0 mW/cm<sup>2</sup> at 254 nm for 5 minutes. After the reaction time, the DMA was rinsed with ethanol and acetone and dried in air flow.

**5.1.6 Solid-phase Thiolactone-Aminolysis Disulfide-Exchange Reaction**

The starting materials (2-pyridyl disulfide derivatives **P1-P16** and thiolactone derivatives **T1-T16**) were used as stock solutions with concentrations of 0.5 M in DMSO. For a round spot with a diameter of 2.8 mm, 3  $\mu$ L of 2-pyridyl disulfide solution and 3  $\mu$ L of the corresponding thiolactone solution were mixed on the spot and incubated for 18h in the dark at room temperature. Corresponding volumes for the smaller pattern (1 mm<sup>2</sup>, square; 900  $\mu$ m diameter, round) were 80 nL for the 2-pyridyl disulfide and the thiolactone. Subsequently, the DMA was rinsed with acetone and ethanol to remove excess reactants.

**5.1.7 Synthesis of the 2-Pyridyl Disulfide Derivatives**

A solution of 1.0 eq. of thiol in MeOH (10 mL) was drop-wise added to a solution of 1.5 eq 2,2'-dipyridyl disulfide in MeOH (10 mL) and the mixture was stirred for 12h at room temperature. Then stirring was stopped and the solvent was removed under reduced pressure to obtain the crude product. It was purified by column chromatography using silica gel (mesh 60-120) as stationary phase and cyclohexane/ethyl acetate (10:1, v/v) as eluent. After removing the solvent under reduced pressure, the pure product was obtained.



**P<sub>1</sub>**

**<sup>1</sup>H NMR (400 MHz, CHLOROFORM-*d*) δ in ppm:** 2.76 - 3.02 (m, 4 H), 7.01 (ddd, *J*=7.21, 4.83, 1.28 Hz, 1 H), 7.09 - 7.24 (m, 5 H), 7.51 - 7.62 (m, 2 H), 8.40 (d, *J*=4.89 Hz, 1 H). **<sup>13</sup>C NMR (101 MHz, CHLOROFORM-*d*) δ in ppm:** 35.35, 40.04, 119.72, 120.64, 126.53, 128.55, 128.65, 137.13, 139.65, 149.54, 160.32. **API-MS:** [M+H]<sup>+</sup> (calc.) = 248.05, [M+H]<sup>+</sup> (found) = 248.00.

**P<sub>2</sub>**

**<sup>1</sup>H NMR (400 MHz, CHLOROFORM-*d*) δ in ppm:** 3.39 (q, *J*=9.66 Hz, 2 H), 7.08 (ddd, *J*=6.85, 5.01, 1.47 Hz, 1 H), 7.55 - 7.64 (m, 2 H), 8.44 (d, *J*=5.04 Hz, 1 H). **<sup>13</sup>C NMR (101 MHz, CHLOROFORM-*d*) δ in ppm:** 29.90, 35.99, 42.39, 50.94, 119.65, 120.24, 136.87, 148.90, 162.22. **API-MS:** [M+H]<sup>+</sup> (calc.) = 225.99, [M+H]<sup>+</sup> (found) = 225.90.

**P<sub>3</sub>**

**<sup>1</sup>H NMR (400 MHz, CHLOROFORM-*d*) δ in ppm:** 7.04 (ddd, *J*=6.60, 4.83, 1.77 Hz, 1 H), 7.17 - 7.22 (m, 2 H), 7.25 - 7.40 (m, 2 H), 7.51 - 7.58 (m, 2 H), 8.41 (d, *J*=5.05 Hz, 1 H). **<sup>13</sup>C NMR (101 MHz, CHLOROFORM-*d*) δ in ppm:** 119.77, 121.15, 128.86, 129.28, 133.43, 134.76, 137.40, 149.66, 159.07. **API-MS:** [M+H]<sup>+</sup> (calc.) = 253.98, [M+H]<sup>+</sup> (found) = 253.90.

**P<sub>4</sub>**

**<sup>1</sup>H NMR (500 MHz, CHLOROFORM-*d*) δ in ppm:** 1.03 (d, *J*=6.71 Hz, 6 H), 1.94 - 2.11 (m, 1H), 2.71 (d, *J*=6.87 Hz, 2 H), 7.10 (ddd, *J*=7.32, 4.88, 0.76 Hz, 1 H), 7.67 (td, *J*=7.71, 1.83 Hz, 1 H), 7.76 (d, *J*=8.09 Hz, 1 H), 8.47 - 8.48 (m, 1 H). **<sup>13</sup>C NMR (126 MHz, CHLOROFORM-*d*) δ in ppm:** 21.74 (s, 1 C), 28.14 (s, 1 C), 48.38 (s, 1 C), 119.62 (s, 1 C), 120.49 (s, 1 C), 137.14 (s, 1 C), 149.37 (s, 1 C), 160.68 (s, 1 C). **API-MS:** [M+H]<sup>+</sup> (calc.) = 200.05, [M+H]<sup>+</sup> (found) = 200.00.

**P<sub>5</sub>**

**<sup>1</sup>H NMR (400 MHz, CHLOROFORM-*d*) δ in ppm:** 2.42 - 2.59 (m, 2 H), 2.92 - 3.00 (m, 2 H), 7.10 (ddd, *J*=6.72, 4.95, 1.65 Hz, 1 H), 7.57 - 7.65 (m, 2 H), 8.45 (d, *J*=4.85 Hz, 1 H). **<sup>13</sup>C NMR (101 MHz, CHLOROFORM-*d*) δ in ppm:** 30.50, 119.39, 120.27, 136.52, 148.50, 157.71. **API-MS:** [M+H]<sup>+</sup> (calc.) = 589.98, [M+H]<sup>+</sup> (found) = 589.95.

**P<sub>6</sub>**

**<sup>1</sup>H NMR (400 MHz, CHLOROFORM-*d*) δ in ppm:** 1.58 (br d, *J*=2.20 Hz, 6 H), 1.81 (d, *J*=3.06 Hz, 6 H), 1.97 (br s, 3 H), 6.98 (ddd, *J*=7.40, 4.89, 1.04 Hz, 1 H), 7.55 (t, *J*=7.47 Hz, 1 H), 7.76 (dt, *J*=8.13, 0.95 Hz, 1 H), 8.35 (d, *J*=5.04 Hz, 1 H). **<sup>13</sup>C NMR (101 MHz,**

**CHLOROFORM-*d*)  $\delta$  in ppm:** 29.90, 35.99, 42.39, 50.94, 119.65, 120.24, 136.87, 148.90, 162.22. **API-MS:**  $[M+H]^+$  (calc.) = 278.10,  $[M+H]^+$  (found) = 278.15.

**P<sub>7</sub>**

**<sup>1</sup>H NMR (400 MHz, DMSO-*d*<sub>6</sub>)  $\delta$  in ppm:** 2.94 (t, *J*=6.97 Hz, 2 H), 3.07 (t, *J*=6.91 Hz, 2 H), 7.27 - 7.37 (m, 1 H), 7.83 (dt, *J*=8.10, 1.02 Hz, 1 H), 7.87 - 7.92 (m, 1 H), 8.54 (d, *J*=5.16 Hz, 1 H), 12.45 (br s, 1 H). **<sup>13</sup>C NMR (101 MHz, DMSO-*d*<sub>6</sub>)  $\delta$  in ppm:** 33.49, 34.05, 119.78, 121.74, 138.29, 150.11, 159.45, 173.13. **API-MS:**  $[M+H]^+$  (calc.) = 216.01,  $[M+H]^+$  (found) = 215.95.

**P<sub>8</sub>**

**<sup>1</sup>H NMR (400 MHz, CHLOROFORM-*d*)  $\delta$  in ppm:** 1.34 - 1.44 (m, 2 H), 1.52 - 1.69 (m, 5 H), 2.24 - 2.45 (m, 2 H), 2.73 (t, *J*=7.27 Hz, 2 H), 7.04 (ddd, *J*=7.34, 4.89, 1.10 Hz, 1 H), 7.53 - 7.63 (m, 1 H), 7.65 - 7.70 (m, 1 H), 8.41 (ddd, *J*=4.89, 1.77, 0.79 Hz, 1 H). **<sup>13</sup>C NMR (101 MHz, CHLOROFORM-*d*)  $\delta$  in ppm:** 23.27, 27.50, 27.78, 32.77, 37.76, 118.83, 119.67, 136.31, 148.28, 159.42, 178.00. **API-MS:**  $[M+H]^+$  (calc.) = 258.05,  $[M+H]^+$  (found) = 257.95.

**P<sub>9</sub>**

**<sup>1</sup>H NMR (400 MHz, CHLOROFORM-*d*)  $\delta$  in ppm:** 1.13 - 1.36 (m, 17 H), 1.49 (quin, *J*=6.85 Hz, 2 H), 1.62 (quin, *J*=7.40 Hz, 2 H), 2.72 (t, *J*=7.34 Hz, 2 H), 3.57 (t, *J*=6.60 Hz, 2 H), 7.00 (t, *J*=6.07 Hz, 1 H), 7.57 (br t, *J*=7.64 Hz, 1 H), 7.64 - 7.68 (m, 1 H), 8.38 (br d, *J*=4.65 Hz, 1 H).

**<sup>13</sup>C NMR (101 MHz, CHLOROFORM-*d*)  $\delta$  in ppm:** 25.73, 28.45, 28.91, 29.13, 29.39, 29.43, 29.53, 32.80, 39.03, 63.04, 119.55, 120.45, 136.93, 149.56, 160.76.

**API-MS:**  $[M+H]^+$  (calc.) = 314.15,  $[M+H]^+$  (found) = 314.10

**P<sub>10</sub>**

**<sup>1</sup>H NMR (500 MHz, CHLOROFORM-*d*)  $\delta$  in ppm:** 0.88 - 0.92 (m, 3 H), 1.14 - 1.44 (m, 18 H), 1.66 - 1.84 (m, 2 H), 2.80 - 2.83 (m, 2 H), 7.12 (t, *J*=6.31 Hz, 1 H), 7.66 (t, *J*=7.84 Hz, 1 H), 7.78 (d, *J*=8.09 Hz, 1 H), 8.49 (dd, *J*=4.88, 0.92 Hz, 1 H). **<sup>13</sup>C NMR (126 MHz, CHLOROFORM-*d*)  $\delta$  in ppm:** 14.14, 22.71, 28.50, 28.55, 28.95, 29.18, 29.25, 29.25, 29.35, 29.48, 29.54, 29.58, 29.64, 29.64, 29.67, 31.93, 39.08, 39.23, 119.74, 120.53, 137.28, 149.20, 160.68. **API-MS:**  $[M+H]^+$  (calc.) = 312.17,  $[M+H]^+$  (found) = 312.10.

**P<sub>11</sub>**

**<sup>1</sup>H NMR (500 MHz, CHLOROFORM-*d*)  $\delta$  in ppm:** 0.86 - 0.92 (m, 3 H), 1.23 - 1.32 (m, 12 H), 1.34 - 1.44 (m, 3 H), 1.65 - 1.82 (m, 2 H), 2.79 - 2.83 (m, 2 H), 7.10 (ddd, *J*=7.32, 4.88,

0.76 Hz, 1 H), 7.64 (t,  $J=7.77$  Hz, 1 H), 7.76 (d,  $J=8.09$  Hz, 1 H), 8.48 (dd,  $J=4.81, 0.84$  Hz, 1 H).  **$^{13}\text{C}$  NMR (126 MHz, CHLOROFORM-*d*)  $\delta$  in ppm:** 14.13, 19.35, 22.68, 28.50, 28.55, 28.94, 29.18, 29.25, 29.30, 29.33, 29.38, 29.48, 29.53, 29.57, 29.69, 31.88, 39.06, 39.22, 119.66, 120.50, 137.17, 149.31, 160.70. **API-MS:**  $[\text{M}+\text{H}]^+$  (calc.) = 284.14,  $[\text{M}+\text{H}]^+$  (found) = 284.10.

**P<sub>12</sub>**

**$^1\text{H}$  NMR (500 MHz, CHLOROFORM-*d*)  $\delta$  in ppm:** 0.88 (t,  $J=7.17$  Hz, 3 H), 1.21 - 1.42 (m, 4 H), 1.69 (quin,  $J=7.40$  Hz, 2 H), 2.77 - 2.81 (m, 2 H), 7.08 (dd,  $J=7.32, 4.88$  Hz, 1 H), 7.65 (t,  $J=7.72$  Hz, 1 H), 7.74 (d,  $J=7.93$  Hz, 1 H), 8.46 (d,  $J=5.10$  Hz, 1 H).  **$^{13}\text{C}$  NMR (126 MHz, CHLOROFORM-*d*)  $\delta$  in ppm:** 13.93, 22.25, 28.62, 30.63, 39.01, 119.58, 120.49, 137.06, 149.42, 160.68. **API-MS:**  $[\text{M}+\text{H}]^+$  (calc.) = 214.06,  $[\text{M}+\text{H}]^+$  (found) = 213.95.

**P<sub>13</sub>**

**$^1\text{H}$  NMR (400 MHz, CHLOROFORM-*d*)  $\delta$  in ppm:** 0.81 (br t,  $J=6.60$  Hz, 3 H), 1.07 - 1.32 (m, 22 H), 1.38 - 1.66 (m, 2 H), 2.72 (t,  $J=7.34$  Hz, 2 H), 6.93 - 7.06 (m, 1 H), 7.51 - 7.61 (m, 1 H), 7.63 - 7.67 (m, 1 H), 8.38 (br d,  $J=4.65$  Hz, 1 H).  **$^{13}\text{C}$  NMR (101 MHz, CHLOROFORM-*d*)  $\delta$  in ppm:** 14.12, 22.69, 28.50, 28.94, 29.18, 29.52, 29.64, 29.66, 31.93, 39.08, 119.54, 120.43, 136.90, 149.57, 160.78. **API-MS:**  $[\text{M}+\text{H}]^+$  (calc.) = 340.21,  $[\text{M}+\text{H}]^+$  (found) = 340.15.

**P<sub>14</sub>**

**$^1\text{H}$  NMR (400 MHz, CHLOROFORM-*d*)  $\delta$  in ppm:** 0.81 (t,  $J=6.72$  Hz, 3 H), 1.13 - 1.33 (m, 16 H), 1.51 - 1.69 (m, 2 H), 2.72 (t,  $J=7.34$  Hz, 2 H), 6.89 - 7.11 (m, 1 H), 7.51 - 7.60 (m, 1 H), 7.63 - 7.68 (m, 1 H), 8.39 (br d,  $J=4.77$  Hz, 1 H).  **$^{13}\text{C}$  NMR (101 MHz, CHLOROFORM-*d*)  $\delta$  in ppm:** 1.02, 14.11, 22.69, 28.50, 28.54, 28.94, 29.18, 29.25, 29.32, 29.47, 29.52, 29.58, 29.58, 31.91, 39.08, 39.25, 77.23, 119.55, 120.44, 136.90, 149.57, 160.78. **API-MS:**  $[\text{M}+\text{H}]^+$  (calc.) = 298.16,  $[\text{M}+\text{H}]^+$  (found) = 298.10.

**P<sub>15</sub>**

**$^1\text{H}$  NMR (400 MHz, CHLOROFORM-*d*)  $\delta$  in ppm:** 0.80 (t,  $J=6.79$  Hz, 3 H), 1.14 - 1.35 (m, 6 H), 1.62 (quin,  $J=7.43$  Hz, 2 H), 2.72 (t,  $J=7.34$  Hz, 2 H), 7.01 (dd,  $J=6.36, 5.75$  Hz, 1 H), 7.58 (t,  $J=7.76$  Hz, 1 H), 7.64 - 7.69 (m, 1 H), 8.39 (br d,  $J=4.77$  Hz, 1 H).  **$^{13}\text{C}$  NMR (101 MHz, CHLOROFORM-*d*)  $\delta$  in ppm:** 14.01, 22.51, 28.17, 28.90, 31.36, 39.07, 119.59, 120.47, 137.01, 149.48, 160.73. **API-MS:**  $[\text{M}+\text{H}]^+$  (calc.) = 228.08,  $[\text{M}+\text{H}]^+$  (found) = 228.00.

**P<sub>16</sub>**

**<sup>1</sup>H NMR (400 MHz, CHLOROFORM-*d*) δ in ppm:** 3.96 (s, 2 H), 6.08 - 6.10 (m, 1 H), 6.12 (s, 1 H), 6.96 (t, *J*=6.14 Hz, 1 H), 7.20 - 7.24 (m, 1 H), 7.40 (d, *J*=8.28 Hz, 1 H), 7.49 (t, *J*=7.35 Hz, 1 H), 8.35 (dt, *J*=4.89, 0.86 Hz, 1 H). **<sup>13</sup>C NMR (101 MHz, CHLOROFORM-*d*) δ in ppm:** 35.88, 109.57, 110.73, 119.36, 120.46, 137.00, 142.56, 149.21, 149.37, 160.02. **API-MS:** [M+H]<sup>+</sup> (calc.) = 224.01, [M+H]<sup>+</sup> (found) = 224.00.

**5.1.8 Synthesis of the Homocysteine Thiolactone Derivatives**

A solution of 2.50 eq. triethylamine in DCM (5mL) was drop-wise added to a solution of 1.0 eq. acid chloride and 1.0 eq. homocysteine thiolactone in DCM (10 mL) at 0°C. After addition, the mixture was allowed to warm to room temperature and was stirred for 12h. Then stirring was stopped and the organic phase was washed with saturated NaHCO<sub>3</sub> and water, followed by drying over MgSO<sub>4</sub>. After removing the solvent under reduced pressure, the pure product was obtained.

**T<sub>1</sub>**

**<sup>1</sup>H NMR (500 MHz, CHLOROFORM-*d*) δ in ppm:** 1.17 - 1.30 (m, 3 H), 1.45 - 1.47 (m, 2 H), 1.81 (br d, *J*=10.99 Hz, 2 H), 1.85 - 2.05 (m, 4 H), 2.17 (tt, *J*=11.73, 3.45 Hz, 1 H), 2.98 (dt, *J*=12.28, 6.07 Hz, 1 H), 3.27 (dd, *J*=11.29, 6.87 Hz, 1 H), 3.38 (td, *J*=11.79, 5.11 Hz, 1 H), 4.50 (dt, *J*=12.78, 6.35 Hz, 1 H), 5.95 (br s, 1 H). **<sup>13</sup>C NMR (126 MHz, CHLOROFORM-*d*) δ in ppm:** 25.61, 25.64, 25.67, 27.62, 29.53, 29.64, 32.21, 45.20, 59.39, 176.66, 205.81. **API-MS:** [M+H]<sup>+</sup> (calc.) = 228.32, [M+H]<sup>+</sup> (found) = 228.05.

**T<sub>2</sub>**

**<sup>1</sup>H NMR (500 MHz, CHLOROFORM-*d*) δ in ppm:** 1.85 - 2.06 (m, 3 H), 2.12 - 2.25 (m, 2 H), 2.25 - 2.35 (m, 2 H), 2.92 - 3.01 (m, 1 H), 3.03 - 3.14 (m, 1 H), 3.27 (dd, *J*=11.29, 7.02 Hz, 1 H), 3.31 - 3.44 (m, 1 H), 4.46 - 4.58 (m, 1 H), 5.82 - 5.96 (m, 1 H). **<sup>13</sup>C NMR (126 MHz, CHLOROFORM-*d*) δ in ppm:** 18.14, 25.32, 25.32, 27.60, 32.14, 39.59, 59.40, 175.53, 205.79. **API-MS:** [M+H]<sup>+</sup> (calc.) = 200.27, [M+H]<sup>+</sup> (found) = 200.05.

**T<sub>3</sub>**

**<sup>1</sup>H NMR (500 MHz, CHLOROFORM-*d*) δ in ppm:** 0.98 (br t, *J*=6.03 Hz, 6 H), 1.93 (qd, *J*=12.46, 7.02 Hz, 1 H), 2.07 - 2.20 (m, 3 H), 2.97 (dt, *J*=12.21, 5.95 Hz, 1 H), 3.27 (dd, *J*=11.22, 6.94 Hz, 1 H), 3.32 - 3.43 (m, 1 H), 4.55 (dt, *J*=12.78, 6.35 Hz, 1 H), 5.99 (br s, 1 H). **<sup>13</sup>C NMR (126 MHz, CHLOROFORM-*d*) δ in ppm:** 22.37, 22.44, 26.16, 27.60, 32.08, 45.66, 59.46, 173.06, 205.61. **API-MS:** [M+H]<sup>+</sup> (calc.) = 202.08, [M+H]<sup>+</sup> (found) = 202.05.

**T<sub>4</sub>**

**<sup>1</sup>H NMR (400 MHz, CHLOROFORM-*d*) δ in ppm:** 1.96 (qd, *J*=12.49, 6.91 Hz, 1 H), 3.04 (dddd, *J*=12.32, 6.82, 5.26, 1.16 Hz, 1 H), 3.21 - 3.29 (m, 1 H), 3.32 - 3.40 (m, 1 H), 4.61 (ddd, *J*=12.72, 6.79, 5.56 Hz, 1 H), 6.56 (br s, 1 H), 7.35 - 7.41 (m, 2 H), 7.43 - 7.56 (m, 1 H), 7.74 (d, *J*=7.65 Hz, 2 H). **<sup>13</sup>C NMR (101 MHz, CHLOROFORM-*d*) δ in ppm:** 27.76, 32.26, 60.03, 127.13, 128.69, 132.06, 133.39, 167.79, 205.69. **API-MS:** [M+H]<sup>+</sup> (calc.) = 222.05, [M+H]<sup>+</sup> (found) = 222.00.

**T<sub>5</sub>**

**<sup>1</sup>H NMR (400 MHz, CHLOROFORM-*d*) δ in ppm:** 1.46 - 1.58 (m, 2 H), 1.61 - 1.89 (m, 7 H), 2.47 - 2.58 (m, 1 H), 2.91 (dddd, *J*=12.32, 6.82, 5.26, 1.16 Hz, 1 H), 3.15 - 3.33 (m, 2 H), 4.37 - 4.46 (m, 1 H), 5.81 (br s, 1 H). **<sup>13</sup>C NMR (101 MHz, CHLOROFORM-*d*) δ in ppm:** 25.93, 27.62, 30.49, 32.25, 45.53, 59.60, 176.83, 205.77. **API-MS:** [M+H]<sup>+</sup> (calc.) = 214.08, [M+H]<sup>+</sup> (found) = 214.05.

**T<sub>6</sub>**

**<sup>1</sup>H NMR (400 MHz, CHLOROFORM-*d*) δ in ppm:** 0.81 (t, *J*=6.72 Hz, 3 H), 1.14 - 1.25 (m, 16 H), 1.49 - 1.65 (m, 3 H), 1.84 (qd, *J*=12.47, 6.85 Hz, 1 H), 2.09 - 2.24 (m, 2 H), 2.89 (dt, *J*=12.29, 5.96 Hz, 1 H), 3.18 (dd, *J*=11.31, 6.79 Hz, 1 H), 3.29 (td, *J*=11.74, 5.14 Hz, 1 H), 4.44 (dt, *J*=12.81, 6.37 Hz, 1 H), 5.77 - 5.97 (m, 1 H). **<sup>13</sup>C NMR (101 MHz, CHLOROFORM-*d*) δ in ppm:** 14.11, 22.68, 25.53, 27.60, 29.22, 29.32, 29.46, 29.59, 31.90, 32.15, 36.43, 59.49, 77.24, 173.69, 205.68. **API-MS:** [M+H]<sup>+</sup> (calc.) = 300.19, [M+H]<sup>+</sup> (found) = 300.15.

**T<sub>7</sub>**

**<sup>1</sup>H NMR (400 MHz, CHLOROFORM-*d*) δ in ppm:** 1.93 (qd, *J*=12.49, 7.03 Hz, 1 H), 2.98 - 3.05 (m, 1 H), 3.24 - 3.39 (m, 2 H), 4.42 (dt, *J*=12.56, 6.25 Hz, 1 H), 6.76 (br s, 1 H). **<sup>13</sup>C NMR (101 MHz, CHLOROFORM-*d*) δ in ppm:** 25.54, 30.15, 58.72, 192.63. **API-MS:** [M+H]<sup>+</sup> (calc.) = 513.99, [M+H]<sup>+</sup> (found) = 514.00.

**T<sub>8</sub>**

**<sup>1</sup>H NMR (400 MHz, CHLOROFORM-*d*) δ in ppm:** 2.24 - 2.52 (m, 1 H), 2.54 - 2.76 (m, 1 H), 3.22 - 3.40 (m, 2 H), 4.38 - 4.47 (m, 1 H), 6.85 (br s, 1 H). **<sup>13</sup>C NMR (101 MHz, CHLOROFORM-*d*) δ in ppm:** 26.65, 30.11, 58.48, 202.32. **API-MS:** [M+H]<sup>+</sup> (calc.) = 214.01, [M+H]<sup>+</sup> (found) = 124.05.

**T<sub>9</sub>**

**<sup>1</sup>H NMR (400 MHz, DMSO-*d*<sub>6</sub>) δ in ppm:** 1.97 - 2.20 (m, 1 H), 2.26 - 2.47 (m, 1 H), 2.89 - 3.03 (m, 1 H), 3.23 - 3.31 (m, 1 H), 3.34 - 3.47 (m, 1 H), 3.59 - 3.70 (m, 1 H), 4.11 - 4.35 (m, 4 H), 4.51 - 4.74 (m, 1 H), 5.48 (br d, *J*=7.70 Hz, 1 H), 6.98 (td, *J*=7.18, 2.26 Hz, 1 H), 7.03 - 7.11 (m, 1 H), 7.20 (dd, *J*=5.62, 2.08 Hz, 1 H), 7.23 - 7.36 (m, 3 H), 7.38 - 7.44 (m, 2 H), 7.52 (td, *J*=18.19, 8.25 Hz, 1 H), 7.61 - 7.71 (m, 2 H), 7.85 - 7.92 (m, 2 H), 8.43 (br d, *J*=7.58 Hz, 1 H), 10.83 (br s, 1 H). **<sup>13</sup>C NMR (101 MHz, DMSO-*d*<sub>6</sub>) δ in ppm:** 23.77, 27.24, 30.51, 30.66, 41.14, 47.05, 47.13, 47.24, 58.72, 66.14, 66.14, 110.58, 118.67, 118.96, 120.53, 120.57, 121.29, 124.38, 124.38, 125.61, 125.81, 127.52, 128.06, 141.12, 141.19, 141.19, 144.21, 144.41, 156.19, 156.26, 157.26. **API-MS:** [M+H]<sup>+</sup> (calc.) = 526.17, [M+H]<sup>+</sup> (found) = 526.15.

**T<sub>10</sub>**

**<sup>1</sup>H NMR (400 MHz, DMSO-*d*<sub>6</sub>) δ in ppm:** 2.14 (qd, *J*=12.25, 6.91 Hz, 1 H), 2.40 (t, *J*=7.21 Hz, 2 H), 2.46 - 2.54 (m, 1 H), 3.26 - 3.33 (m, 2 H), 3.46 - 3.61 (m, 2 H), 4.28 - 4.41 (m, 3 H), 4.70 (dt, *J*=12.90, 7.43 Hz, 1 H), 7.36 - 7.46 (m, 3 H), 7.51 (t, *J*=7.50 Hz, 2 H), 7.78 (d, *J*=7.46 Hz, 2 H), 7.98 (d, *J*=7.46 Hz, 2 H), 8.34 (br d, *J*=8.31 Hz, 1 H). **<sup>13</sup>C NMR (101 MHz, DMSO-*d*<sub>6</sub>) δ in ppm:** 47.16, 58.55, 120.60, 125.64, 127.54, 128.09, 141.19, 144.37. **API-MS:** [M+H]<sup>+</sup> (calc.) = 411.13, [M+H]<sup>+</sup> (found) = 411.05.

**T<sub>11</sub>**

**<sup>1</sup>H NMR (400 MHz, DMSO-*d*<sub>6</sub>) δ in ppm:** 1.17 - 1.33 (m, 3 H), 1.94 - 2.26 (m, 1 H), 2.32 - 2.47 (m, 1 H), 3.27 - 3.44 (m, 2 H), 4.00 - 4.15 (m, 1 H), 4.17 - 4.34 (m, 3 H), 4.51 - 4.69 (m, 1 H), 7.34 (t, *J*=7.47 Hz, 2 H), 7.42 (t, *J*=7.52 Hz, 2 H), 7.54 (br t, *J*=7.03 Hz, 1 H), 7.74 (td, *J*=7.00, 2.87 Hz, 2 H), 7.90 (d, *J*=7.60 Hz, 2 H), 8.24 (br dd, *J*=14.30, 8.31 Hz, 1 H). **<sup>13</sup>C NMR (101 MHz, DMSO-*d*<sub>6</sub>) δ in ppm:** 18.85, 27.20, 30.56, 30.61, 47.12, 50.40, 50.44, 58.52, 58.77, 66.11, 120.57, 125.80, 127.54, 128.10, 141.18, 144.26, 144.39, 156.14, 173.16, 173.33, 205.58, 205.73. **API-MS:** [M+H]<sup>+</sup> (calc.) = 411.13, [M+H]<sup>+</sup> (found) = 411.05.

**T<sub>12</sub>**

**<sup>1</sup>H NMR (400 MHz, CHLOROFORM-*d*) δ in ppm:** 1.94 - 2.06 (m, 1 H), 2.36 (s, 3 H), 2.75 - 2.82 (m, 1 H), 3.14 - 3.21 (m, 2 H), 3.65 (ddd, *J*=12.62, 6.82, 3.06 Hz, 1 H), 5.07 (br s, 1 H), 7.26 (d, *J*=7.78 Hz, 2 H), 7.70 (d, *J*=7.89 Hz, 2 H). **<sup>13</sup>C NMR (101 MHz, CHLOROFORM-*d*) δ in ppm:** 21.59, 27.51, 33.03, 61.88, 127.31, 129.94, 135.86, 144.18, 203.86. **API-MS:** [M+H]<sup>+</sup> (calc.) = 272.03, [M+H]<sup>+</sup> (found) = 271.95.

**T<sub>13</sub>**

**<sup>1</sup>H NMR (400 MHz, CHLOROFORM-*d*) δ in ppm:** 1.84 (qd, *J*=12.49, 6.91 Hz, 1 H) 1.98 (s, 3 H) 2.85 - 2.95 (m, 1 H) 3.15 - 3.33 (m, 2 H) 4.44 (dt, *J*=12.81, 6.37 Hz, 1 H) 5.86 (br s, 1 H). **<sup>13</sup>C NMR (101 MHz, CHLOROFORM-*d*) δ in ppm:** 22.06, 26.58, 31.09, 58.61, 169.54, 204.57. **API-MS:** [M+H]<sup>+</sup> (calc.) = 160.04, [M+H]<sup>+</sup> (found) = 160.00.

**T<sub>14</sub>**

**<sup>1</sup>H NMR (400 MHz, CHLOROFORM-*d*) δ in ppm:** 0.77 - 0.85 (m, 4 H), 1.18 - 1.23 (m, 12 H), 1.46 - 1.63 (m, 2 H), 1.83 (qd, *J*=12.47, 6.97 Hz, 1 H), 2.10 - 2.33 (m, 2 H), 2.87 - 2.96 (m, 1 H), 3.14 - 3.33 (m, 2 H), 4.43 (dt, *J*=12.53, 6.45 Hz, 1 H), 5.78 (br s, 1 H). **<sup>13</sup>C NMR (101 MHz, CHLOROFORM-*d*) δ in ppm:** 14.11, 22.67, 25.53, 27.63, 29.21, 29.26, 29.31, 29.42, 31.85, 32.23, 36.46, 59.55, 173.70, 205.67. **API-MS:** [M+H]<sup>+</sup> (calc.) = 272.16, [M+H]<sup>+</sup> (found) = 272.10.

**T<sub>15</sub>**

**<sup>1</sup>H NMR (400 MHz, CHLOROFORM-*d*) δ in ppm:** 0.73 - 0.89 (m, 3 H), 1.15 - 1.28 (m, 10 H), 1.49 - 1.65 (m, 2 H), 1.73 - 1.95 (m, 1 H), 2.08 - 2.33 (m, 2 H), 2.89 (dt, *J*=12.20, 5.95 Hz, 1 H), 3.14 - 3.23 (m, 1 H), 3.23 - 3.35 (m, 1 H), 4.38 - 4.51 (m, 1 H), 5.89 (br s, 1 H). **<sup>13</sup>C NMR (101 MHz, CHLOROFORM-*d*) δ in ppm:** 14.08, 22.63, 25.53, 27.60, 29.11, 29.22, 29.26, 31.80, 32.14, 36.43, 59.48, 173.69, 205.68. **API-MS:** [M+H]<sup>+</sup> (calc.) = 258.14, [M+H]<sup>+</sup> (found) = 258.10.

**T<sub>16</sub>**

**<sup>1</sup>H NMR (400 MHz, CHLOROFORM-*d*) δ in ppm:** 1.11 (t, *J*=7.15 Hz, 6 H), 2.85 - 3.05 (m, 2 H), 3.14 - 3.32 (m, 6 H), 4.37 (br dd, *J*=12.78, 6.79 Hz, 1 H), 5.00 (br s, 1 H). **<sup>13</sup>C NMR (101 MHz, CHLOROFORM-*d*) δ in ppm:** 1.02, 11.23, 13.61, 27.48, 33.19, 41.73, 42.17, 61.11, 156.75, 206.76. **API-MS:** [M+H]<sup>+</sup> (calc.) = 217.09, [M+H]<sup>+</sup> (found) = 217.05.

**5.1.9 Bacterial assay on Droplet Microarray**

The antibacterial screening was conducted according to the already published protocol<sup>[50]</sup>. In summary, on-chip synthesized compounds were released into the hydrophilic spots by dispensing 150 nL (1 mm<sup>2</sup>, square) deionized water into distinct droplets, followed by UV-A irradiation using a Biolink BLX UV chamber (Witec AG, Sursee, Switzerland) with 2.5 mW/cm<sup>2</sup> at 365 nm for 20 min and drying of the leftover solvent in vacuum. 150 nL (1 mm<sup>2</sup>, square) bacteria suspension of *Klebsiella pneumoniae* in MH medium with an OD<sub>600</sub> value = 0.001 were printed onto individual spots on the prepared DMA slide using a liquid dispenser of type I-DOT mini. After statical incubation of the slide at 37° C for 18 h 100 nL (1 mm<sup>2</sup>, square)

of Cell Counting KIT-8 solution was printed into individual droplets on DMA using I.DOT mini. After another hour of incubation, the slides were placed into a paper scanner to scan the slide using positive-film scan function to generate high-resolution pictures.

#### **5.1.10 Immobilization of Amino Acids**

##### **Deprotection of FAPL**

Deprotection of the surface attached FAPL was carried out by submerging the whole slide in a solution of 20 v% piperidine in DMF for 60 min. Afterwards, slides were rinsed with acetone and ethanol to remove excess reactants.

##### **Immobilization of Fmoc Protected Amino Acids to APL**

Fmoc protected Amino acids (**A1-A13**) were attached to the APL modified surface by adding in each spot (2.8 mm diameter, round) 5  $\mu$ L of a solution containing varying concentrations of the Fmoc protected amino acids (1 eq.), HOBt (1 eq.) and 10 v% DIC in NMP and let react for 18 h. Corresponding volume for the smaller pattern (1 mm<sup>2</sup>, square; 900  $\mu$ m diameter, round) was 150 nL. Subsequently, the DMA was rinsed with acetone and ethanol to remove excess reactants.

#### **5.1.11 Attachment of the Structural Motif OTV**

##### **Deprotection of Surface Attached Fmoc Amino Acids**

Deprotection of the surface attached Fmoc protected amino acids was carried out by submerging the whole slide in a solution of 20 v% piperidine in DMF for 60 min. Afterwards, slides were rinsed with acetone and ethanol to remove excess reactants.

##### **Modification of Surface Attached Deprotected Amino Acids with OTV**

3,4-Difluoro-2-(2-fluoro-4-iodophenylamino)benzoic acid (OTV) was attached to the amino acid modified surface by addition of 5  $\mu$ L of varying concentrations of OTV (1 eq.), HOBt (1 eq.) and 10 v% DIC in NMP to each spot (2.8 mm diameter, round). The slide was incubated for 18 h in the dark at room temperature. Subsequently, the slide was rinsed with acetone and ethanol and submerged in ethanol for 3 h to remove excess reactants.

#### **5.1.12 Solid-phase SUZUKI-MIYaura Reaction**

The solid-phase Suzuki-Miyaura was conducted according to the already published protocol<sup>[1]</sup>. In short, a 0.2 M solution of Na<sub>2</sub>PdCl<sub>4</sub> in H<sub>2</sub>O and a 0.2 M solution of dibenzyl diisopropylphosphoramidite in NMP were dispensed and incubated for 15 min at room temperature to form the precatalyst (1.5  $\mu$ L for 2.8 mm pattern, 40 nL for 900  $\mu$ m pattern). Subsequently, a solution containing 0.5 M boronic acid derivate (**B1-B25**) in NMP (3  $\mu$ L for 2.8



mm pattern, 80 nL for 900  $\mu\text{m}$  pattern) and saturated  $\text{Na}_2\text{CO}_3$  solution (2  $\mu\text{L}$  for 2.8 mm pattern, 40 nL for 900  $\mu\text{m}$  pattern) were added and the DMA was incubated in the dark at room temperature for 18 h. To prevent solvent evaporation during the incubation step, the printed slide was promptly transferred into a humidity-controlled Petri dish (Corning, USA). Subsequently, the slide in the Petri dish was allowed to incubate at room temperature for the specified reaction duration. The reactions were terminated by rinsing off the mixtures with acetone and ethanol before immersing the entire slide in a 0.1 M KCN solution in DMSO/water (1:1) for 3 h to eliminate precipitated palladium. The final washing step utilized only water and ethanol. Waste was collected separately and was treated with hydrogen peroxide and sodium hydroxide.

### 5.1.13 Synthesis of SMR1

Synthesis of intermediate **SMR1a**:

To 5-bromo-2-methyl benzoic acid (1.00 g, 4.65 mmol, 1.00 eq.) in methanol (30 mL) was added p-toluenesulfonic acid (44 mg, 0.23 mmol, 0.05 eq.) and the reaction mixture was refluxed under stirring for 18h. Then stirring was stopped and the solvent was removed under reduced pressure to get the crude product as a colorless liquid. It was purified by column chromatography using silica gel (mesh 60-120) as a stationary phase and cyclohexane/ethyl acetate (10:1, v/v) as eluent. After removing the solvent under reduced pressure, 756 mg (3.30 mmol, 71%) of a colorless liquid was obtained.

**$^1\text{H}$  NMR (500 MHz, CHLOROFORM- $d$ )  $\delta$  in ppm:** 2.57 (s, 3 H), 3.92 (s, 3 H), 7.15 (d,  $J=8.09$  Hz, 1 H), 7.54 (dd,  $J=8.16, 2.21$  Hz, 1 H), 8.07 (d,  $J=2.14$  Hz, 1 H).  **$^{13}\text{C}$  NMR (126 MHz, CHLOROFORM- $d$ )  $\delta$  in ppm:** 21.23, 52.12, 119.12, 131.18, 133.31, 133.36, 134.82, 139.20, 166.71.

Synthesis of intermediate **SMR1b**:

A solution of palladium(II) acetate (2 mg, 0.01 mmol, 0.01 eq.) and triphenylphosphine (16 mg, 0.06 mmol, 0.05 eq.) in 6 mL tetrahydrofuran/water (9:1, v/v) was stirred under an argon atmosphere for 10 min at room temperature. Then phenylboronic acid (160 mg, 1.31 mmol, 1.20 eq.), 26a (250 mg, 1.09 mmol, 1.00 eq.) and potassium carbonate (452 mg, 3.27 mmol, 3.00 eq.) were added to the solution and the reaction mixture was refluxed under argon atmosphere for 18h. Then stirring was stopped and the solvent was removed under reduced pressure to obtain the crude product. It was purified by column chromatography using silica gel (mesh 60-120) as a stationary phase and cyclohexane/ethyl acetate (10:1, v/v) as eluent. After

removing the solvent under reduced pressure, 185 mg (0.82 mmol, 82%) of a colorless liquid was obtained.

**<sup>1</sup>H NMR (500 MHz, CHLOROFORM-d)  $\delta$  in ppm:** 2.67 (s, 3 H), 3.95 (s, 3 H), 7.35 (d,  $J$ =7.93 Hz, 1 H), 7.36 - 7.41 (m, 1 H), 7.48 (t,  $J$ =7.20 Hz, 2 H), 7.61 - 7.68 (m, 3 H), 8.19 (d,  $J$ =1.98 Hz, 1 H). **<sup>13</sup>C NMR (126 MHz, CHLOROFORM-d)  $\delta$  in ppm:** 21.43, 51.94, 123.14, 126.97, 127.48, 128.86, 129.22, 130.44, 132.25, 144.93, 169.13, 170.13, 180.15, 191.62.

#### Synthesis of **SMR1**:

To a solution of 26b (185 mg, 0.82 mmol, 1.00 eq.) in 5 mL dichloromethane/methanol (9:1, v/v) was added a solution of sodium hydroxide (131 mg, 3.28 mmol, 4.00 eq.) in 5 ml methanol. The reaction mixture was stirred for 2 h at room temperature. The solvents were then removed under reduced pressure, the residue was diluted with water. The aqueous solution was then cooled, acidified to pH 2 with dilute hydrochloric acid. A white solid precipitated after the addition of the hydrochloric acid. The precipitate was isolated by filtration and redissolved in ethyl acetate. The solvent was removed under reduced pressure to obtain 133 mg (0.63 mmol, 77%) of a white powder.

**<sup>1</sup>H NMR (500 MHz, DMSO-d<sub>6</sub>)  $\delta$  in ppm:** 2.57 (s, 3 H), 7.37 - 7.43 (m, 2 H), 7.49 (t,  $J$ =7.71 Hz, 2 H), 7.68 (d,  $J$ =7.37 Hz, 2 H), 7.76 (dd,  $J$ =7.93, 2.14 Hz, 1 H), 8.08 (d,  $J$ =2.14 Hz, 1 H), 12.98 (br s, 1 H). **<sup>13</sup>C NMR (126 MHz, DMSO-d<sub>6</sub>)  $\delta$  in ppm:** 14.54, 21.36, 40.24, 40.41, 40.57, 51.50, 80.78, 97.35, 113.91, 126.98, 129.52, 130.23, 138.75, 196.72.

#### 5.1.14 Synthesis of MEK Inhibitors

##### Synthesis of **A<sub>2</sub>OTV**:

A solution containing 200 mg 3,4-difluoro-2-(2-fluoro-4-iodophenylamino)benzoic acid (0.5 mmol, 1.00 eq.) and 95 mg Alanine amide\*HCl (0.75 mmol, 1.50 eq.) were dissolved in 3 mL DMSO. 103 mg HOBt (0.75 mmol, 1.50 eq.), 146 mg EDC\*HCl (0.75 mmol, 1.50 eq.) and 168  $\mu$ L N-methylmorpholine (154 mg, 1.5 mmol, 3.00 eq.) were added and the mixture was stirred for 18 h at room temperature. The crude reaction mixture was poured over water to obtain 220 mg of the pure product as white powder (94 %).

**<sup>1</sup>H NMR (500 MHz, DMSO-d<sub>6</sub>)  $\delta$  in ppm:** 1.24 - 1.31 (m, 4 H), 4.16 - 4.36 (m, 1 H), 6.67 (td,  $J$ =8.74, 4.96 Hz, 1 H), 7.04 (s, 1 H), 7.14 - 7.26 (m, 1 H), 7.32 - 7.44 (m, 1 H), 7.45 (br s, 1 H), 7.59 (dd,  $J$ =10.68, 1.68 Hz, 1 H), 7.65 (t,  $J$ =7.39 Hz, 1 H), 8.72 (br d,  $J$ =7.17 Hz, 1 H) 9.09 (s, 1 H). **<sup>13</sup>C NMR (126 MHz, DMSO-d<sub>6</sub>)  $\delta$  in ppm:** 18.21, 49.24, 82.61, 110.31, 120.48, 122.95,

124.04, 124.13, 125.71, 131.66, 131.74, 133.65, 152.10, 153.08, 166.80, 174.43. **HRESI-MS:**  $[M+H]^+$  (calc.) = 464.007,  $[M+H]^+$  (found) = 464.008.

#### Synthesis of **A<sub>2</sub>B<sub>13</sub>**:

A solution of 0.5 mg Pd(OAc)<sub>2</sub> (0.002 mmol, 0.01 eq.) and 2.4 mg PPh<sub>3</sub> (0.009 mmol, 0.05 eq.) in 3 mL THF/H<sub>2</sub>O (9:1, v/v) was stirred for 10 min under argon atmosphere. 33.0 mg 4-chlorophenylboronic acid (0.208 mmol, 1.20 eq.), 80.0 mg A<sub>2</sub>OTV (0.173 mmol, 1.00 eq.) and 72.0 mg K<sub>2</sub>CO<sub>3</sub> (0.519 mmol, 3.00 eq.) were added carefully, afterwards the mixture was stirred under reflux for 16 h. The solvent was removed under reduced pressure and the crude was redissolved in ethyl acetate. The organic phase is washed with water and sodium bicarbonate solution, the aqueous phase is then back extracted with ethyl acetate and the combined organic layers are dried over sodium sulfate. The solvent is again removed under reduced pressure and the crude is purified via column chromatography using silica gel (mesh 60-120) as a stationary phase and DCM:MeOH (9:1, v/v) as eluent. After removing the solvent under reduced pressure, 19.2 mg (25%) of a white powder was obtained.

**<sup>1</sup>H-NMR (400 MHz, d<sub>6</sub>-Acetone) δ in ppm:** 9.35 (s, 1H, NHAr), 8.05 (d, 1H, CONH), 7.74-7.63 (m, 3H, HAr), 7.52-7.35 (m, 4H, HAr), 7.19-6.95 (m, 3H, NH<sub>2</sub>+HAr), 6.52-6.48 (m, 1H, HAr), 4.61 (quin., 1H, CHCH<sub>3</sub>), 1.42 (d, 3H, CH<sub>3</sub>). **<sup>13</sup>C-NMR (400 MHz, d<sub>6</sub>-Acetone) δ in ppm:** 173.85, 166.96, 166.94, 154.96, 154.03, 153.92, 152.54, 151.55, 151.43, 141.85, 141.71, 138.24, 133.50, 132.70, 130.58, 130.46, 128.87, 128.00, 124.70, 124.66, 122.40, 121.42, 113.44, 113.24, 109.20, 109.02, 49.00, 17.71. **HRESI-MS:**  $[M+H]^+$  (calc.) = 448.103,  $[M+H]^+$  (found) = 448.104.

#### Synthesis of **A<sub>2</sub>B<sub>16</sub>**:

A solution of 0.5 mg Pd(OAc)<sub>2</sub> (0.002 mmol, 0.01 eq.) and 2.4 mg PPh<sub>3</sub> (0.009 mmol, 0.05 eq.) in 3 mL THF/H<sub>2</sub>O (9:1, v/v) was stirred for 10 min under argon atmosphere. 37.0 mg 3,4,5-trifluorophenylboronic acid (0.208 mmol, 1.20 eq.), 80.0 mg A<sub>2</sub>OTV (0.173 mmol, 1.00 eq.) and 72.0 mg K<sub>2</sub>CO<sub>3</sub> (0.519 mmol, 3.00 eq.) were added carefully, afterwards the mixture was stirred under reflux for 16 h. The solvent was removed under reduced pressure and the crude was redissolved in ethyl acetate. The organic phase is washed with water and sodium bicarbonate solution, the aqueous phase is then back extracted with ethyl acetate and the combined organic layers are dried over sodium sulfate. The solvent is again removed under reduced pressure and the crude is purified via column chromatography using silica gel (mesh

60-120) as a stationary phase and DCM:MeOH (9:1, v/v) as eluent. After removing the solvent under reduced pressure, 24.2 mg (30%) of a white powder was obtained.

**<sup>1</sup>H NMR (400 MHz, acetone) δ in ppm:** 1.38 - 1.44 (m, 3 H), 4.52 - 4.67 (m, 1 H), 6.93 - 7.16 (m, 3 H), 7.39 - 7.46 (m, 2 H) 7.46 - 7.58 (m, 3 H) 7.66 - 7.77 (m, 1 H), 8.04 (br d, J=6.11 Hz, 1 H), 9.36 (br s, 1 H). **<sup>13</sup>C-NMR (400 MHz, d6-Acetone) δ in ppm:** 173.70, 166.83, 166.94, 154.96, 154.03, 153.92, 152.54, 151.55, 151.43, 141.85, 141.71, 138.24, 133.50, 132.70, 130.58, 130.46, 128.87, 128.00, 124.70, 124.60, 122.40, 121.42, 113.44, 113.24, 109.37, 109.02, 49.00, 17.71. **HRESI-MS:** [M+H]<sup>+</sup> (calc.) = 468.114, [M+H]<sup>+</sup> (found) = 468.114.

#### Synthesis of **A<sub>2</sub>B<sub>18</sub>**:

A solution of 0.5 mg Pd(OAc)<sub>2</sub> (0.002 mmol, 0.01 eq.) and 2.4 mg PPh<sub>3</sub> (0.009 mmol, 0.05 eq.) in 3 mL THF/H<sub>2</sub>O (9:1, v/v) was stirred for 10 min under argon atmosphere. 25.4 mg phenylboronic acid (0.208 mmol, 1.20 eq.), 80.0 mg A<sub>2</sub>OTV (0.173 mmol, 1.00 eq.) and 72.0 mg K<sub>2</sub>CO<sub>3</sub> (0.519 mmol, 3.00 eq.) were added carefully, afterwards the mixture was stirred under reflux for 16 h. The solvent was removed under reduced pressure and the crude was redissolved in ethyl acetate. The organic phase is washed with water and sodium bicarbonate solution, the aqueous phase is then back extracted with ethyl acetate and the combined organic layers are dried over sodium sulfate. The solvent is again removed under reduced pressure and the crude is purified via column chromatography using silica gel (mesh 60-120) as a stationary phase and DCM:MeOH (9:1, v/v) as eluent. After removing the solvent under reduced pressure, 45.7 mg (62%) of a white powder was obtained.

**<sup>1</sup>H NMR (400 MHz, DMSO-d<sub>6</sub>) δ in ppm:** 1.32 - 1.37 (m, 3 H), 4.35 - 4.44 (m, 1 H), 6.91 - 7.06 (m, 1 H), 7.09 (s, 1 H), 7.19 - 7.33 (m, 1 H), 7.37 - 7.53 (m, 5 H), 7.61 (dd, J=12.88, 2.00 Hz, 1 H), 7.68 - 7.76 (m, 3 H), 8.79 (d, J=7.25 Hz, 1 H), 9.25 (s, 1 H). **<sup>13</sup>C NMR (101 MHz, DMSO-d<sub>6</sub>) δ in ppm:** 174.21, 169.98, 154.82, 152.42, 139.13, 134.25, 130.38, 130.38, 129.4, 127.7, 126.67, 125.8, 125.8, 122.8, 122.49, 119.00, 113.87, 113.67, 109.93, 109.7, 49.26, 18.22. **HRESI-MS:** [M+H]<sup>+</sup> (calc.) = 414.142, [M+H]<sup>+</sup> (found) = 414.142.

#### Synthesis of **A<sub>2</sub>B<sub>21</sub>**:

A solution of 0.5 mg Pd(OAc)<sub>2</sub> (0.002 mmol, 0.01 eq.) and 2.4 mg PPh<sub>3</sub> (0.009 mmol, 0.05 eq.) in 3 mL THF/H<sub>2</sub>O (9:1, v/v) was stirred for 10 min under argon atmosphere. 35.0 mg 3,4-(methylenedioxy)phenylboronic acid (0.208 mmol, 1.20 eq.), 80.0 mg A<sub>2</sub>OTV (0.173 mmol, 1.00 eq.) and 72.0 mg K<sub>2</sub>CO<sub>3</sub> (0.519 mmol, 3.00 eq.) were added carefully, afterwards the mixture was stirred under reflux for 16 h. The solvent was removed under reduced pressure and

the crude was redissolved in ethyl acetate. The organic phase is washed with water and sodium bicarbonate solution, the aqueous phase is then back extracted with ethyl acetate and the combined organic layers are dried over sodium sulfate. The solvent is again removed under reduced pressure and the crude is purified via column chromatography using silica gel (mesh 60-120) as a stationary phase and DCM:MeOH (9:1, v/v) as eluent. After removing the solvent under reduced pressure, 10.9 mg (12%) of a white powder was obtained.

**<sup>1</sup>H-NMR (400 MHz, d<sub>6</sub>-Acetone) δ in ppm:** 9.32 (s, 1H, NHAr), 8.05 (d, 1H, CONH), 7.74-7.51 (m, 2H, HAr), 7.42-7.36 (m, 1H, HAr), 7.33-7.28 (m, 1H, HAr), 7.18-7.08 (m, 3H, HAr), 7.08-6.85 (m, 3H, NH<sub>2</sub>+HAr), 6.53-6.45 (m, 1H, HAr), 6.03 (s, 1H, CH<sub>2</sub>), 4.61 (quin., 1H, CHCH<sub>3</sub>), 1.42 (d, 3H, CH<sub>3</sub>). **<sup>13</sup>C-NMR (400 MHz, d<sub>6</sub>-Acetone) δ in ppm:** 173.87, 167.02, 169.99, 148.42, 147.21, 135.02, 134.95, 133.45, 131.85, 131.75, 128.62, 128.50, 124.68, 122.09, 119.98, 118.96, 113.27, 113.08, 108.89, 108.71, 108.46, 106.82, 101.33, 49.00, 17.71. **HRESI-MS:** [M+H]<sup>+</sup> (calc.) = 458.132, [M+H]<sup>+</sup> (found) = 458.132.

#### 5.1.15 Cell Based Assay on Droplet Microarray

HEMAcoEDMA slides were prepared according to the specified protocol. All 1.4 mm spots were initially modified with cysteamine and subsequently treated with potential MEK inhibitors. The modified slides underwent a thorough washing process with acetone and ethanol, followed by submersion in ethanol for 4 h. The slides were then transferred into 70% ethanol and dried under sterile conditions.

For the assay, 700 nL of medium (Dulbecco's modified eagle medium (DMEM) with DMSO at a ratio of 699:1, without phenol red, without fetal bovine serum (FBS), and with 1% penicillin/streptomycin (P/S) for sample spots as well as negative control), 350 nL of medium for the positive control, or 1000 nL of medium for the blank spots were dispensed. The slides were sealed in a petri dish containing 2 mL of PBS in the bottom and irradiated with UVA light for 40 min to achieve an assay concentration of 10 μM. Subsequently, 350 nL of control in medium (*mirdametinib*, 28.6 μM) was added to the positive control spots to attain a final PD concentration of 10 μM. A humidifying pad with 5 mL PBS was added to the lid, and the slides were incubated overnight at 37 °C. For cell printing, 300 nL of cell suspension (1.0 × 10<sup>6</sup> cells/mL, HT-29) in medium (DMEM, no phenol red, 30% FBS, 1% P/S) were dispensed onto every spot, excluding the blank spots, resulting in 300 cells per spot. The slide was incubated at 37 °C for 72 h. Afterward, 100 nL of a staining solution (990 μL PBS, 10 μL propidium iodide 10 mg/mL in water) was added to each spot, and the slide was further incubated at 37 °C

for 15 min. Finally, the slide was sealed in a 4-well plate with humidifying pads in the adjacent chambers and imaged through fluorescence microscopy.

#### **5.1.16 Cell Based Assay in 384-Well Plate**

For the assay, 15  $\mu\text{L}$  of the tested compounds, as well as positive controls in medium (DMEM/DMSO 699:1 (v/v), +10% FBS, +0.1% P/S) in different concentrations between 0.1 to 100  $\mu\text{M}$  were added to the respective well. Subsequently, 8000 cells in medium (DMEM, +10% FBS, +0.1% P/S) were added to each well containing compounds, yielding a total volume of 25  $\mu\text{L}$  per well. The plate was incubated at 37  $^{\circ}\text{C}$  for 72 h. Afterward, the plate was allowed to equilibrate to room temperature for 30 min. Subsequently, 25  $\mu\text{L}$  of CellTiter Glo reagent was added to each well, and the plate was incubated at room temperature for 10 min before being analyzed for luminescence using a CLARIOstar Plus plate reader.

#### **5.1.17 Solid-phase Heck Reaction**

0.2 M of palladium source and a 0.2 M solution of ligand, both in the respective solvent, were dispensed and incubated for 15 min at room temperature to form the precatalyst (1.5  $\mu\text{L}$  for 2.8 mm pattern). Subsequently, a solution containing 0.5 M alkene derivate (3  $\mu\text{L}$  for 2.8 mm pattern) and 0.3 M solution of the respective base in solution (2  $\mu\text{L}$  for 2.8 mm pattern) were added and the DMA was incubated in the dark at the specified temperature for 18 h. To prevent solvent evaporation during the incubation step, the printed slide was promptly transferred into a humidity-controlled Petri dish (Corning, USA). Subsequently, the slide in the Petri dish was allowed to incubate at the specified temperature for the specified reaction duration. The reactions were terminated by rinsing off the mixtures with acetone and ethanol before immersing the entire slide in a 0.1 M KCN solution in DMSO/water (1:1) for 3 h to eliminate precipitated palladium. The final washing step utilized only water and ethanol. Waste was collected separately and was treated with hydrogen peroxide and sodium hydroxide.

#### **5.1.18 Cleavage from the Surface**

To release the compounds from the polymer layer for analysis, the hydrophilic spots (round,  $d = 2.8\text{ mm}$ ) were filled with 5  $\mu\text{L}$  deionized water and irradiated with UV light at 365 nm in a Biolink BLX UV chamber (Witec AG, Sursee, Switzerland) with 2.5  $\text{mW}/\text{cm}^2$  for 20 minutes. The solution was then pipetted off the surface and each spot was filled with additional 5  $\mu\text{L}$  of DMF to dissolve all cleavage products from the polymer layer. The water and DMF were combined and analyzed via LC-MS. For the smaller spot sizes (1  $\text{mm}^2$ , square; 900  $\mu\text{m}$  diameter, round) 100 nL of water was dispensed in every spot.

### 5.1.19 Analytical Methods

#### MALDI-TOF-MS Measurements

On-chip MALDI-TOF MSI measurements were performed on a timsTOF fleX (Bruker Daltonics GmbH, Bremen, Germany) in negative and positive ion mode with a lateral step size and laser spot size of 100  $\mu\text{m}$  each, 400 laser shots per pixel and a repetition rate of 10,000 Hz, with a laser intensity of 75%. The ‘focus pre TOF’ parameters ‘prepulse storage’ and ‘transfer time’ were set to 10  $\mu\text{s}$  and 110  $\mu\text{s}$ , respectively. The collision cell RF was set to 25000.0 Vpp, with a collision cell energy offset of -10 V. Funnel 0 RF was set to 200 Vpp and Funnel 1 Rf to 350 Vpp. Prior to MSI data acquisition, external mass calibration was performed via the electrospray ionization source using ESI-Low Concentration Tuning Mix (Agilent Technologies, Santa Clara, USA) and an enhanced quadratic calibration model.

Ground steel plate MALDI-TOF-MS measurements were performed on a RapifleX MALDI-TOF system (Bruker Daltonics GmbH, Bremen, Germany). The tested compounds were transferred onto a MTP 384 ground steel MALDI target plate (Bruker Daltonics GmbH, Bremen, Germany). NEDC matrix (7 mg/mL NEDC in 70% methanol:H<sub>2</sub>O (v:v)) or DHB matrix (20 mg/mL DHB in acetonitrile/water/TFA 1:1:0.05 (v/v/v)) was sprayed onto the target plate using an HTX M5 sprayer (HTX Tech., Chapel Hill, NC, USA). Mass spectra were recorded in reflector negative or positive ion mode covering a mass range of  $m/z$  250 to  $m/z$  1000. The laser power was set to 40% with a repetition rate of 10 kHz. The laser field size was set to 104  $\mu\text{m}$  (Smartbeam M5 defocus in ‘MS dried droplet’ mode). For each spot, 4000 shots were accumulated using ‘random walk’ with 50 laser shots per raster spot. Mass calibration was performed using clusters of red phosphorus by a quadratic correction.

MS/MS was performed on a solariX 7T XR Fourier transform Ion Cyclotron Resonance (FT-ICR) mass spectrometer (Bruker Daltonics GmbH, Bremen, Germany) with a smartbeam II 2 kHz laser using ftms control 2.3.0 software. Mass spectra were acquired in negative ion mode using ‘single MS mode’ over a  $m/z$  range from 100-1200, accumulating 100 shots with a laser intensity of 30% and a frequency of 2000 Hz, with a mass resolution at  $m/z$  400 of approximately 150000. The isolation window of the target masses was set to  $\pm 3$  Da.

#### LC-MS

LCMS measurements were performed on an Agilent 1260 Infinity II system consisting of a quaternary pump (GB7111B;), autosampler (G7129A, 100  $\mu\text{L}$  sample loop), a temperature-controlled column oven (G7114A) and a variable UV–vis detector (G7114 A, VWD, flow cell G7114A 018,  $d = 10$  mm,  $V = 14$   $\mu\text{L}$ ). Separation was performed on a C18 HPLC-column

(Agilent Poroshell 120 EC-C18 4,6×100 mm, 2,7 μm) operating at 40 °C. A gradient of ACN:H<sub>2</sub>O 10:90 – 80:20 v/v (additive 10 mmol L<sup>-1</sup> NH<sub>4</sub>CH<sub>3</sub>CO<sub>2</sub>) at a flow rate of 1 mL·min<sup>-1</sup> during 15 min was used as the eluting solvent. The flow was directed into an Agilent MSD (G6136BA, AP-ESI ion source). The instrument was calibrated in the m/z range 118–2121 in the positive mode and 113–2233 in the negative using a premixed calibration solution (Agilent). The following parameters were used: spray chamber flow: 12 L min<sup>-1</sup>; drying gas temperature: 350 K, Capillary Voltage: 3000 V, Fragmentor Voltage: 100 V. Spectra were analyzed via “Spectrum Processor” software (Advanced Chemistry Development Inc., Toronto, Canada).

### NMR

<sup>1</sup>H and <sup>13</sup>C nuclear magnetic resonance (NMR) spectra of the synthesized molecules were either recorded on a Bruker Avance III HD 500 MHz (500 and 126 MHz, respectively) or a Bruker Ascend 400 (400 and 101 MHz, respectively) at room temperature. The peak shifts were declared in parts per million (ppm). The solvent peak served as a reference. For multiplets, the signal area was declared, for centrosymmetric signals, the center of the signal was declared. The description of the proton splitting occurred by using the abbreviations s for singlet, d for doublet, t for triplet, q for quartet and m for multiplet.

### Fluorescence Microscopy

Automated fluorescence microscopy of stained cells was performed with a Leica Thunder 3D Imager (Leica Microsystems, Germany).

### Digital Microscope

Digital microscope images of the droplets and dried NEDC matrix on-chip were taken with a KEYENCE VHX 7000 from top or with different angles.

### Document Scanner

Images of the Droplet Microarray were taken with a document scanner CanoScan 8800F from CANON Deutschland GmbH (Krefeld, Germany) at 70% exposure. The images are shown in the figures without any color modification.

### Image Analysis

#### ImageJ

Automated cell counting was performed using ImageJ's macro-based batch processing tool.



**Image analysis for color depth**

The color depth of each droplet was analyzed using MATLAB R2020b using a program provided by Prof. MARKUS REISCHL.

**Ion images**

Ion images obtained via MALDI-TOF-MS imaging were created with SCiLS Lab (Bruker, USA).

Graphics throughout the thesis were partially created with BioRender.com.

## 6 List of Abbreviations

°C	degrees Celsius
μ	micro (10 <sup>-6</sup> )
4-DMAP	4-dimethylaminopyridine
ATP	adenosine triphosphate
CCK-8	Cell Counting Kit-8
DCM	dichloromethane
DDP	dibenzyl- <i>N,N</i> -diisopropyl-phosphoramidite
DESI	desorption electrospray ionization
DHB	2,5-dihydroxybenzoic acid
DIC	<i>N,N'</i> -diisopropylcarbodiimide
DMA	Droplet Microarray
DMAc	dimethylacetamide
DMEM	Dulbecco's modified eagle medium
DMF	dimethyl formamide
DMPAP	2,2-dimethoxy-2-phenylacetophenone
DMSO	dimethyl sulfoxide
EDMA	ethylene dimethacrylate
EGFR	epidermal growth factor receptor
FAPL	Fmoc-amino photolinker
FBS	fetal bovine serum
FDA	Food and Drug Administration
GBL	γ-butyrolactone
h	hour
HCl	hydrochloric acid

HEMA	2-hydroxyethyl methacrylate
HEPL	hydroxyethyl photolinker
HL	hydrophilic
HOBt	1-hydroxybenzotriazole
HPLC	High Performance/Pressure Liquid Chromatography
HT	High-Throughput
HTS	high-throughput screening
ITO	indium tin oxide
KCN	potassium cyanide
Kp	Klebsiella pneumoniae
LC-MS	liquid chromatography mass spectrometry
LLE	Liquid-Liquid Extraction
MALDI	matrix-assisted laser desorption/ionization
MAPKs	Mitogen-activated protein kinases
MeCN	acetonitrile
MeOH	methanol
MIC	minimum inhibitory concentration
min	minute
MISER	multiple injections in a single experiment run
MS	mass spectrometry
mW	milli watts
n	nano ( $10^{-9}$ )
NaOH	sodium hydroxide
NEDC	<i>N</i> -(1-Naphthyl)ethylenediamine hydrochloride
NMP	N-methyl-2-pyrrolidone

NMR	Nuclear Magnetic Resonance
OBOC	one bead one compound
OTV	3,4-difluoro-2-(2-fluoro-4-iodophenylamino)benzoic acid
P/S	penicillin/streptomycin
PDS	2-pyridyl disulfide
PFDT	1 <i>H</i> ,1 <i>H</i> ,2 <i>H</i> ,2 <i>H</i> -perfluorodecanthiol
PI	propidium iodide
PROTACs	proteolysis targeting chimeras
s	second
SAMDI	self-assembled monolayer desorption ionization
SML	synthetic molecule libraries
SMR	SUZUKI-MIYAUURA reaction
SPS	solid-phase synthesis
t	time
TADE	thiolactone aminolysis-disulfide exchange
TFA	trifluoroacetic acid
TOF	time of flight
UPLC	ultra-performance liquid-chromatography
UV	ultraviolet
Vis	visible

## 7 List of Figures

- Figure 1: Schematic depiction of different contact angle scenarios. (a) Contact angle of a liquid on an ideal surface. (b) Contact angle described by WENZEL, including the surface roughness increasing the overall wetted area. (c) Contact angle described by CASSIE and BAXTER. Surface cavities are partially occupied by trapped air..... 6
- Figure 2: Image of a Droplet Microarray containing 672 square spots containing water. The spots have an edge length of 1 mm. .... 8
- Figure 3: Schematic representation of the surface modifications involved in the manufacturing of the HEMAcOEDMA DMA. (a) Covalent attachment of 3-(trimethoxysilyl)propyl methacrylate which serves as an anchor point for the subsequent steps. (b) Photoinduced radical polymerization of nanoporous HEMAcOEDMA polymer. (c) Introduction of alkyne groups to the surface via STEGLICH esterification using 4-pentynoic acid. (d) Surface patterning through UV induced thiol-yne click chemistry using PFDT and cysteamine..... 9
- Figure 4: Schematic representation of the creation of the dendritic structure on DMA. R represents the immobilized silane on the glass substrate. The dendrons are synthesized by alternating the UV induced thiol-ene reaction using thioglycerol with Steglich esterification using 4-pentenoic acid..... 10
- Figure 5: Application of the Dendrimer DMA for the solid-phase synthesis of lipid-like compounds. (a) Schematic representation of the experimental setup. Amine solutions are applied on DMA A in a column-wise manner, while thiolactone/2-pyridyl disulfide mixtures are applied in row-wise manner on DMA B. (b) Sandwiching of the slides leads to merging of the droplets, thus the start of the reaction. After 2 h of reaction time, the slides were detached from another, yielding the synthesized library of lipid-like compounds. (c) Schematic depiction of the mechanism of the used TADE reaction. The driving force of the reaction is the pyridine-2(1H)thione that prevents the reverse reaction..... 13
- Figure 6: Overview reaction of the solid-phase synthesis of tripeptides on HEMAcOEDMA DMA. Starting with the immobilization of amino acids to the surface bound photolinker via Steglich esterification (i), followed by the standard solid-phase peptide synthesis containing deprotection of the immobilized amino acid (ii), coupling of the next amino acid (iii). These steps will be repeated (iv-vi) until the respective tripeptide is formed. .... 14
- Figure 7: Generalized mechanism of the UV induced cleavage of the photolinker utilized for solid-phase synthesis on DMA.<sup>[63]</sup> Hydrophilic spots on the HEMAcOEDMA DMA serve as solid-support. .... 15
- Figure 8: Generalized mechanism of the Ugi four-component reaction. The reaction is initiated with the formation of an imine, which is subsequently protonated by a carboxylic acid. Following this, the isocyanide is added to the protonated imine. Further addition of the carboxylic acid results in the formation of an imidate. It's important to note that all reaction steps in this sequence are reversible up to the point of the Mumm rearrangement. The Mumm rearrangement then occurs, yielding the bisamide product.<sup>[65]</sup> ..... 16

- Figure 9: Scheme showing a generalized workflow using the DMA platform. Covalent immobilization of a photolabile linker in the hydrophilic (HL) spots forms the anchor for the solid phase combinatorial synthesis. Synthesized compounds can be released by UV irradiation at 365 nm into distinct nanodroplets formed in the hydrophilic spots to be either screened in biological assays or analyzed, e.g., via MALDI-TOF mass spectrometry. .... 21
- Figure 10: Scheme of the synthetic sequence for the on-chip high-throughput synthesis of a chemical library of antimicrobial compounds: i) Ugi four-component reaction with surface anchored succinic acid, 4-pentenal, variable entries for surface-anchored amines  $A_x$  and isocyanides  $I_x$ . ii) Thiol-ene reaction to introduce an amine functionality. iii) Three component thiolactone-disulfide reaction, followed by UV induced cleavage from the surface to yield the desired lipid-like product, variable entries for 2-pyridyl disulfide derivatives  $P_x$  and thiolactone derivatives  $T_y$ . Representation of the solid-phase chemistry: UV-cleavable linker (hydroxyethyl photolinker, HEPL) is covalently immobilized in the hydrophilic spots of the DMA, forming the anchor of the solid-phase combinatorial synthesis. .... 22
- Figure 11: Workflow for the synthesis of library of lipid-like molecules on DMA via a sequence of a) covalent attachment of the hydroxyethyl photolinker (HEPL) to the HL spots as an anchor for the solid phase synthesis, b) immobilization of succinic acid to introduce a surface bound carboxylic acid, c) four component Ugi reaction with variable entries for amines  $A_x$  and isocyanides  $I_x$ , d) Thiol-ene click reaction to convert the vinyl moiety into an amine functionality, e) three component TADE reaction with variable entries for homocysteine thiolactone derivatives  $T_x$  and 2,2'-pyridyl disulfide derivatives  $P_x$ . .... 23
- Figure 12: Scheme of the four component Ugi reaction between the surface bound succinic acid, amine  $A_x$ , isocyanide  $I_x$  and 4-pentenal. .... 24
- Figure 13: Conversion of the vinyl group of the Ugi headgroup to a primary amine using the thiol-ene reaction. Cysteamine is employed as a simple combination of thiol and amine. .... 26
- Figure 14: (a) Ugi product  $A_4I_2$  (blue asterisk) was synthesized on the photolinker and the UV induced thiol-ene reaction was carried out by applying a solution of 25 wt% cysteaminium chloride and 1 wt% DMPAP in MeOH to each HL spot to form the thioether (red asterisk). Irradiation wavelength was 254 nm with varied irradiation time. (b) Fraction of the product peak from the summarized peak areas of the starting material (blue asterisk) and product (red asterisk) plotted against the irradiation time. Longer irradiation times increased the conversion of the Ugi product to the thioether. Peak areas were determined by spectroscopic analysis of the solutions at 220 nm using a LC/MS system. (c) Overlay of LC/MS chromatograms at 220 nm after different irradiation times during the thiol-ene reaction of compound  $A_4I_2$ . Asterisks indicate corresponding structures. .... 28
- Figure 15: TADE reaction and subsequent UV induced cleavage from the surface to yield the desired lipid-like compound with four tunable moieties  $A_x$ ,  $I_x$ ,  $T_x$  and  $P_x$ . .... 29
- Figure 16: Chromatograms at 254 nm of the released compounds after every step of the synthesis (left) and the corresponding structures of the synthesized compounds (right). (a) after Ugi reaction forming Ugi product  $A_7I_4$  indicated by the green

asterisk, (b) after the formation of the thioether via UV induced thiol-ene reaction denoted by the orange asterisk and (c) after aminolysis of the thiolactone and disulfide exchange yielding compound A<sub>7</sub>I<sub>4</sub>P<sub>1</sub>T<sub>4</sub> highlighted by the red asterisk. The blue asterisk indicates the main side product. .... 32

Figure 17: (a) Overlay of LC-MS chromatograms at 254 nm of compound A<sub>7</sub>I<sub>4</sub>P<sub>1</sub>T<sub>4</sub> after different UV irradiation times. Only the respective product peak is shown. (b) 3D waterfall plot of the chromatograms at 254 nm after different irradiation times of compound A<sub>7</sub>I<sub>4</sub>P<sub>1</sub>T<sub>4</sub>. .... 33

Figure 18: (a) Schematic workflow of the combinatorial synthesis followed by the droplet transfer to the ground steel target plate for MALDI-TOF-MS analysis. Each color represents a different compound. Rows D and E on the ground steel plate represent DHB and NEDC to acquire background spectra. (b) Representative MALDI-MS spectra of compound A<sub>7</sub>I<sub>4</sub>P<sub>4</sub>T<sub>1</sub> acquired in positive mode (left) using DHB as matrix and in negative mode (right) using NEDC as matrix. Asterisks indicate the corresponding structures. .... 37

Figure 19: (a) Schematic workflow for the preparation of the ITO-DMA for MALDI-MS measurements: after the synthesis of the lipid-like compounds, water is applied in each hydrophilic spot. i) The DMA is irradiated with UV light at 365 nm for 20 minutes to release the compounds into distinct droplets. ii) Corresponding MALDI-matrix solution is dispensed onto the respective spots and the slide is dried in vacuum before being handed over to MALDI-TOF analysis. (b) MALDI-TOF-MS imaging of an ITO-DMA modified with round 900 µm spots in which the solid-phase synthesis of A<sub>7</sub>I<sub>4</sub>P<sub>4</sub>T<sub>1</sub> was carried out. Measurement was conducted in positive mode. Different amounts of DHB were dispensed in triplicates (top to bottom), ranging from 22 nmol (left) to 44 nmol (right) per spot. Orange color indicates the intensity of the [M+H]<sup>+</sup> ion. (c) Microscopic pictures of dried DHB on a hydrophilic spot (900 µm, round) on ITO-DMA. DMF was used as the solvent. . 39

Figure 20: Comparison between the MALDI-MS spectra of compound A<sub>7</sub>I<sub>4</sub>P<sub>1</sub>T<sub>4</sub> obtained from ground steel target plate after droplet transfer from DMA (top) and directly from ITO-DMA (bottom, average spectrum of the spot) in (a) positive mode using DHB as matrix and (b) negative mode using NEDC as matrix. Colored bands mark the corresponding [M+H]<sup>+</sup> (red, green) and the [M+Na]<sup>+</sup> adduct (grey), as well as the isotopic pattern. .... 40

Figure 21: (a) MALDI-TOF-MS imaging of an ITO-DMA modified with round 900 µm spots. Only DHB was dispensed in the most left column. Second left column was left blank, while the 6 exemplary compounds of the 128 membered library have been synthesized in duplicates in the two columns on the right. Each color represents one compound and the respective structures are shown in the table. Color depth represent the intensity of the [M+H]<sup>+</sup> adduct. (b) and (c) show exemplary mass spectra obtained from on-chip MALDI-TOF-MS. Compounds were identified by their [M+H]<sup>+</sup> (red asterisk), [M+Na]<sup>+</sup> and [M+K]<sup>+</sup> adducts. .... 43

Figure 22: Schematic representation of the workflow of the biological assay on DMA. .... 45

Figure 23: Formation of the orange-colored WST-8 formazan. (a) Schematic of the reduction of WST-8 to orange-color WST-8 formazan in presence of electron carrier 1-mPMS (b) Reduction of the electron carrier by the dehydrogenase in living bacteria. .... 46

- Figure 24: Viability of the assay. (a) Layout of the preliminary experiments to validate the screening conditions on polymer-based DMA. Colors represent negative and positive controls, as well as blanks. Numbers represent the final concentration of colistin sulfate in a 150 nL droplet per spot. (b) Scanned image of stained droplets containing Kp incubated overnight on DMA with square spots with an edge length of 1 mm. Previous shown layout was employed. .... 47
- Figure 25: Evaluation of the viability test. (a) with cleaved HEPL (b) without cleaved HEPL ..... 49
- Figure 26: Screening for antibacterial activity of 128 lipid-like compounds. (a) Layout of the slide. Compounds have been randomly distributed across the DMA. Colistin served as positive control in eight randomly placed repetitions. Leftover spots were filled up negative controls and blanks. (b) Scanned image of stained droplets containing Kp incubated overnight on DMA with square spots with an edge length of 1 mm. Previous shown layout was employed..... 50
- Figure 27: Results of the screening for antibacterial activity of 128 compounds against Kp. The first three entries in each plot correspond to blank, negative control (neg), and positive control (pos). Each data point is the average of three measurements. Error bars represent standard deviations..... 51
- Figure 28: Synthetic route to decrease the steps in the synthesis of lipid-like compounds on DMA. (a) Four component UGI reaction to introduce the reactive 2-pyridyl disulfide moiety to the surface. (b) TADE reaction including a primary amine, a thiolactone derivative and the immobilized PDS derivative to form the lipid-like compounds. Utilizing this approach only needs two steps to synthesize the final compound, while still having four different moieties for diversification. .... 52
- Figure 29: (a) Exemplary reaction to form the reactive intermediate  $I_6Al_2P_8$  utilizing a solid-phase approach. Exemplary chromatograms of synthesized reactive intermediates (b)  $I_6Al_2P_8$  and (c)  $I_6Al_2P_7$  at 254 nm. Asterisk indicate the product peak..... 53
- Figure 30: (a) Exemplary TADE reaction to form the lipid like compound  $I_6Al_2P_8A_6T_4$ . (b) Representative chromatogram at 254 nm of the synthesized lipid like compound. (c) Overview of the purities of exemplary lipid like compounds synthesized via two-step approach. <sup>[a]</sup>Purity was calculated as the fraction of the product's peak integral with respect to the sum of integrals of all peaks at 254 nm absorbance. <sup>[b]</sup>Purity was calculated using the total ion chromatogram (TIC). <sup>[c]</sup>unsuccessful synthesized compounds were excluded. .... 55
- Figure 31: Formation of the dimer of the reactive intermediate during the TADE reaction as the major side-product of the synthetic cascade. i) TADE reaction ii) UV induced release from the surface..... 55
- Figure 32: General workflow to obtain a 800 membered library of biphenyls in nanoliter scale using the Suzuki-Miyaura reaction. (a) Immobilization of the photolinker to the hydrophilic spots. HEPL or FAPL, HOBt, DIC in NMP. (b) Binding of different aryl halides to the surface anchored photolinker: carboxylic acid, DIC, 4-DMAP in NMP. (c) SMR with variable boronic acids: aryl boronic acid,  $Na_2CO_3$ ,  $Na_2PdCl_4$ , dibenzyl diisopropylphosphoramidite in NMP/H<sub>2</sub>O (9:1). (d) UV induced cleavage



of the desired biphenylic compound into distinct droplets: 365 nm, 2.5 mW/cm<sup>2</sup> for 20 minutes in H<sub>2</sub>O. The image is used from the joint publication<sup>[1]</sup>..... 57

Figure 33: (a) Schematic representation of the synthetic pathway for the production of biphenyl XX on DMA for the evaluation of UV-induced photorelease kinetics: i) Immobilization of HEPL onto hydrophilic spots on DMA. ii) covalent attachment of 5-bromo-2-methyl benzoic acid to the immobilized photolinker. iii) Solid-phase SMR employing phenylboronic acid. iv) UV induced cleavage from the surface leading to the formation of the target biphenylic compound SMR1. (b) Analysis of UV-triggered release kinetics of XX into 5  $\mu$ L droplets following various irradiation durations. Determination carried out through spectroscopic examination of solutions at 280 nm using an LC/MS system. Each data point is an average derived from three measurements, and error bars denote standard deviation. (c) Depiction of HEMAcOEDMA DMA with 2.8 mm round spots before (top, filled with 5  $\mu$ L H<sub>2</sub>O) and after (bottom) UV-induced cleavage. The emergence of a yellow color signifies the occurrence of cleavage. The figure has been adapted from Höpfner et al.<sup>[1]</sup> ... 59

Figure 34: (a) Schematic illustration of the synthetic route employed for the formation of biphenylic compound XX: i) Solid-phase SMR utilizing immobilized 4-bromophenylacetic acid and phenylboronic acid. ii) UV induced cleavage from the surface, resulting in the production of the desired biphenylic compound SMR2. (b) UV chromatogram recorded at 254 nm. Post-irradiation, the volume of five spots with a diameter of 2.8 mm (50  $\mu$ L in total) was extracted from the surface and analyzed via LC-MS. The red asterisk denotes the corresponding peak. (c) UV chromatogram at 254 nm. Following irradiation, a cumulative volume of 50  $\mu$ L was collected from all HL spots and subsequently analyzed using LC-MS. The red asterisk highlights the associated peak. This figure has been adapted from<sup>[1]</sup>..... 61

Figure 35: Schematic representation of the ERK-signaling cascade, starting with the activation of RAS through EGFR. This activation triggers a sequence of events, including the phosphorylation of RAF, MEK, and ERK, ultimately influencing transcription processes..... 63

Figure 36: Structures of FDA approved MEK inhibitors trametinib, selumetinib, binimetinib and cobimetinib. .... 65

Figure 37: Structures of FDA approved MEK inhibitor cobimetinib, along with clinical trial MEK inhibitors mirdametinib and RO4987655. Core structure 3,4-Difluoro-2-(2-fluoro-4-iodophenylamino)benzoic acid is presented on the right, with red rectangles indicating potential moieties for diversification. .... 66

Figure 38: Scheme of the synthetic cascade for the on-chip solid-phase high-throughput synthesis of potential MEK inhibitors using the HL spots of the DMA. The usage of 13 amino acids (A<sub>1</sub>-A<sub>13</sub>) and 25 boronic acid derivatives (B<sub>1</sub>-B<sub>25</sub>) leads to the formation of a 325 membered library of novel compounds. i) Immobilization of the photocleavable linker to the HL spots. ii) Attachment of Fmoc-protected amino acids through amide coupling follows by Fmoc deprotection. iii) Coupling of the core structure motif (3,4-difluoro-2-((2-fluoro-4-iodophenyl)amino)benzoic acid to the free amines of the surface bound amino acids. iv) Solid-phase SMR to modify the iodo-aniline fragment. v) UV induced cleavage of the target compounds..... 67

- Figure 39: (a) Schematic depiction of the synthetic steps involved in the (i) immobilization of Fmoc-A<sub>2</sub> to the photolinker modified surface and (ii) subsequent UV induced release as Fmoc-A<sub>2</sub>-NH<sub>2</sub> from the surface. (b) Amount of released Fmoc-A<sub>2</sub>-NH<sub>2</sub> in relation to the irradiation time with UV light at 365 nm, determined via LC-MS. The release reaches a plateau after more than 30 min of UV irradiation. (c) Calibration curve of Fmoc-alanine at 254 nm with linear fit (red). A dilution series of Fmoc-alanine was prepared and absorbance of every was measured for its absorbance at 254 nm. .... 70
- Figure 40: (a) Schematic representation of the synthesis of the amino-acid intermediate. Immobilization and subsequent deprotection of FAPL to the surface (i) is followed by modification of the linker with an Fmoc protected amino acid. Subsequent deprotection yields the reactive amino acid modified surface (ii). Application of the coupling solution containing the core structural motif OTV leads to the formation of the amino acid intermediate (iii). UV induced cleavage from the surface releases the amino acid-intermediate into distinct droplets (iv). (b) Purity of eight exemplary amino-acid intermediates after UV induced release from the surface. Purity was measured as percentage of the product's integral divided by the total integration value of the HPLC chromatogram at 254 nm. Error bars represent standard deviation between two independent repetitions. (c) Representative chromatogram of amino acid intermediate A<sub>1</sub>OTV. The corresponding product peak is highlighted with the blue asterisk. .... 71
- Figure 41: (a) Schematic representation of the conversion of the amino-acid intermediate's iodine utilizing the SMR, with subsequent UV induced cleavage from the surface. Representative chromatograms at 254 nm for final compound (b) A<sub>4</sub>B<sub>5</sub> and (c) A<sub>12</sub>B<sub>18</sub>. Red asterisk highlights the corresponding product peak in the chromatogram. .... 72
- Figure 42: (a) Reaction Scheme for the preparation of compounds A<sub>2</sub>OTV and A<sub>2</sub>B<sub>18</sub> through solid-phase cascade synthesis. (i) Modification of the linker with Fmoc-A<sub>2</sub> and subsequent deprotection. (ii) Immobilization of OTV to the reactive amino acid. (iii) UV induced release of amino acid intermediate A<sub>2</sub>OTV. (iv) Solid-phase SMR with boronic acid B<sub>18</sub> and (v) subsequent cleavage from the surface to yield A<sub>2</sub>B<sub>18</sub>. (b) Released amount of A<sub>2</sub>OTV after 40 min of UV treatment for different concentrations of photolinker-modification solutions. The corresponding assay concentration of A<sub>2</sub>B<sub>18</sub> was calculated for a 1 µL solution, with an 85% yield in the Suzuki-Coupling step. Each value represents the average of three repetitions, and error bars indicate the standard deviation. (c) Released amount of A<sub>2</sub>OTV after different irradiation times for two concentrations of photolinker-modification solutions and the respective assay concentration of A<sub>2</sub>B<sub>18</sub> calculated for 1 µL solution and a yield in the Suzuki-Coupling step of 86 %. Each value represents the average of three repetitions, and error bars indicate the standard deviation. .... 75
- Figure 43: Representative MALDI-MS spectra of compound (a) A<sub>1</sub>B<sub>14</sub> and (b) A<sub>5</sub>B<sub>6</sub> acquired on a ground steel target plate in negative mode using NEDC as matrix. Compounds were synthesized on 1.4 mm spots and the cleavage solution was transferred to the plate. Asterisks indicate the corresponding structures. (c) MALDI-TOF-MS imaging of an ITO-DMA modified with 900 µm spots in which the synthetic cascade was carried out. Colors indicate the intensity of the [M-H]<sup>-</sup> ion for seven different chemical formulas. Target structures with the corresponding color of their [M-H]<sup>-</sup> peak are given on the right. .... 77

- Figure 44: Workflow of the on-chip screening of MEK inhibitors for anti-cancer activity. (1) Solid-phase synthesis of MEK inhibitors on DMA, followed by UV release of the compounds into distinct droplets. (2) Addition of 300 cells per spot using Certus Flex by Gyger and subsequent incubation of the DMA for 72 h at 37 °C. (3) Addition of PI staining solution to each droplet. After 15 min of incubation the DMA was imaged through fluorescence microscopy. .... 81
- Figure 45: Results of the on-chip screening for anti-cancer activity of 300 novel compounds. Graphs present the number of dead cells per spot for each compound. Each bar represents the average of three repetitions. Error bars indicate the standard deviation. Red bars indicate the number of dead cells in the positive control spots, green bars the number of dead cells in negative control spots. (a) Increase of dead cells per spot in respect to the positive control for compounds 26 – 75. (b – d) Relatively low anti-cancer activity for compounds 76-300. .... 83
- Figure 46: (a) Overview of the normalized cell death for all 325 compounds. Compounds 26 – 75 show substantial increase in anti-cancer activity, reaching a maximum of over three-fold activity compared to the positive control. (b) Magnification of the most active compounds. (c) Comparison of the initial on-chip screening data of compounds 26 – 75 with a reproduction of the screening. General increase of anti-cancer activity of amino acids A<sub>2</sub> and A<sub>3</sub> could be reproduced, while the effects of the boronic acid derivatives B<sub>1</sub>-B<sub>25</sub> differed from the initial screening. Each bar represents the average of three repetitions. Values were normalized to the difference of positive and negative control. Error bars indicate the standard deviation. .... 84
- Figure 47: (a) Structures of the synthesized compounds that showed high anti-cancer activity in the on-chip screening (A<sub>2</sub>B<sub>13</sub>, A<sub>2</sub>B<sub>16</sub>, A<sub>2</sub>B<sub>21</sub>) and the amino acid-intermediate A<sub>2</sub>OTV. (b) Schematic representation of the CELLTITER-GLO assay. Firefly luciferase consumes ATP in the presence of luciferin, oxygen and magnesium (II) to emit light. ATP is an indicator of metabolically active cells. .... 85
- Figure 48: Normalized luminescence of the CellTiter-Glo assay of compound (a) A<sub>2</sub>B<sub>13</sub>, (b) A<sub>2</sub>B<sub>21</sub> (c) amino acid-intermediate A<sub>2</sub>OTV and (d) the positive control mirdametinib. All compounds were measured in a concentration range between 0.1 and 100 µM. Each data point is the average of three repetitions, error bars indicate standard deviations. Values were normalized to the negative control. .... 87
- Figure 49: Simplified catalytic cycle of the palladium-catalyzed HECK reaction. .... 88
- Figure 50: (a) Structure of E-stilbene. (b) Structure of stilbene derivative resveratrol. .... 90
- Figure 51: Schematic depiction of the synthetic pathway to synthesize stilbenes and cinnamates on DMA. a) Immobilization of the photolinker. b) Modification of the linker with different aryl bromides. c) HECK reaction with variable alkenes. d) UV induced cleavage of the desired compound from the surface. .... 91
- Figure 52: (a) Exemplary reaction utilizing immobilized 4-bromophenylacetic acid and butyl acrylate, yielding product H1. (b) Overview of the chromatograms of cleaved product H1. The highlighted area contains the product peak. Indicated numbers on the right (1 – 6) refer to Table 11. .... 93

- Figure 53: (a) Exemplary solid-phase HECK reaction between 4-bromobenzoic acid and butyl acrylate to form compound H2 utilizing the Pd(OAc)<sub>2</sub> and NEt<sub>3</sub> in DMF.. (b) Chromatogram of cleaved compound H2 at 254 nm. The chromatogram shows the formation of two isomers of the desired product indicated by the blue (Z-isomer) and red (E-isomer) asterisk..... 95
- Figure 54: On-chip Heck reaction with various starting materials to yield compounds H3 – H8. a) Heck reaction employing Pd(OAc)<sub>2</sub> and NEt<sub>3</sub> in DMF. b) UV induced release from the surface. None of the reactions led to the synthesis of the desired compound. .... 96
- Figure 55: Calibration curve of SMR1 at 254 nm with linear fit (red). A dilution series of SMR1 was prepared and absorbance of every concentration was measured for its absorbance at 254 nm. .... 148
- Figure 56: Calibration curve of A<sub>2</sub>OTV at 254 nm with linear fit (red). A dilution series of A<sub>2</sub>OTV was prepared and absorbance of every concentration was measured for its absorbance at 254 nm. .... 150
- Figure 57: Calibration curve of A<sub>2</sub>B<sub>18</sub> at 254 nm with linear fit (red). A dilution series of A<sub>2</sub>B<sub>18</sub> was prepared and absorbance of every concentration was measured for its absorbance at 254 nm. .... 154
- Figure 58: MS/MS spectra and respective fragment structures of compound A<sub>1</sub>B<sub>1</sub>..... 155
- Figure 59: MS/MS spectra and respective fragment structures of compound A<sub>1</sub>B<sub>1</sub>..... 156
- Figure 60: Evaluation of the linearity of the CellTiter Glo assay between 0 and 10.000 cells per well. Each data point is the average of 3 repetitions. Error bars represent standard deviations..... 180

## 8 List of Tables

Table 1: Structures of tested amines $A_x$ and isocyanides $I_y$ for the Ugi reaction which formed the headgroups of the products. This set of starting materials was selected based on the structures reported by Brehm et al. <sup>[88]</sup> .....	25
Table 2: Exemplary structures of used 2-pyridyl disulfide derivatives $P_x$ and thiolactone derivatives $T_y$ for the solid-phase aminolysis and subsequent disulfide exchange reaction. ....	30
Table 3: Purity of exemplary compounds synthesized in 2.8 mm spots to monitor synthetic success via LC-MS analysis. Product was identified by MS, while purity was calculated as the fraction of the product's peak integral (product peak and oxidized product peak) with respect to the sum of integrals of all peaks at 254 nm absorbance. Conversion was calculated as the ratio between the absorbance of the thioether-amino intermediate and the product at 254 nm. <sup>[a]</sup> purity and conversion was calculated using the total ion chromatogram (TIC).....	31
Table 4: Overview of the used starting materials for the reaction cascade: Succinic acid (Ac) is attached to the surface through the photolinker. In the initial step, 4-pentenal (Al), isocyanides ( $I_1$ - $I_5$ ) and amines ( $A_1$ - $A_8$ ) undergo the Ugi reaction to form the respective headgroups. Subsequently, 2-pyridyl disulfide derivatives ( $P_1$ - $P_{16}$ ) and the thiolactone derivatives ( $T_1$ - $T_{16}$ ) participate in the three-component thiolactone ring-opening reaction leading to the generation of the lipid-like compounds. These 47 starting materials lead to the synthesis of 10240 different compounds. ....	35
<b>Table 5:</b> <i>Overview of the used starting materials for the synthesis of a 128 membered library on ITO-DMA.</i> .....	42
Table 6: Identification rate of each starting material used in the solid-phase synthesis of the 128 membered sub-library of lipid-like compounds. ....	44
Table 7: Classification of $Z'$ values in assays according to Zhang et al. <sup>[99]</sup> .....	48
Table 8: Overview of the used building blocks in the formation of the 325 membered library of potential MEK inhibitors. 13 different amino acids ( $A_1$ - $A_{13}$ ) and 25 different boronic acids ( $B_1$ - $B_{25}$ ) have been employed.....	68
Table 9: Purity of the final product and conversion of the amino acid-intermediate to the product for reaction paths involving various amino acids and different boronic acids. Purity was determined as a percentage, calculated by dividing the product integral by the total integration value of the HPLC chromatogram. The conversion rate was calculated as the ratio of the product's integral divided by the sum of the product and the amino acid-intermediate integrals. ....	73
Table 10: Identification rates of final products in MALDI-TOF-MS were determined for each tested building block in measurements on the ground steel target plate (MTP) and ITO-DMA, respectively. ....	79
Table 11: Overview of a subset of the utilized catalytic systems to investigate the on-chip HECK reaction on DMA. Purity was calculated as the fraction of the product's peak integral with respect to the sum of integrals of all peaks at 254 nm absorbance. <sup>[a]</sup> Unsuccessful setup 4 was excluded in the calculation. ....	94

Table 12: Combinations of thiolactone T <sub>x</sub> , 2-pyridyl disulfide Px and amine Ax to investigate the reactivity of the derivatives in solution prior to on-chip reaction. All reactants were used in 0.5 M solutions in DMSO. Product formation was checked via LC-MS.	179
---	-----

## 9 Literature

- [1] J. Höpfner, M. Brehm, P. A. Levkin, *Small* **2023**.
- [2] A. R. Mirza, M. S. Anson, K. Hellgardt, M. P. Leese, D. F. Thompson, L. Tonks, J. M. Williams, *Organic Process Research & Development* **1998**, *2*, 325-331.
- [3] J. A. DiMasi, H. G. Grabowski, R. W. Hansen, *Journal of health economics* **2016**, *47*, 20-33.
- [4] R. Liu, X. Li, K. S. Lam, *Current opinion in chemical biology* **2017**, *38*, 117-126.
- [5] N. A. Boyle, K. D. Janda, *Current opinion in chemical biology* **2002**, *6*, 339-346.
- [6] Z. Yu, M. Bradley, *current opinion in chemical biology* **2002**, *6*, 347-352.
- [7] R. B. Merrifield, *Journal of the American Chemical Society* **1963**, *85*, 2149-2154.
- [8] C. Blackburn, *Peptide Science* **1998**, *47*, 311-351.
- [9] A. Heckel, E. Mross, K.-H. Jung, J. Rademann, R. R. Schmidt, *Synlett* **1998**, *1998*, 171-173.
- [10] O. H. Aina, R. Liu, J. L. Sutcliffe, J. Marik, C.-X. Pan, K. S. Lam, *Molecular pharmaceutics* **2007**, *4*, 631-651.
- [11] R. Frank, *Journal of immunological methods* **2002**, *267*, 13-26.
- [12] H. E. Blackwell, *Current opinion in chemical biology* **2006**, *10*, 203-212.
- [13] A. Buitrago Santanilla, E. L. Regalado, T. Pereira, M. Shevlin, K. Bateman, L.-C. Campeau, J. Schneeweis, S. Berritt, Z.-C. Shi, P. Nantermet, *Science* **2015**, *347*, 49-53.
- [14] K. Gao, S. Shaabani, R. Xu, T. Zarganes-Tzitzikas, L. Gao, M. Ahmadianmoghaddam, M. R. Groves, A. Dömling, *RSC Medicinal Chemistry* **2021**, *12*, 809-818.
- [15] P. W. Fedick, R. L. Schrader, S. T. Ayrton, C. J. Pulliam, R. G. Cooks, *Journal of Chemical Education* **2018**, *96*, 124-131.
- [16] D. Perera, J. W. Tucker, S. Brahmabhatt, C. J. Helal, A. Chong, W. Farrell, P. Richardson, N. W. Sach, *Science* **2018**, *359*, 429-434.
- [17] J. Wingfield, I. D. Wilson, *Vol. 21*, SAGE Publications Sage CA: Los Angeles, CA, **2016**, pp. 109-110.
- [18] E. E. Kempa, K. A. Hollywood, C. A. Smith, P. E. Barran, *Analyst* **2019**, *144*, 872-891.
- [19] F. Pu, N. L. Elsen, J. D. Williams, *ACS Medicinal Chemistry Letters* **2020**, *11*, 2108-2113.
- [20] C. J. Welch, X. Gong, W. Schafer, E. C. Pratt, T. Brkovic, Z. Pirzada, J. F. Cuff, B. Kosjek, *Tetrahedron: Asymmetry* **2010**, *21*, 1674-1681.
- [21] E. Regalado, T. Pereira, M. Shevlin, K. Bateman, L. Campeau, J. Schneeweis, S. Berritt, Z. Shi, P. Nantermet, Y. Liu, *Science (New York, NY)* **2014**, *347*, 49-53.

- [22] D. S. Cornett, M. D. Scholle, *Vol. 22*, SAGE Publications Sage CA: Los Angeles, CA, **2017**, pp. 1179-1181.
- [23] R. P. Simon, M. Winter, C. Kleiner, R. Ries, G. Schnapp, A. Heimann, J. Li, L. Zuvela-Jelaska, T. Bretschneider, A. H. Luippold, *SLAS DISCOVERY: Advancing the Science of Drug Discovery* **2020**, *25*, 372-383.
- [24] J. Chandler, C. Haslam, N. Hardy, M. Leveridge, P. Marshall, *SLAS DISCOVERY: Advancing Life Sciences R&D* **2017**, *22*, 1262-1269.
- [25] M. Mrksich, *ACS nano* **2008**, *2*, 7-18.
- [26] C. Haslam, J. Hellicar, A. Dunn, A. Fuetterer, N. Hardy, P. Marshall, R. Paape, M. Pemberton, A. Resemannand, M. Leveridge, *Journal of biomolecular screening* **2016**, *21*, 176-186.
- [27] T. Häbe, C. Liu, T. Covey, DOI, **2020**.
- [28] K. J. DiRico, W. Hua, C. Liu, J. W. Tucker, A. S. Ratnayake, M. E. Flanagan, M. D. Troutman, M. C. Noe, H. Zhang, *ACS Medicinal Chemistry Letters* **2020**, *11*, 1101-1110.
- [29] N. M. Morato, D. T. Holden, R. G. Cooks, *Angewandte chemie* **2020**, *132*, 20639-20644.
- [30] M. Wleklinski, B. P. Loren, C. R. Ferreira, Z. Jaman, L. Avramova, T. J. Sobreira, D. H. Thompson, R. G. Cooks, *Chemical science* **2018**, *9*, 1647-1653.
- [31] S. A. Biyani, Q. Qi, J. Wu, Y. Moriuchi, E. A. Larocque, H. O. Sintim, D. H. Thompson, *Organic Process Research & Development* **2020**, *24*, 2240-2251.
- [32] P. W. Fedick, K. Iyer, Z. Wei, L. Avramova, G. O. Capek, R. G. Cooks, *Journal of The American Society for Mass Spectrometry* **2019**, *30*, 2144-2151.
- [33] H. Dodiuk, P. Rios, A. Dotan, S. Kenig, *Polymers for Advanced Technologies* **2007**, *18*, 746-750.
- [34] Y. Yu, H. Chen, Y. Liu, V. S. Craig, Z. Lai, *Advances in colloid and interface science* **2016**, *235*, 46-55.
- [35] D. Seo, J. Lee, C. Lee, Y. Nam, *Scientific reports* **2016**, *6*, 1-11.
- [36] C. G. Jothi Prakash, R. Prasanth, *Journal of Materials Science* **2021**, *56*, 108-135.
- [37] T. Young, *Philosophical transactions of the royal society of London* **1805**, 65-87.
- [38] A. Cassie, S. Baxter, *Transactions of the Faraday society* **1944**, *40*, 546-551.
- [39] R. N. Wenzel, *Industrial & engineering chemistry* **1936**, *28*, 988-994.
- [40] M. Zhang, S. Feng, L. Wang, Y. Zheng, *Biotribology* **2016**, *5*, 31-43.



- [41] P. A. Levkin, F. Svec, J. M. Fréchet, *Advanced functional materials* **2009**, *19*, 1993-1998.
- [42] F. L. Geyer, E. Ueda, U. Liebel, N. Grau, P. A. Levkin, *Angewandte Chemie International Edition* **2011**, *50*, 8424-8427.
- [43] Y. Liu, T. Tronser, R. Peravali, M. Reischl, P. A. Levkin, *Advanced biosystems* **2020**, *4*, 1900257.
- [44] W. Feng, L. Li, E. Ueda, J. Li, S. Heißler, A. Welle, O. Trapp, P. A. Levkin, *Advanced Materials Interfaces* **2014**, *1*, 1400269.
- [45] B. Neises, W. Steglich, *Angewandte Chemie* **1978**, *90*, 556-557.
- [46] M. Benz, A. Asperger, M. Hamester, A. Welle, S. Heissler, P. A. Levkin, *Nature Communications* **2020**, *11*, 5391.
- [47] A. N. Efremov, E. Stanganello, A. Welle, S. Scholpp, P. A. Levkin, *Biomaterials* **2013**, *34*, 1757-1763.
- [48] H. Cui, X. Wang, J. Wesslowski, T. Tronser, J. Rosenbauer, A. Schug, G. Davidson, A. Popova, P. A. Levkin, *Advanced materials* **2021**, *33*, 2006434.
- [49] J. J. Wiedmann, Y. N. Demirdögen, S. Schmidt, M. A. Kuzina, Y. Wu, F. Wang, B. Nestler, C. Hopf, P. A. Levkin, *Small* **2023**, *19*, 2204512.
- [50] W. Lei, K. Demir, J. Overhage, M. Grunze, T. Schwartz, P. A. Levkin, *Advanced Biosystems* **2020**, *4*, 2000073.
- [51] A. A. Popova, C. Depew, K. M. Permana, A. Trubitsyn, R. Peravali, J. Á. G. Ordiano, M. Reischl, P. A. Levkin, *SLAS TECHNOLOGY: Translating Life Sciences Innovation* **2017**, *22*, 163-175.
- [52] A. A. Popova, T. Tronser, K. Demir, P. Haitz, K. Kuodyte, V. Starkuviene, P. Wajda, P. A. Levkin, *Small* **2019**, *15*, 1901299.
- [53] T. Tronser, K. Demir, M. Reischl, M. Bastmeyer, P. A. Levkin, *Lab on a Chip* **2018**, *18*, 2257-2269.
- [54] W. Lei, J. Bruchmann, J. L. Rüping, P. A. Levkin, T. Schwartz, *Advanced Science* **2019**, *6*, 1900519.
- [55] A. A. Popova, D. Marcato, R. Peravali, I. Wehl, U. Schepers, P. A. Levkin, *Advanced Functional Materials* **2018**, *28*, 1703486.
- [56] A. A. Popova, S. Dietrich, W. Huber, M. Reischl, R. Peravali, P. A. Levkin, *SLAS TECHNOLOGY: Translating Life Sciences Innovation* **2021**, *26*, 274-286.
- [57] H. Cui, T. Tronser, X. Wang, J. Wesslowski, G. Davidson, A. A. Popova, P. A. Levkin, *Droplet* **2023**, *2*, e39.

- [58] H. Cui, X. Wang, J. Wesslowski, T. Tronser, J. Rosenbauer, A. Schug, G. Davidson, A. A. Popova, P. A. Levkin, *Adv Mater* **2021**, *33*, e2006434.
- [59] W. Lei, A. Deckers, C. Luchena, A. Popova, M. Reischl, N. Jung, S. Brase, T. Schwartz, I. K. Krimmelbein, L. F. Tietze, P. A. Levkin, *Adv Biol (Weinh)* **2022**, *6*, e2200166.
- [60] M. Seifermann, P. Reiser, P. Friederich, P. A. Levkin, *Small Methods*, 2300553.
- [61] M. Benz, M. R. Molla, A. Böser, A. Rosenfeld, P. A. Levkin, *Nature communications* **2019**, *10*, 2879.
- [62] A. Rosenfeld, M. Brehm, A. Welle, V. Trouillet, S. Heissler, M. Benz, P. A. Levkin, *Materials Today Bio* **2019**, *3*, 100022.
- [63] P. Klán, T. Solomek, C. G. Bochet, A. Blanc, R. Givens, M. Rubina, V. Popik, A. Kostikov, J. Wirz, *Chemical reviews* **2013**, *113*, 119-191.
- [64] M. Brehm, S. Heissler, S. Afonin, P. A. Levkin, *Small* **2020**, *16*, 1905971.
- [65] N. Chéron, R. Ramozzi, L. E. Kaïm, L. Grimaud, P. Fleurat-Lessard, *The Journal of organic chemistry* **2012**, *77*, 1361-1366.
- [66] Z.-Q. Liu, *Current Organic Chemistry* **2014**, *18*, 719-739.
- [67] G. D. Wright, *ACS Infectious Diseases* **2015**, *1*, 80-84.
- [68] F. D. Lowy, *The Journal of Clinical Investigation* **2003**, *111*, 1265-1273.
- [69] N. Raheem, S. K. Straus, *Frontiers in Microbiology* **2019**, *10*.
- [70] M. S. Butler, M. A. Blaskovich, M. A. Cooper, *The Journal of Antibiotics* **2017**, *70*, 3-24.
- [71] L. L. Silver, *Clinical microbiology reviews* **2011**, *24*, 71-109.
- [72] M. F. Chellat, L. Raguz, R. Riedl, *Angewandte Chemie International Edition* **2016**, *55*, 6600-6626.
- [73] J. M. Blair, M. A. Webber, A. J. Baylay, D. O. Ogbolu, L. J. Piddock, *Nature reviews microbiology* **2015**, *13*, 42-51.
- [74] R. Köck, A. Mellmann, F. Schaumburg, A. W. Friedrich, F. Kipp, K. Becker, *Dtsch Arztebl International* **2011**, *108*, 761-767.
- [75] Y. Cong, S. Yang, X. Rao, *Journal of Advanced Research* **2020**, *21*, 169-176.
- [76] N. Buetti, N. Wassilew, V. Rion, L. Senn, C. Gardiol, A. Widmer, J. Marschall, C. Balmelli, M. C. Eisenring, S. Harbarth, S. P. Kuster, V. M. Spicher, D. Pittet, C. Ruef, H. Sax, M. Schlegel, A. Schweiger, N. Troillet, G. Zanetti, S. for, *Antimicrobial Resistance & Infection Control* **2019**, *8*, 16.
- [77] J. O'Neill, *Tackling Drug-resistant Infections Globally: Final Report and Recommendations*, Government of the United Kingdom (London), UK, **2016**.

- [78] S. A. Waksman, *Microbial antagonisms and antibiotic substances*, Vol. 59, LWW, **1945**.
- [79] M. A. Fischbach, C. T. Walsh, *Science* **2009**, 325, 1089-1093.
- [80] J. C. Nielsen, S. Grijseels, S. Prigent, B. Ji, J. Dainat, K. F. Nielsen, J. C. Frisvad, M. Workman, J. Nielsen, *Nature microbiology* **2017**, 2, 1-9.
- [81] A. Coates, Y. Hu, *British journal of pharmacology* **2007**, 152, 1147-1154.
- [82] A. P. Desbois, V. J. Smith, *Applied Microbiology and Biotechnology* **2010**, 85, 1629-1642.
- [83] N. Mookherjee, M. A. Anderson, H. P. Haagsman, D. J. Davidson, *Nature Reviews Drug Discovery* **2020**, 19, 311-332.
- [84] M. Zhou, M. Zheng, J. Cai, *ACS applied materials & interfaces* **2020**, 12, 21292-21299.
- [85] Q. Y. Lau, Y. Y. F. Tan, V. C. Y. Goh, D. J. Q. Lee, F. M. Ng, E. H. Ong, J. Hill, C. S. B. Chia, *Antibiotics* **2015**, 4, 424-434.
- [86] W. Younis, S. Thangamani, M. N Seleem, *Current pharmaceutical design* **2015**, 21, 4106-4111.
- [87] M. N. Thaker, N. Waglechner, G. D. Wright, *nature protocols* **2014**, 9, 1469-1479.
- [88] M. Brehm, Dissertation, Karlsruhe, Karlsruher Institut für Technologie (KIT), 2021
- [89] M. R. Molla, A. Böser, A. Rana, K. Schwarz, P. A. Levkin, *Bioconjugate Chemistry* **2018**, 29, 992-999.
- [90] Y. Shai, Z. Oren, *Peptides* **2001**, 22, 1629-1641.
- [91] V. De Cesare, J. Moran, R. Traynor, A. Knebel, M. S. Ritorto, M. Trost, H. McLauchlan, C. J. Hastie, P. Davies, *Nature Protocols* **2020**, 15, 4034-4057.
- [92] C. Ramalloguevara, D. Paulssen, A. A. Popova, C. Hopf, P. A. Levkin, *Advanced Biology* **2021**, 5, 2000279.
- [93] J. Kim, B.-H. Cho, Y.-S. Jang, *Journal of Microbiology and Biotechnology* **2023**, 33, 288.
- [94] R. E. Hancock, H.-G. Sahl, *Nature biotechnology* **2006**, 24, 1551-1557.
- [95] W. Lei, A. Deckers, C. Luchena, A. Popova, M. Reischl, N. Jung, S. Bräse, T. Schwartz, I. K. Krimmelbein, L. F. Tietze, P. A. Levkin, *Advanced Biology* **2022**, 6, 2200166.
- [96] X. Yang, Y. Zhong, D. Wang, Z. Lu, *Analytical Methods* **2021**, 13, 5211-5215.
- [97] D. Yahav, L. Farbman, L. Leibovici, M. Paul, *Clinical microbiology and infection* **2012**, 18, 18-29.
- [98] J. K. Oh, Y. Yegin, F. Yang, M. Zhang, J. Li, S. Huang, S. V. Verkhoturov, E. A. Schweikert, K. Perez-Lewis, E. A. Scholar, *Scientific reports* **2018**, 8, 17247.

- [99] J.-H. Zhang, T. D. Chung, K. R. Oldenburg, *Journal of biomolecular screening* **1999**, 4, 67-73.
- [100] S. Zhang, Y. Chen, S. Xiong, G. Wang, J. Chen, G. Yang, *Journal of the American Society for Mass Spectrometry* **2010**, 21, 154-160.
- [101] X. Dong, J. Cheng, J. Li, Y. Wang, *Analytical chemistry* **2010**, 82, 6208-6214.
- [102] C. P. Mullens, S. R. Anugu, W. Gorski, S. B. Bach, *International Journal of Mass Spectrometry* **2011**, 308, 311-315.
- [103] B. S. Chhikara, K. Parang, *Chemical Biology Letters* **2023**, 10, 451-451.
- [104] R. Roskoski Jr, *Pharmacological Research* **2017**, 117, 20-31.
- [105] I. Wortzel, R. Seger, *Genes & cancer* **2011**, 2, 195-209.
- [106] M. Cargnello, P. P. Roux, *Microbiology and molecular biology reviews* **2011**, 75, 50-83.
- [107] A.-M. Tsimberidou, *Cancer chemotherapy and pharmacology* **2015**, 76, 1113-1132.
- [108] W. E. Tidymann, K. A. Rauen, *Current opinion in genetics & development* **2009**, 19, 230-236.
- [109] K. T. Flaherty, I. Puzanov, K. B. Kim, A. Ribas, G. A. McArthur, J. A. Sosman, P. J. O'Dwyer, R. J. Lee, J. F. Grippo, K. Nolop, P. B. Chapman, *N Engl J Med* **2010**, 363, 809-819.
- [110] R. Kefford, H. Arkenau, M. P. Brown, M. Millward, J. R. Infante, G. V. Long, D. Ouellet, M. Curtis, P. F. Lebowitz, G. S. Falchook, *Journal of Clinical Oncology* **2010**, 28, 8503-8503.
- [111] R. B. Corcoran, H. Ebi, A. B. Turke, E. M. Coffee, M. Nishino, A. P. Cogdill, R. D. Brown, P. Della Pelle, D. Dias-Santagata, K. E. Hung, K. T. Flaherty, A. Piris, J. A. Wargo, J. Settleman, M. Mino-Kenudson, J. A. Engelmann, *Cancer Discov* **2012**, 2, 227-235.
- [112] J. Han, Y. Liu, S. Yang, X. Wu, H. Li, Q. Wang, *Journal of Hematology & Oncology* **2021**, 14.
- [113] C. J. Caunt, M. J. Sale, P. D. Smith, S. J. Cook, *Nature Reviews Cancer* **2015**, 15, 577-592.
- [114] S. Fawdar, E. W. Trotter, Y. Li, N. L. Stephenson, F. Hanke, A. A. Marusiak, Z. C. Edwards, S. Ientile, B. Waszkowycz, C. J. Miller, *Proceedings of the National Academy of Sciences* **2013**, 110, 12426-12431.
- [115] A. K. Salama, K. B. Kim, *Current oncology reports* **2013**, 15, 473-482.
- [116] Y. Zhao, A. A. Adjei, *Nature reviews Clinical oncology* **2014**, 11, 385-400.

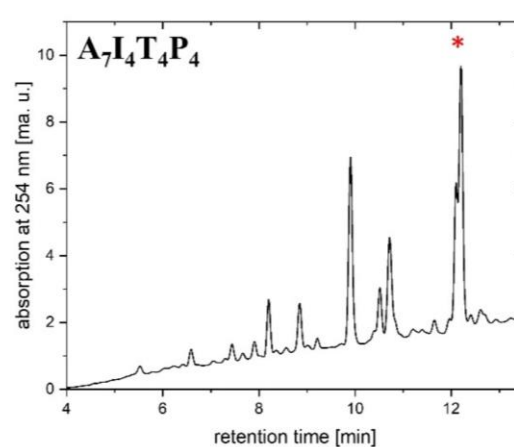
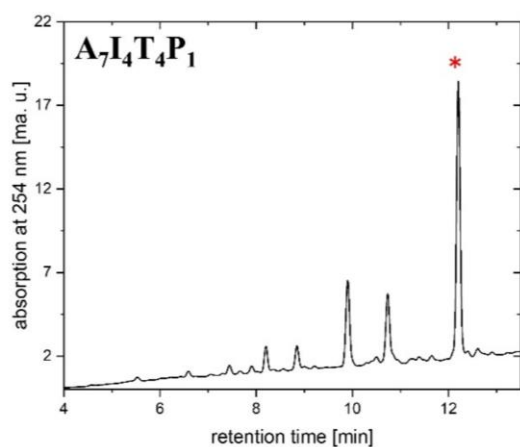
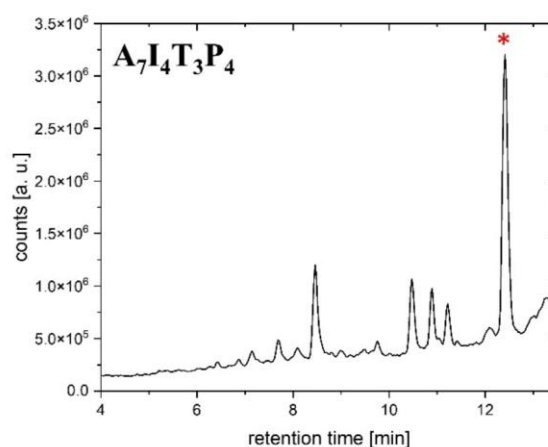
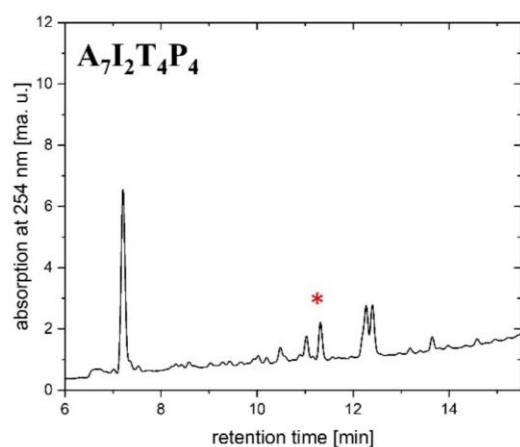
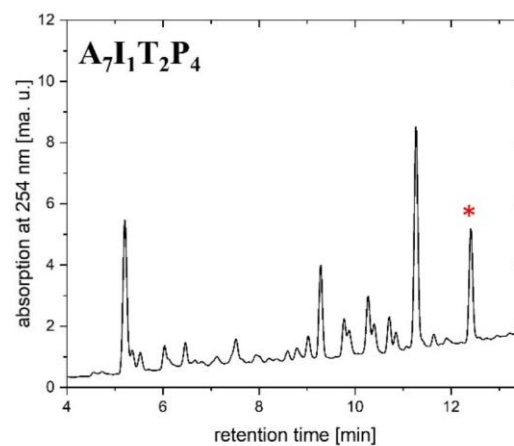
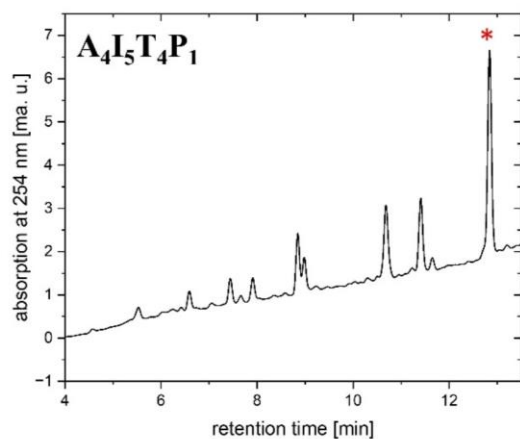
- [117] H. Wong, L. Vernillet, A. Peterson, J. A. Ware, L. Lee, J.-F. Martini, P. Yu, C. Li, G. D. Rosario, E. F. Choo, *Clinical Cancer Research* **2012**, *18*, 3090-3099.
- [118] S. P. Patel, A. J. Lazar, N. E. Papadopoulos, P. Liu, J. R. Infante, M. R. Glass, C. S. Vaughn, P. M. LoRusso, R. B. Cohen, M. A. Davies, *Cancer* **2013**, *119*, 799-805.
- [119] U. Banerji, D. R. Camidge, H. M. Verheul, R. Agarwal, D. Sarker, S. B. Kaye, I. M. Desai, J. N. Timmer-Bonte, S. G. Eckhardt, K. D. Lewis, *Clinical Cancer Research* **2010**, *16*, 1613-1623.
- [120] B. Tran, M. S. Cohen, *Expert opinion on drug discovery* **2020**, *15*, 745-754.
- [121] B. D. Weiss, P. L. Wolters, S. R. Plotkin, B. C. Widemann, J. H. Tonsgard, J. Blakeley, J. C. Allen, E. Schorry, B. Korf, N. J. Robison, *Journal of Clinical Oncology* **2021**, *39*, 797.
- [122] Y. Isshiki, Y. Kohchi, H. Iikura, Y. Matsubara, K. Asoh, T. Murata, M. Kohchi, E. Mizuguchi, S. Tsujii, K. Hattori, *Bioorganic & medicinal chemistry letters* **2011**, *21*, 1795-1801.
- [123] Z. Zhao, L. Xie, P. E. Bourne, *PLoS One* **2017**, *12*, e0179936.
- [124] A. A. Popova, T. Tronser, K. Demir, P. Haitz, K. Kuodyte, V. Starkuviene, P. Wajda, P. A. Levkin, *Small* **2019**, *15*, 1901299.
- [125] H. Cui, X. Sun, M. Schilling, C. Herold-Mende, M. Reischl, P. A. Levkin, A. A. Popova, Ş. Turcan, *Advanced Healthcare Materials* **2023**, *12*.
- [126] Y. Tian, M. Seifermann, L. Bauer, J. J. Wiedmann, C. Luchena, S. Schmidt, A. Geisel, S. Afonin, J. Höpfner, M. Brehm, X. Liu, C. Hopf, A. A. Popova, P. A. Levkin, *[Manuscript submitted for publication]* **2023**.
- [127] K. K. Ciombor, T. Bekaii-Saab, *Expert opinion on investigational drugs* **2015**, *24*, 111-123.
- [128] M. Watanabe, Y. Sowa, M. Yogosawa, T. Sakai, *Cancer science* **2013**, *104*, 687-693.
- [129] S. Gong, D. Xu, J. Zhu, F. Zou, R. Peng, *Cellular Physiology and Biochemistry* **2018**, *47*, 680-693.
- [130] R. Hannah, M. Beck, R. Moravec, T. Riss, *Promega Cell Notes* **2001**, *2*, 11-13.
- [131] J. Bada, in *Chemistry and biochemistry of the amino acids*, Springer, **1985**, pp. 399-414.
- [132] T. Mizoroki, K. Mori, A. Ozaki, *Bulletin of the Chemical Society of Japan* **1971**, *44*, 581-581.
- [133] R. F. Heck, J. Nolley Jr, *The Journal of organic chemistry* **1972**, *37*, 2320-2322.
- [134] M. OESTREICH, **2009**.

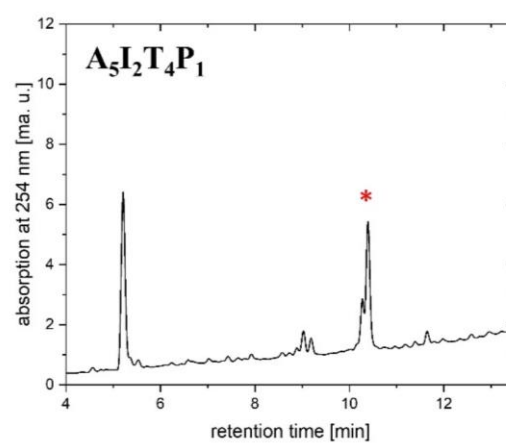
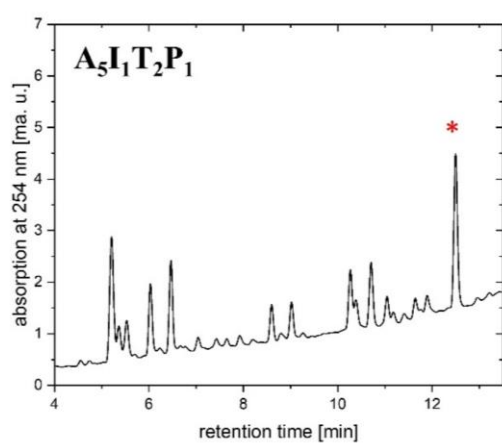
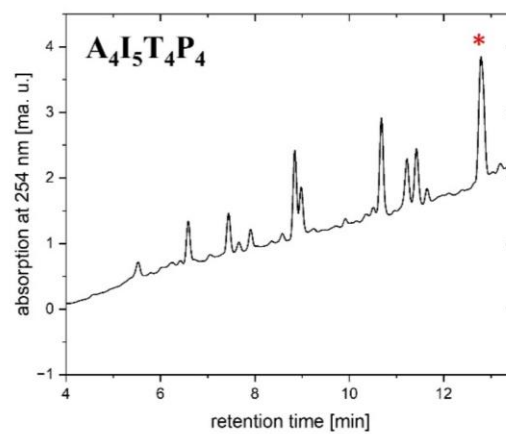
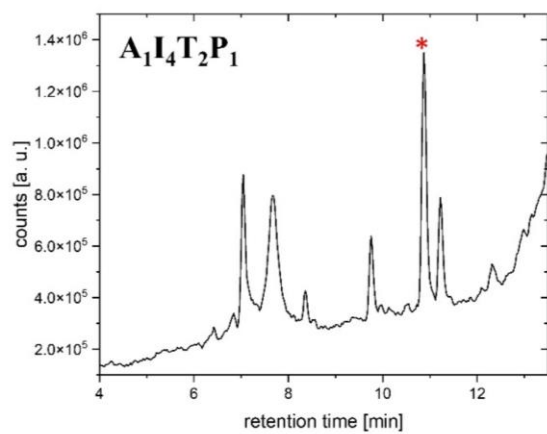
- [135] I. P. Beletskaya, A. V. Cheprakov, *Chemical Reviews* **2000**, *100*, 3009-3066.
- [136] T. Jeffery, *Journal of the Chemical Society, Chemical Communications* **1984**, 1287-1289.
- [137] C. Riviere, A. D. Pawlus, J.-M. Merillon, *Natural product reports* **2012**, *29*, 1317-1333.
- [138] T. Shen, X.-N. Wang, H.-X. Lou, *Natural product reports* **2009**, *26*, 916-935.
- [139] S. Molino, M. Dossena, D. Buonocore, F. Ferrari, L. Venturini, G. Ricevuti, M. Verri, *Life sciences* **2016**, *161*, 69-77.
- [140] E. Giacomini, S. Rupiani, L. Guidotti, M. Recanatini, M. Roberti, *Current medicinal chemistry* **2016**, *23*, 2439-2489.
- [141] C. Li, J. S. Fang, W. W. Lian, X. C. Pang, A. L. Liu, G. H. Du, *Chemical Biology & Drug Design* **2015**, *85*, 427-438.
- [142] S. Fulda, *Drug discovery today* **2010**, *15*, 757-765.
- [143] C. K. Singh, M. A. Ndiaye, N. Ahmad, *Biochimica et Biophysica Acta (BBA)-Molecular Basis of Disease* **2015**, *1852*, 1178-1185.
- [144] J. B. Metternich, D. G. Artiukhin, M. C. Holland, M. von Bremen-Kühne, J. Neugebauer, R. Gilmour, *The Journal of Organic Chemistry* **2017**, *82*, 9955-9977.
- [145] M. Beller, H. Fischer, K. Kühlein, C.-P. Reisinger, W. Herrmann, *Journal of organometallic chemistry* **1996**, *520*, 257-259.
- [146] F. Zhao, B. M. Bhanage, M. Shirai, M. Arai, *Journal of Molecular Catalysis A: Chemical* **1999**, *142*, 383-388.

## 10 Appendix

### 10.1 LC-MS Spectra

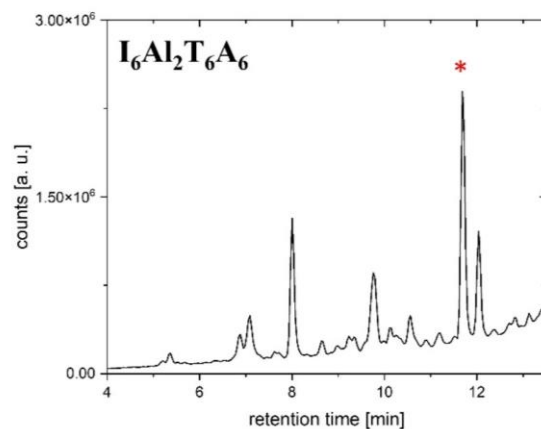
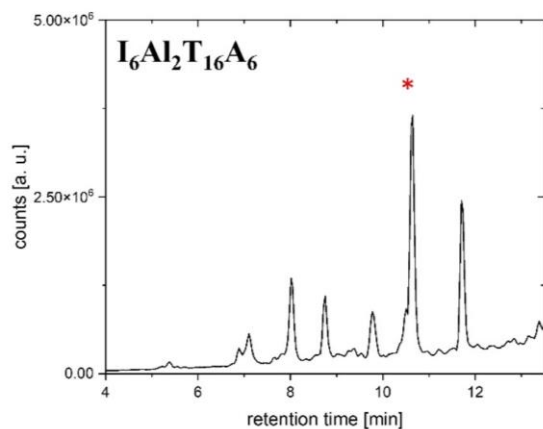
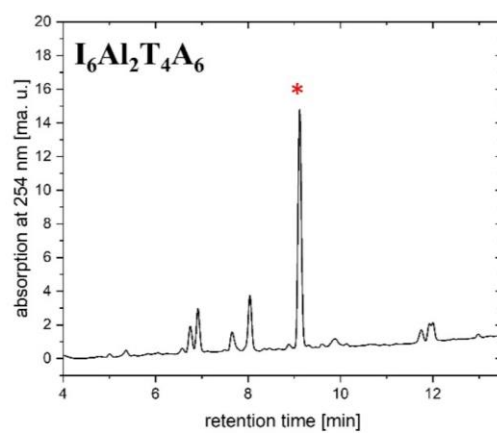
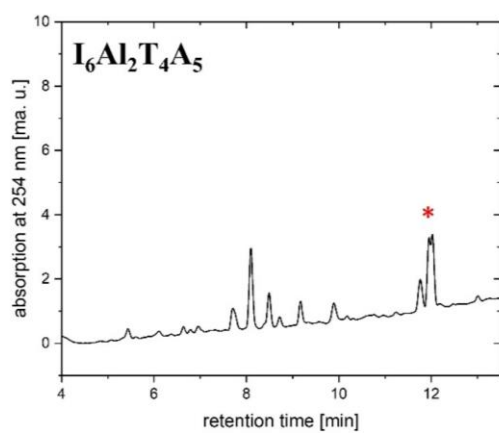
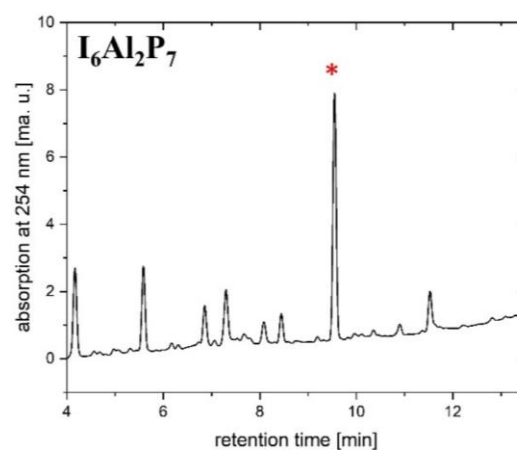
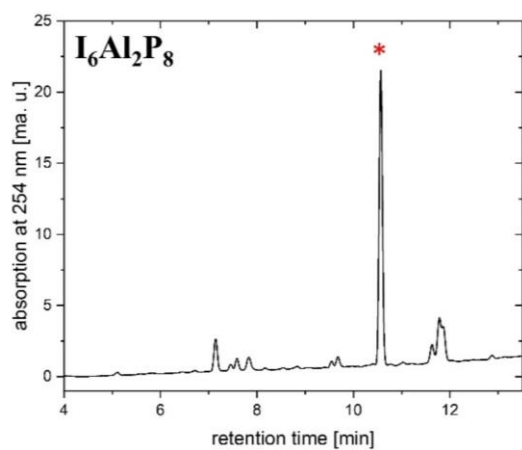
#### Chapter 3.1.2



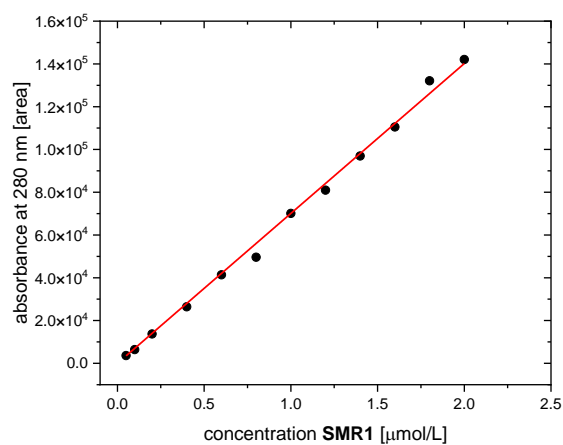




## Chapter 3.1.5

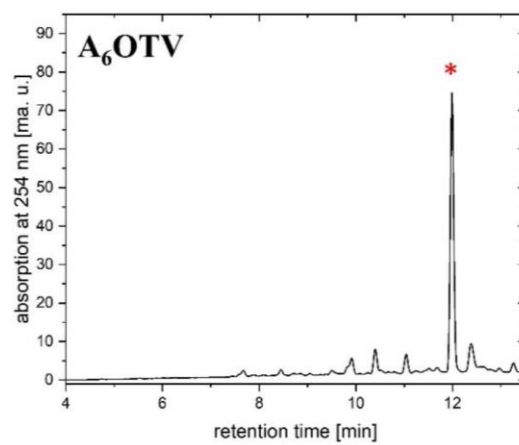
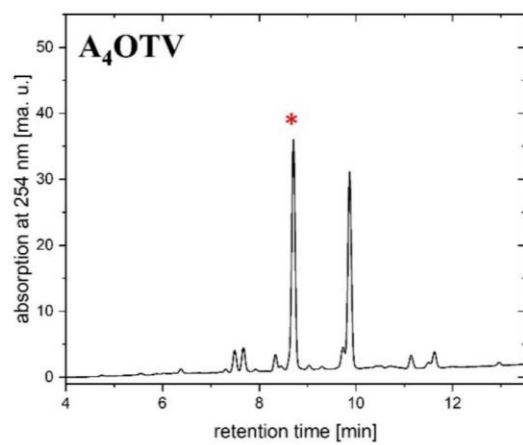
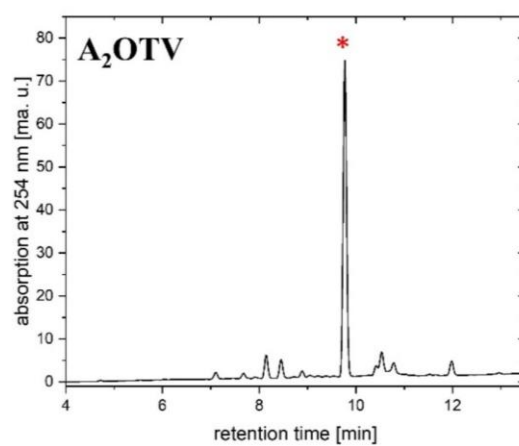
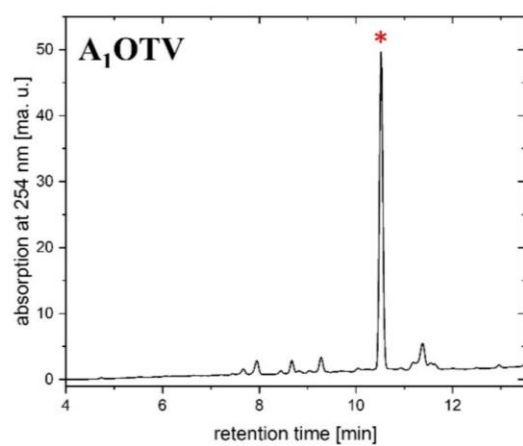


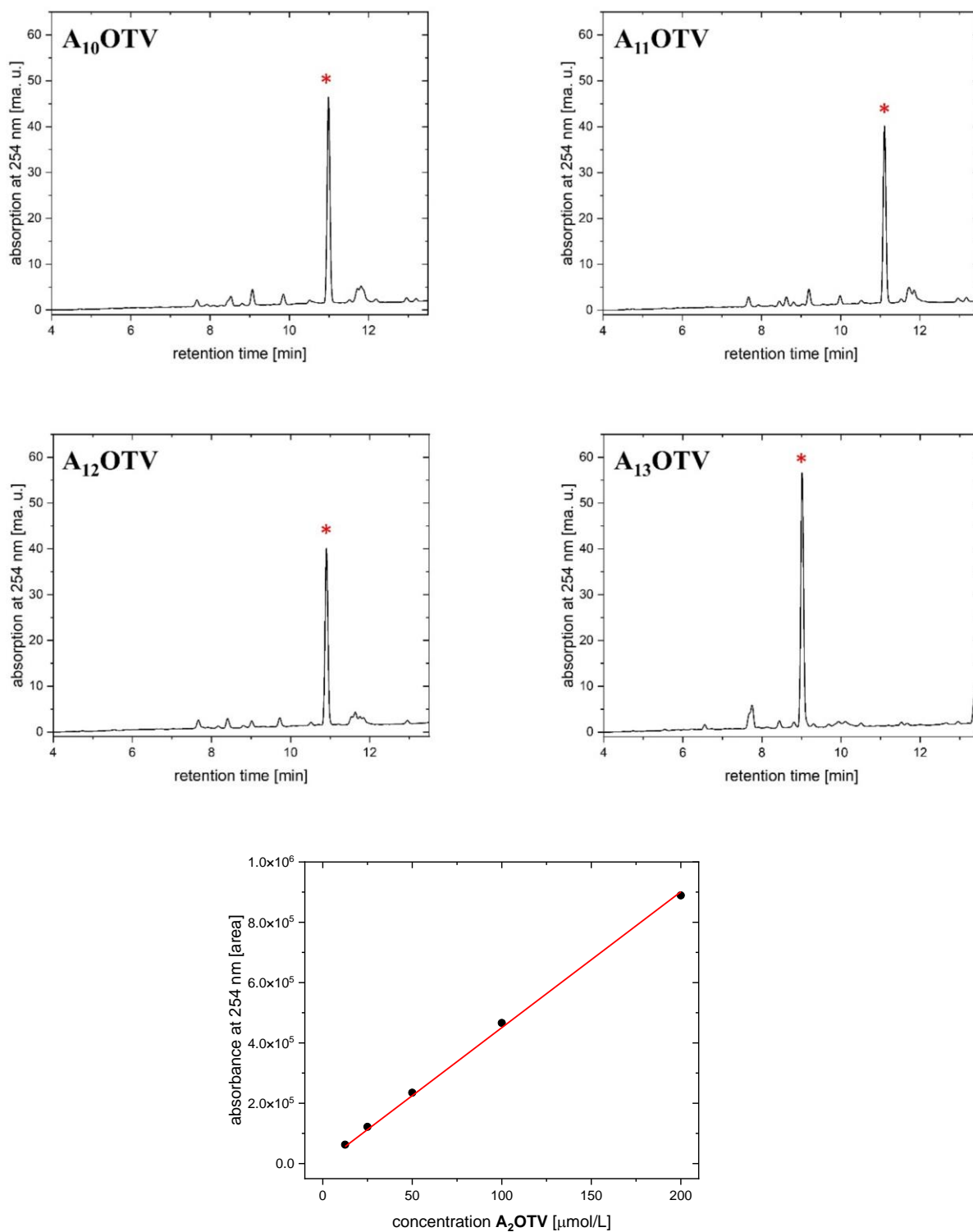
## Chapter 3.2.1



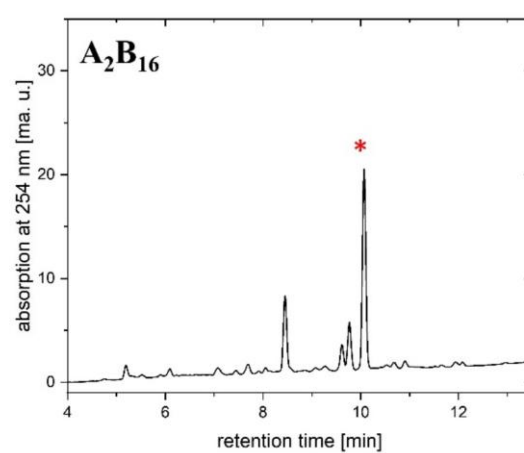
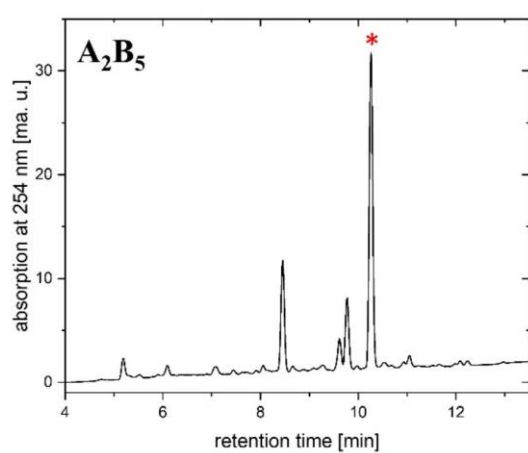
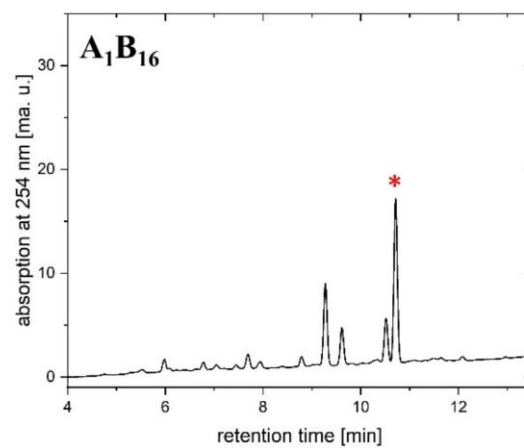
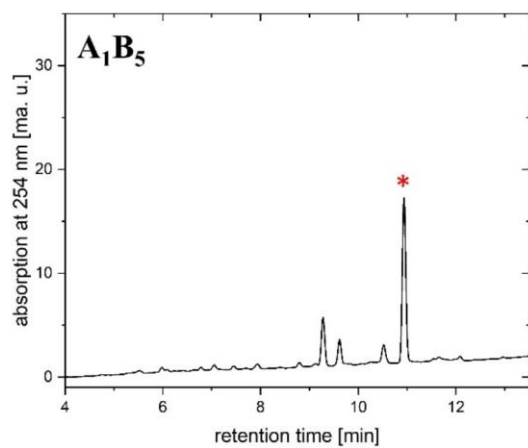
**Figure 55:** Calibration curve of **SMRI** at 254 nm with linear fit (red). A dilution series of **SMRI** was prepared and absorbance of every concentration was measured for its absorbance at 254 nm.

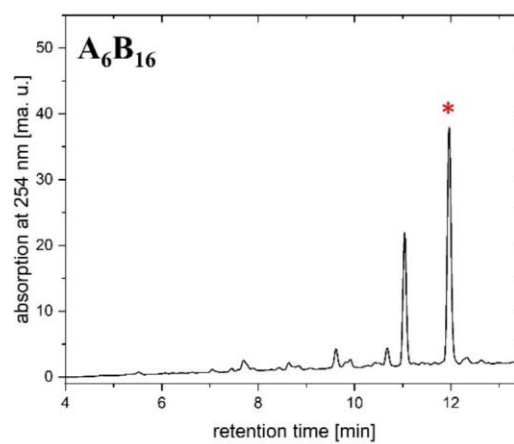
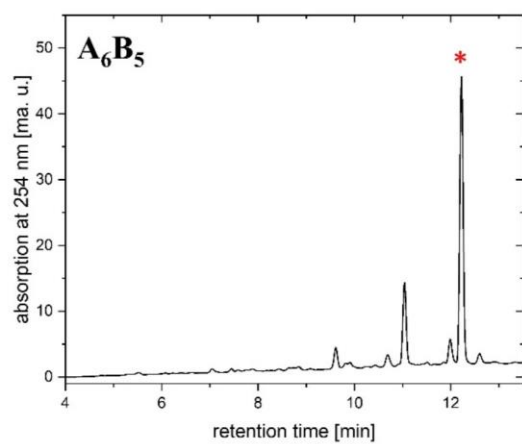
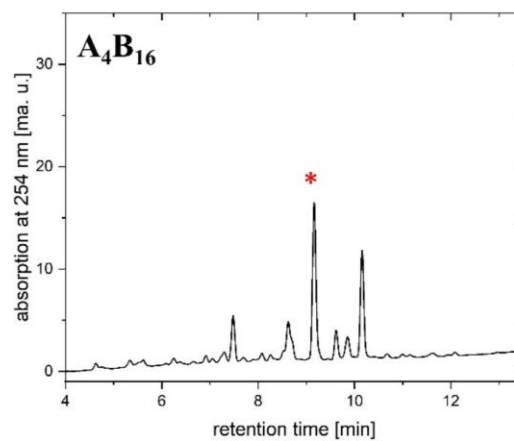
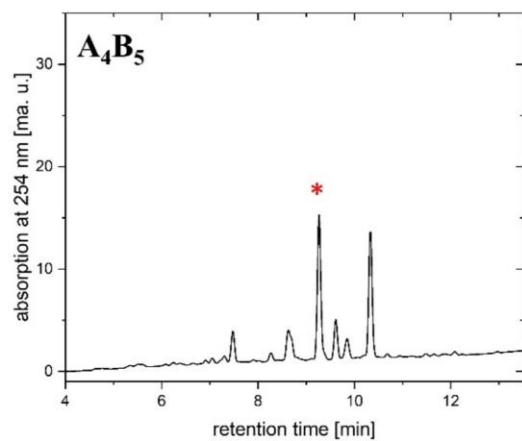
## Chapter 3.2.3

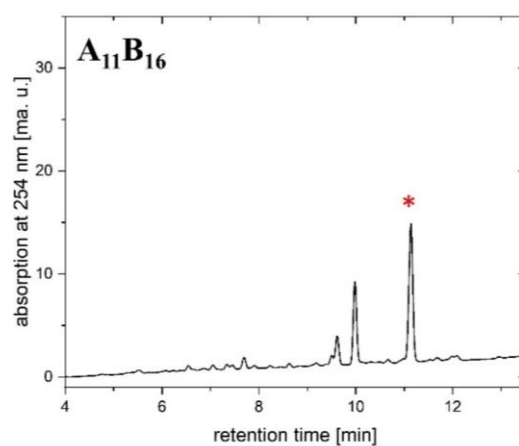
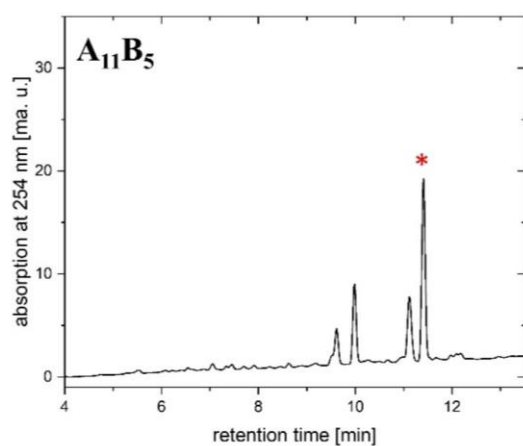
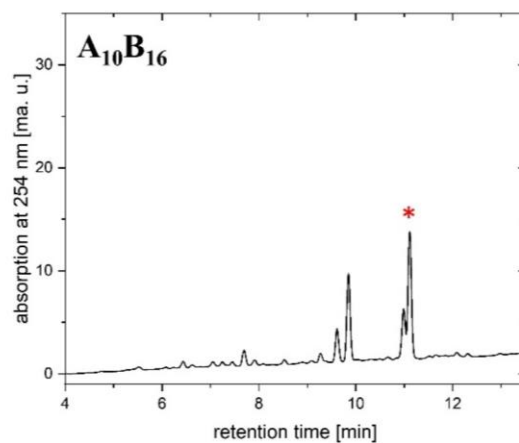
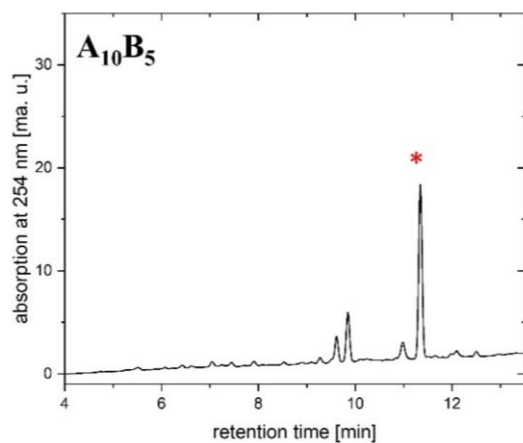


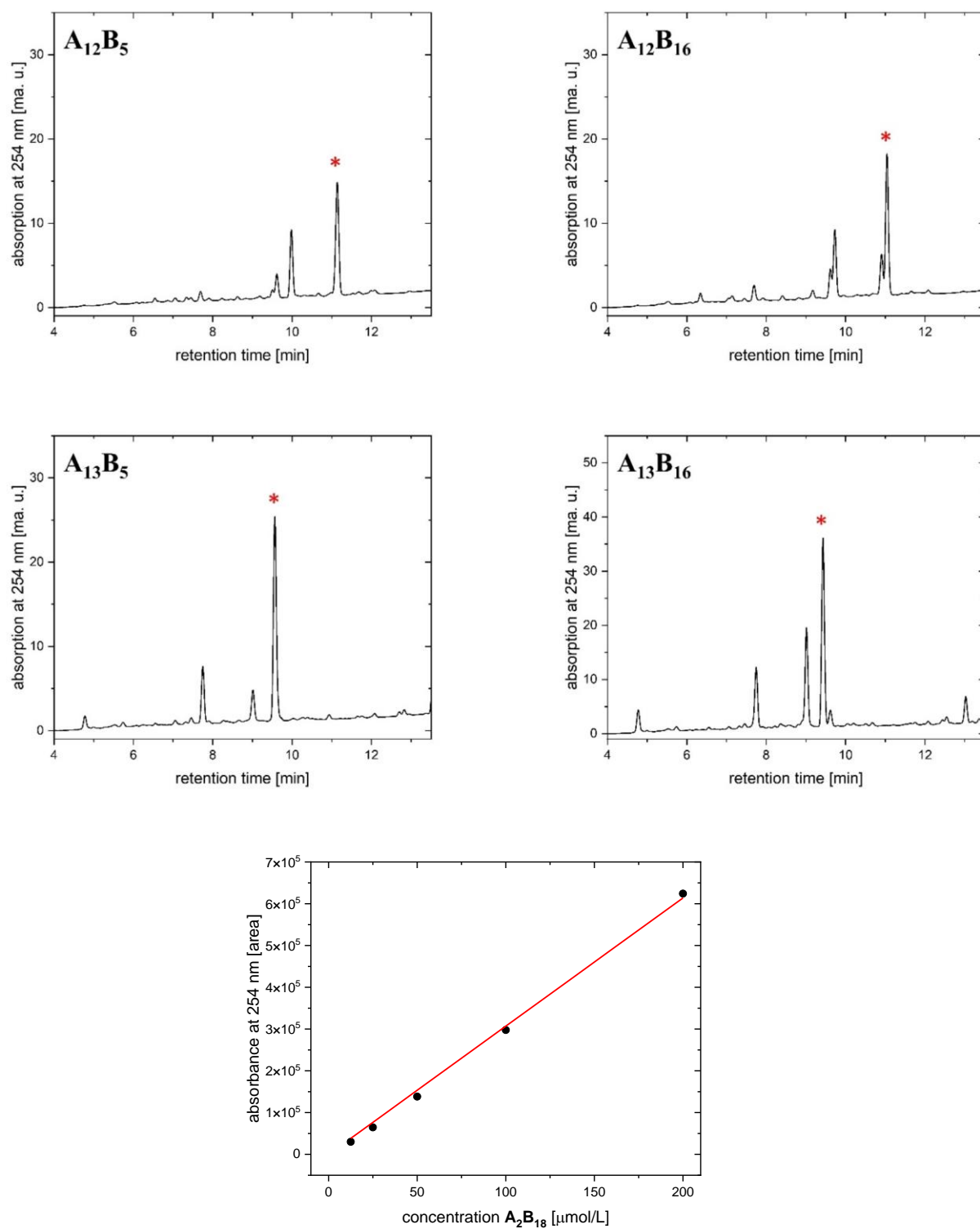


**Figure 56:** Calibration curve of A<sub>2</sub>OTV at 254 nm with linear fit (red). A dilution series of A<sub>2</sub>OTV was prepared and absorbance of every concentration was measured for its absorbance at 254 nm.





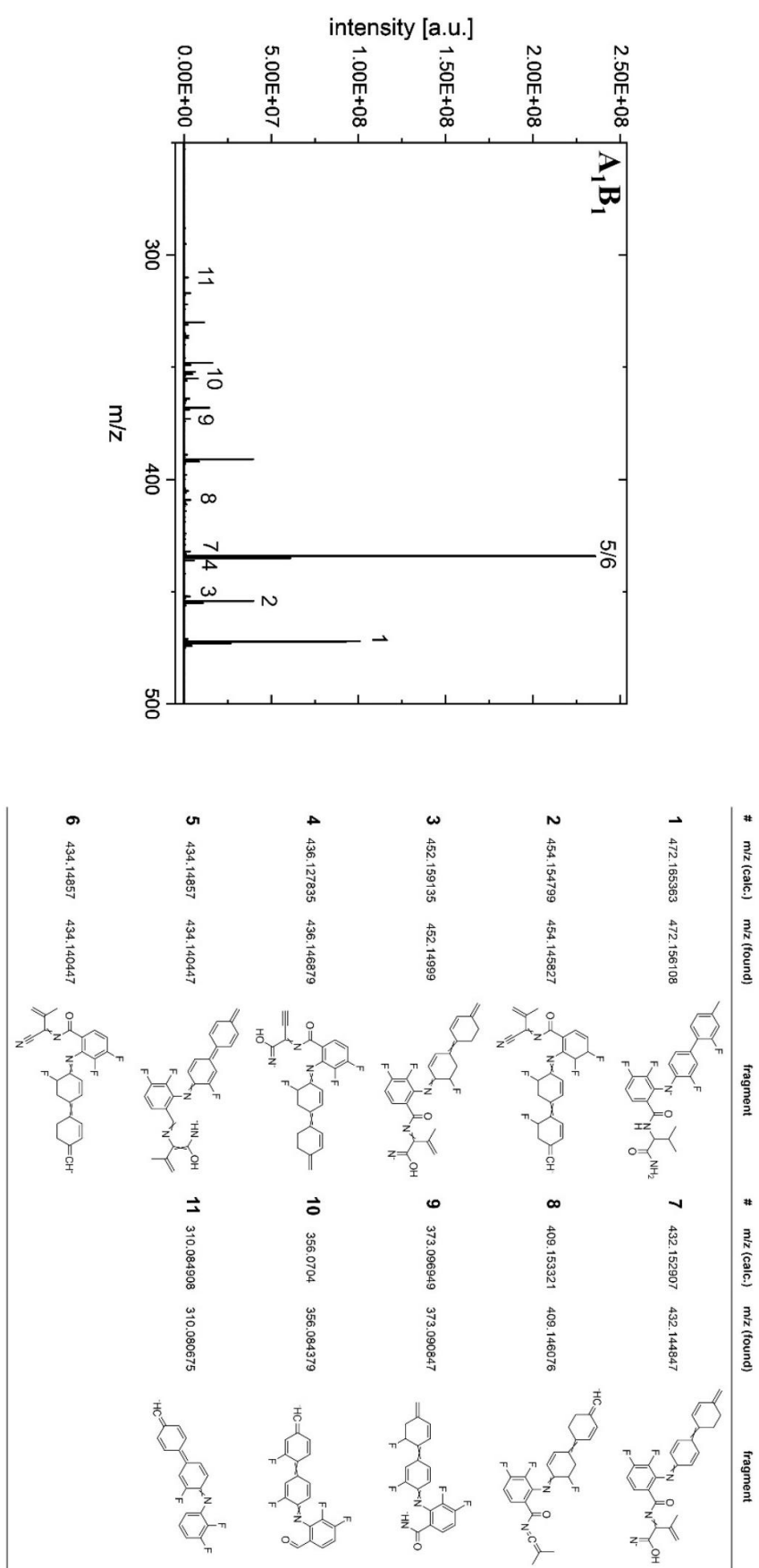


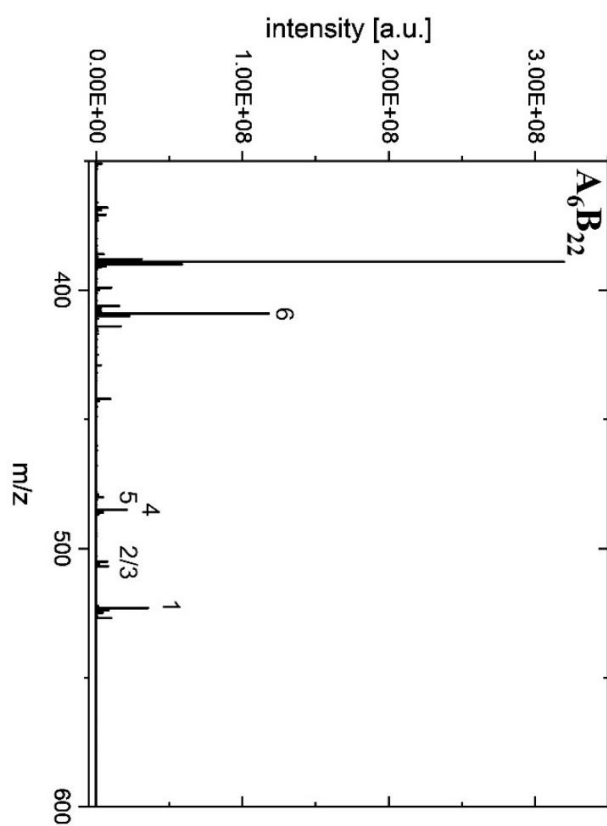


**Figure 57:** Calibration curve of  $A_2B_{18}$  at 254 nm with linear fit (red). A dilution series of  $A_2B_{18}$  was prepared and absorbance of every concentration was measured for its absorbance at 254 nm.



## Chapter 3.2.4

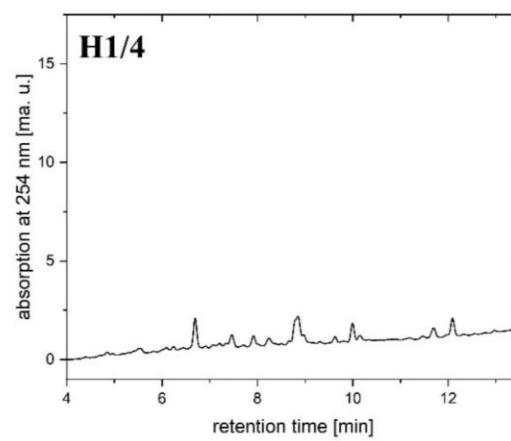
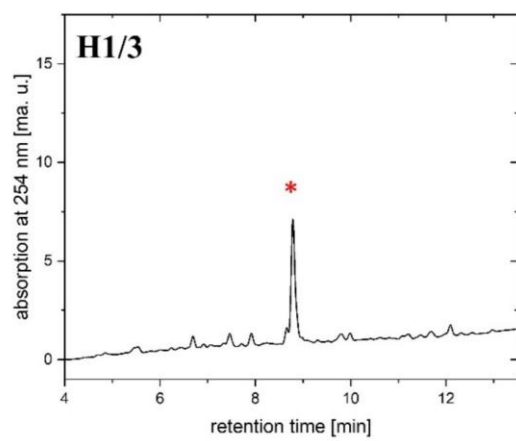
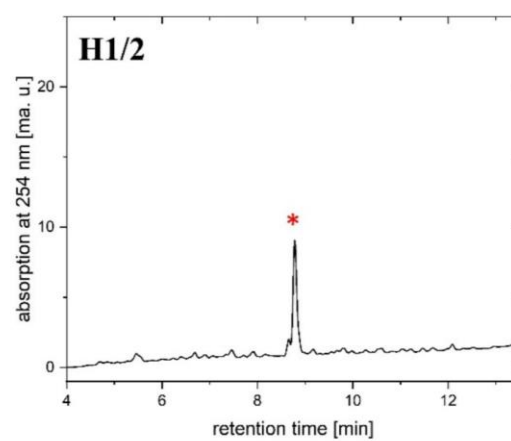
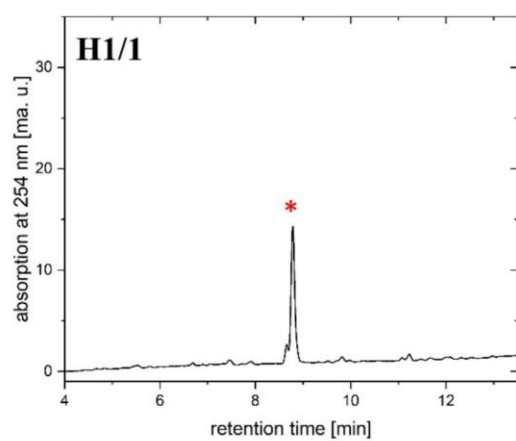
Figure 58: MS/MS spectra and respective fragment structures of compound A<sub>1</sub>B<sub>1</sub>.

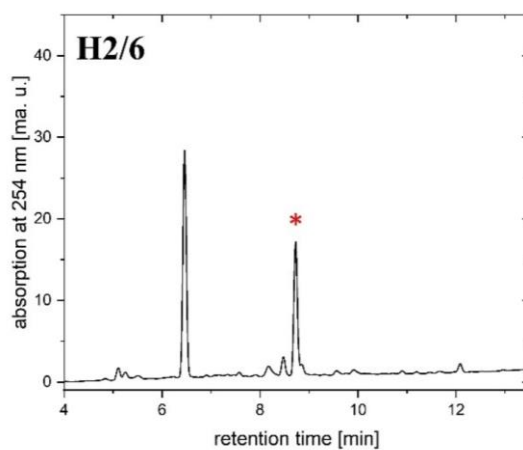
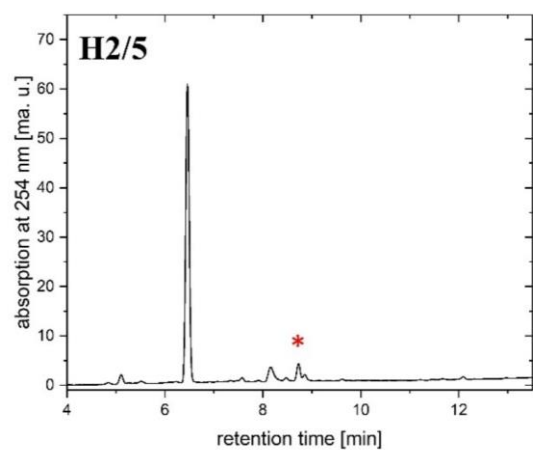
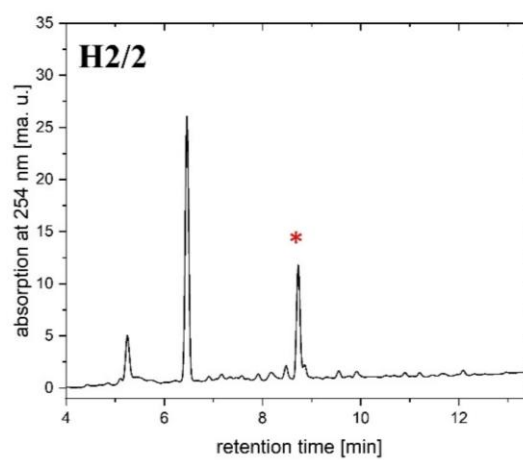
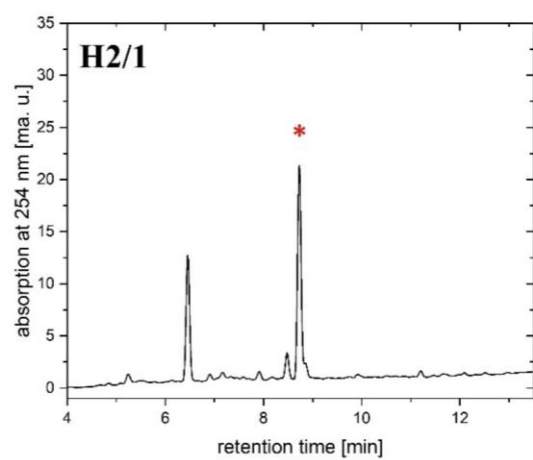
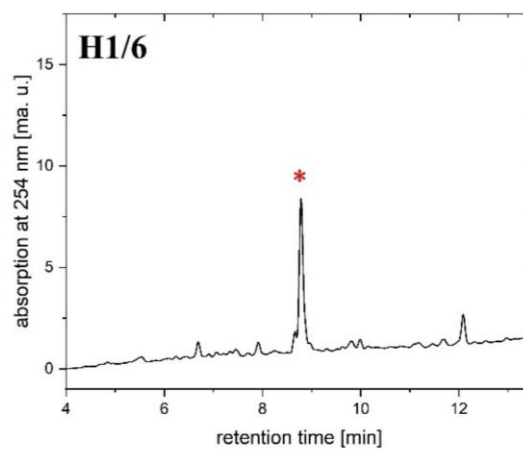
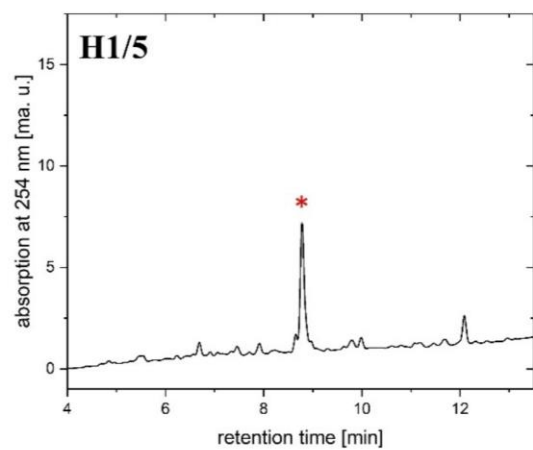


#	<i>m/z</i> (calc.)	<i>m/z</i> (found)	fragment	#	<i>m/z</i> (calc.)	<i>m/z</i> (found)	fragment
1	523.1210333	523.108686		4	485.1042404	485.094032	
2	506.0944942	506.943538		5	480.1152197	480.181571	
3	505.1104686	505.09857		6	409.0781059	409.078106	

**Figure 59:** MS/MS spectra and respective fragment structures of compound **A<sub>1</sub>B<sub>1</sub>**.

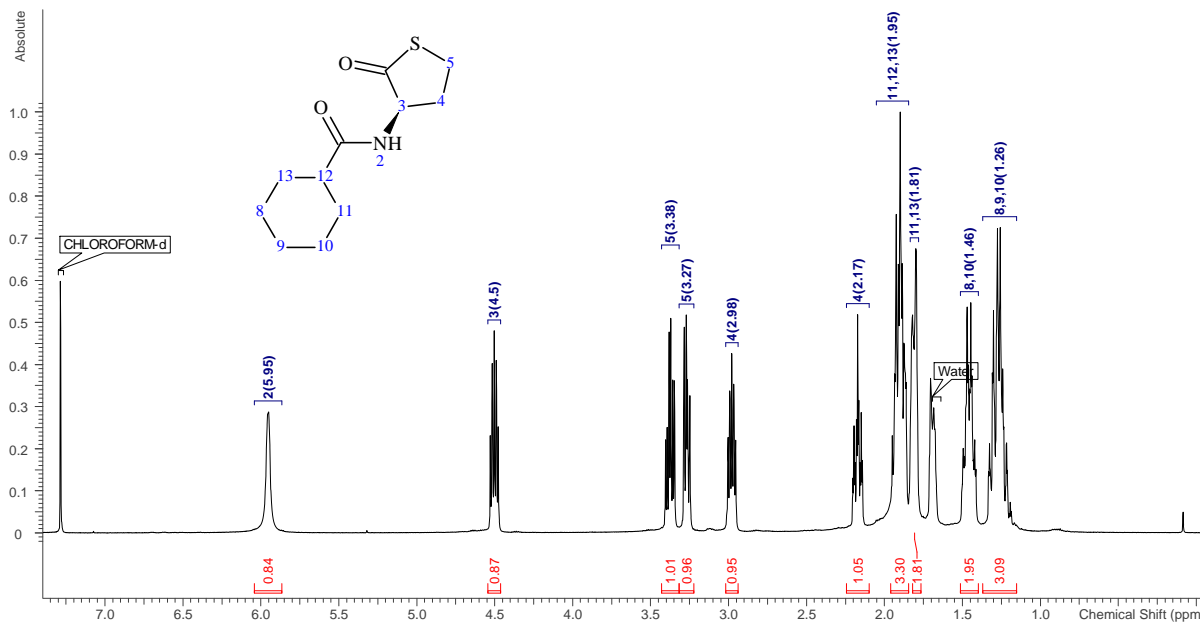
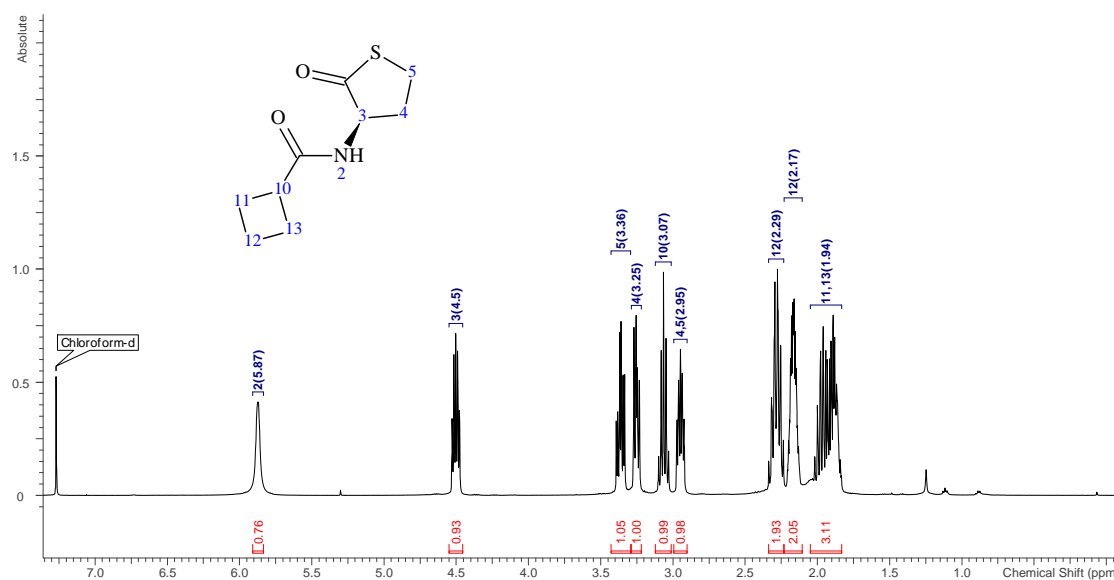
## Chapter 3.3.3

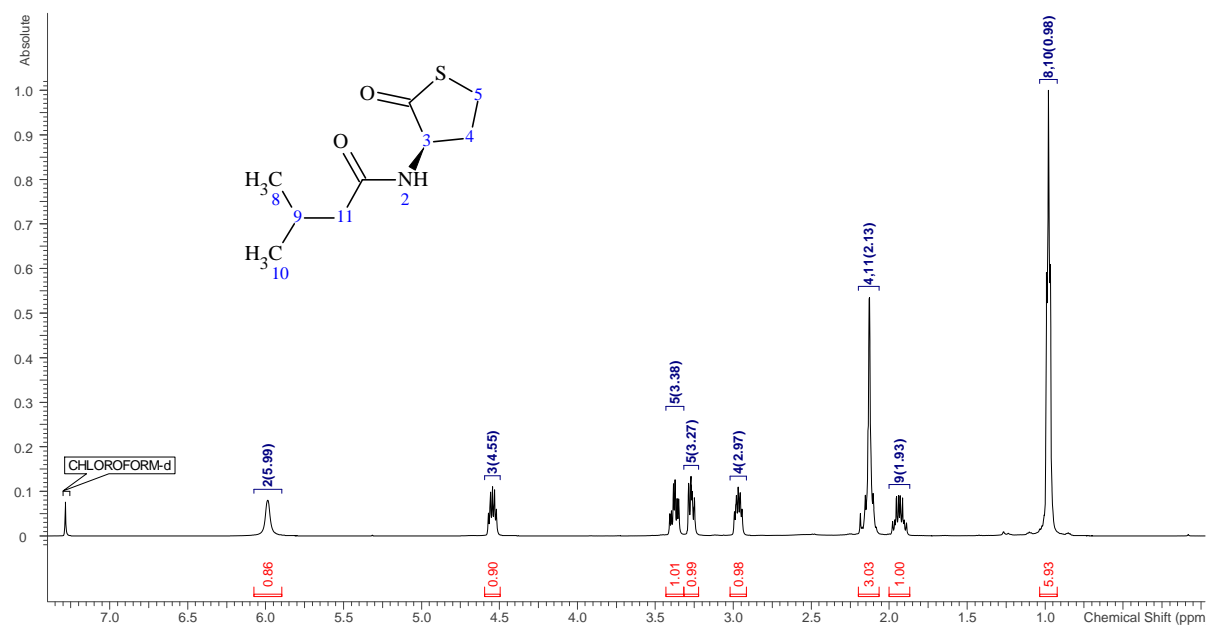
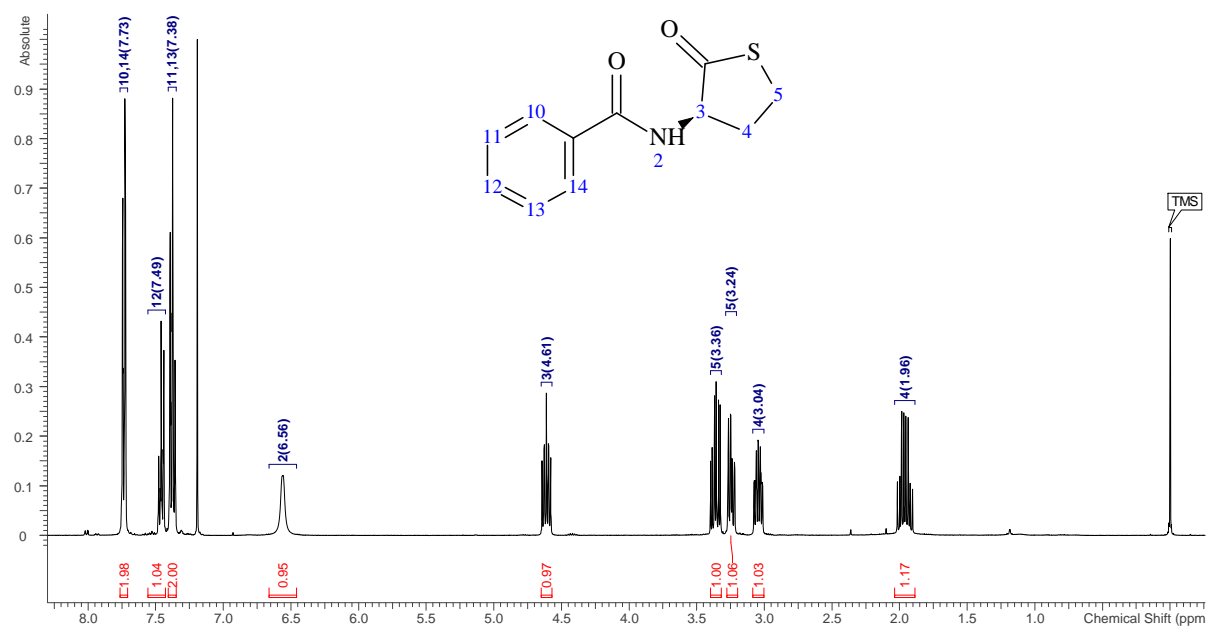


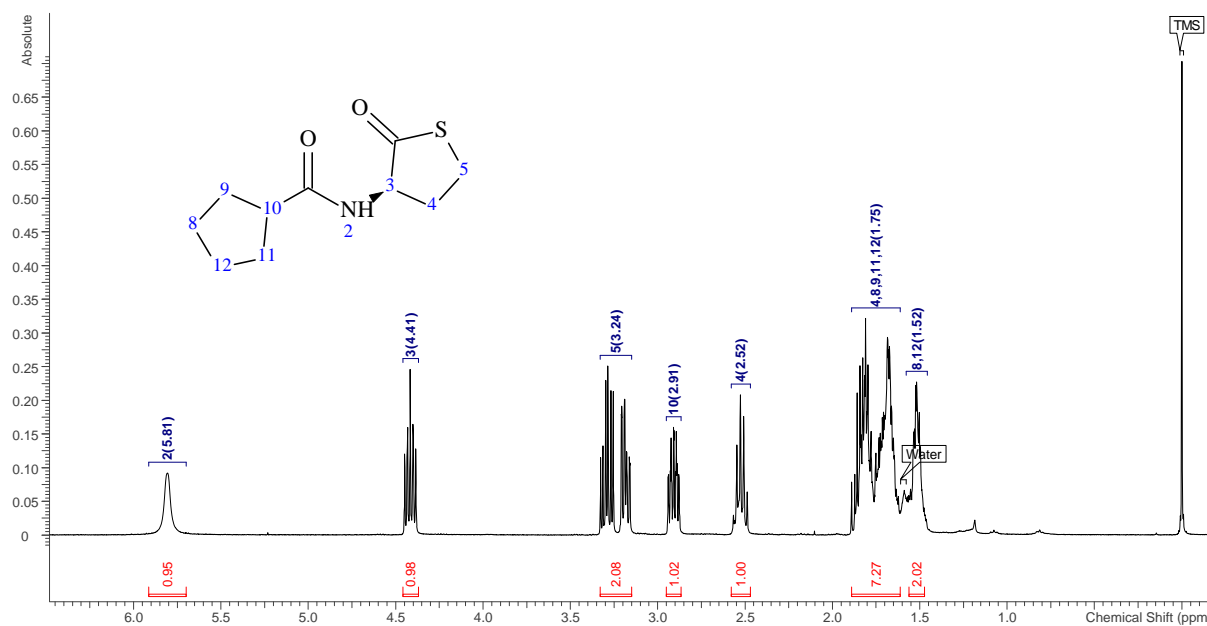
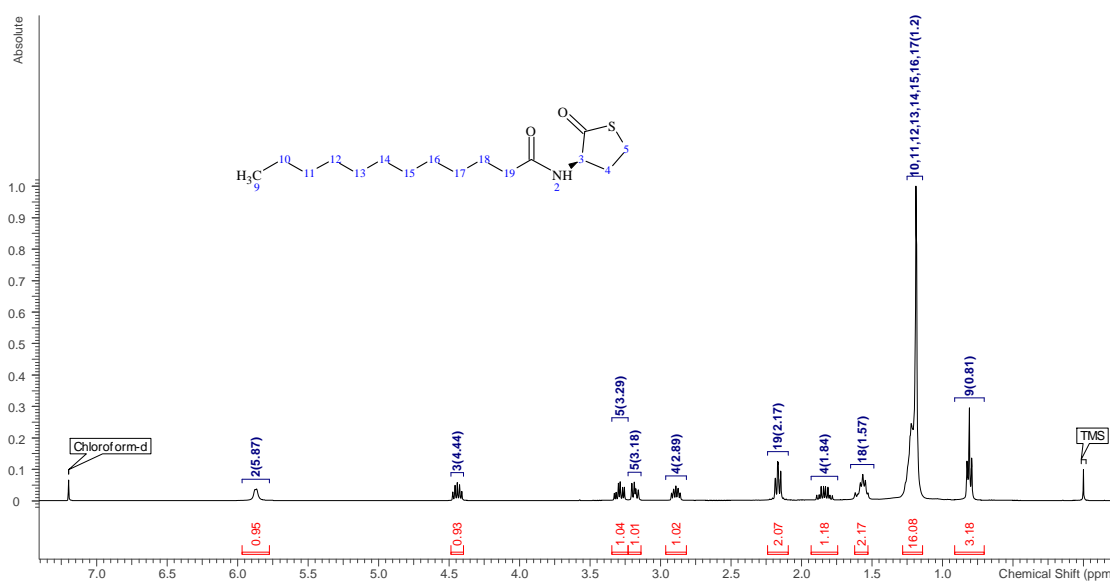


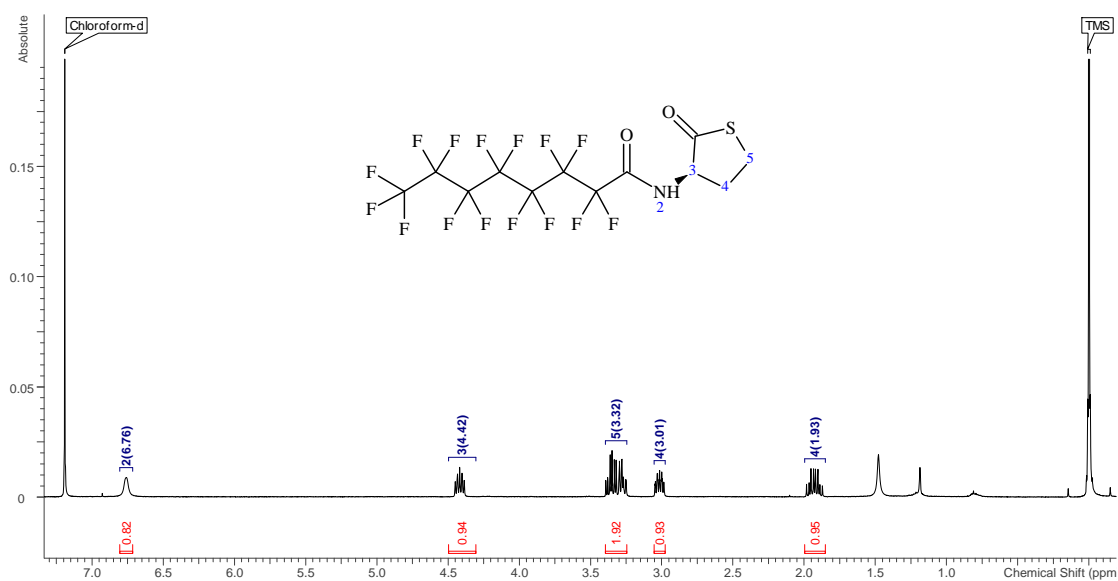
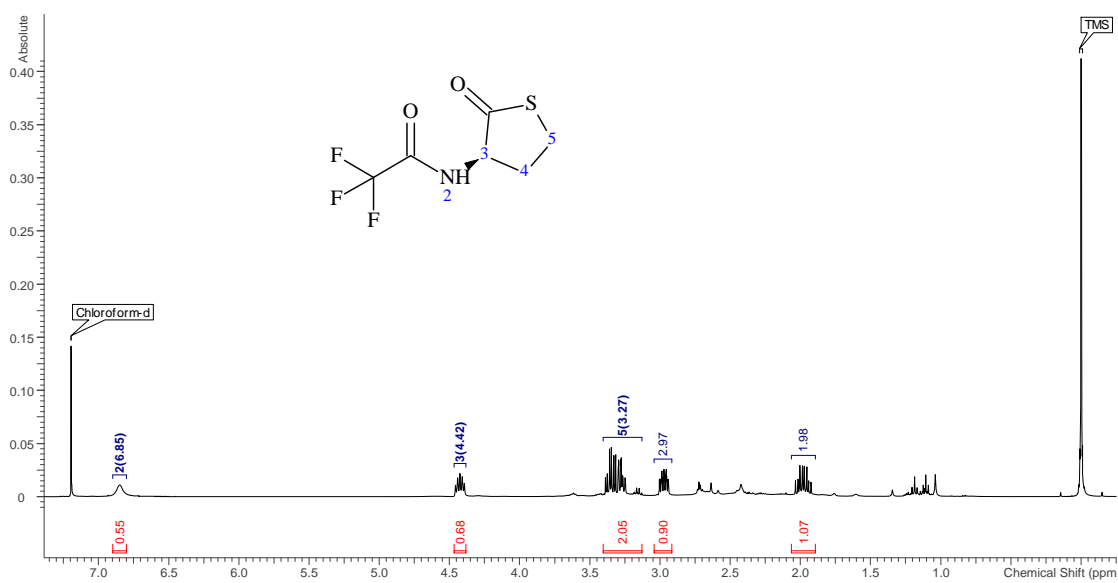
## 10.2 NMR spectra

### Chapter 3.1.2

**T<sub>1</sub>****T<sub>2</sub>**

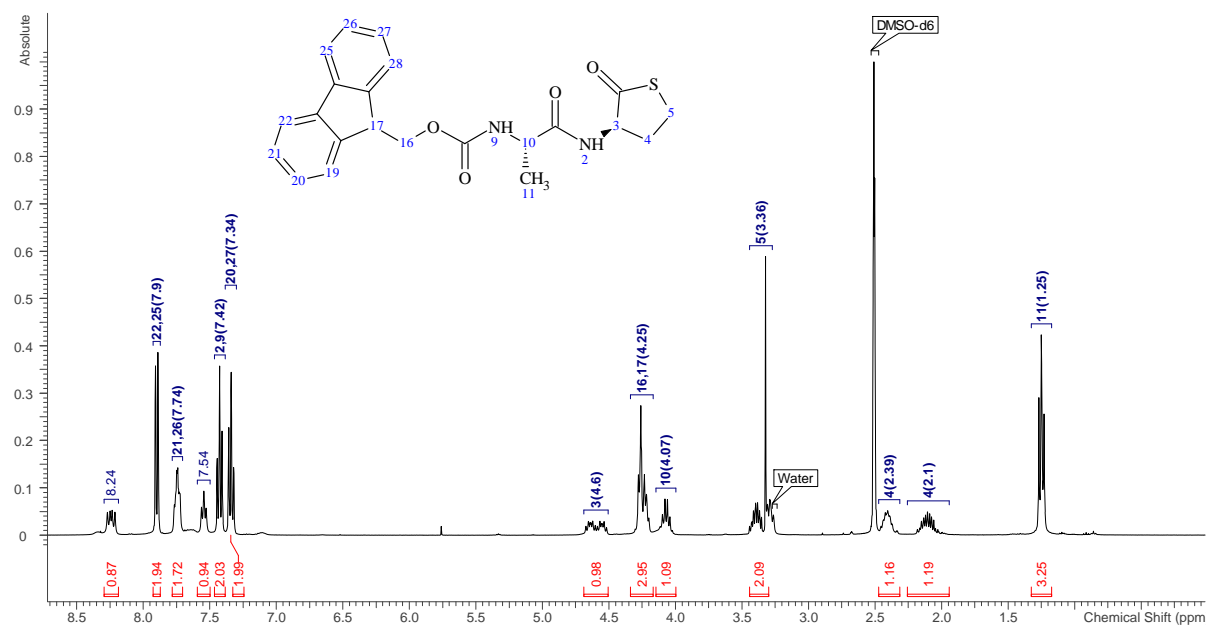
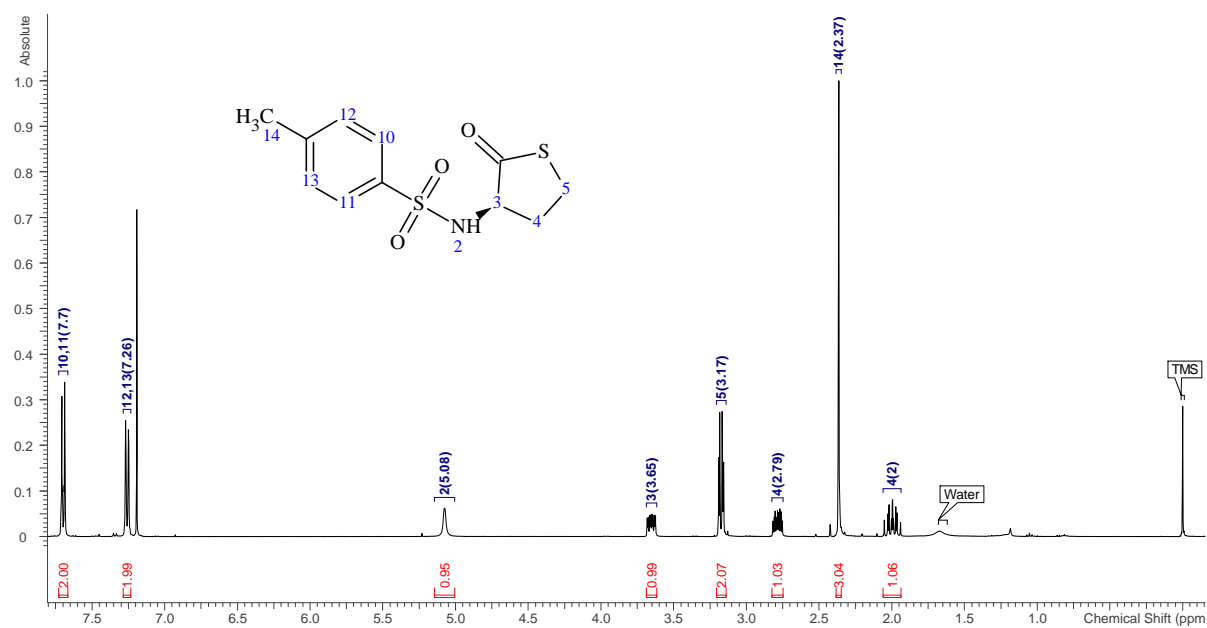
**T<sub>3</sub>****T<sub>4</sub>**

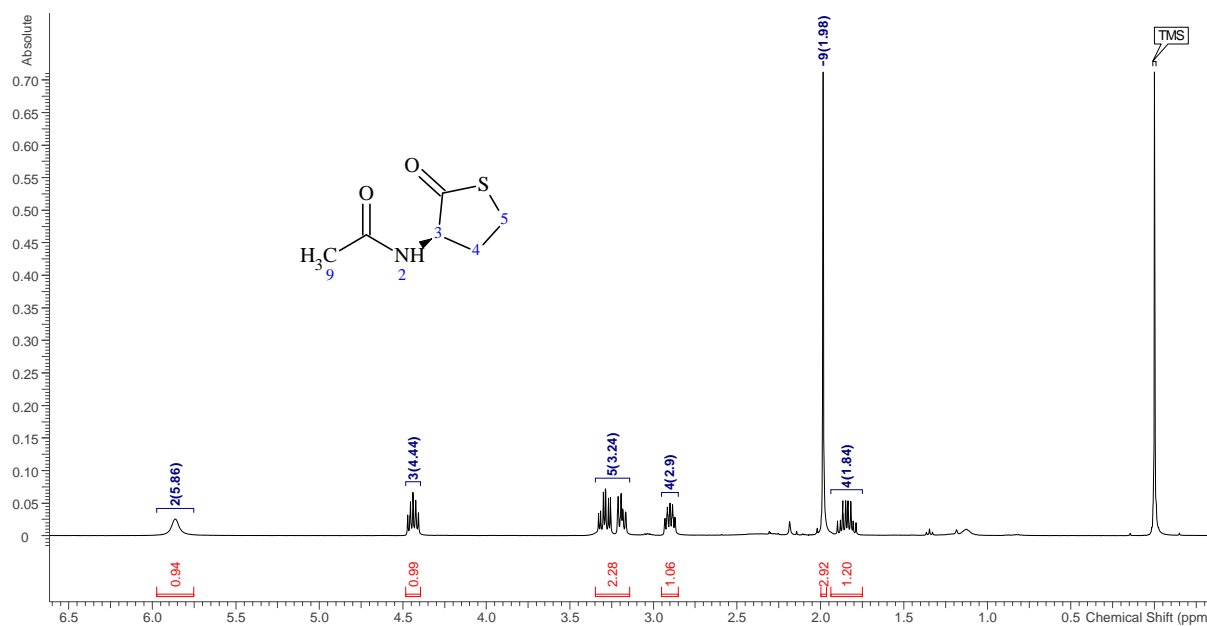
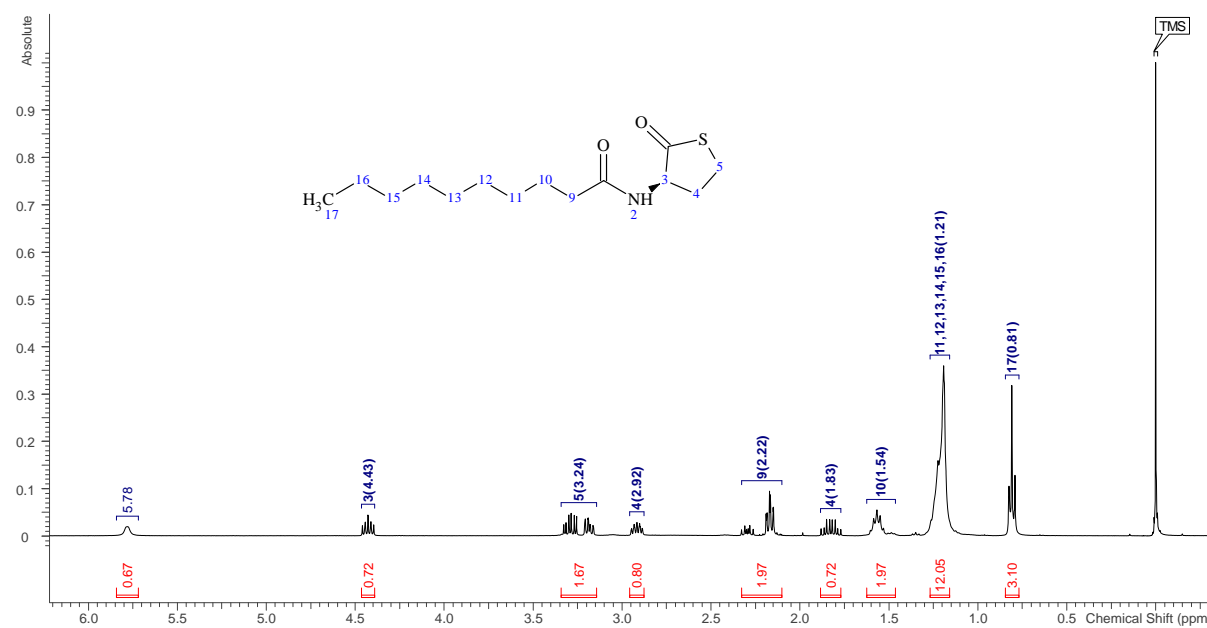
**T<sub>5</sub>****T<sub>6</sub>**

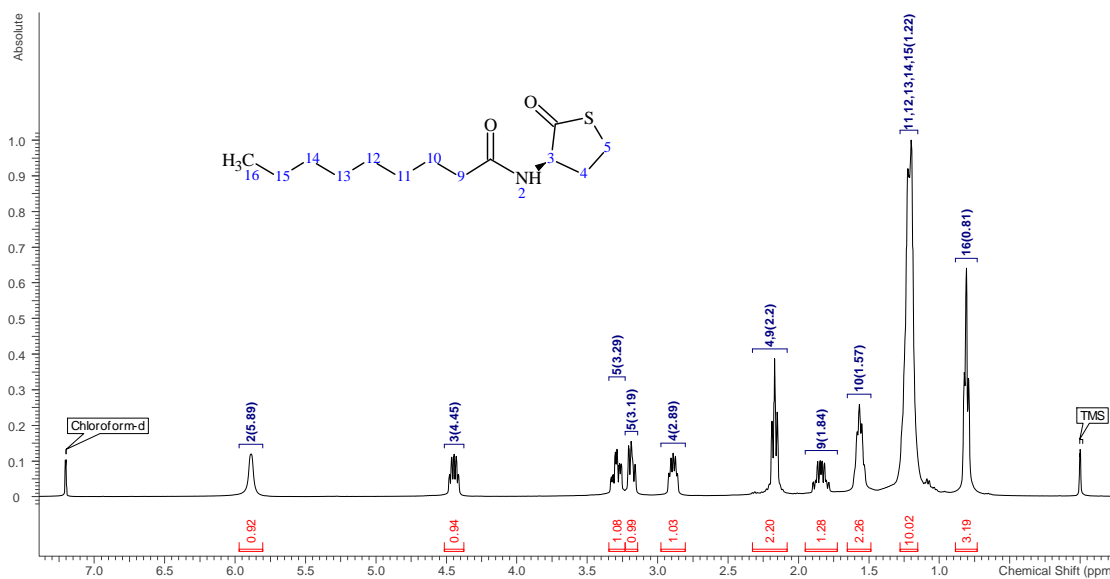
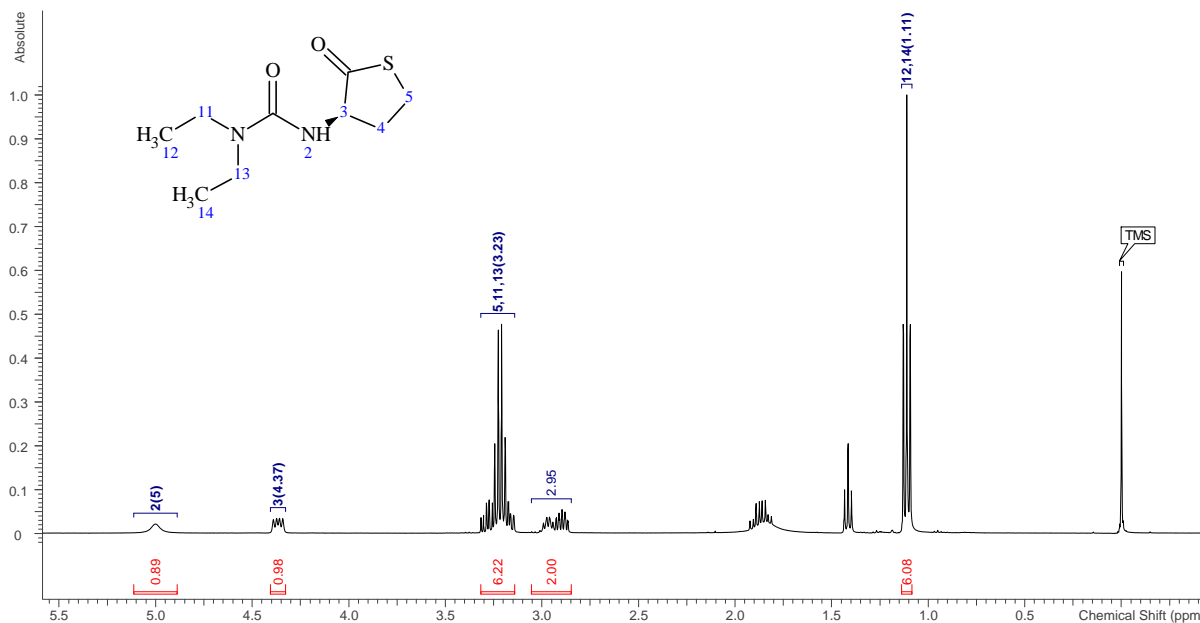
**T<sub>7</sub>****T<sub>8</sub>**

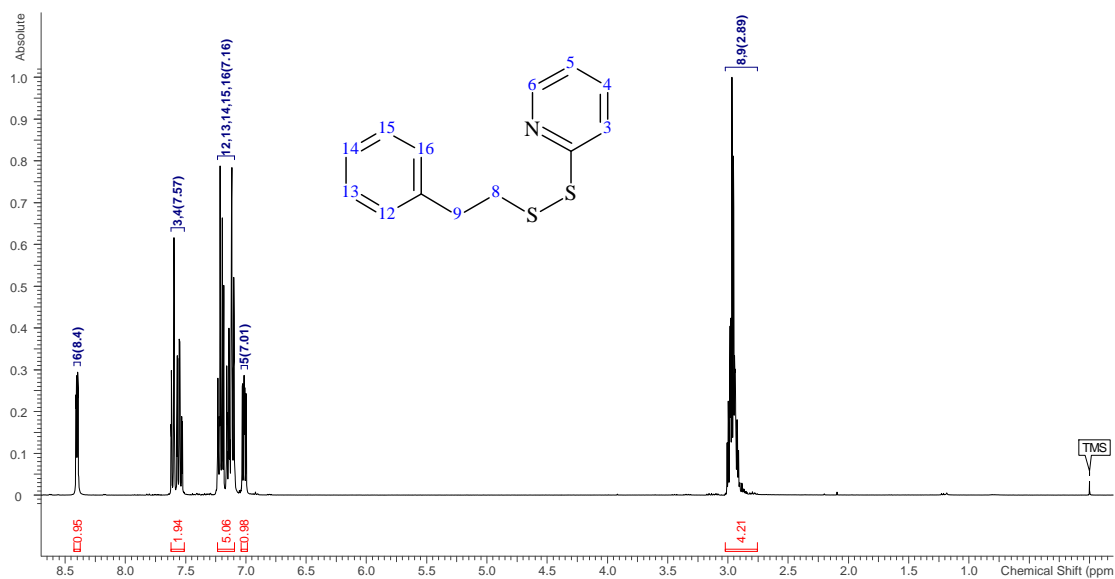
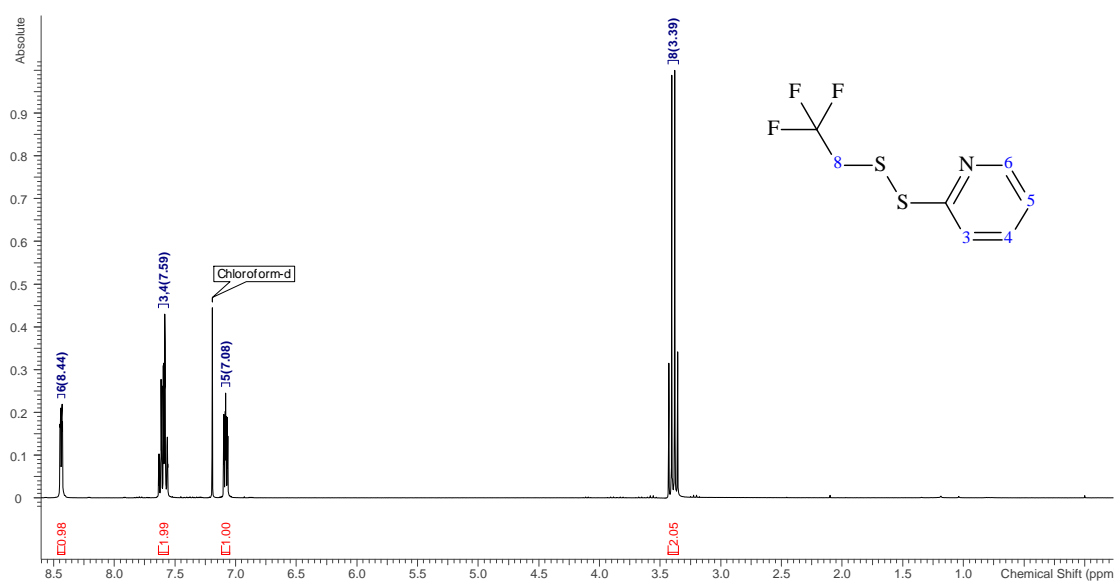


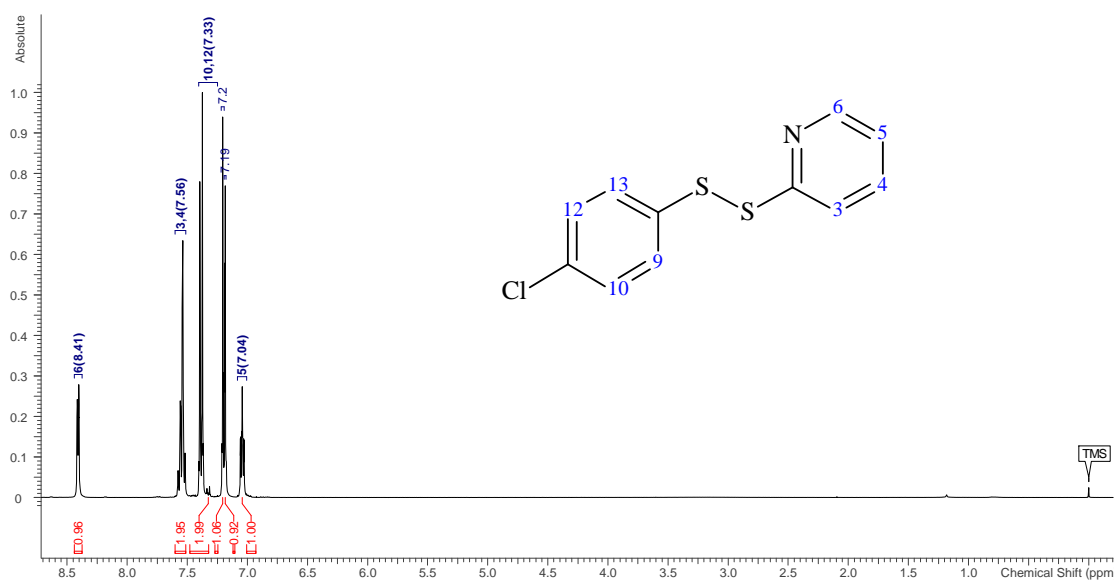
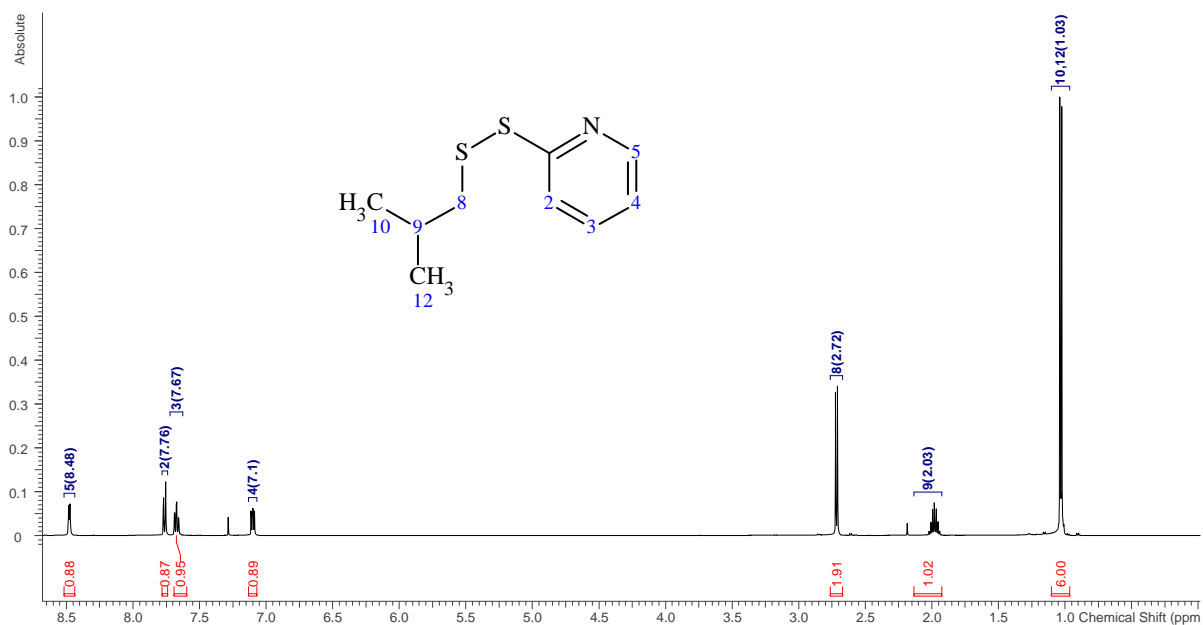


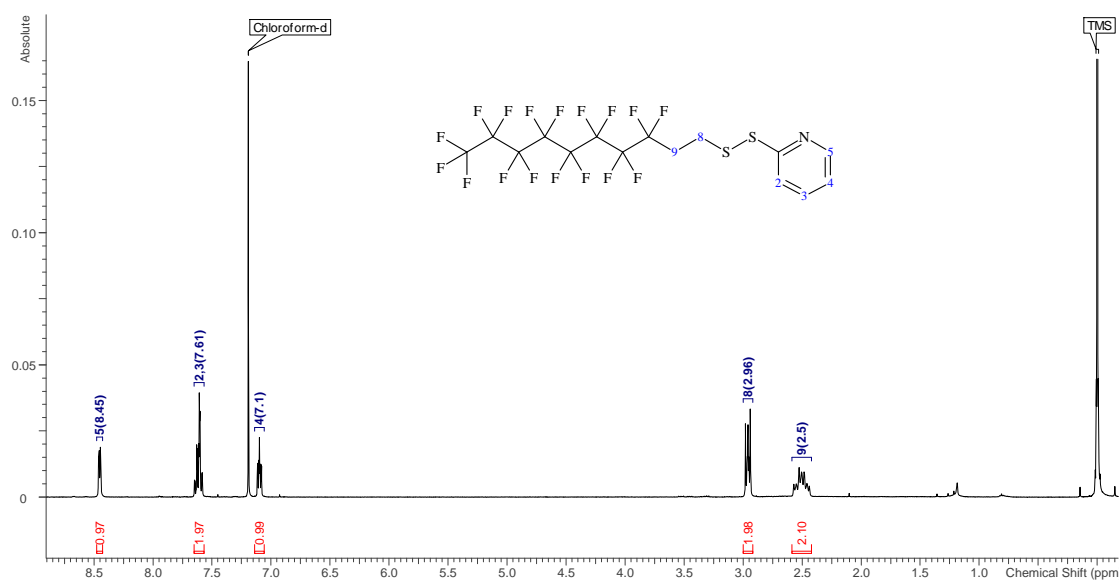
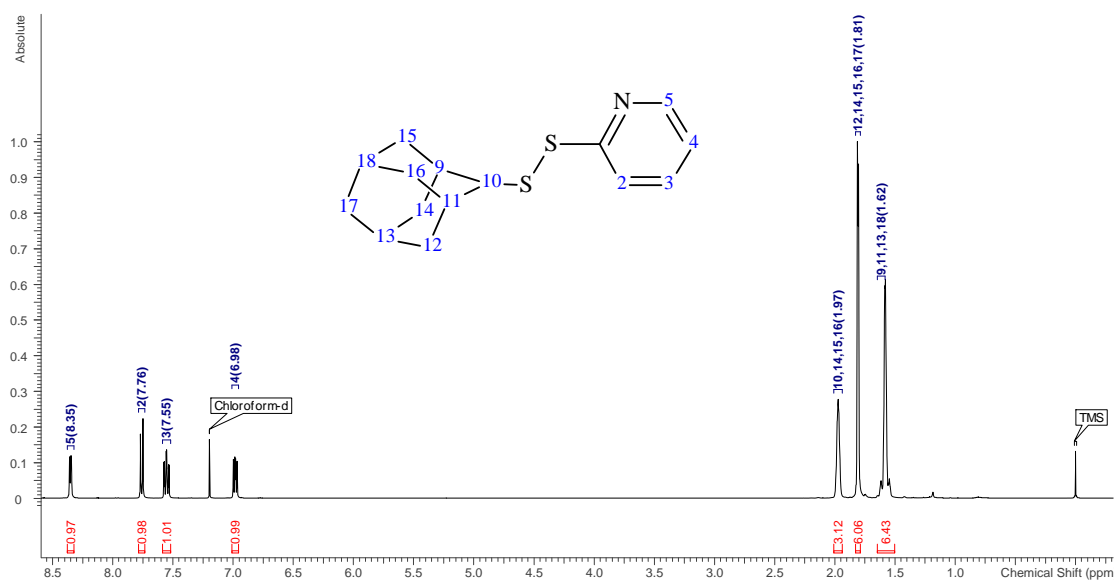
**T<sub>11</sub>****T<sub>12</sub>**

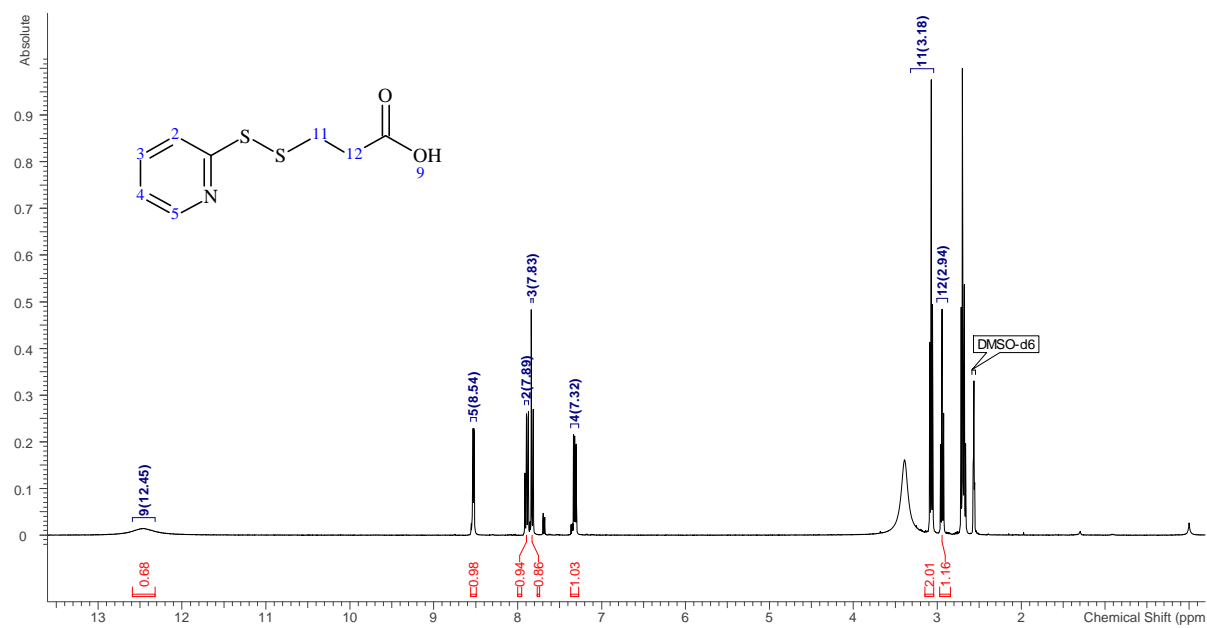
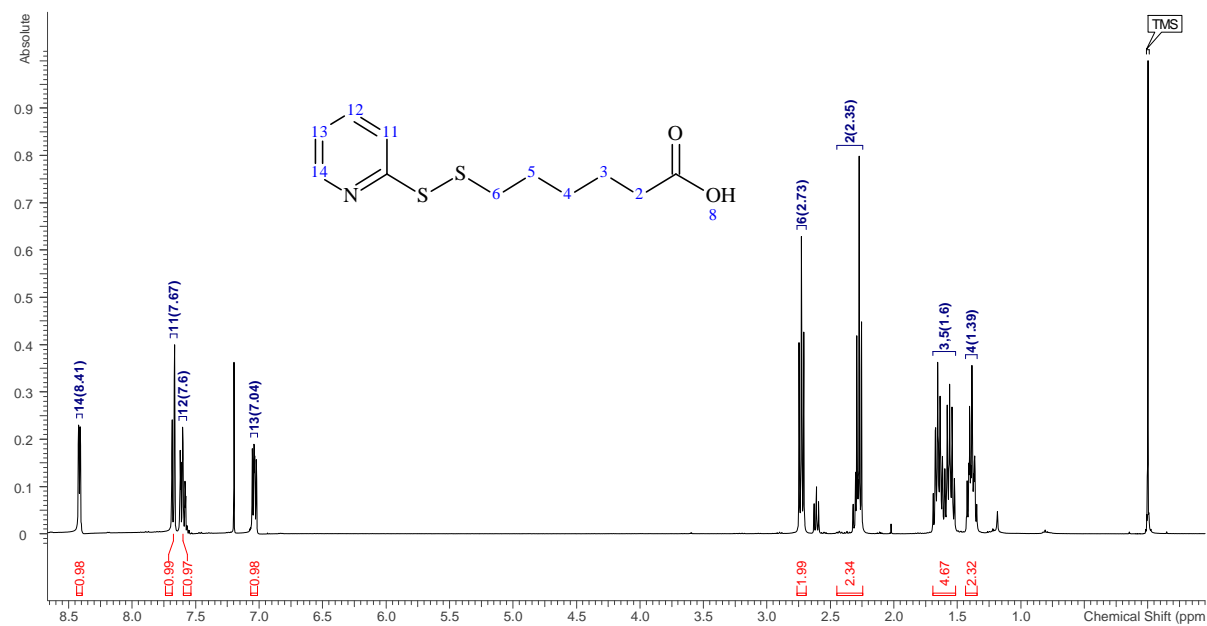
**T<sub>13</sub>****T<sub>14</sub>**

T<sub>15</sub>T<sub>16</sub>

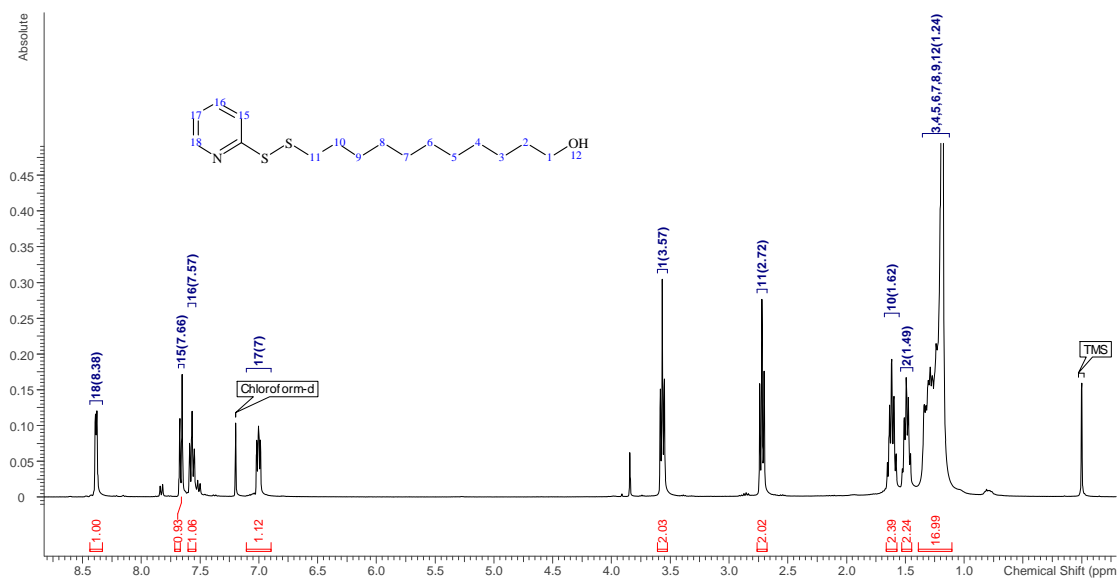
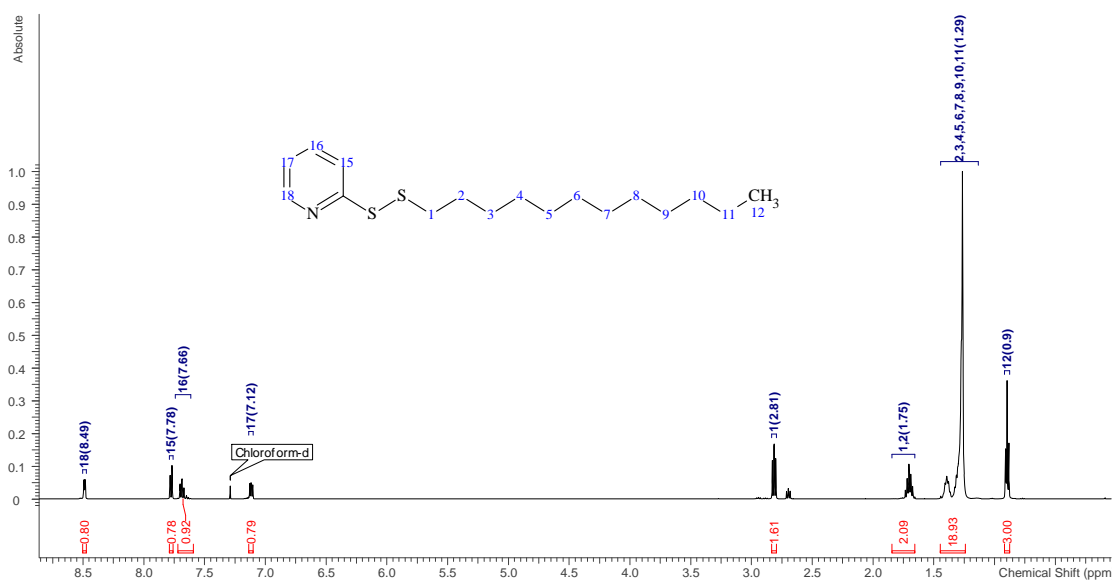
**P<sub>1</sub>****P<sub>2</sub>**

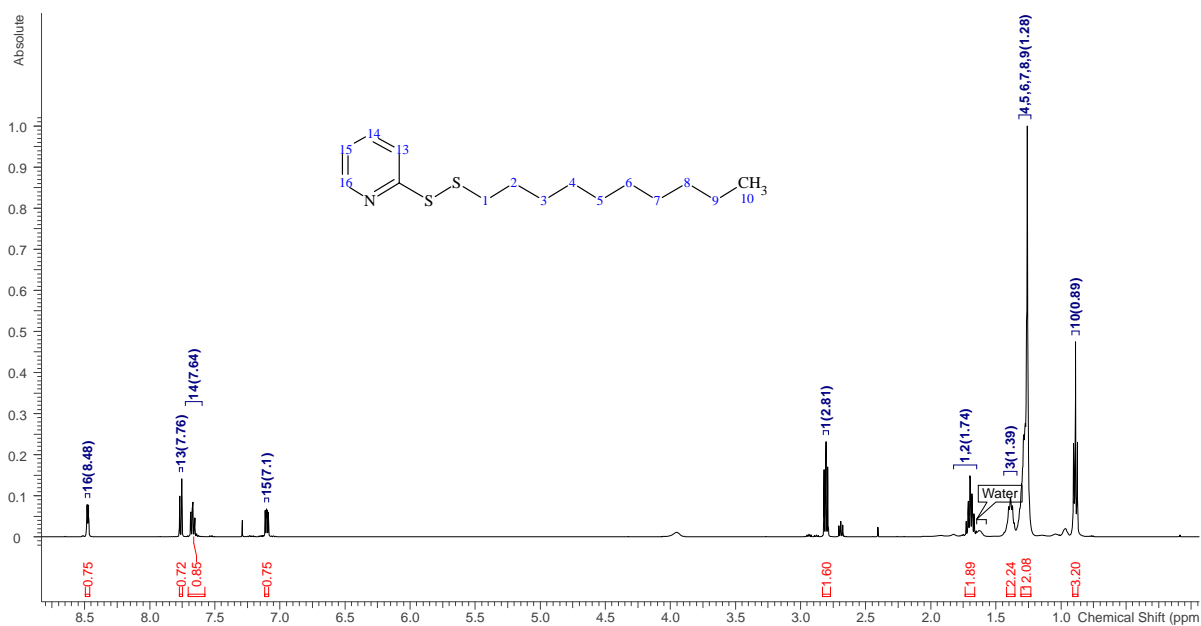
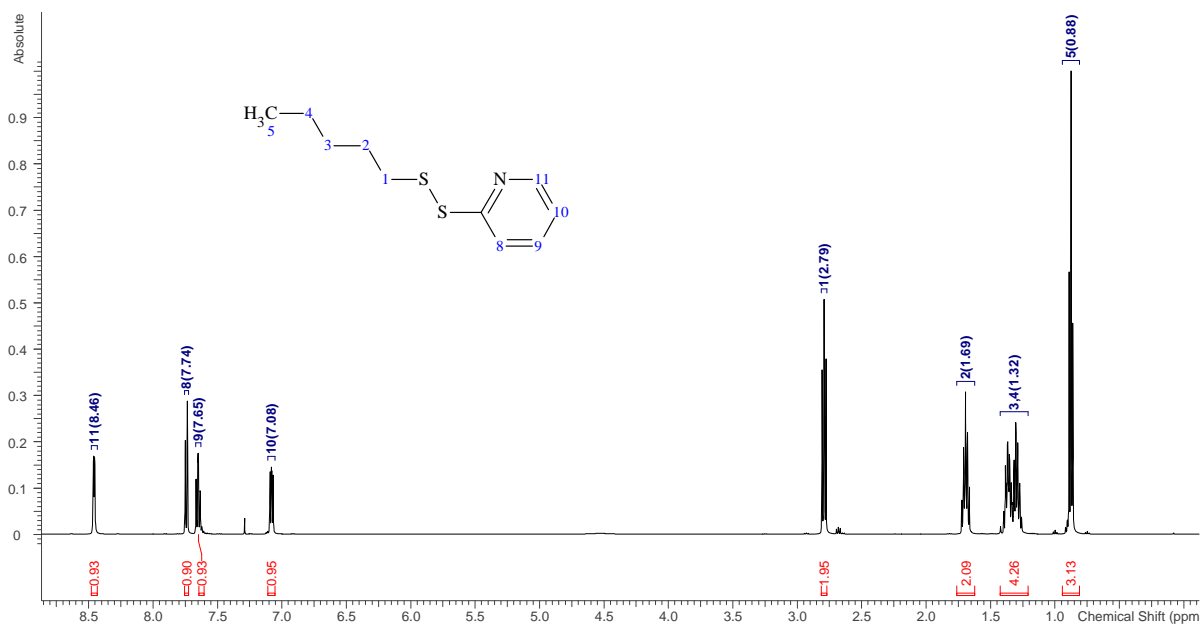
P<sub>3</sub>P<sub>4</sub>

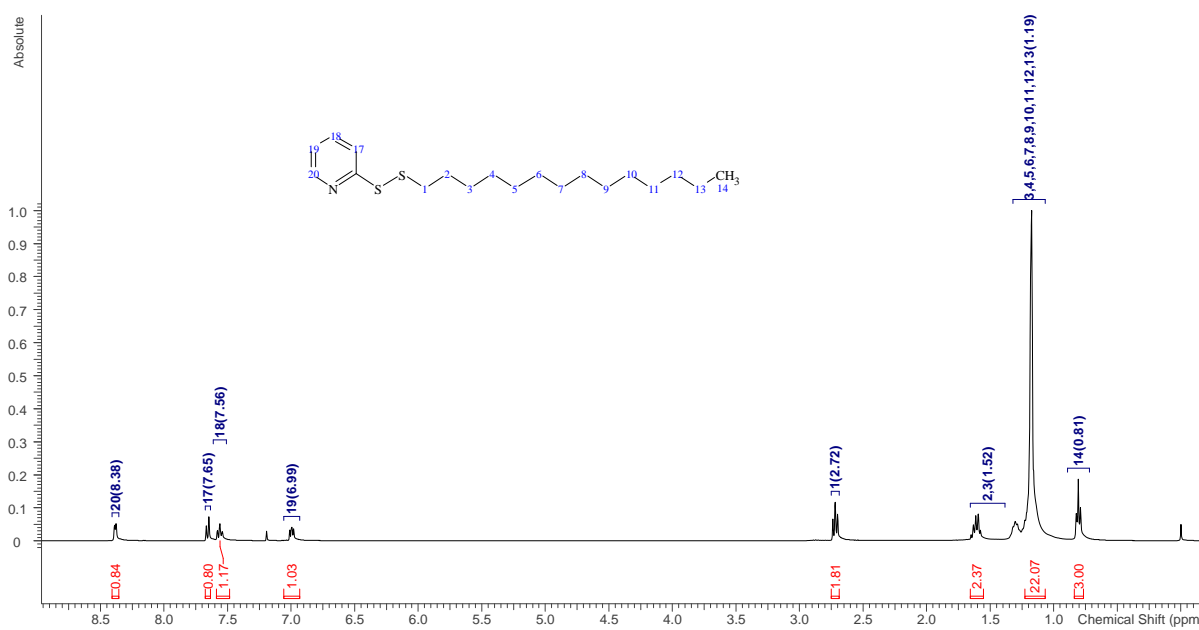
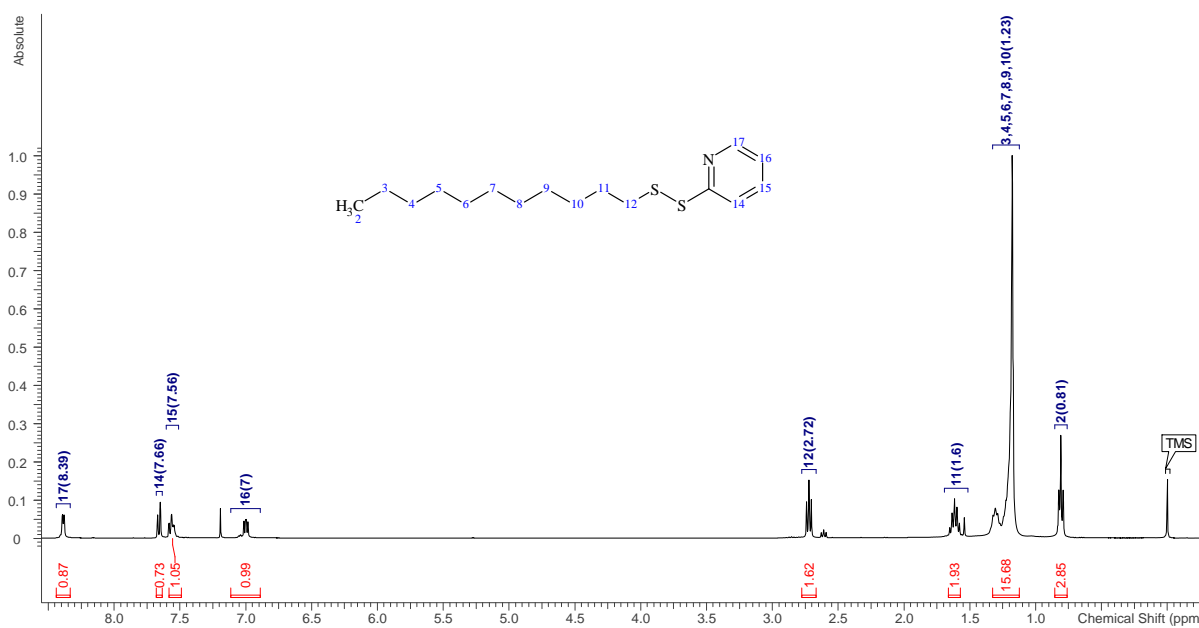
**P<sub>5</sub>****P<sub>6</sub>**

P<sub>7</sub>P<sub>8</sub>

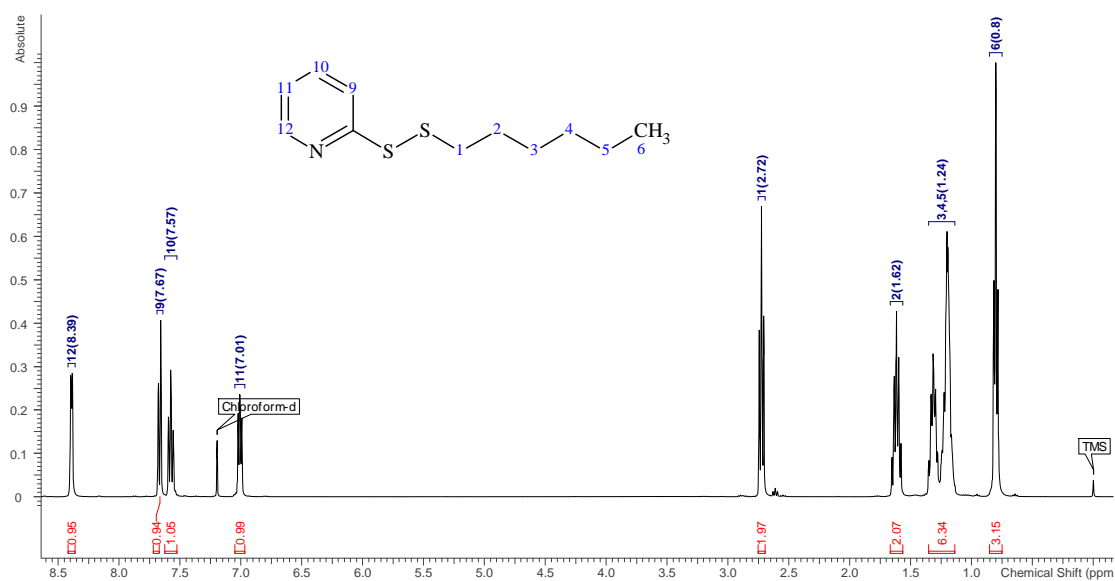


**P<sub>9</sub>****P<sub>10</sub>**

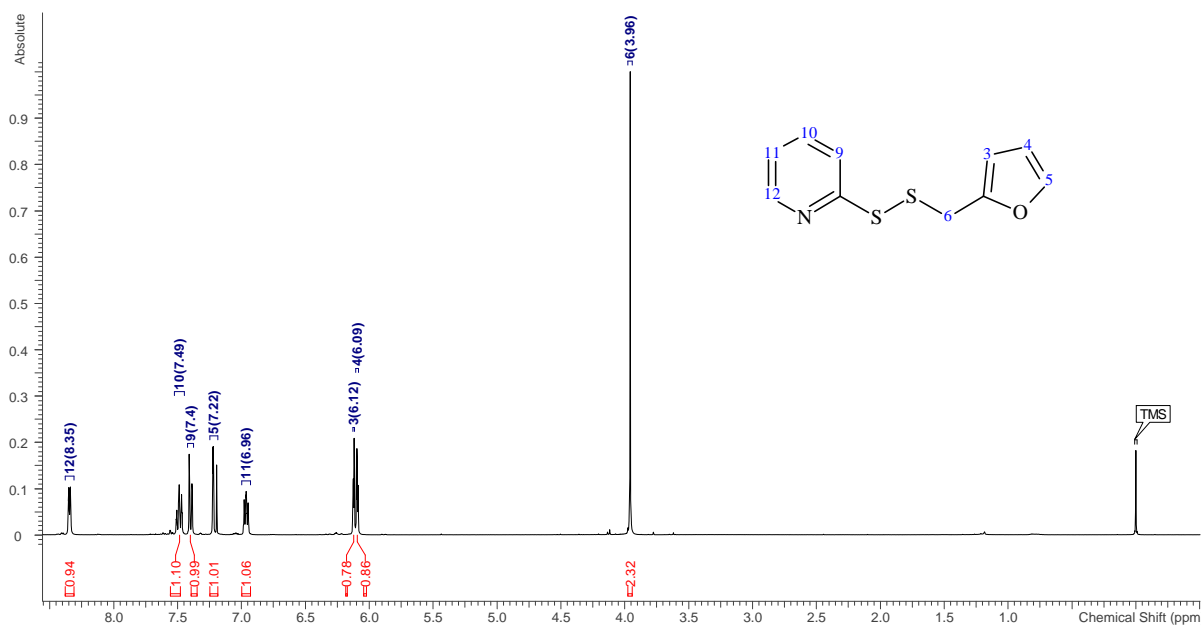
P<sub>11</sub>P<sub>12</sub>

P<sub>13</sub>P<sub>14</sub>

## P15

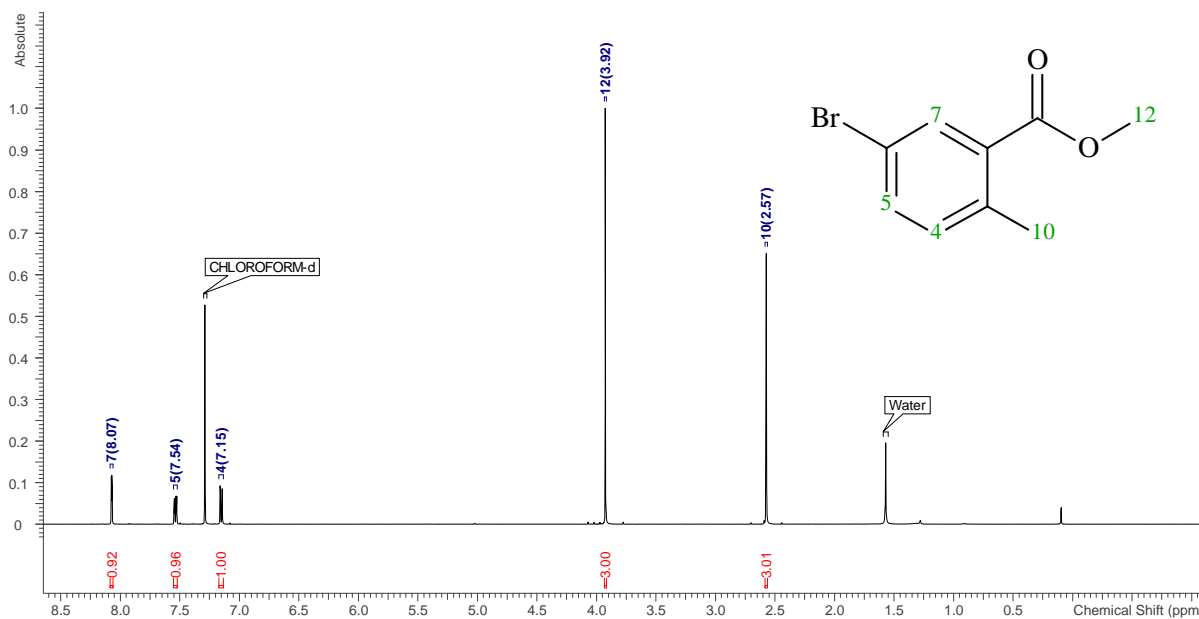


## P16

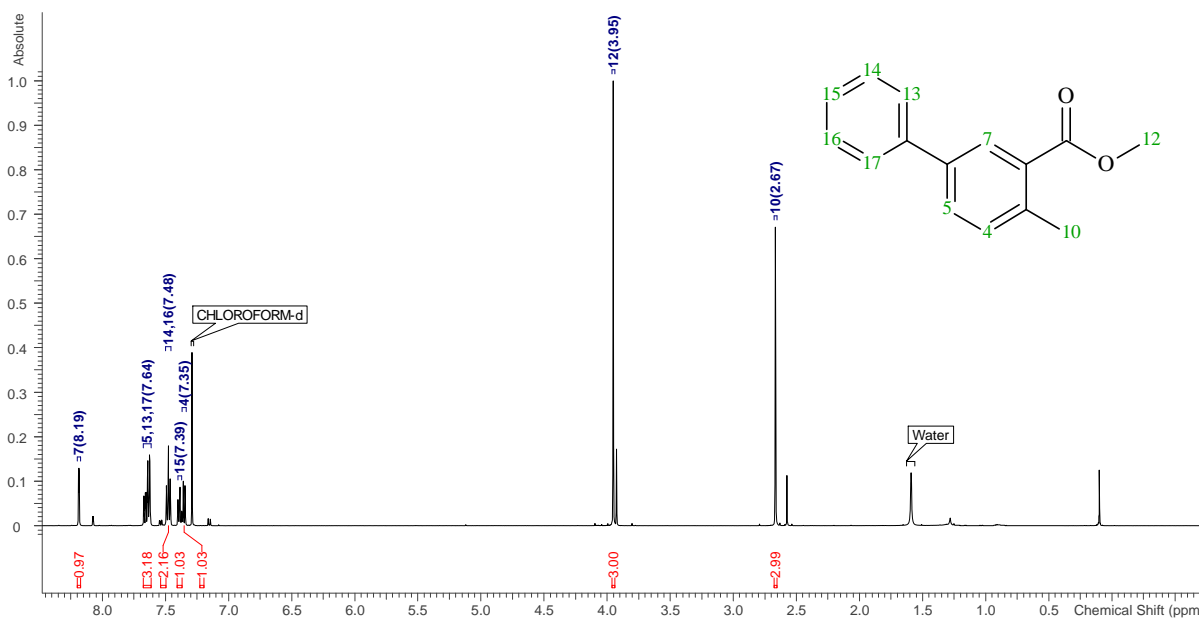


## Chapter 3.2.1

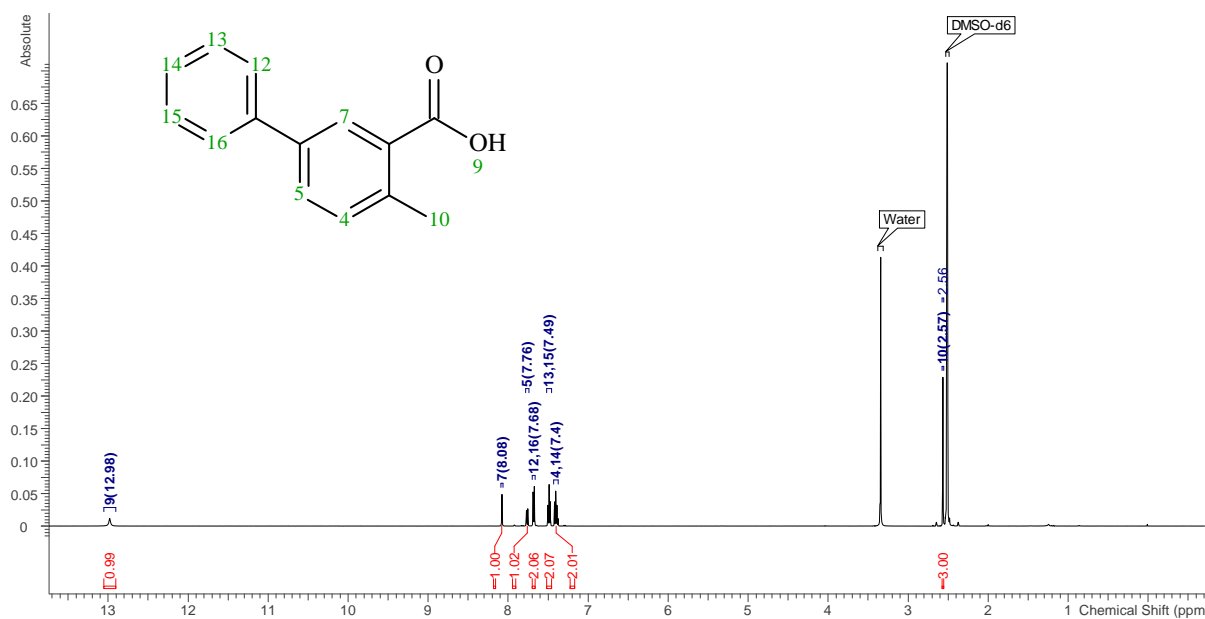
## Intermediate SMR1a



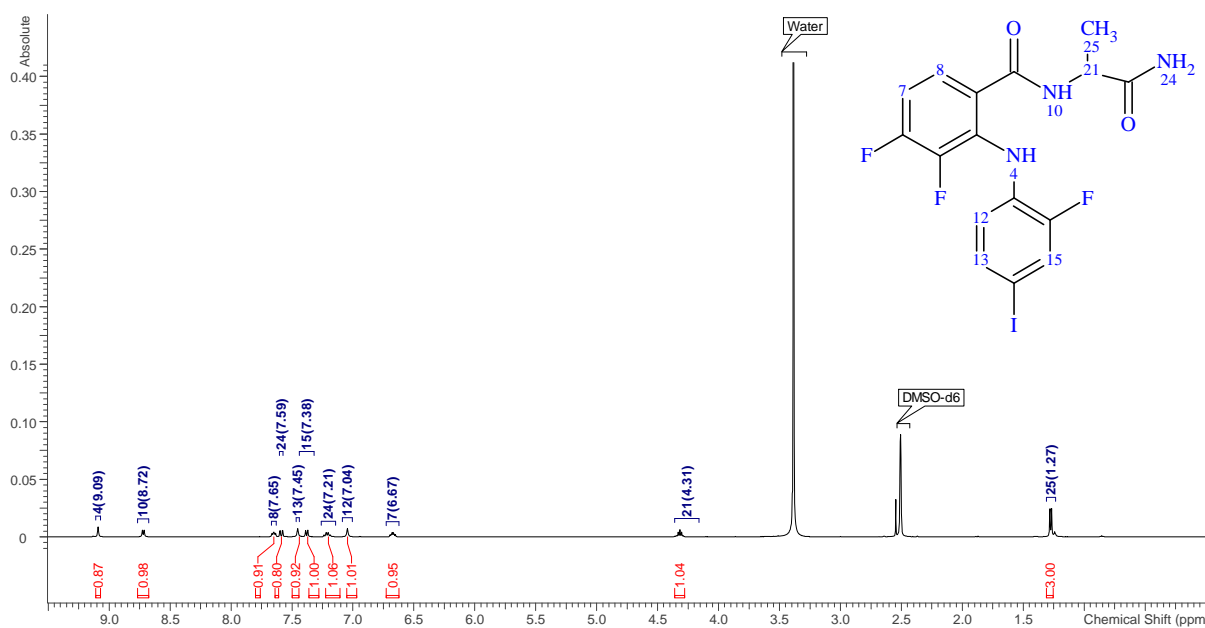
## Intermediate SMR1b

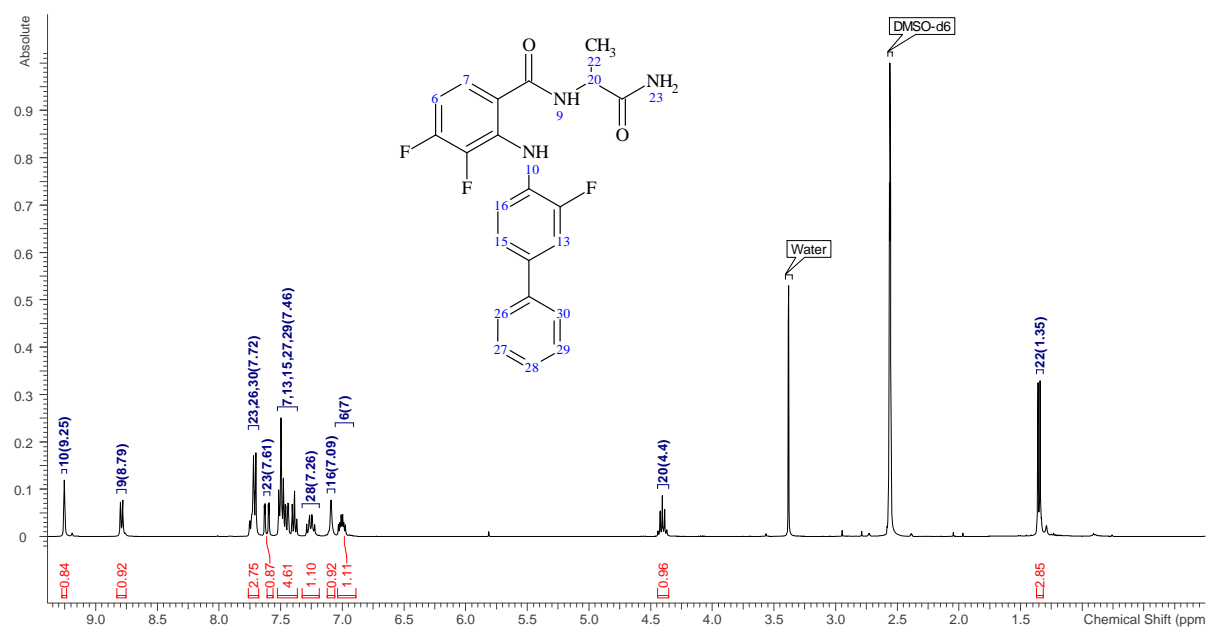


## SMR1

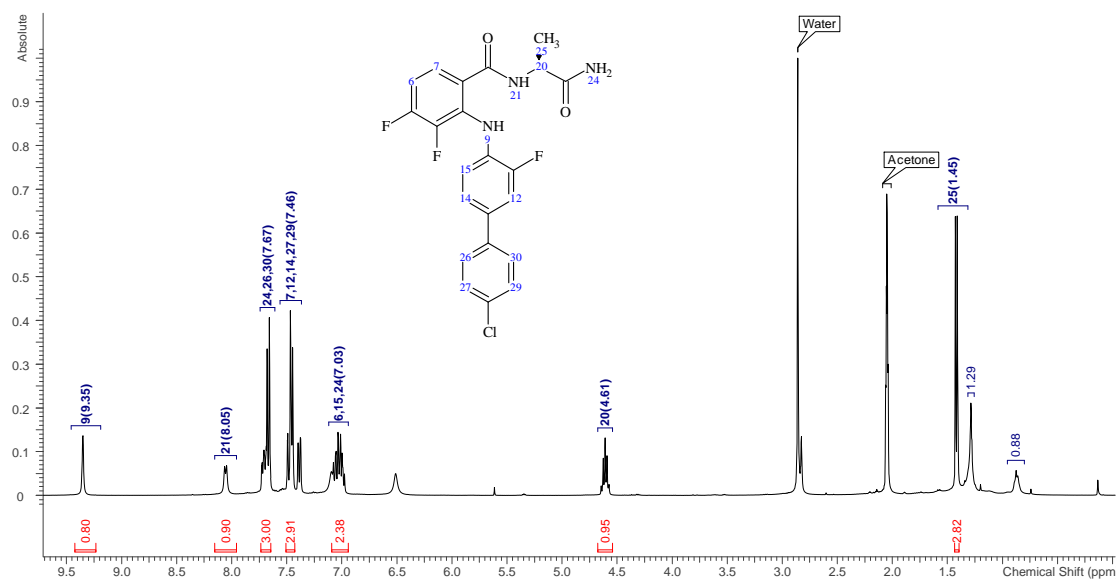


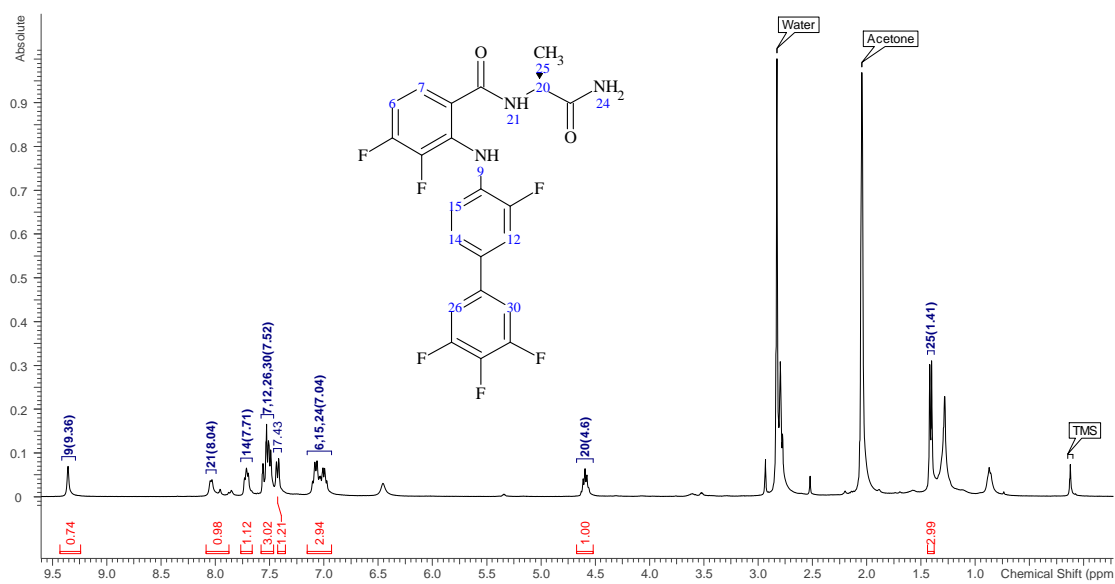
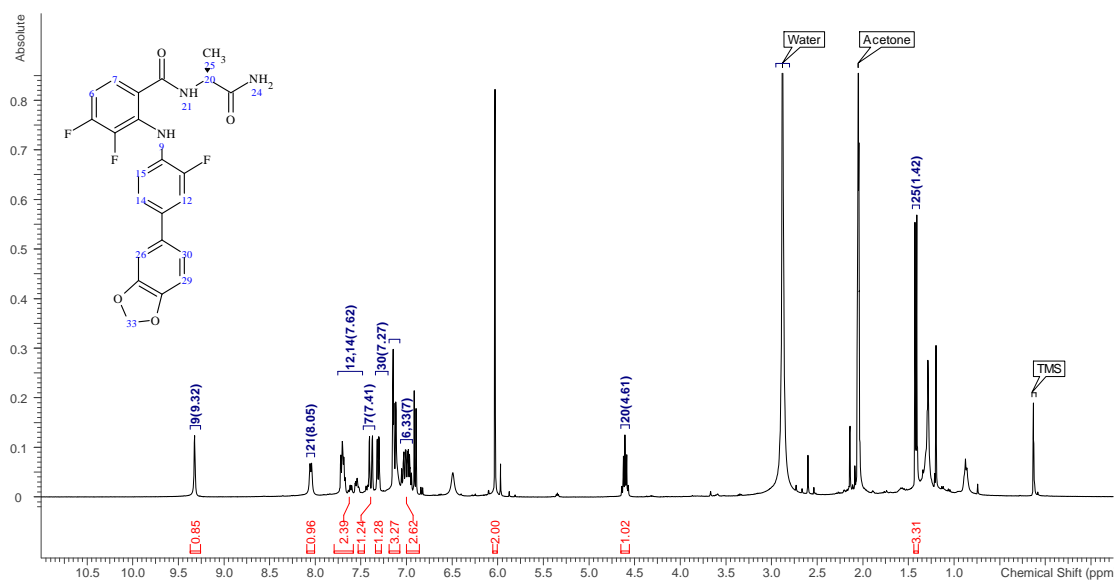
## Chapter 3.2.3

A<sub>2</sub>OTV

A<sub>2</sub>B<sub>18</sub>

## Chapter 3.2.5

A<sub>2</sub>B<sub>13</sub>

A<sub>2</sub>B<sub>16</sub>A<sub>2</sub>B<sub>21</sub>

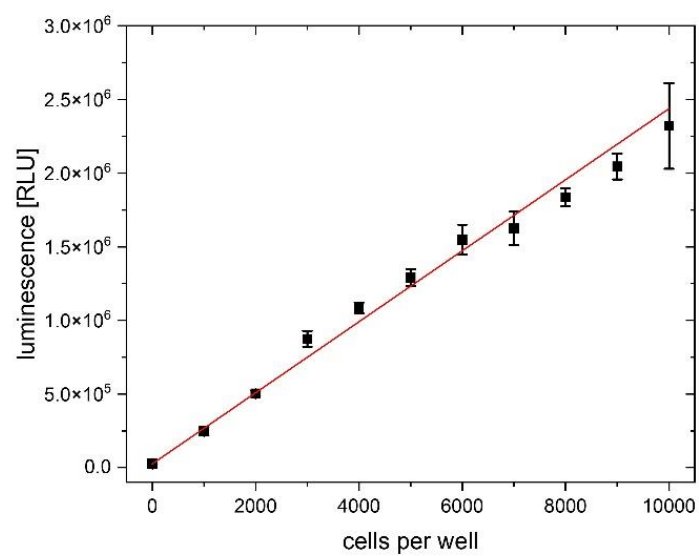


### 10.3 Tables

**Table 12:** Combinations of thiolactone  $T_x$ , 2-pyridyl disulfide  $P_x$  and amine  $A_x$  to investigate the reactivity of the derivatives in solution prior to on-chip reaction. All reactants were used in 0.5 M solutions in DMSO. Product formation was checked via LC-MS.

Thiolactone $T_y$	2-Pyridyl disulfide $P_x$	Amine $A_x$	Product formation
$T_4$	$P_{13}$	$A_5$	No
$T_4$	$P_7$	$A_5$	Yes
$T_4$	$P_1$	$A_5$	Yes
$T_4$	$P_{16}$	$A_5$	Yes
$T_4$	$P_6$	$A_5$	Yes
$T_5$	$P_6$	$A_5$	Yes
$T_5$	$P_7$	$A_5$	Yes
$T_5$	$P_{16}$	$A_5$	Yes
$T_5$	$P_{12}$	$A_5$	Yes
$T_5$	$P_1$	$A_5$	Yes
$T_{14}$	$P_6$	$A_5$	Yes
$T_{14}$	$P_7$	$A_5$	Yes
$T_{14}$	$P_{16}$	$A_5$	Yes
$T_{14}$	$P_{12}$	$A_5$	Yes
$T_{14}$	$P_{11}$	$A_5$	Yes
$T_{16}$	$P_6$	$A_5$	Yes
$T_{16}$	$P_7$	$A_5$	Yes
$T_{16}$	$P_{16}$	$A_5$	Yes
$T_{16}$	$P_{12}$	$A_5$	Yes
$T_{16}$	$P_{11}$	$A_5$	Yes

## 10.4 CellTiter Glo



**Figure 60:** Evaluation of the linearity of the CellTiter Glo assay between 0 and 10.000 cells per well. Each data point is the average of 3 repetitions. Error bars represent standard deviations.

## Acknowledgments

First of all, I want to thank Prof. Pavel Levkin for giving me the opportunity to create this work under his supervision. Thank you for your constructive feedback and support. Also thank you, for always pushing me to my limits, even though it was not always easy. I understand, that it helped me to become a better scientist!

Next, I want to thank Prof. Carsten Hopf from CeMOS for the great collaboration during the last three years. Thank you for all MALDI-screenings performed in your lab.

Special appreciation goes to Prof. Thomas Schwartz for your engagement in discussions and feedback on bacterial-related matters over the past two years. The time spent at your lab working with bacteria was truly enriching, and I thoroughly enjoyed our conversations.

Thanks goes to Dr. Gary Davidson for his useful feedback and criticism at Friday Seminars and my TAC reports!

A massive thanks to Dr. Stefan Schmidt for overseeing all MALDI-MS measurements at CeMOS. Working with you has been a pleasure. You were ALWAYS there, if any question needed to be answered!

I would like to express my gratitude to Sylvia Vanderheiden-Schroen and Dr. Patrick Hodapp from ComPlat for their assistance with borrowed chemicals and analytical devices. Additionally, Dr. Florian Feist's support in measuring numerous samples at the LC-MS at INT is greatly appreciated.

A shoutout to the Levkin Lab for fostering a fantastic working atmosphere. Special thanks to former group member Dr. Marius Brehm, who supervised my master's thesis and played a significant role in my decision to continue as a Ph.D. student in the Levkin Lab. A special thank you to all the people that have been located on "Chemistry Floor" throughout the years! A big Thank for Mariia Kuzina for always being there and helping wherever you could. You were one of the reasons, that the group dynamics was so well balanced! Big thanks to Jovana Topalovska, who started her training at the same time as me and shared the journey through the last three years! Thank you to Michelle Christ, who helped me a lot with the bacterial experiments and thank you to Charlotte Luchena, who was responsible for basically everything in the Levkin Lab. Special thanks to the "Chinese Gang" from Chemistry floor: Zhenwu and Sida, I really enjoyed all of the fun conversations with you, about science and football! You are always invited to see me on the pitch again! A massive thanks to Lutong Lu, who was always

there for me, if I wanted to talk about anything! Massive thanks also to Weiyi Liu for always bringing a smile to my face. Thank you also to Joaquin Urrutia, who was incredible fun to talk to about the most random stuff! Thank you to all the great students that have been to our lab and especially to Maria Lahm, Moritz Enghofer and Maxim Leskov!

Last but not least I want to thank Maximilian Seifermann and Janne Wiedmann! We went through all this time together, managed all the rough times and enjoyed our stays in London and Zagreb together! I don't think that I would have made it through my PhD without you! You both became real close friends and after all, that is one of most important things that I gathered throughout my time at the Levkin Lab! I hope we will always stay in contact!

I also want to thank my grandmother Monika Wand and her husband Herbert Wand! You were always there for me, if I was in need of anything!

And finally, there goes an incredibly huge thanks to Anna-Lena Schnizer! You were always there for me, helping me with everything possible, supporting me in every aspect and just being the most amazing person that exists! Thank you for always believing in me. I love you!

Und Danke Papa, dass du immer für mich da gewesen bist! Ich denke jeden Tag an dich!